National Centre for Nuclear Research

Doctoral Thesis

Constraining neutrino cross-section and flux models using T2K Near Detector with proton information in Markov chain Monte Carlo framework

Author:
Kamil Skwarczyński

Supervisor:
Justyna Łagoda

A thesis submitted in fulfillment of the requirements
for the degree of Doctor of Philosophy

in the

High Energy Physics Division

NATIONAL
CENTRE
FOR NUCLEAR
RESEARCH
ŚWIERK

February 2023

Declaration of Authorship

I, Kamil SKWARCZYŃSKI, declare that this Thesis titled, "Constraining neutrino cross-section and flux models using T2K Near Detector with proton information in Markov chain Monte Carlo framework" and the work presented in it are my own. I confirm that:

- This work was done wholly or mainly while in candidature for a research degree at the National Centre for Nuclear Research.
- Where any part of this Thesis has previously been submitted for a degree or any other qualification at the National Centre for Nuclear Research or any other institution, this has been clearly stated.
- Where I have consulted the published work of others, this is always clearly attributed.
- Where I have quoted from the work of others, the source is always given. With the exception of such quotations, this Thesis is entirely my own work.
- I have acknowledged all main sources of help.
- Where the Thesis is based on work done by myself jointly with others, I have made clear exactly what was done by others and what I have contributed myself.

Signed:

Date:

NATIONAL CENTRE FOR NUCLEAR RESEARCH

Abstract

Constraining neutrino cross-section and flux models using T2K Near Detector with proton information in Markov chain Monte Carlo framework

Kamil SKWARCZYŃSKI

T2K (Tokai to Kamioka) is a long-baseline neutrino oscillation experiment located in Japan. It uses the near detector ND280 and the far detector (FD) Super-Kamiokande to measure neutrino oscillations and determine whether CP is violated in the lepton sector or not. The work presented herein details the process of using data collected by ND280 to constrain the predicted event spectra at Super-Kamiokande. The analysis uses the Markov chain Monte Carlo method without assumptions on the underlying posterior probability density function. The Thesis describes new event samples splitting data based on the presence of protons, as well as new systematic parameters describing neutrino cross-section. Thanks to the use of the ND280 data, it was possible to decrease the uncertainty on FD spectra prediction by a factor of six. This error reduction enabled the precise measurement of neutrino oscillation parameters. T2K data show a preference for nearly maximal CP violation in the lepton sector, with the value of δ_{CP} close to $-\pi/2$ and exclude CP conserving values of 0 and π within 90% credible intervals. In addition, T2K data suggest the normal mass hierarchy and lower θ_{23} octant, and provide the most precise measurement of $\sin^2\theta_{23} = 0.552^{+0.022}_{-0.053}$. The work described in the Thesis has been included in the T2K official results presented at the Neutrino 2022 conference. The Thesis presents exploratory studies using proton kinematic variables and sensitivity studies with the use of the upgraded ND280 detector.

NATIONAL CENTRE FOR NUCLEAR RESEARCH

Streszczenie

Ograniczanie modeli oddziaływań i strumienia neutrin dzięki wykorzystaniu bliskiego detektora T2K z użyciem informacji o protonach w pakiecie próbkującym Monte Carlo łańcuchami Markowa

Kamil SKWARCZYŃSKI

T2K (Tokai to Kamioka) jest neutrinowym eksperymentem z długą bazą znajdującym się w Japonii. T2K używa zarówno bliskiego detektora ND280, jak i dalekiego detektora Super-Kamiokande (SK), aby mierzyć oscylacje neutrin w celu określenia, czy symetria CP jest łamana w sektorze leptonowym, czy też nie. Praca ta opisuje użycie danych zebranych przez ND280 w celu ograniczenia błędu na rozkłady przypadków przewidywane w SK. W analizie użyto próbkowania Monte Carlo łańcuchami Markowa bez żadnych założeń co do funkcji rozkładu prawdopodobieństwa. W pracy opisano nowe próbki przypadków z podziałem w zależności pd obecności protonu oraz nowe parametry opisujące niepewność przekroju czynnego. Dzięki użyciu danych ND280 udało się zmniejszyć błąd na przewidywania w SK o czynnik sześć. To pozwoliło dokonać precyzyjnego pomiaru parametrów oscylacji neutrin. Dane eksperymentu T2K wskazują na prawie maksymalne łamanie CP w sektorze leptonowym z wartością δ_{CP} blisko $-\pi/2$ i wykluczają wartości zachowujące CP, 0 i π, z 90% przedziałem wiarygodności. Ponadto dane T2K sugerują normalna hierarchię mas oraz niższy oktant kąta mieszania θ_{23}, dostarczając również najdokładniejszego na świecie pomiaru $\sin^2\theta_{23} = 0.552^{+0.022}_{-0.053}$. Analiza ta stała się częścią oficjalnych wyników T2K pokazanych na konferencji Neutrino 2022. Rozprawa opisuje również studia eksploracyjne z użyciem zmiennych kinematycznych protonu, jak i studia czułości z wykorzystaniem ulepszonego detektora ND280.

Acknowledgements

I am extremely grateful to my supervisor Justyna Łagoda for bearing with me those 4 years, providing consistent support and guidance, introducing me to the OA group and for countless discussions that helped me better understand the nuances of T2K analysis. Moreover, she pushed me to perform additional analyses, including a sensitivity study with SFGD.

I am deeply indebted to Clarence Wret for carefully reviewing all my Pull Requests, guiding me through the nuances of the analysis, and being like an auxiliary supervisor to me. I would like to express my deepest gratitude to Patrick Dunne for always being ready to answer my even most ridiculous question, for guarding group well-being, and pushing the whole group to deliver the best possible results. I am extremely grateful to Asher Kaboth for his knowledge and assistance with the understanding of the Markov Chain and Bayesian p-value. I thank other members of the MaCh3 group for helping me to start work on the software, for countless sparkling discussions on Slack, as well as for giving many interesting ideas on how to speed up the code, in particular Daniel Barrow, Edward Atkin, Henry Israel and Ewan Miller. I wish to express my gratitude to Stephen Dolan and Luke Pickering for aiding me with dial implementation and helping me understand the beautiful world of neutrino interactions. I am thankful to people from the BANFF group, Tristan Doyle and Ciro Riccio, for helping with cross-validating my work and to FD analysers Thomas Holvey and Kenji Yasutome for using work within my Thesis to obtain brilliant oscillation results. I would like to recognise the help of Alexander Izmaylov for sharing his psyche/highland2 expertise and Lukas Berns and his statistical wisdom.

I would like to extend my sincere thanks to the members of the Warsaw Neutrino Group for the warm atmosphere, in particular Tomas Nosek, Lakshmi S. Mohan, Piotr Kalaczynski, and to my roommates Yashwanth S. Prabhu and Maitrayee Mandal, who unintentionally introduced me to Bollywood movies. I recognise the assistance of the head of the Polish Neutrino Group, Prof. Ewa Rondio.

I want to express my sincere appreciation to Wojtek Misiak, Mateusz Dobrzeniecki, Aleksander Horne and Robert Kluz for helping me to stay sane, engaging in non-neutrino discussions, and helping me to find new hobbies, especially bouldering. Hopefully, now you have a better opinion about `C++`. Moreover, many thanks to Wojtek Niedziałkowski and his physics-related questions, explaining physics on a popular level is challenging but fun. I want to thank Wojtek Żurek and KinKpin band for producing great music which I listened to while writing this thesis. In addition, I want to thank Michał Pośpiech, Maciek Palczyński, Aleksander "Kubań" Michał, Joanna Lesiak, Maciek Goszczycki, Kasia Kowalczuk, Mikołaj Grabowski, Konrad Kawałkiewicz.

Special thanks to my family, including my bro Paweł, parents colonel Artur and Jadwiga, as well as "wujek" Bartosz with his supportive family, Magdalena, Emanuel, Beniamin, princess Estera, and my grandparents, Janusz, Maria and Anna. I hope you will be proud of doctor Skwarczyński who can't cure.

Big thanks to Wiórek, the most bizarre cat I have ever met, who always cheers up my mood.

Words cannot express my gratitude to Centrum Informatyczne Świerk (CIŚ) cluster for computing resources and all those CPUs/GPUs I could use and play with. Without them, preparing this Thesis would have been much more difficult or even impossible.

This work is partially supported by the Ministry of Education and Science (DIR/WK/2017/ /05) and the National Science Centre (UMO-2018/30/E/ST2/00441).

Contents

To mother nature for being so god damn complex

Introduction

> Alea iacta est.
>
> **Julius Caesar**

Why do we exist, what is time, or when will the world end? These are some questions asked by scientists; some seem trivial, others complex; however, it is the property of science that even those seemingly bizarre, uninteresting questions increase our understanding of the surrounding world. One such question that is tackled in this Thesis is: why do we observe mostly matter in the Universe? As suggested by Sakharov [1], this mystery can be solved by violation of CP symmetry. CP violation in the lepton sector can manifest itself in a different behaviour of neutrinos and their antimatter counterparts. The parameter describing CP violation is δ_{CP}, with allowed values from $-\pi$ to π.

Neutrinos are quite peculiar elementary particles that are very hard to detect and have a very small mass. Three neutrino flavours have been observed (e, μ, τ) and LEP measurements [2] suggest there are no more types of light active neutrinos. Neutrinos can oscillate, which means that a neutrino of one flavour can change into another flavour while propagating through time and space. If $\sin\delta_{CP}$ is non-zero, we will observe different oscillation amplitudes for neutrinos and antineutrinos. The measurement of δ_{CP} is the main goal of modern neutrino experiments.

One of the experiments studying CP violation in the lepton sector is Tokai-to-Kamioka (T2K). T2K is a long-baseline neutrino experiment using a near detector station (ND280 and others) and a far detector, Super-Kamiokande. T2K uses a muon-neutrino beam created at the J-PARC laboratory in eastern Japan. The beam is first measured at the Near Detector station, which is close to the neutrino beam production point and where the oscillation effect is negligible, while Super-Kamiokande is located at such a distance for which the effect is maximal. The event rates in Super-Kamiokande depend on the neutrino flux, cross-section and oscillation probabilities. One of the detectors in the near detector station, namely ND280, is used to reduce the cross-section and flux uncertainty, thus allowing to greatly constrain predicted event rates in the far detector. The latest T2K results favour nearly maximal CP violation [3].

Modelling of the neutrino cross-section is the leading systematic error in the T2K experiment; therefore, ND280 uses several event samples tailored towards constraining particular reaction modes. One of many important effects is related to Final State Interactions (FSI): when a particle produced in a neutrino interaction and propagating through the target nucleus can interact with nucleons inside it (scattering, absorption, etc.). Such interactions can strongly affect the topology of an event that we are able to observe. Another interesting effect is due to the so-called Two Particles Two Holes (2p2h) model: an interaction of a neutrino with a correlated pair of nucleons inside the target nucleus. For neutrinos, a 2p2h interaction can occur on either a neutron-neutron (nn) pair or a neutron-proton pair (pn).

The Author of this Thesis is a member of the T2K collaboration and was one of the main analysts for the Oscillation Analysis (OA) presented for the first time at the Neutrino 2022 conference [3] and later by the Author at the ICHEP 2022 conference [4]. The Author participated in the writing of six Technical Notes covering the details of various aspects of the analysis.

This Thesis describes the development and inclusion of a new ND280 event sample, namely a CC ν_μ sample with no pions, no photons and no protons (CC0π-0p-0γ) or multiple protons (CC0π-Np-0γ) in the observed final state, into the ND280-related part of T2K oscillation analysis. CC0π-0p-0γ and CC0π-Np-0γ samples (henceforth called "proton-tagged samples") have different properties in many regards. As it will be shown, ND280 can reconstruct protons with momentum above the detection threshold of about 450 MeV/c, which means that CC0π-0p-0γ events tend to have overall lower values of four-momentum transfer (Q^2) than events classified as CC0π-Np-0γ. Many effects are dependent on Q^2, such as Pauli blocking, and the proton-tagged samples are highly sensitive to them. The nucleon FSI has a big impact on final nucleon kinematic variables; consequently, proton-tagged samples can help in constraining this systematic uncertainty. Moreover, new samples are sensitive to the 2p2h pair ratio as pn and nn have different distributions of outgoing proton kinematic variables.

Additionally, the Author made multiple improvements to the analysis software used by the collaboration. The technical work is not described in the Thesis, as it was focused on bug fixes and software optimization and validations. The Author was also involved in data acquisition and beam tests for new detector prototypes.

The Thesis consists of the following Chapters:

Chapter 1 serves as an introduction to neutrino physics. A big emphasis is placed on neutrino oscillations and CP violation in the lepton sector. Furthermore, the interactions of ~1 GeV neutrinos are outlined, and in addition, the Spectral Function, FSI and other nuclear effects are described to fully understand the difficulties in measuring neutrinos.

Chapter 2 contains a description of the T2K experiment, including neutrino beam production and near and far detectors. The main attention is placed on the near detector ND280, its role in the T2K experiment, and its detection capabilities.

Chapter 3 describes all event samples used in the ND280 detector. The key point of this Chapter is the description of proton-tagged samples (CC0π-0p-0γ and CC0π-Np-0γ) developed by the Author. Cuts used, sample composition, basis properties, and binning studies are described in detail.

Chapter 4 outlines the sources of systematic uncertainties in ND280 analysis, which are flux modelling, interactions modelling, and detector effects. All uncertainties are described briefly. The Author has implemented the systematic error related to nucleon FSI (previously only pion FSI were available). Furthermore, the Author introduced the systematic error affecting the modelled ratio of pn to nn interactions in 2p2h. The impact of both uncertainties on proton kinematics is studied.

Chapter 5 is an introduction to the T2K Oscillation Analysis (OA), which uses two approaches to obtain results: frequentist grid search and Bayesian Markov chain Monte Carlo (MCMC). The Author used the latter one, which is described in detail. Furthermore, the Chapter describes methods to analyse the output of MCMC, for example, posterior predictive distributions, extracting correlations, and the highest posterior density method.

Chapter 6 describes the T2K results which were presented at the ICHEP conference [4]. The emphasis was placed on parts in which the Author had the largest contribution, which includes the posterior predictive distribution and the postfit values for systematic parameters. Finally, the neutrino oscillation results are presented, which were not done directly by the Author, but would not be possible without the Author's work.

Chapter 7 presents a sensitivity study realized by the Author using proton kinematic variables in the fit for the first time in T2K. Sensitivity studies with upgraded ND280 are also carried out. The upgraded ND280 uses a new detector consisting of novel scintillation cubes. The impact of correlations of parameters related to carbon and oxygen nuclei was estimated. Both studies are important first steps for future analyses.

Finally, Chapter 8 summarizes the results, compares them to other neutrino experiments and discusses future prospects.

Appendix A describes multiple additional studies conducted by the Author to help better understand the presented results, but not necessary for comprehending and following the Thesis. Lastly, Appendix B depicts plots for all samples and parameters, as the main part of the Thesis is mostly focused on a particular set of parameters or particular samples. These plots are not necessary to follow the main part of the Thesis, but they might be of interest to some Readers.

Whenever a new term is introduced for the first time, an explanation is given; however, for the Reader's convenience, all acronyms used with short descriptions are listed at the end of the Thesis.

Some plots shown in the Thesis can be found only in T2K Technical Notes, but proper references are made nonetheless to help distinguish what was done by the Author from what was done by other members of the T2K collaboration.

1

Neutrino Physics

> In war, theory is all right so far as general principles are concerned; but in reducing general principles to practice there will always be danger. Theory and practice are the axis about which the sphere of accomplishment revolves.
>
> **Napoléon Bonaparte**

1.1 Historical Introduction

Neutrinos (ν_e, ν_μ, ν_τ) are lepton type elementary particles with spin 1/2. Contrary to other lepton family members (e, μ, τ), they rarely interact, which makes them difficult to observe. As a consequence, there are still many properties of neutrinos that are not well studied. One such property is the neutrino mass, which for a long time was assumed to be 0. Now we know that neutrinos do have a mass, but it is very small ($\sim$ eV/c^2) [5].

Although the first neutrinos were created a long time ago, shortly after the Big Bang, human studies of neutrino physics are relatively recent. Everything started in the city of Tübingen [6]. On December 4th, 1930, Wolfgang Pauli proposed the existence of a neutral weakly interacting fermion to solve the missing energy mystery in the β decay, as a "verzweifelten Ausweg" (desperate remedy). Neutrinos were measured for the first time in June 1956 by Reines and Cowan [7]. They used a nuclear reactor as a source of antineutrinos and observed positrons emerging in a liquid scintillator from antineutrino interactions (inverse beta decay process, $\bar{\nu}_e + p \rightarrow n + e^+$), as well as delayed coincident gamma photons from neutron capture.

The next mystery that arose around neutrinos was the so-called solar neutrino problem. It was observed in the 1960s by the Homestake experiment, which measured the solar neutrino flux of ν_e to be much lower than expected based on the model of thermonuclear processes inside the Sun [8]. This conundrum remained unsolved for many decades, although a few hypotheses tried to explain it, one of which was neutrino oscillations. Due to the oscillations, ν_e (the only flavour created in the Sun core) could change into ν_μ or ν_τ, resulting in a decrease of ν_e flux and an increase of ν_μ flux, but overall neutrino flux would be conserved. The Homestake experiment was relying on the following reaction to measure neutrinos

$$\nu_e + {}^{36}\mathrm{Cl} \rightarrow {}^{37}\mathrm{Ar}^+ + e^-, \tag{1.1}$$

and since solar neutrinos have energy of a few MeV, the production of μ and τ is impossible, so a measurement of ν_μ and ν_τ is inaccessible.

The concept of neutrino oscillations was first proposed in 1957 by Pontecorvo in analogy to kaon oscillations $K^0 \leftrightarrows \bar{K}^0$ [9]. However, the vacuum oscillation hypothesis couldn't fully explain the measured solar flux. The observation of neutrino oscillations came from studying neutrinos from another source, i. e. Earth's atmosphere.

The discovery was achieved by the Super-Kamiokande collaboration in 1998 [10]. Cosmic rays interacting with Earth's atmosphere produce mesons decaying into neutrinos. Super-Kamiokande observed a deficit of ν_μ coming from below. Since the zenith angle is related to the distance travelled by neutrino in Earth, we can observe the angular dependence of incoming ν_μ flux.

In the case of the solar neutrino puzzle, it is necessary to include yet another effect, called Mikheyev–Smirnov–Wolfenstein (MSW) [11], to the oscillation framework. A neutrino travelling through matter can interact, introducing additional potential to the Hamiltonian, affecting oscillation probabilities. That's why the MSW effect is often referred to as "matter effects". Neutrinos produced in the solar core are affected by the matter effect; hence, the experimental results didn't agree with the vacuum oscillation hypothesis. The solar neutrino mystery was finally solved in 2003 by SNO [12], which used 1 kt of ultra-pure heavy water to measure the total flux of all neutrinos $\phi(\nu_e) + \phi(\nu_\mu) + \phi(\nu_\tau)$ coming from the Sun.

Neutrino physics is a very active field of study with many yet unresolved questions. One of them is the CP violation in the lepton sector, and this topic will be tackled in this Thesis.

1.2 Neutrino Oscillations

Neutrino oscillations are a quantum effect when a neutrino of one flavour changes to another flavour while propagating through time and space. They manifest themselves due to neutrino flavour states (ν_μ, ν_e, ν_τ) being superpositions of neutrino mass states (ν_1, ν_2, ν_3).

In general, the oscillations may be studied in two modes:

- Appearance - measured neutrino has a different flavour than in the initial state, for example: $\nu_\mu \to \nu_e$;
- Disappearance - measured neutrino has the same flavour as in the initial state, for example: $\nu_\mu \to \nu_\mu$.

To better illustrate neutrino oscillations formalism, let's consider for a moment that only two neutrino flavours exist (ν_μ and ν_e). The superposition of states can be expressed using a simple rotation matrix with mixing angle θ (for two flavour system there is only one mixing angle).

$$\begin{bmatrix} \nu_\mu \\ \nu_e \end{bmatrix} = \begin{bmatrix} \cos\theta & \sin\theta \\ -\sin\theta & \cos\theta \end{bmatrix} \begin{bmatrix} \nu_1 \\ \nu_2 \end{bmatrix} \tag{1.2}$$

Knowing this, we can write the time-dependent equation for the flavour state:

$$\nu_\mu(t) = \cos\theta\, \nu_1(0) e^{-iE_1 t} + \sin\theta\, \nu_2(0) e^{-iE_2 t} = \cos^2\theta\, \nu_\mu(0) e^{-iE_1 t} + \sin^2\theta\, \nu_\mu(0) e^{-iE_2 t}. \tag{1.3}$$

The oscillation probability amplitude has the following form:

$$A_\mu = \frac{\nu_\mu(t)}{\nu_\mu} = \cos^2\theta e^{-iE_1 t} + \sin^2\theta e^{-iE_2 t}. \tag{1.4}$$

In such a case, the neutrino disappearance probability is given by the following formula:

$$P(\nu_\mu \to \nu_\mu) = A_\mu A_\mu^* = 1 - \sin^2(2\theta) \sin^2\left(\frac{1.27 \Delta m^2 [\mathrm{eV}^2] L[\mathrm{km}]}{E[\mathrm{GeV}]}\right), \tag{1.5}$$

while the appearance probability is expressed as:

$$P(\nu_\mu \to \nu_e) = \sin^2(2\theta)\sin^2\left(\frac{1.27\Delta m^2[\text{eV}^2]L[\text{km}]}{E[\text{GeV}]}\right), \tag{1.6}$$

where $\Delta m^2 = m_2^2 - m_1^2$, L is the distance travelled by the neutrino (called the baseline), E is neutrino energy and θ is the mixing angle. Factor 1.27 is a consequence of using units convenient for experiments. It is important to notice that the masses aren't directly incorporated into equations, but the squared differences of the masses are.

For neutrinos propagating in matter, we include the interaction term or self-energy V related to coherent forward elastic scattering. All three neutrino flavours can interact via Z^0 exchange in matter. However, only ν_e can interact with electrons via $W^\pm$ exchange resulting in a ΔV potential difference between two mass eigenstates:

$$\Delta V = V_1 - V_2 = 2\sqrt{2}G_F E\rho_e, \tag{1.7}$$

where G_F is the Fermi constant, E is the neutrino energy, and ρ_e is the local electron density in matter. By adding potential to relativistic energy momentum dependence we obtain:

$$E^2 - p^2 = m_i^2 \implies (E+V)^2 - p^2 \approx m_i^2 + 2EV. \tag{1.8}$$

Thus, we can define the effective mass $m_i^2 \to m_i^2 + 2EV$. The full derivation of oscillation probabilities can be found in [13]. Neutrino oscillation probability with matter effects in a two-flavour approximation is given by:

$$P_m(\nu_e \to \nu_\mu) = \sin^2(2\theta_m)\sin^2\left(\frac{1.27\Delta m_m^2 L}{E}\right), \tag{1.9}$$

where:

$$\sin(2\theta_m) = \frac{\sin(2\theta)}{\sqrt{(\Delta V/\Delta m^2 - \cos(2\theta))^2 + \sin^2(2\theta)}} \tag{1.10}$$

$$\Delta m_m^2 = \Delta m^2\sqrt{(\Delta V/\Delta m^2 - \cos(2\theta))^2 + \sin^2(2\theta)}. \tag{1.11}$$

This shows that for the oscillations in matter, the same expression as in vacuum can be used, but with effective PMNS matrix parameters.

Let's consider edge cases to better understand the implications of this effect.

When $\Delta V \to 0$, we get the oscillations in vacuum. However, if $\Delta V \to \infty$, then $\sin^2(2\theta_m) \to 0$, implying that there are no oscillations in very dense matter. Last but not least, an important effect is the so-called MSW resonance, when $\Delta V/\Delta m^2 \to \cos^2(2\theta)$, resulting in $\sin(2\theta_m) \to 1$. That means that even if the mixing angle in a vacuum is very small, due to resonance, we may observe maximal mixing.

A crucial property of the MSW effect is that it allows for determining the sign of the mass difference. If we replace $\Delta m^2 \to -\Delta m^2$ in Eq. 1.10, we get a different value of the effective mixing angle, resulting in different oscillation probabilities, which we can use to compare to experimental results and distinguish between hierarchies.

If we move from the two-flavour approximation to the three-flavour framework, we have three mass eigenstates and two mass differences Δm_{21}^2 and Δm_{32}^2. Since we know from solar and reactor neutrino measurements [14, 15] that $m_2 > m_1$, this leads to two possible neutrino mass hierarchies: normal hierarchy (NH): $m_3 > m_2 > m_1$, or inverted hierarchy (IH): $m_2 > m_1 > m_3$, as shown in Fig. 1.1. Mass hierarchy can be resolved thanks to matter effects although there is also another approach by JUNO experiment [16].

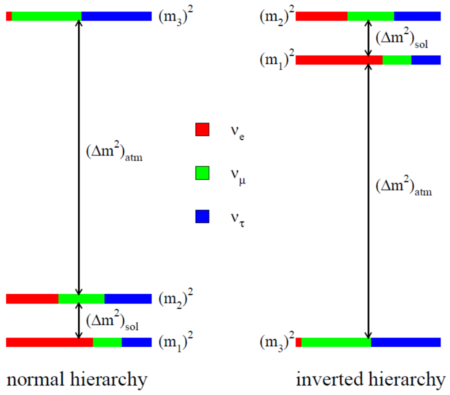

FIGURE 1.1: A schematic drawing showing both possible neutrino mass hierarchies, normal (left) and inverted (right). Colours show the fraction of each flavour in each mass eigenstate [17].

Neutrino oscillations in the full three-flavour formalism are governed by the Pontecorvo-Maki-Nakagawa-Sakata (PMNS) matrix, similarly as quark mixing is governed by the Cabibbo-Kobayashi-Maskawa (CKM) matrix. The PMNS matrix is usually parametrised in the following form:

$$\begin{bmatrix}\nu_e\\ \nu_\mu\\ \nu_\tau\end{bmatrix} = \begin{bmatrix}1 & 0 & 0\\ 0 & c_{23} & s_{23}\\ 0 & -s_{23} & c_{23}\end{bmatrix}\begin{bmatrix}c_{13} & 0 & s_{13}e^{-i\delta_{CP}}\\ 0 & 1 & 0\\ -s_{13}e^{i\delta_{CP}} & 0 & c_{13}\end{bmatrix}\begin{bmatrix}c_{12} & s_{12} & 0\\ -s_{12} & c_{12} & 0\\ 0 & 0 & 1\end{bmatrix}\begin{bmatrix}\nu_1\\ \nu_2\\ \nu_3\end{bmatrix} \tag{1.12}$$

Since the PMNS matrix is a rotation matrix in three dimensions, it depends on three rotation angles θ_{12}, θ_{13}, θ_{23} in contrary to only one mixing angle θ appearing in the two flavour example (Eq. 1.2). By carefully choosing the baseline and energy range of the neutrinos, we can perform an experiment sensitive to a particular set of oscillation parameters, as shown in Tab. 1.1. This Thesis focuses solely on the accelerator neutrino experiment.

Type	L	E	Sensitivity
Solar	10^{11} km	0.1-10 MeV	Δm^2_{21}, θ_{12}
Atmospheric	10–10^4 km	0.1-100 GeV	θ_{23}, Δm^2_{32}
Reactor short baseline	1 km	1 MeV	Δm^2_{21}, θ_{13}
Reactor long baseline	100 km	1 MeV	Δm^2_{21}, θ_{12}
Accelerator	100–1000 km	0.5-5 GeV	θ_{23}, θ_{13}, Δm^2_{32}, δ_{CP}

TABLE 1.1: Types of neutrino experiments with typical baseline length (L), neutrino energy (E) and oscillation parameters to which they are most sensitive.

Currently, it is unknown whether θ_{23} is greater or smaller than 45°, often called upper octant (UO) or lower octant (LO), respectively. Theories attempting to explain why very small (θ_{13}) and almost maximal (θ_{23}) mixing angles exist for neutrinos tend to introduce some underlying symmetries and possible common origin of the smallest mixing angle θ_{13} and the deviation of θ_{23} from the maximal mixing [18]. Additionally, there are suggested beyond the Standard Model extensions to neutrino oscillations framework, which are often linked to the octant; however, such speculations are not further discussed in this Thesis. More information can be found in ref [19].

By careful examination of the PMNS matrix, one might notice a parameter that has not yet been mentioned, namely δ_{CP}. This parameter is responsible for the CP violation in the lepton sector, and the next Section is dedicated to this subject. δ_{CP}, θ_{23} octant and mass hierarchy are open questions of neutrino physics by the time this Thesis is written, and are further studied in experiments.

The best-fit values of oscillation parameters are listed in Tab. 1.2.

parameter	Normal Hierarchy (best fit)	Inverted Hierarchy
$\Delta m^2_{21} [10^-5 \text{ eV}^2]$	$7.42^{+0.21}_{-0.20}$	$7.42^{+0.21}_{-0.20}$
$\Delta m^2_{31}\ [10^-3 \text{ eV}^2]$	$+2.510^{+0.027}_{-0.027}$	$-2.490^{+0.026}_{-0.028}$
$\sin^2\theta_{12}$	$0.304^{+0.012}_{-0.012}$	$0.304^{+0.013}_{-0.012}$
$\sin^2\theta_{23}$	$0.450^{+0.019}_{-0.016}$	$0.570^{+0.016}_{-0.022}$
$\sin^2\theta_{13}$	$0.02246^{+0.000062}_{-0.000062}$	$0.02241^{+0.000074}_{-0.000062}$
δ_{cp}	230^{+36}_{-25}	278^{+22}_{-30}

TABLE 1.2: Three-flavor oscillation parameters from fit to global data with the inclusion of atmospheric neutrino data provided by Super-Kamiokande [20].

1.3 CP Violation

Studying symmetries is the goal of many physics experiments. In particle physics, one such symmetry is a combination of Parity (P) and Charge (C) conjugate, which will be denoted as CP. It was discovered that weak interactions violate CP symmetry in the quark sector [21]. The violation manifested itself in different oscillations of neutral kaons. An obvious question may then arise: what about the lepton sector? If CP is violated in the lepton sector, neutrinos and antineutrinos have different amplitudes for the oscillations, as will be discussed in this Section.

The Jarlskog invariant [22] tells us about the strength of CP violation. The general formula is as follows:

$$J_{CP,l} = \frac{1}{8}\,\mathrm{Im}\left[U_{\mu 3}U_{e2}U^*_{\mu 2}U^*_{e3}\right]. \tag{1.13}$$

The same formula can be used for the CKM matrix. To calculate the Jarlskog invariant, we can first multiply matrices appearing in Eq. 1.12 and obtain:

$$\begin{bmatrix} U_{e1} & U_{e2} & U_{e3} \\ U_{\mu 1} & U_{\mu 2} & U_{\mu 3} \\ U_{\tau 1} & U_{\tau 2} & U_{\tau 3} \end{bmatrix} = \begin{bmatrix} c_{12}c_{13} & s_{12}c_{13} & s_{13}e^{-i\delta_{CP}} \\ -s_{12}c_{23} - c_{12}s_{23}s_{13}e^{i\delta_{CP}} & c_{12}c_{23} - s_{12}s_{23}s_{13}e^{i\delta_{CP}} & s_{23}c_{13} \\ s_{12}s_{23} - c_{12}c_{23}s_{13}e^{i\delta_{CP}} & -c_{12}s_{23} - s_{12}s_{23}s_{13}e^{i\delta_{CP}} & c_{23}c_{13} \end{bmatrix}. \tag{1.14}$$

By substituting PMNS matrix elements into the Jarlskog invariant equation, we obtain:

$$J_{CP,l} = \frac{1}{8}\cos(\theta_{13})\sin(2\theta_{12})\sin(2\theta_{23})\sin(2\theta_{13})\sin(\delta_{CP}). \tag{1.15}$$

Using known values of PMNS mixing angles (see Tab. 1.2) we can further simplify it to:

$$J_{CP,l} \approx 0.033\sin(\delta_{CP}). \tag{1.16}$$

Since δ_{CP} is an argument of sine function, its values are often presented in the range of $\delta_{CP} \in [-\pi, \pi]$. For $\delta_{CP} = \pm\pi/2$, the $J_{CP,l}$ takes maximal value, i. e. $J_{CP,l} = \pm 3 \times 10^{-2}$. Sakharov [1] stated that violation of CP is one of the conditions to resolve the surplus of matter over antimatter in the observed Universe. The Jarlskog invariant in the quark sector is equal to $J_{CP,q} = 3 \times 10^{-5}$ [23], thus CP violation in the lepton sector has the potential to be three orders of magnitude larger, which could help to explain the imbalance. That is the reason why studying CP violation in the lepton sector is so important and interesting.

Neutrino experiments looking for CP violation use $\nu_\mu(\bar{\nu}_\mu)$ beam for measuring oscillations. Therefore, let's concentrate on the formula describing the oscillations in $\nu_\mu(\bar{\nu}_\mu)$ appearance modes[1]:

$$\begin{aligned} \mathrm{P}(\nu_\mu(\bar{\nu}_\mu) \to \nu_e(\bar{\nu}_e)) \approx & \sin^2(2\theta_{13})\sin^2(2\theta_{23})\sin^2\left(\frac{1.27\Delta m^2_{32}L}{E}\right) \\ & \mp J_{CP,l}\frac{1.27 m^2_{21}L}{E} 8\sin^2\left(\frac{1.27\Delta m^2_{32}L}{E}\right). \end{aligned} \tag{1.17}$$

It is important to notice that this equation consists of two parts: the former is identical for neutrinos and antineutrinos, while the latter has the opposite sign for neutrinos and antineutrinos. Furthermore, there is $J_{CP,l}$ dependence in the latter term. If $J_{CP,l}$ is non-zero or, to be more precise, if $\sin(\delta_{CP})$ is non-zero, neutrinos and antineutrinos oscillate with different probabilities.

On the other hand, if we take a look at Eq. 1.18, showing the neutrino oscillations probability for the $\nu_\mu(\bar{\nu}_\mu)$ disappearance mode, we may notice that the formula doesn't include the $J_{CP,l}$ term:

$$\begin{aligned} P(\nu_\mu(\bar{\nu}_\mu) \to \nu_\mu(\bar{\nu}_\mu)) \approx & 1 - 4\cos^2(\theta_{13})\sin^2(\theta_{23}) \\ & \times \left(1 - \cos^2(\theta_{13})\sin^2(\theta_{23})\right)\sin^2\left(\frac{1.27\Delta m^2_{32}L}{E}\right). \end{aligned} \tag{1.18}$$

In other words, we may observe CP violation only in the appearance mode. However, studying disappearance mode is still important due to possible constraints on other oscillation parameters in the appearance probability formula.

1.4 Weak Interactions

Neutrino interactions play an important role in this Thesis and since neutrinos interact only via weak interactions, it is worth reminding some basic information in this regard.

Weak interactions are described using Lagrangian and SU(2) gauge symmetry, which in many ways resembles QED. However, there are crucial differences, such as Parity (P) violation. As a consequence, it is easy to explain the weak interactions using knowledge of QED formalism as a foundation.

In QED, the current has a vector form $j^\mu = \bar{\psi}\gamma^\mu\phi$. Due to parity violation in weak interactions, we can have an axial vector form given by $\bar{\psi}\gamma^\mu\gamma^5\phi$. The most general Lorentz-invariant form for the interaction takes the following form:

$$j^\mu \propto \bar{u}(p')(g_V\gamma^\mu + g_A\gamma^\mu\gamma^5)u(p), \tag{1.19}$$

where g_V and g_A are vector and axial vector coupling constants, respectively, and $u(p)$ is a four-component spinor [24].

It is known from experiments [25] that the weak charged current has a form of V-A ("vector minus axial"). The full leptonic four-current is then equal to:

$$j^\mu = \frac{g_W}{\sqrt{2}}\bar{u}(p')\frac{1}{2}\gamma^\mu(1-\gamma^5)u(p), \tag{1.20}$$

where g_W is the W boson coupling constant.

---

[1] We only show an approximation here; the complete equation can be found in Appendix B.1

Weak interactions are mediated by $W^{\pm}$ and Z^0 bosons, which do have a mass, contrary to photons in QED. These masses are approximately equal to $m_W = 80$ GeV/c^2 and $m_Z = 91$ GeV/c^2 [23]. This fact is reflected in the formula for the weak boson propagator, which includes the boson mass and for the W boson takes the form:

$$\frac{-1}{q^2 - m_W^2}\left(g^{\mu\nu} - \frac{q^{\mu}q^{\nu}}{m_W^2}\right), \tag{1.21}$$

where q is four-momentum of the exchanged virtual particle and $g^{\mu\nu}$ is Minkowski metric element. To obtain the propagator for Z^0, one needs to replace m_W^2 with m_Z^2.

In accelerator neutrino experiments, we measure mostly neutrino interactions on nucleons inside a nucleus, not on a point-like object. This makes the reasoning presented here even more complex, and we have to include form factors into the interaction formalism.

1.5 Form Factors

The first measurement of the lepton scattering on a nucleus was performed by Rutherford in his famous experiment [26] when he discovered the existence of the nucleus. He calculated the cross-section for this process assuming a lepton interacted with a point-like object. Mott then expanded the formalism by including the spin effect into Rutherford's formula [27]. However, the Mott cross-section agrees with experiments only for three-momentum transfer $|\vec{q}_3| \to 0$. For higher values of $|\vec{q}_3|$ experimental data give lower values of the cross-section than the theoretical predictions. The problem lies in the spatial extension of nuclei. For higher $|\vec{q}_3|$, the virtual photon "can see" only part of the nucleus charge, in other words, we are probing the inner structure of a nucleus, not the nucleus as a whole. This inner structure can be described using form factors, which can be defined as:

$$F(\vec{q}^2{}_3) = \int e^{i\vec{q}_3 x/\hbar} f(x) d^3x. \tag{1.22}$$

After including the form factor in the Mott cross-section formula, we obtain:

$$\left(\frac{d\sigma}{d\Omega}\right)_{exp} = \left(\frac{d\sigma}{d\Omega}\right)_{Mott} |F(\vec{q}^2{}_3)|^2. \tag{1.23}$$

For scattering on nucleons, the problem gets even more complicated. We need to include information about the charge but also the magnetic moment of a nucleon. The equation that takes that into account is called the Rosenbluth formula and has the following form:

$$\left(\frac{d\sigma}{d\Omega}\right) = \left(\frac{d\sigma}{d\Omega}\right)_{Mott} \cdot \left(\frac{G_E^2(Q^2) + \tau G_M^2(Q^2)}{1+\tau} + 2\tau G_M^2(Q^2)\tan^2\left(\frac{\theta}{2}\right)\right), \tag{1.24}$$

where Q^2 is four-momentum transfer, $G_E^2(Q^2)$ and $G_M^2(Q^2)$ are the electric and magnetic form factor, respectively, while $\tau = \frac{Q^2}{4M^2c^2}$ with M being nucleon mass [28].

The limiting values for proton and neutron are [27]:

$$\begin{array}{ll} G_E^p(Q^2=0) = 1 & G_E^n(Q^2=0) = 0 \\ G_M^p(Q^2=0) = 2.793 & G_M^n(Q^2=0) = -1.913 \end{array} \tag{1.25}$$

It is assumed that the target nucleon charge distribution has an exponential shape as the extent of not being point-like, and the charge distribution is the Fourier transform of the form factor, thus this equation has the following form:

$$F(Q^2) \propto \frac{1}{\left(1+\frac{Q^2}{m^2}\right)^2}, \tag{1.26}$$

where m^2 is in the units of Q^2. The charge of neutrino is consistent with zero; however, it may have a charge distribution like a neutron. Therefore, this dipole form of form factor will be important for neutrino interactions physics [29].

1.6 Neutrino Interactions

Neutrinos undergo only weak interactions, but that doesn't make interaction description simple; on the contrary, it is quite complex. Firstly, we can divide neutrino interactions depending on which boson is the force carrier. If the interaction was mediated by $W^{\pm}$ we call it Charged Current (CC), while the cases with Z^0 are known as Neutral Current (NC). CC are crucial for studying oscillations, as the lepton created in such a process allows to identify the flavour of the interacting neutrino, and therefore it is possible to check if the flux of a particular neutrino flavour has changed. NC are very often the background for studied oscillation channels.

Furthermore, we can also classify interactions based on neutrino energy, Q^2 and the final state. The cross-section as a function of muon (anti)neutrino energy, with contributions from different reaction modes, is shown in Fig. 1.2. It is clear that there is a dependence between the interaction type and neutrino energy. In the following Sections, all reaction modes presented in the plots are described in a more detailed manner.

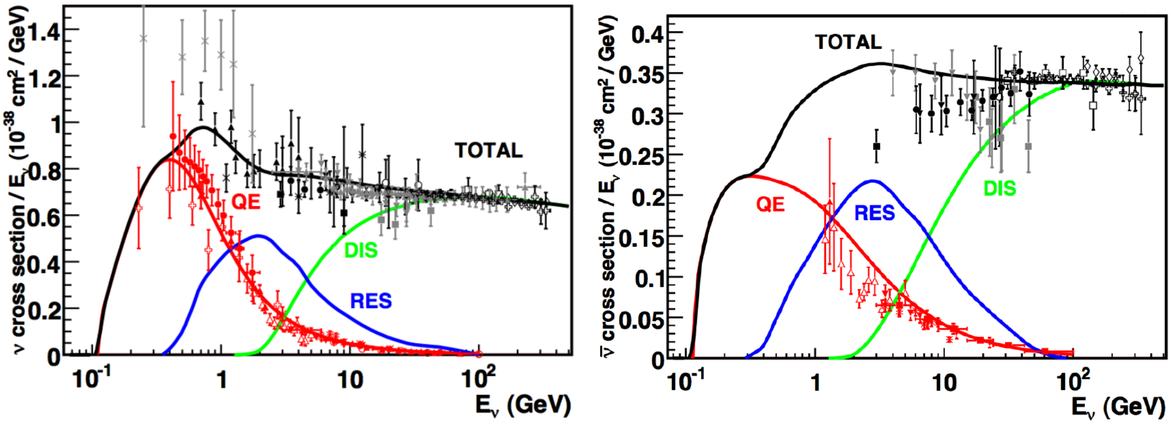

FIGURE 1.2: Muon neutrino (left) and antineutrino (right) cross-sections for an isoscalar target as a function of the (anti)neutrino energy. The curves are averaged over protons and neutrons. The lines mark interaction modes [17].

Quasi-Elastic-like

The type of neutrino interactions most important for this Thesis is Charge Current Quasi-Elastic Scattering (CCQE) for which the Feynman diagram is shown in Fig. 1.3. The cross-section of the CCQE interaction on a single nucleon is parameterized in terms of four nucleon form factors: electric, magnetic, pseudoscalar and axial form factors. The axial form factor is

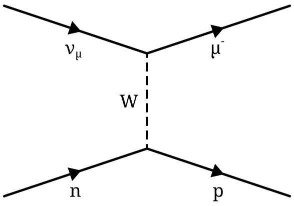

FIGURE 1.3: Feynman diagram for a CCQE interaction of ν_μ [30].

the main source of error in the microscopic description of neutrino interactions at the nucleon level [31]. In analogy to Eq. 1.26 it takes form:

$$F_A(Q^2) = \frac{g_A}{\left(1 + \frac{Q^2}{\left(M_A^{QE}\right)^2}\right)^2}, \tag{1.27}$$

where $g_A = F_A(Q^2 = 0) = 1.2670 \pm 0.0035$ [32] is a normalisation factor and M_E^{QE} is axial mass [33]. Axial form factor describes the weak charge distribution and M_E^{QE} resembles a mass term, hence such a name is commonly used. There are alternative descriptions reaching beyond simple exponential form, like the 2-component model [34] or the Z-expansion model [35].

For nucleons inside a nucleus, many correlations may exist between them, which can affect the final outcome of an interaction. One type of such correlations is Meson-Exchange-Current (MEC), sometimes also called Long-Range Correlations (LRC). In MEC, there is a meson exchange between a pair of correlated nucleons. Most often, a pion is assumed in the calculations, but more advanced models take ρ mesons into account as well. One can interpret that a nucleon not interacting with neutrino via boson propagator can still participate in the interaction via meson propagator. In such interactions, two nucleons are ejected from the nucleus in the final state; therefore, it is also often called Two Particles Two Holes (2p2h). An example of 2p2h for muon neutrino is depicted in Fig. 1.4.

A neutrino can interact with a neutron which can be correlated with either a proton or a neutron; therefore, we have two possible pairs: neutron-proton (np) or neutron-neutron (nn). For antineutrino, the isospin symmetry is assumed, in consequence nn is replaced by pp and np by pn.

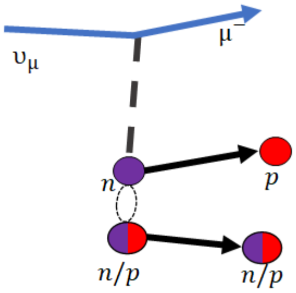

FIGURE 1.4: Pseudo-Feynman diagram showing 2p2h interaction with two possible pairs.

Nothing is preventing correlations between more than two particles; thus, there are models proposing even 3p3h. Since this is still a new concept, it will not be discussed further, as 3p3p is not implemented in the simulation used in this Thesis. However, if the reader is interested, more information can be found in [36].

Concerning the meson propagators, we can have two types of diagrams: Δ-like and non Δ-like. In the first case, a virtual Δ resonance decays to π and a nucleon. Examples of Feynman diagrams with non Δ-like and Δ-like cases are shown in Fig. 1.5.

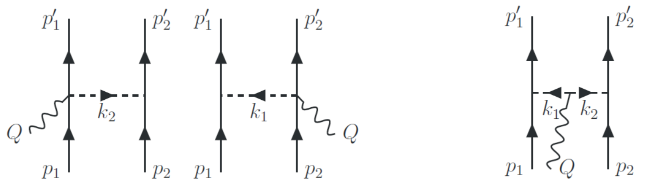

(a) Contact terms.

(b) The pion - in - flight term.

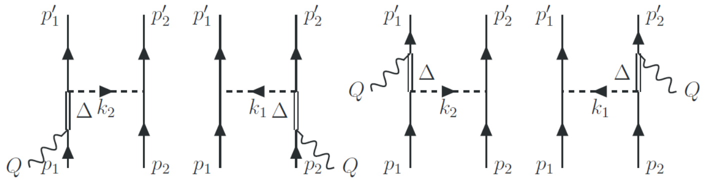

(c) Δ pole and Δ pole crossed terms.

FIGURE 1.5: Δ-like and non Δ-like diagrams of 2p2h interactions [37].

There are experiments that cannot detect the outgoing proton due to the reconstruction threshold. Hence, a clever method of reconstructing neutrino energy is required. For a two-body process like CCQE, there is a possibility to reconstruct the neutrino energy using the following formula[2]:

$$E_{\nu}^{rec} = \frac{m_p^2 - \left(m_n - E_b^2\right)^2 - m_l^2 + 2\left(m_n - E_b\right)E_l}{2\left(m_n - E_b - E_l + p_l\cos(\theta_l)\right)}. \tag{1.28}$$

It is crucial that this equation depends only on the charged lepton kinematics, i.e. lepton momentum (p_l), lepton direction with respect to the beam direction ($\cos\theta_l$) and lepton energy (E_l), while the other parameters, such as neutron mass m_n and binding energy E_b, are of known value.

However, Eq. 1.28 assumes the interaction with a stationary nucleon. It is s well-established fact, that nucleons bound in nuclei are not stationary due to Fermi motion. In consequence, it is important to have a proper formalism describing nucleons in a nucleus.

One such model is the Spectral Function (SF). SF is an advanced model that takes into account the shell structure of the nucleus and is tuned to electron scattering data $(e, e'p)$ [38, 39]. SF describes the probability of ejecting a nucleon with momentum $\vec{p}$ and leaving the nucleus in an excited state of energy E. It can be described using the following formula [37]:

$$P(\vec{p}, E) = \sum_n \left| \left\langle \psi_n^{A-1} \middle| a_p \middle| \psi_0^A \right\rangle \right|^2 \delta(E + E_0 - E_n), \tag{1.29}$$

where ψ_0^A is the initial state with A nucleons with energy E_0, and a_p is the annihilation operator with momentum $\vec{p}$. We sum over all possible energy final states ψ_n^{A-1} with $A-1$ nucleons and energy E_n.

SF can be divided into Mean Field (MF) and Short-Range-Correlations (SRC) components. The former involves the nucleon interaction with the mean potential of the nucleus only, in

---

[2] The formula can also be used for resonant scattering, which is described later. In such a case, the mass of Δ(1232) is assumed instead of a proton.

the latter, we take into account the nucleon-nucleon correlations:

$$P(\vec{p}, E) = P_{MF}(\vec{p}, E) + P_{SRC}(\vec{p}, E). \tag{1.30}$$

The $P(\vec{p}, E)$ distributions for carbon and oxygen can be seen in Fig. 1.6, with the white line separating MF and SRC regions. Since there is a big repulse of nucleons in SRC, they appear at higher momentum p, also referred to as missing momentum p_m, and energy E (also known as missing energy E_m). The spectral function is based on electron scattering data, and from those measurements, we extract p_m and E_m, hence those terms are used interchangeably.

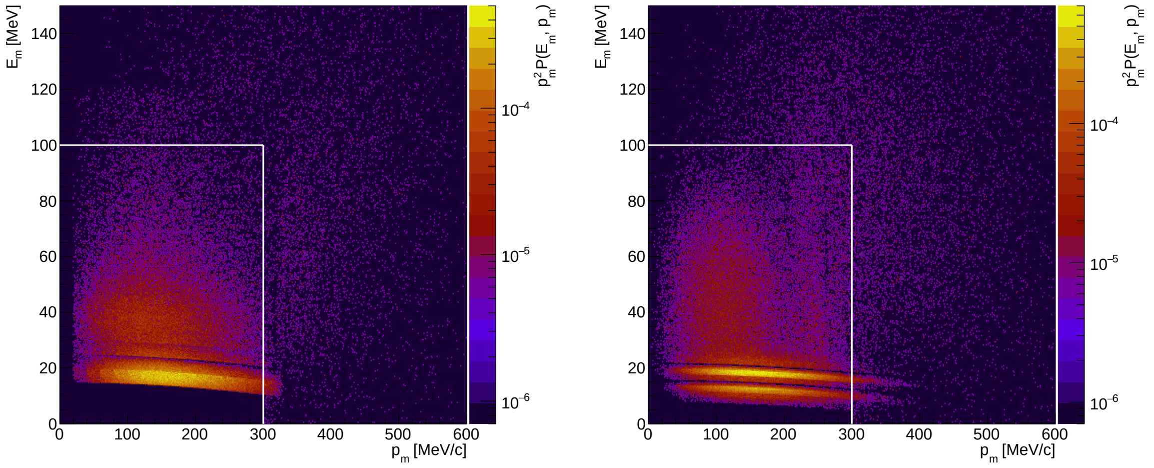

FIGURE 1.6: Two-dimensional distribution of missing energy (E_m) and missing momentum (p_m) for Carbon (left) and Oxygen (right) in NEUT generator [40] used by the T2K experiment. The white lines indicate the cuts used to separate the MF region (low E_m, p_m) from the SRC region (high E_m, p_m) [41].

Although SRC are considered a type of 2p2h interactions, they are treated in the neutrino interaction generator used in the Thesis as CCQE. This is due to the fact that SRC are described using the SF formalism, which is currently only implemented for CCQE.

Due to the Pauli principle, two fermions cannot occupy the same state, so the interaction in which a final nucleon would be in an already occupied state is forbidden (such an effect is called Pauli blocking). One method to include Pauli Blocking in SF is to multiply $P(\vec{p}, E)$ by the Heaviside step function, as suggested in [42], this way we receive:

$$P(\vec{p}, E) \to P(\vec{p}, E)\Theta\left(|\vec{p} + \vec{q}_3| - \bar{p}_F\right), \tag{1.31}$$

where $\bar{p}_F$ is average Fermi momentum, and $\vec{q}_3$ is three-momentum transfer.

Pion Production

High-energy neutrinos can undergo Single Pion Production (SPP). Very often in such interactions, a short-lived resonance is created; we call them Resonant interactions (RES). The resonances are mostly Delta baryons (Δ^+, Δ^-, Δ^{++}), which immediately decay to a pion and a nucleon, as can be seen in Eq. 1.32 and Fig. 1.7:

$$\begin{aligned}
&\Delta^{++} \to \pi^+ + p \\
&\Delta^{\pm} \to \pi^{\pm} + n \\
&\Delta^{+} \to \pi^0 + p \\
&\Delta^{0} \to \pi^- + p \\
&\Delta^{0} \to \pi^0 + n
\end{aligned} \tag{1.32}$$

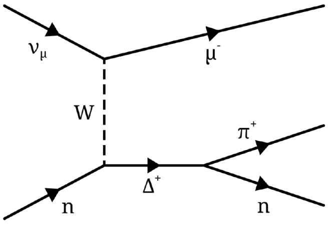

FIGURE 1.7: Feynman diagram for a resonant interaction of ν_μ [30].

Several models describing resonant interactions have been proposed, such as the Sato-Lee model [43] or the Rein-Sehgal model [44]. However, only the latter one is considered further due to being used by NEUT. Because the interaction can occur with the creation of different resonances, we have interference terms between different resonances when calculating the cross-section in a quantum mechanical manner. Therefore, the pion production modelling is complicated, but there are still similarities to the CCQE model. The cross-section can be factorised into two parts as in Eq. 1.33, the first one being associated with the resonance production and depending on form factors (Q^2 and W dependent), and the second one describing the pion kinematics using Adler angles affecting only the outgoing hadronic system:

$$\frac{d^2\sigma}{dQ^2 dW}\frac{d\sigma}{d\Omega} = \frac{d^2\sigma}{dQ^2 dW}\frac{d\sigma}{d\cos\theta d\phi}. \tag{1.33}$$

The form factor for resonant interaction is presented in Eq. 1.34, where M_A^{RES} is the resonant axial mass and $C_5^A(Q^2=0)$ is the normalisation of the axial form factor proposed by Graczyk and Sobczyk [45]. $C_5^A(Q^2=0)$ plays similar role as g_A in CCQE, however, C_5^A is not precisely measured as only a few measurements were performed [46]. More information on RES form factors can be found in [45, 47].

$$F_A^{RES}(Q^2) = \frac{C_5^A(0)}{\left(1+\frac{Q^2}{\left(M_A^{RES}\right)^2}\right)^2}. \tag{1.34}$$

It is also possible to produce a single pion without going through a resonant intermediate state (commonly called a non-resonant background). There are different channels for isospins $I_{1/2}$ and $I_{3/2}$. Based on bubble chamber data, the effects of isospin $I_{3/2}$ are small [48, 49]; as a consequence, most generators only model $I_{1/2}$ channel. For low four-momentum transfer, there is also the possibility of pion production from so-called Coherent Scattering (COH), where neutrinos scatter on a nucleus as a whole, as can be seen in Fig. 1.8, leaving the nucleus in the same state.

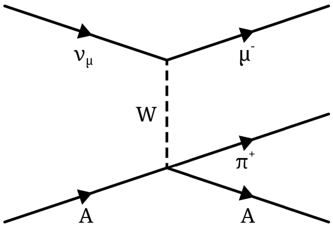

FIGURE 1.8: Feynman diagram for coherent scattering of ν_μ [30].

For neutrino energies of the order of a few GeV, it is possible to produce more than one π, which is often called Multi-π interaction. However, different neutrino MC generators implement this process very differently, which is related to the transition region, discussed next.

For very high-energy neutrinos, the intermediate boson may probe the quark structure of a nucleon, leading to Deep Inelastic Scattering (DIS), as can be seen in Fig. 1.9. To describe such a process, two scaling variables are used: Bjorken x denotes the fraction of nucleon momentum carried by the struck quark, and y is the fraction of neutrino energy transferred to the hadronic system.

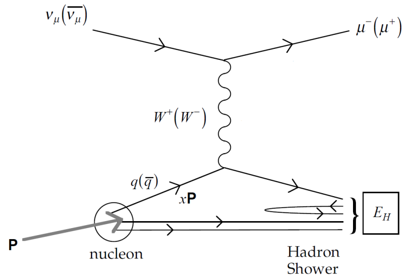

FIGURE 1.9: Feynman diagram for DIS of $\nu_\mu(\bar{\nu}_\mu)$ [50].

In general, we can divide high energy neutrino interactions into low and high invariant mass W regions, as shown in Fig. 1.10. Since the transition is not well known, some generators perform an arbitrary split depending on the value of hadronic mass W. This is needed to avoid double counting of the same effect/interaction. The region limits for the generator used in this Thesis are as follows:

- $W < 2$ GeV/c^2 - Multi-π mode
- $W > 2$ GeV/c^2 - DIS (PYTHIA) mode

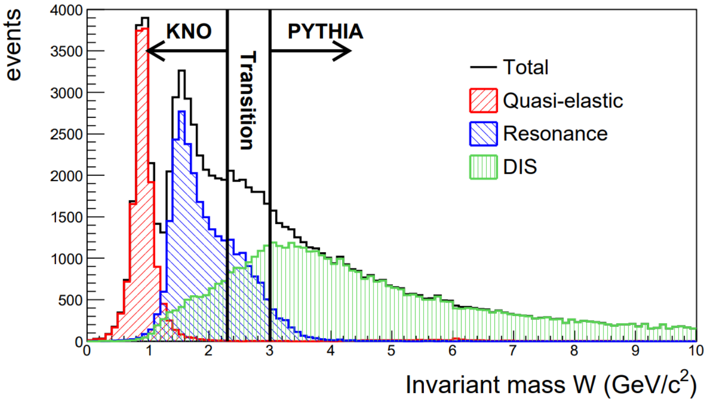

FIGURE 1.10: W distribution for neutrino interactions in the GENIE generator. The W distribution can be split into three regions: the KNO scaling-based model region, the PYTHIA region, and the transition region [51].

There are several models describing the effects important at low W:

- Andreopoulos-Gallagher-Kehayias-Yang (AGKY) [52] is a hadronization model that provides information about the multiplicities and kinematics of the outgoing hadrons
- Koba-Nielsen-Olesen scaling law (KNO) [53, 54] states that the cross-section for producing n charged particles is independent of energy and is function of $n/\langle n \rangle$.
- Bodek and Yang (BY) introduced a correction [55] to inclusive DIS cross-section to better fit the data, as QCD becomes non-perturbative at low Q^2.

The high W region is often generated by PYTHIA. More information can be found in [56].

1.7 Final State Interactions

Neutrino interactions described up to this point (except COH) occur on nucleons bound inside a nucleus. This means that the products of the interaction also appear inside the nucleus. As a consequence, they need to propagate through the nucleus and leave it, so we could detect them in an experiment. During this propagation, the particles can undergo different reactions, like scattering or absorption, called Final State Interactions (FSI).

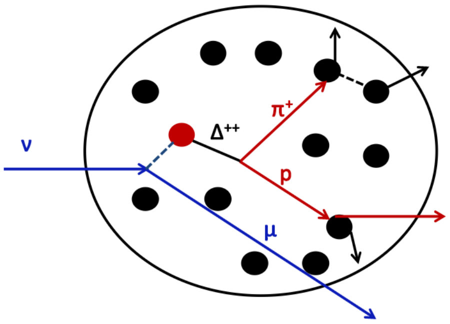

FIGURE 1.11: Schematic view of possible final state interactions for a RES event. In the given example, the proton scattered on another nucleon ejecting additional nucleon from the nucleus, while π^+ underwent the absorption process.

Due to FSI, a pion can undergo the following interactions inside a nucleus:

- Absorption,
- Quasi-Elastic scattering,
- Single charge exchange,
- Hadron (N+nπ) production.

As for a nucleon, it can undergo the following interactions:

- Quasi-Elastic scattering,
- Inelastic scattering,
- π production.

Precise measurements of neutrino interaction are a relatively new branch of physics, with quick development in recent years. If the Reader is interested, more information can be found in [29, 57–59]. There are several generators available, like Genie [60], NuWro [61] and NEUT [40], which differ in used models and implementation. In the Thesis, the NEUT generator is used, and details about model parametrisation shall be discussed in Chapter 4.

2

Tokai-to-Kamioka Experiment

> No plan survives contact with the enemy.
>
> **Helmuth von Moltke**

2.1 T2K Introduction

The Tokai-to-Kamioka (T2K) is an international experiment located in Japan, dedicated to study of neutrino and antineutrino oscillations. T2K experiment measures the oscillations in two modes: appearance ($\nu_\mu \to \nu_e$ or $\bar{\nu}_\mu \to \bar{\nu}_e$) and disappearance ($\nu_\mu \to \nu_\mu$ or $\bar{\nu}_\mu \to \bar{\nu}_\mu$). The main scheme of the experiment is as follows: $\nu_\mu(\bar{\nu}_\mu)$ beam is created at the Japan Proton Accelerator Research Complex (J-PARC), then the neutrinos are measured at the near detector station, which is located 280 m away from the beam production. At such a distance the oscillation effects are negligible. Next, the neutrino beam is measured in the far detector Super-Kamiokande (SK), which is placed at a distance of 295 km away from J-PARC where the effects of neutrino oscillations are clearly visible. The overview of T2K experiment can be seen in Fig. 2.1.

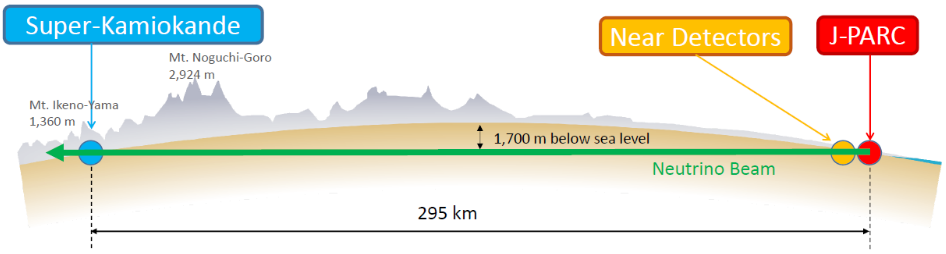

FIGURE 2.1: The overview of T2K experiment. J-PARC and the near detector station are placed on the east coast of Japan, while Super-Kamiokande is located in western Japan.

T2K uses an off-axis neutrino beam, which means that the far detector (FD) is placed at the angle of 2.5° with respect to the beam direction. This provides a few advantages, as illustrated in Fig. 2.2. The bottom histogram shows the ν_μ flux as a function of neutrino energy E_ν for on-axis configuration (0°) and two off-axis configurations (2° and 2.5°), assuming $L = 295$ km and no oscillations. One might notice that in the off-axis configuration the flux has narrower distribution, which is also shifted to lower values of E_ν. Thanks to that fact, Charged Current Quasi-Elastic interactions are the dominant channel in the T2K. Since CCQE is a two-body process, it allows to reconstruct neutrino energy using only lepton kinematics, as discussed in Section 1.6. The top and middle plots of the same Fig. 2.2 show neutrino oscillation probabilities as functions of E_ν for disappearance ($\nu_\mu \to \nu_\mu$) and appearance ($\nu_\mu \to \nu_e$) channels, respectively (also for the baseline $L = 295$ km). It can be seen that the flux for the 2.5° off-axis angle is peaked at the energy where the probability of ν_e appearance (ν_μ survival) is at its maximum (minimum).

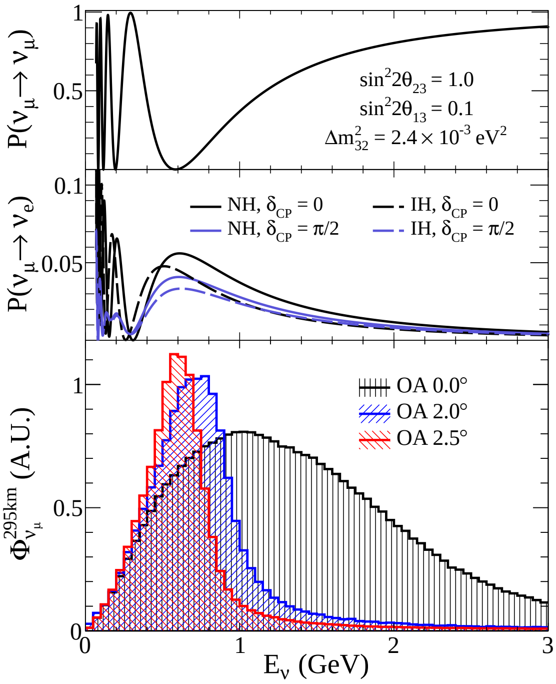

FIGURE 2.2: Probability of neutrino oscillations as a function of neutrino energy for the ν_μ disappearance channel (top) and ν_e appearance channel (middle). The bottom plot shows T2K flux at on-axis and two off-axis configurations (plot taken from [62]).

By further investigation of the middle plot, one might observe that even at the oscillation peak the appearance probability for ν_e is low ($\sim$0.05), and as consequence the number of ν_e ($\bar{\nu}_e$) observed at FD is low. Most of ν_μ oscillate into ν_τ, but SK cannot detect oscillated ν_τ, as their energy is mostly below τ production threshold and they can only interact via NC. In consequence, T2K can measure only the $\nu_\mu \to \nu_e$ and $\bar{\nu}_\mu \to \bar{\nu}_e$ appearance channels.

2.2 Beam Production

The T2K beam starts at J-PARC, where protons are accelerated to 30 GeV. They are grouped in $\sim 50\mu$s long spills, with each spill containing 8 very short (58 ns) bunches. This characteristic time structure is very important as it is used for the selection of proper events. In other words, thanks to cutting on the expected bunch time, we can reject most of events that which do not originate from the T2K beam, like cosmic rays or atmospheric neutrinos.

The T2K beamline is depicted in Fig. 2.3. Starting from the left side, we can notice protons accelerated in the J-PARC accelerator chain hitting the graphite target. Proton interactions with carbon nuclei produce many secondary particles, mostly pions and kaons. After escaping the target, the secondary particles enter three magnetic horns, which can operate in two configurations: Forward Horn Current (FHC) where positively charged particles are focused and negatively charged are defocused, or Reverse Horn Current (RHC) which focuses negatively charged particles and positively charged are defocused. Eqs. 2.1 and 2.2 show the dominant decay modes of positively and negatively charged pions and kaons, respectively.

Since positively charged secondary particles decay to neutrinos, FHC corresponds to the neutrino beam mode, while RHC to the antineutrino beam mode.

$$\pi^+ \to \mu^+ + \nu_\mu, \qquad K^+ \to \mu^+ + \nu_\mu \tag{2.1}$$

$$\pi^- \to \mu^- + \bar{\nu}_\mu, \qquad K^- \to \mu^- + \bar{\nu}_\mu \tag{2.2}$$

Due to the conductor shape, there is no magnetic field in the centre of the magnetic horns, as can be seen in Fig. 2.4. Therefore, particles travelling forward through the horns are not affected by the magnetic field, and as a consequence, there is contamination of the commonly named "wrong sign" component in the T2K beam ($\bar{\nu}_\mu$ for FHC mode, ν_μ for RHC). Moreover, one needs to remember that the initial interaction of the proton and carbon nucleus has an excess of positive charge, which leads to more positively charged secondary particles being produced. Due to those two facts, the contamination of the wrong sign component in RHC is much higher than in FHC. This effect is presented in Fig. 2.5, where the left plot shows the flux composition for FHC and the right for RHC.

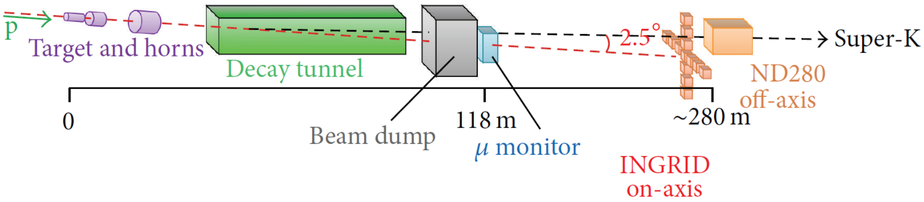

FIGURE 2.3: Overview of the $\nu_\mu(\bar{\nu}_\mu)$ beamline in the T2K experiment [63].

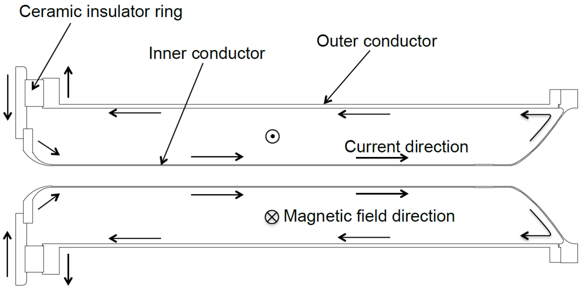

FIGURE 2.4: Cross-section of a magnetic horn with current and magnetic field directions marked [64].

Moving to the right in Fig. 2.3, one can see a decay tunnel which is ~96 m long, to allow most secondary particles to decay in flight. The detailed breakdown of decay channels for the most common secondary particles is summarized in Tab. 2.1. As can be seen, K can decay into ν_e which constitute the background (so-called intrinsic ν_e) in the search for neutrino oscillations in $\nu_\mu \to \nu_e$ channel. Additionally, some tertiary muons can decay into ν_e producing a low energy contribution to intrinsic ν_e flux.

At the end of the decay tunnel, the beam dump is placed, made of 75 tons of graphite. Since neutrinos hardly interact, most of them leave the beam dump in an unchanged state, while other particles stop, except for highly energetic muons. Those muons are measured on a spill-by-spill basis in the last part of the beamline, which is the muon monitor. It consists of ionization chambers and allows for better control of the direction and intensity of the (anti)neutrino beam.

Decay Channel	Branching Ratio (%)
$\pi^+ \rightarrow \mu^+\nu_\mu$	99.9877
$\pi^+ \rightarrow e^+\nu_e$	$1.23{\cdot}10^{-4}$
$K^+ \rightarrow \mu^+\nu_\mu$	63.55
$K^+ \rightarrow \pi^0\mu^+\nu_\mu$	3.353
$K^+ \rightarrow \pi^0 e^+\nu_e$	5.07
$K^0_L \rightarrow \pi^-\mu^+\nu_\mu$	27.04
$K^0_L \rightarrow \pi^- e^+\nu_e$	40.55
$\mu^+ \rightarrow e^+\bar{\nu}_\mu\nu_e$	100

TABLE 2.1: Neutrino parents decay modes with branching ratios [65].

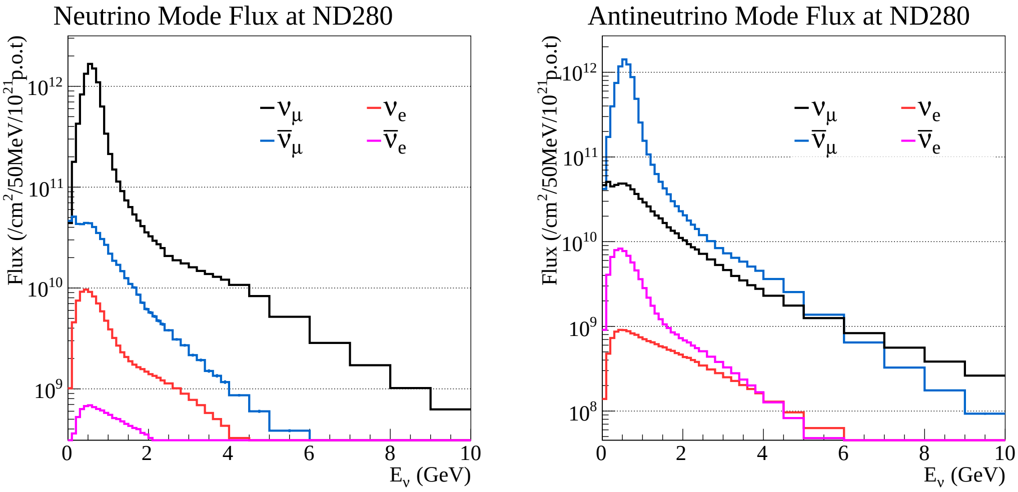

FIGURE 2.5: T2K flux at ND280 for neutrino mode (FHC) and antineutrino mode (RHC). Colours represent different (anti)neutrino flavours.

2.3 On-axis Near Detector - INGRID

The use of the off-axis method introduces the need for measuring the beam direction and stability, as change in the off-axis angle affects the neutrino energy distribution. Hence, T2K uses an on-axis near detector Interactive Neutrino GRID known as INGRID.

INGRID is placed 280 m from the target. The detector consists of 14 identical scintillation modules arranged in the shape of a cross (see Fig. 2.6) and 2 additional modules. The overall size of the detector is 10 m × 10 m. The beam is aimed at the centre of INGRID.

The main purpose of INGRID is to measure neutrino (antineutrino) interactions with enough statistics to allow a daily diagnosis of the beam direction and intensity. The role of the two additional modules is to check the axial symmetry of the neutrino beam. Furthermore, INGRID is used to tune T2K flux predictions.

2.4 Off-axis Near Detector - ND280

Neutrinos from the beam are also measured by ND280, which is located 2.5° off-axis with respect to the beam direction. ND280 is a multi-purpose detector consisting of several subsystems. ND280 is essential for T2K analysis as well as for this Thesis.

The main part of ND280 is the tracker, which consists of two Fine Grained Detectors (FGD, marked by green colour in Fig. 2.8) and three Time Projection Chambers (TPC, marked in

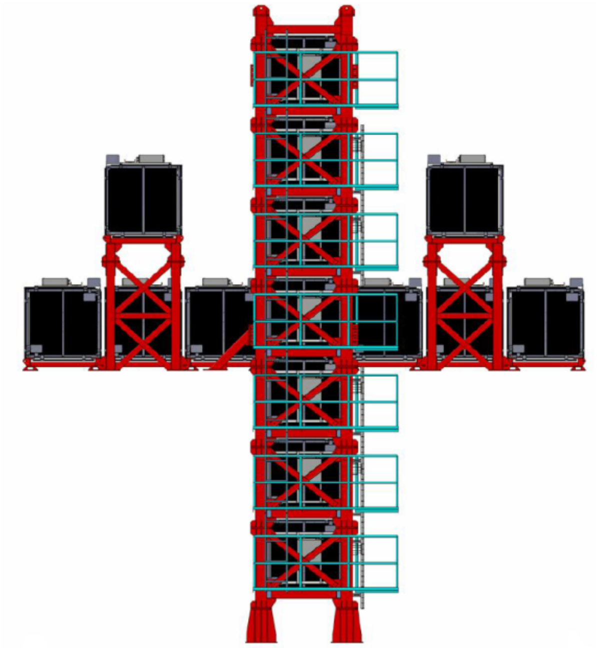

FIGURE 2.6: Schematic view of the on-axis near detector INGRID [66].

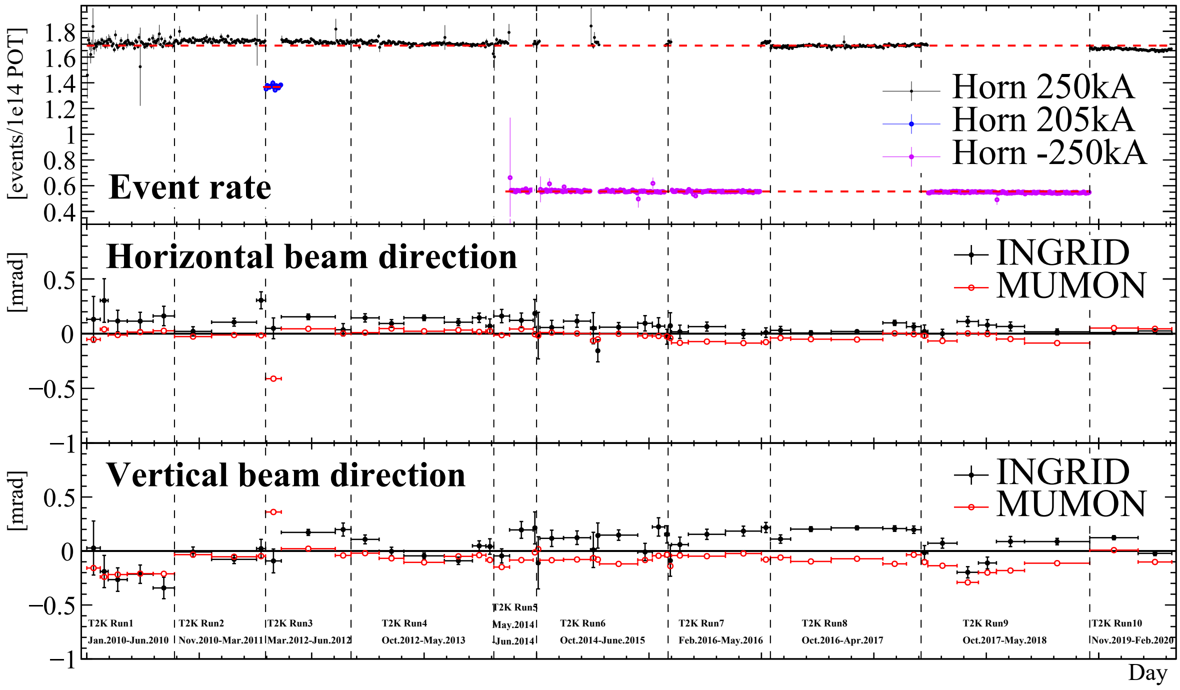

FIGURE 2.7: Beam characteristics measured by INGRID and MUMON. Black dots on the top plot correspond to FHC, while pink ones to RHC.

orange in Fig. 2.8). Upstream of the tracker (with respect to the beam direction), the Pi-zero-detector (P0D) is placed. P0D's primary task is to measure the production of neutral pions in neutral current interactions $\nu_\mu + N \to \nu_\mu + N' + \pi^0 + X$ on water which is an important background in the far detector.

P0D and tracker are surrounded by the electromagnetic calorimeter (ECal) and UA1 magnet, used previously in the famous CERN UA1 experiment, which discovered W and Z bosons [67]. The magnet generates a magnetic field of 0.2 T, and the magnet yoke is instrumented with scintillator slabs forming the Side Muon Range Detector (SMRD). The main functions of SMRD are the reconstruction of high-angle muons and the triggering on cosmic-ray muons, both of which are irrelevant to this Thesis.

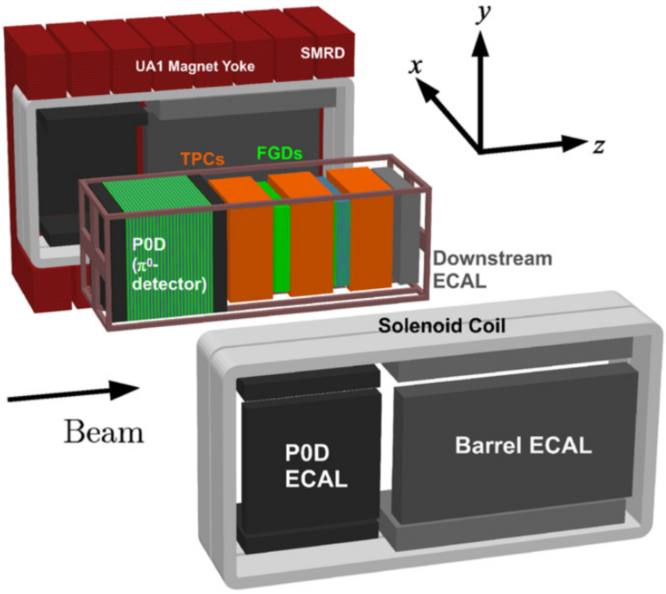

FIGURE 2.8: Schematic view of the ND280 detector [66].

ND280 tracker is used in many T2K analyses, both cross-section measurements and the input to the oscillation analysis. Therefore, all parts of the tracker are described in the next Sections with an emphasis on parts relevant for this Thesis.

2.4.1 Fine Grained Detector - FGD

FGDs [68] are constructed of bars of extruded polystyrene scintillator, which are oriented in either the horizontal (x) or vertical (y) direction, perpendicularly to the beam direction (see Fig. 2.8). Each scintillator bar has a wavelength shifting fibre going through its centre. One end of each fibre is attached to a solid-state Multi-Pixel Photon Counter (MPPC).

The upstream FGD (FGD1) consists of 5,760 scintillator bars, arranged into 15 XY modules of 192 bars each. The downstream FGD (FGD2) is a water-rich detector consisting of seven XY modules of plastic scintillator alternating with six 2.5 cm thick layers of water. FGD2 contains in total 2,688 active scintillator bars. Each FGD has outer dimensions of $2300 \times 2400 \times 365\ \mathrm{mm}^3$.

The main purpose of FGDs is to be the target for neutrino interactions. In FGD1, neutrinos interact mostly with carbon nuclei, whereas in FGD2 with both carbon and water (oxygen nuclei). Water is the target in the far detector, so using the FGD2 water target allows for better understanding of predictions for the far detector.

FGDs can be used for the identification (PID) of stopping particles by studying the energy deposits as a function of track length. Fig. 2.9 shows measured energy deposits as a function of track length in FGD1 and theoretical predictions for the proton, muon and pion hypotheses. What is important for later parts of the Thesis, that it is relatively easy to distinguish protons from muons and pions, which is a consequence of much higher proton mass. Because FGD2 has fewer scintillation bars (active material), the particle reconstruction is in general less efficient than in FGD1. PID for tracks that leave FGD is performed by TPC, since it has superior capabilities in this regard.

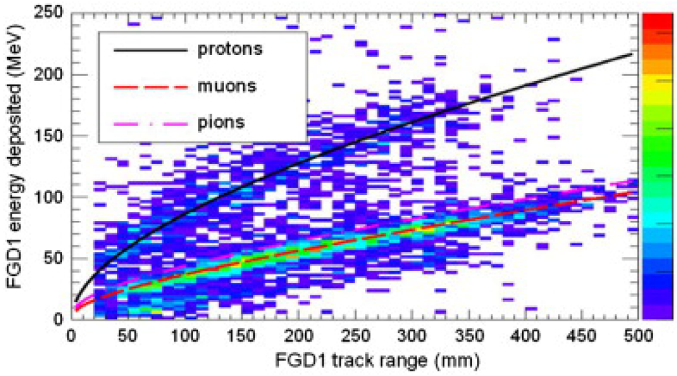

FIGURE 2.9: Deposited energy as a function of range for particles stopping in FGD1 [68].

FGD can also measure particle momentum by range. Knowing the distance a particle has travelled and its mass (after PID) we can easily calculate momentum.

2.4.2 Time Projection Chamber - TPC

TPCs are gaseous argon-based Time Projection Chambers. Charged particles passing through TPC produce electrons that drift in the electric field towards the MicroMegas detectors [69], where the electrons are multiplied and sampled by the readout pads with dimensions of 7.0 mm × 9.8 mm (vertical × horizontal) each. Thanks to the high granularity of MicroMegas the TPCs have much better reconstruction capabilities than FGDs.

ND280 tracker is placed in the magnetic field, which causes curvature of the tracks of charged particles. By fitting a helix to a track, it is possible to measure particle momentum and charge. Particle Identification (PID) in TPC is based on measured ionisation loss per unit length (dE/dx). Fig. 2.10 shows the Bethe-Bloch curve [23] and measured dE/dx in TPC for selected particles.

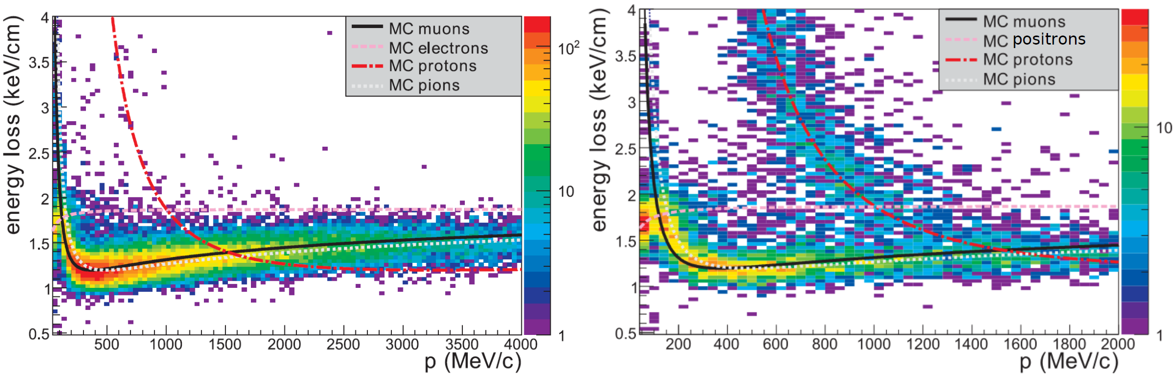

(A) Negatively charged particles (B) Positively charged particles

FIGURE 2.10: Energy loss per unit length as a function of particle momentum, with theoretical curves for different particles [70].

TPC1 is placed upstream of FGD1 (with respect to beam direction), and therefore it is used as a veto detector for muons that didn't originate from neutrino interactions in FGD1. TPC2 plays a similar role for interactions in FGD2.

2.4.3 Global Reconstruction

Since ND280 consists of several sub-detectors, each with its own reconstruction algorithm, there is a need to use the global reconstruction (GR) which combines the information from at least two detectors. Due to the fact, that TPC has the best reconstruction capabilities, GR looks for tracks in TPC first, and then tries to combine a TPC track with hits in a neighbouring FGD to create a TPC-FGD matched object. If both FGDs have hits, it is possible to create an FGD1-TPC2-FGD2 object or even an FGD1-TPC2-FGD2-TPC3 one. An example of an event with tracks passing through several sub-detectors is shown in Fig. 2.11.

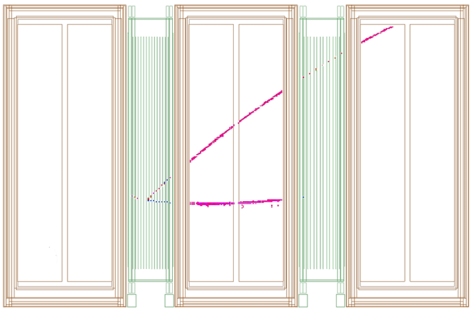

FIGURE 2.11: Example of a neutrino interaction happening in FGD1 sub-detector and producing a muon and a proton travelling through several sub-detectors.

2.5 Far Detector - Super-Kamiokande

Super-Kamiokande (SK) is a famous Cherenkov detector known for the discovery of neutrino oscillations [10]. SK is a cylinder of 39 m in diameter and 42 m in height, as can be seen in Fig. 2.12. It is filled with ultrapure water (now doped with salts of gadolinium [71]) of a total mass of 50 kt. SK is equipped with roughly 13,000 photo-multiplier tubes (PMTs). It is divided into Inner Detector (ID) and Outer Detector (OD). OD serves mostly as a veto for events originating outside of SK.

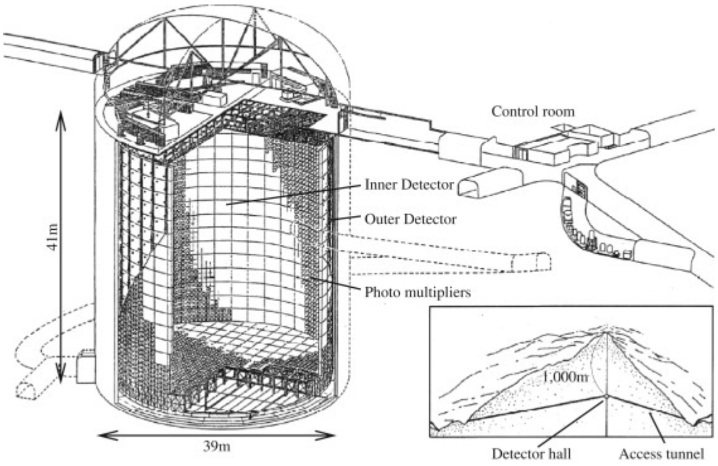

FIGURE 2.12: Schematic view of the Super-Kamiokande detector [66].

Particles travelling faster than light in a given medium ($\beta > 1/n$, where $n = 1.33$ for water) produce Cherenkov radiation. Therefore, the Cherenkov threshold is 0.569 MeV/c for electrons, 115.7 MeV/c for muons and 1.04 GeV/c for protons. For T2K beam energy, most protons are below the Cherenkov threshold. In consequence, SK cannot perform a calorimetric measurement to estimate the energy of neutrinos. However, for a two-body process like quasi-elastic interaction, it is possible to reconstruct neutrino energy by measuring only lepton kinematics (see Eq. 1.28).

The main lepton signatures SK is looking for are muons and electrons appearing inside the detector. Such signatures are μ-like and e-like Cherenkov rings. The edge of a μ-like ring is sharp, while that of an e-like one is fuzzy, as electrons have lower mass and are more likely to scatter. Examples of e-like and μ-like rings and the discrimination parameter are shown in Fig. 2.13. SK is not equipped with magnetic field, so it is unable to differentiate between a lepton and its antiparticle counterpart. Recently, salts of gadolinium were added to water, which allows for efficient neutron detection. Since neutrons are statistically more likely to be emitted from antineutrino interactions, the signal of neutron capture can be used to identify ν and $\bar{\nu}$. However, this is not yet used in the analysis.

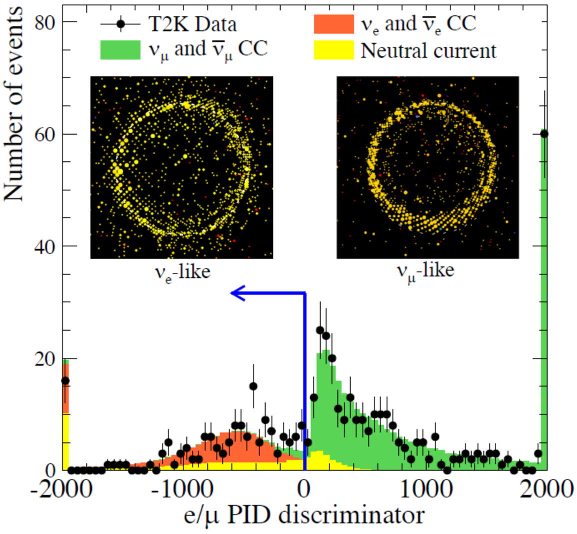

FIGURE 2.13: Distribution of SK PID parameter separating μ-like and e-like rings, with colours indicating the true origin of the rings. The top left and right pictures show examples of e-like and μ-like rings, respectively [72].

SK detector cannot detect oscillated ν_τ from the T2K beam, as with $E_\nu \sim 1$ GeV τ leptons are below the production threshold (~3.5 GeV). Furthermore, due to their relatively high mass (1776.82 MeV/c^2) and very short lifetime ($290.6 \cdot 10^{-15}$ s) τ leptons are quite difficult to detect and identify. Such measurements are performed by SK using atmospheric neutrinos data [73].

The interactions of neutrinos from the T2K beam are divided into six samples. First, the events are divided into FHC or RHC beam data. As the dominant interaction channel at T2K energies is CCQE, the most numerous samples contain events with one visible ring produced by the charged lepton. Then, the main criterion is the identification of e-like or μ-like rings as such event topologies are the main signature of oscillated and unoscillated neutrinos. Moreover, there are two samples enriched in resonant interactions and containing events with an additional π-like ring or delayed signal coming from Michel electron (from $\pi \to \mu \to e$ decay). An example of an event with more than one ring can be seen in Fig. 2.14.

The overall summary of FD samples used in this Thesis is as follows:

- FHC 1Rμ - one muon-like ring in FHC mode;
- RHC 1Rμ - one muon-like ring in RHC mode;
- FHC ν_μCC1π - one muon-like ring with additional ring coming from π or a delayed Michel electron signal in FHC mode;
- FHC 1Re - one electron-like ring in FHC mode;
- RHC 1Re - one electron-like ring in RHC mode;
- FHC 1Re1de - one electron-like ring and one Michel electron signature in FHC mode.

The event rates for each SK sample are summarised in Tab. 2.2.

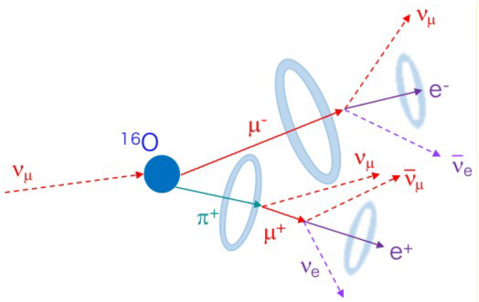

FIGURE 2.14: Sketch of FHC ν_μCC1π sample.

Sample	Events in Data
FHC 1Rμ	318
FHC ν_μCC1π	135
FHC 1Re	94
FHC 1Re1d.e	14
RHC 1Rμ	137
RHC 1Re	16
Total FHC	467
Total RHC	153
Total	620

TABLE 2.2: The total number of data events for each FD sample.

2.6 Collected Data and Results

T2K has been collecting data since 2010. The amount of accumulated data is expressed using Protons on Target (POT), which is a common unit used in accelerator neutrino physics, indicating how many neutrino interactions we can expect. The data-taking periods are denoted as runs with increasing numbers. Since the start of T2K, J-PARC has undergone many updates that resulted in an increase of beam intensity. The number of accumulated POTs in T2K for both FHC and RHC runs is shown in Fig. 2.15 as a function of time.

Tab. 2.3 summarizes the collected POTs for each T2K run that was used in the ND280 analysis described in this Thesis. ND and FD were exposed to the same number of POT, however, it can happen that one detector stops collecting data due to maintenance, DAQ problems, etc., therefore the data POT is different for ND and FD: Run 1 is not included in the current ND280

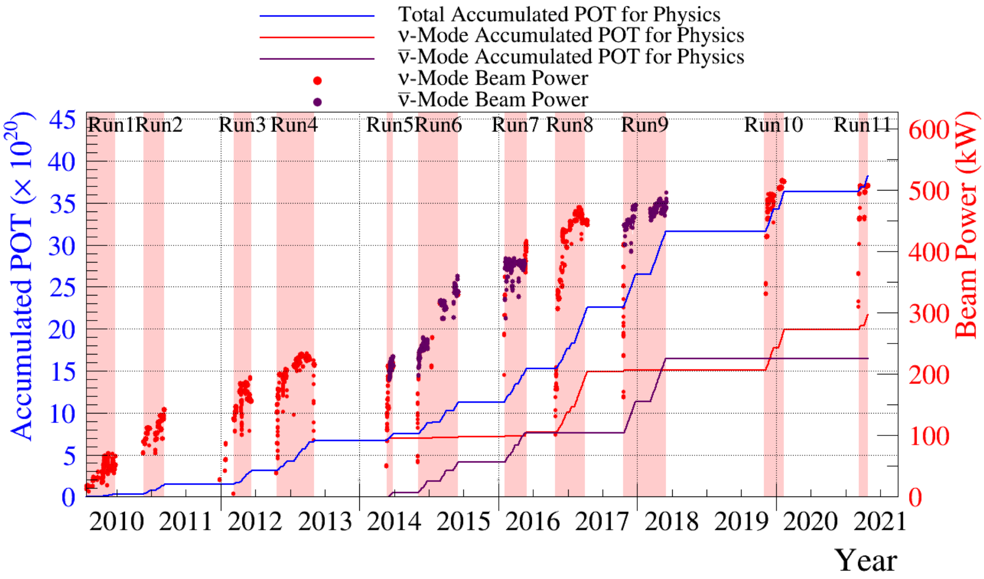

FIGURE 2.15: Accumulated number of POT as a function of time. The blue line shows the total accumulated POT, while the red and purple lines denote FHC and RHC, respectively. The dots correspond to beam power in kW, red for FHC and purple for RHC. The analysis described here doesn't include Run 11.

analysis because at that time ECAL was not complete (different geometry of ND280) and a different calibration was used for this run, while Run 10 is excluded due to a malfunction of the detector. Run 11 is the first one collected with SK doped with gadolinium, however, these data and neutron tagging are not used in this analysis yet.

Monte Carlo simulations (MC) are generated with around ten times more POT than actually collected data to reduce statistical fluctuations in MC. The ratio of data and MC POT is used as a scaling factor to be applied to MC.

For ND280 an additional type of MC is generated, namely Sand MC [74]. The beam neutrinos can interact both with the sand surrounding the ND280 pit and all walls and structures inside the pit. So-called sand muons (but in general also protons, pions or neutrons) produced in such interactions can enter ND280 and pass the selection cuts. Generating Sand MC requires different geometry (whole pit and surroundings, not just ND280), and as a consequence, it is generated as a separate set of MC.

With data collected so far, T2K managed to discover the electron neutrino appearance in muon neutrino beam [75] and to deliver the most precise measurement of θ_{23} [4]. Moreover, T2K has provided the first hints for CP violation in the lepton sector [72].

2.7 T2K Phase II

T2K is preparing for the second phase of the experiment. One of the elements is the upgrade of the beamline and horn focusing (more details can be found in [76]). The most relevant informations are shown in Fig. 2.16, where one can see that the beam power will increase from ~515 kW to ~750 kW, allowing for faster data collection. Additionally, the horn current will increase from 250 kA to 320 kA, allowing for better focusing and a 10% increase in the neutrino flux.

When it comes to the ND280 upgrade, P0D is being replaced with a new tracking detector consisting of a Super-FGD (SFGD) scintillator detector sandwiched between two horizontal

Run	Data (10^{19})	MC (10^{19})	Sand (10^{19})
2 FHC	7.94	288.4	214.6
3 FHC	15.93	307.80	107.30
4 FHC	34.84	722.45	214.6
5 RHC	4.45	221.10	120.25
6 RHC	34.22	346.98	120.25
7 RHC	24.39	333.20	120.25
8 FHC	57.31	717.01	214.6
9 RHC	23.03	266.07	120.25
Total FHC	116.02	2035.63	751.08
Total RHC	86.1	1167.24	480.98
Total	202.12	3202.87	1232.06

TABLE 2.3: Size of collected and simulated event samples expressed in protons-on-target (POT) for ND280 data and MC used in this Thesis.

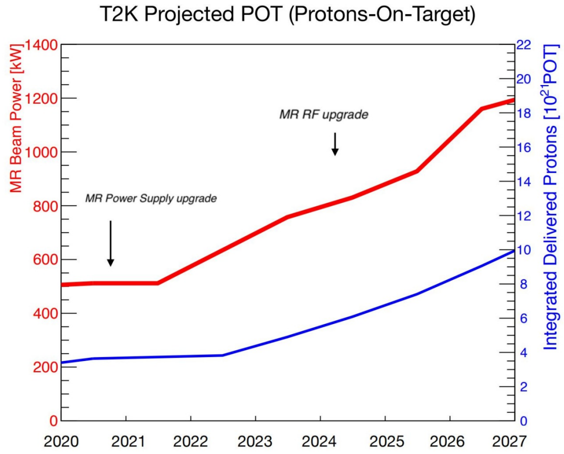

FIGURE 2.16: Current and expected POT and beam power after the J-PARC facility upgrade.

High Angle TPCs (HA-TPC), and a time-of-flight system surrounding these detectors, as can be seen in Fig. 2.17.

Super-FGD [77] will be the main part of the ND280 upgrade. What makes it exceptional is the use of small ($1 \times 1 \times 1$ cm^3) scintillator cubes rather than bars. Three fibres, connected to MPPCs, pass through each cube, allowing 3D track reconstruction and much better resolution at higher emission angles in comparison to the currently used FGDs. An example of a scintillator cube can be seen in Fig. 2.18. The cubes are covered with a reflecting layer (a white polystyrene micropore deposit) to reduce cross-talk effect.

Thanks to the high granularity, the new sub-detector will have a significantly better threshold and efficiency of proton reconstruction, while the cubes structure and HA-TPC ensure much higher angular acceptance. The comparison to current FGDs performance can be seen in Fig. 2.19.

SFGD was also proven to be able to tag neutrons with high efficiency, and to use neutron time of flight (ToF) to measure their energy [78].

For the purpose of oscillation analysis, it is crucial to stress that the currently used tracker will not be changed. Since SFGD has a mass approximately twice as large as the single FGD detector, after the upgrade we will double the overall target mass.

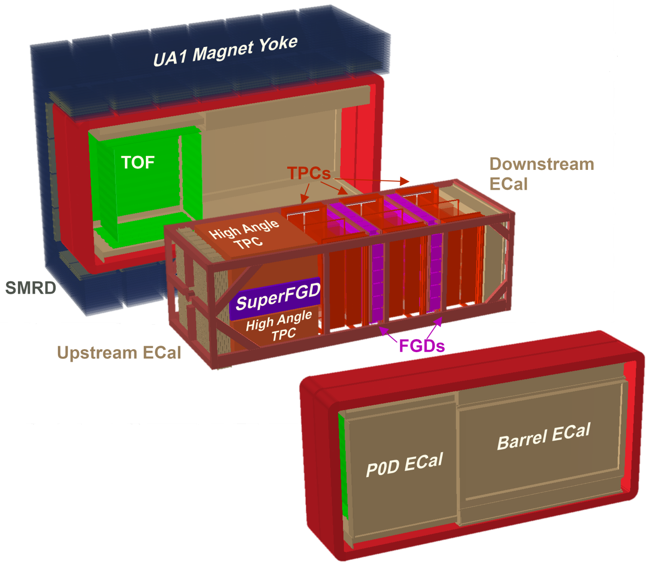

FIGURE 2.17: Schematic view of the upgraded ND280.

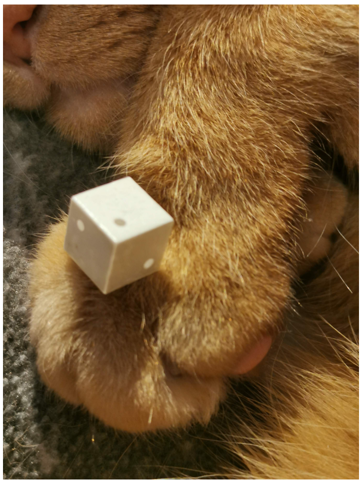

FIGURE 2.18: SFGD cube (1 cm × 1 cm × 1 cm) with cat's pawn for a scale.

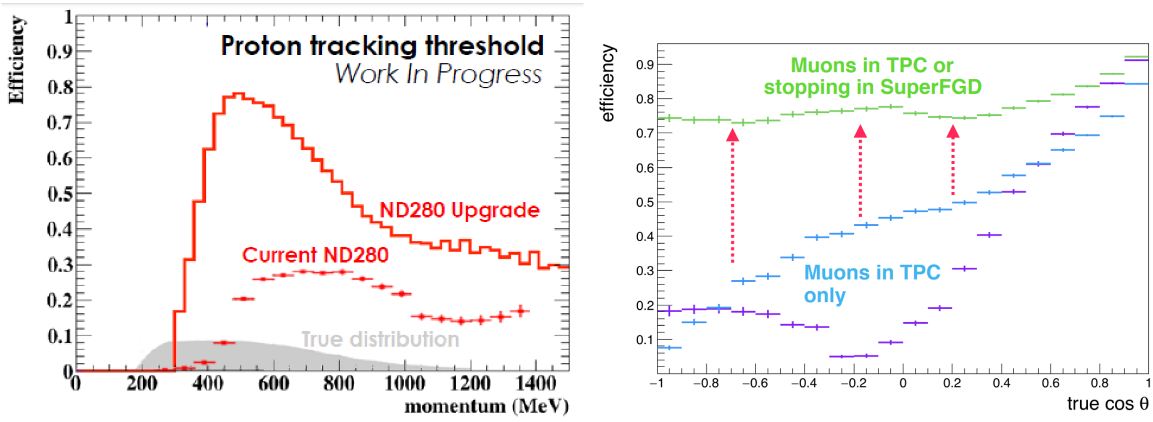

FIGURE 2.19: Proton reconstruction efficiency as a function of the momentum and muon angular acceptance for the current ND280 detector and after the upgrade.

3

ND280 Analysis

> Never interrupt your enemy when he is making a mistake.
>
> **Napoléon Bonaparte**

ND280 selections are an important part of T2K analysis, as more sophisticated selection (more event samples enriched in particular interactions) can allow to better probe cross-section and flux models. This Section describes the event selections used in the main ND280 analysis, emphasis is placed on selections included in the analysis by the Author of this Thesis.

3.1 General Description of ND280 Event Samples

In the analysis, CC events are used and their signature is a μ track which is in most cases the Highest Momentum Negative Track (HMNT) for ν_μ or Highest Momentum Positive Track (HMPT) for $\bar{\nu}_\mu$. Therefore, the primary criteria used in ND280 are designed to select "good" events with a μ track starting in either FGD and crossing a TPC. The μ candidate kinematic properties are used directly in the analysis; hence, it is necessary to extract them from TPC rather than FGD. ND280 has two FGD targets, therefore there are two sets of event samples. The main difference between the sets is the condition to have the interaction vertex in either FGD1 or FGD2.

Each event has to pass a sequence of general cuts to be included in so-called CC inclusive selection. Those cuts are as follows:

- *Event quality*: The event has to appear during a bunch time period, and all sub-detectors should be fully operational.
- *Total multiplicity*: The event contains at least one track crossing a TPC.
- *Quality and fiducial volume*: The interaction has to start in an FGD, moreover, the vertex has to be distant at least 5 scintillation bars from the edge of the FGD. Additionally, in order to reject very short tracks, for which the reconstruction in TPC is less reliable, only tracks with more than 18 clusters are selected.
- *Upstream background veto*: This cut excludes events where the second-highest momentum track (if any) starts 150 mm upstream of the muon candidate track. This allows to reject events in which a muon undergoing a large scattering could be reconstructed as two tracks.
- *Broken track cut*: The starting position of the muon candidate track is less than 425 mm away from the FGD upstream edge if the same event has at least one reconstructed

FGD-only track. The cut rejects events in which the reconstruction has broken a track into two, creating one track fully contained in an FGD (isoFGD track) and one with TPC-matching starting at the FGD edge.

- *Muon PID*: HMNT/HMPT has to be identified as the muon as described below.

The TPC particle identification is based on energy loss. For each particle hypothesis i ($i = \mu, \pi, p, e$), the likelihood L_i is defined as:

$$L_i = \frac{e^{-Pull_i^2}}{\sum_l e^{-Pull_l^2}}, \tag{3.1}$$

where $Pull_i$ is defined as:

$$Pull_i^{TPC} = \frac{dE/dx_{measured} - dE/dx_{expected,i}}{\sigma\left(dE/dx_{measured} - dE/dx_{expected,i}\right)}. \tag{3.2}$$

Muons are selected by requiring:

$$L_\mu > 0.05. \tag{3.3}$$

Additionally, we reject low energy electrons using the following condition:

$$L_{MIP} = \frac{L_\mu + L_\pi}{1 - L_p} > 0.8 \text{ if } p < 500\text{MeV/c}. \tag{3.4}$$

Events that passed the CC inclusive selection are split based on the presence of photons into CC Photon and CC NoPhoton (0γ). Photon tagging is very recent and was used for the first time in the analysis described further in the Thesis. The description of its development and technical details can be found in [79], but some basic information will be provided below.

Photons can originate from the following decay channels:

- $\pi^0 \to \gamma + \gamma$
- $\eta \to \pi^0 + X \to \gamma + \gamma + X$
- $\eta \to \gamma + \gamma$
- $\Lambda \to \pi^0 + X \to \gamma + \gamma + X$
- $K \to \pi^0 + X \to \gamma + \gamma + X$

where X can be a variety of particles depending on the specific decay mode. The enlisted particles are mostly created in DIS or RES reactions; therefore, the CC Photon sample is enriched in these interactions.

A photon candidate is an isolated object in the ECal (not associated with any TPC or FGD tracks) with the log-likelihood ratio of the proton and electron hypotheses `PIDEmHip` < 0 [79].

The events classified as CC-0γ are further divided into samples using a π multiplicity cut. Pion candidates have to start in the same FGD as the muon candidate and come from the same bunch. Depending on their momenta and directions, pions can be tagged in three ways: using TPC-FGD matched track, FGD-only track, or by observing a Michel electron in FGD, created in the following decay chain:

$$\begin{aligned} \pi^+ \to & \mu^+ + \nu_\mu \\ & \to e_d^+ + \nu_e + \bar{\nu}_\mu, \end{aligned} \tag{3.5}$$

where the Michel electron is denoted as $e_d^{\pm}$. Since Michel electrons are delayed with respect to the time of interaction by ~2.19 μs, we can tag them by looking for a delayed signal in FGD.

For the pions that crossed the TPC, we apply the following cuts:

$$L_{MIP} = \frac{L_\mu + L_\pi}{1 - L_p} > 0.8 \text{ if } p < 500 \text{ MeV/c}, \tag{3.6}$$

$$L_\pi > 0.3. \tag{3.7}$$

If a pion was contained in FGD (isoFGD track), FGD PID may be used for tagging. The FGD pulls are defined as:

$$Pull_i^{FGD} = \frac{E_{measured} - E_i(L_{measured})}{\sigma_{E_i(L_{measured})}}, \tag{3.8}$$

where $E_{measured}$ is the measured energy deposit and $E_i(L_{measured})$ is the expected energy deposit for a track of length $L_{measured}$ and particle type i. For isoFGD π to be accepted, the following condition has to be met:

$$-2 < Pull_\pi^{FGD} < 2.5. \tag{3.9}$$

For pions that did not leave a track in FGD because of low energy or high emission angle, the only tagging method is with the signal from the Michel electron.

CC-0γ is split into the following samples, depending on the number of tagged pions:

- **CC0π-0γ** - 0 reconstructed pions and 0 Michel electrons.
- **CC1π-0γ** - 1 reconstructed π^+ or 1 Michel electron.
- **CC-Other-0γ** - other combinations of pions and Michel electrons.

Since SK is now doped with gadolinium and can much more effectively detect neutrons, ND280 needs to constrain more complex physical phenomena (see Section 1.6). Thanks to the accumulated data statistics (see Section 2.6), the brand new samples using proton multiplicity cut were introduced. Even though neutron tagging in SK is not ready yet, it is supposed to be used in the next T2K analysis, so the development on the ND280 side is an important step forward.

Events belonging to CC0π-0γ samples are further divided into:

- **CC0π-0p-0γ** - 0 reconstructed protons.
- **CC0π-Np-0γ** - at least one reconstructed proton.

The proton-tagged samples are described extensively in the next Section.

Fig. 3.1 displays the distributions of reconstructed muon momenta for all FHC FGD1 event samples. CC1π-0γ sample is enhanced in RES scattering, CC-Other-0γ is dominated by DIS, and CC Photon consists mostly of RES and DIS, being the most diverse sample. Those results are expected and mean that each sample is suited for probing different effects.

So far, the FHC selections have been discussed. For RHC, the situation is more complicated: as mentioned in Section 2.2, there is quite large contamination from the wrong sign component. In consequence, there are samples that measure both signal ($\bar{\nu}$) and background (ν) in RHC mode. In the following chapters, RHC $\bar{\nu}_\mu$ samples will be referred to as RHC samples, while RHC ν_μ ones as RHC BKG samples.

The cuts used in RHC selections are mostly analogous to those used in FHC, the details can be found in [80]. Furthermore, the photon and proton tagging are not yet introduced in RHC, only the pion multiplicity cuts are used. The potential effect of using proton tagging in RHC and RHC BKG samples was studied and is presented in Appendix A.1.

A summary of all event samples used in the analysis can be seen in Tab. 3.1.

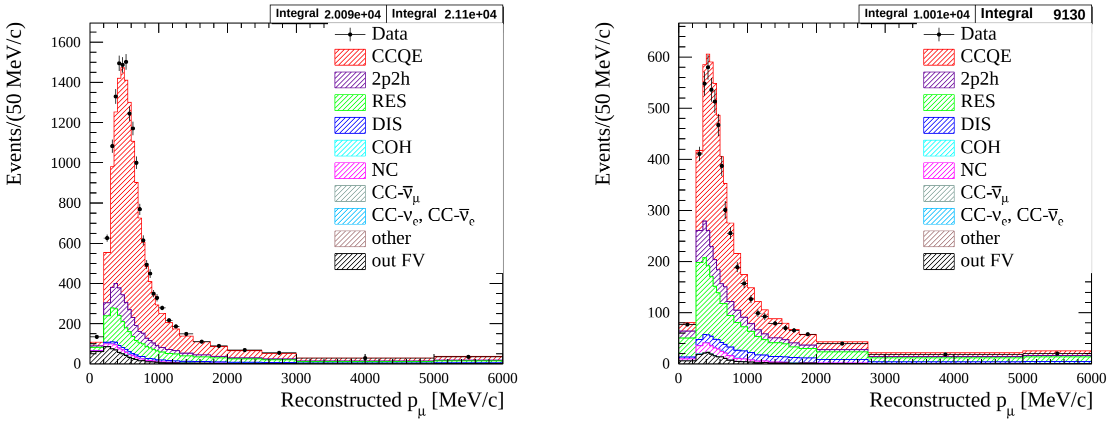

(A) FGD1 CC0π-0p-0γ

(B) FGD1 CC0π-Np-0γ

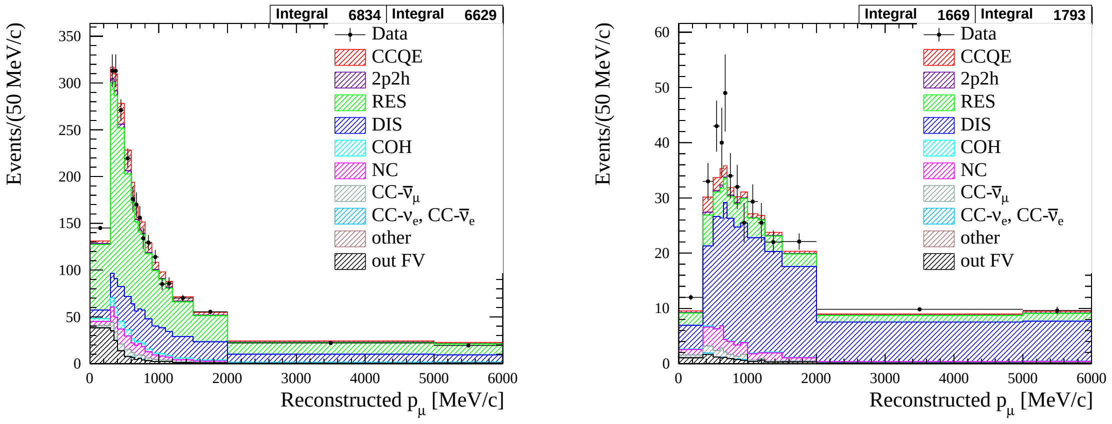

(C) FGD1 CC1π-0γ

(D) FGD1 CC-Other-0γ

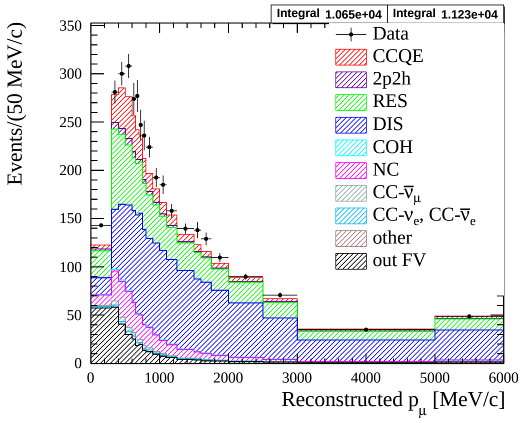

(E) FGD1 CCPhoton

FIGURE 3.1: Reconstructed p_μ distributions for all FHC FGD1 samples with reactions indicated by colours.

	All Reconstructed Events	
$\swarrow$	$\downarrow$	$\searrow$
FHC ν_μ CC-Inclusive	RHC $\bar{\nu}_\mu$ CC-Inclusive	RHC ν_μ CC-Inclusive
(FGD1 and FGD2)	(FGD1 and FGD2)	(FGD1 and FGD2)
$\downarrow$	$\downarrow$	$\downarrow$
CC0π-0p-0γ CC0π-Np-0γ CC1π^+-0γ CC-Other-0γ CC-Photon	CC0π CC1π^- CC-Other	CC0π CC1π^+ CC-Other

TABLE 3.1: Event samples used in the ND280 analysis.

3.2 ND280 Proton-Tagged Samples

3.2.1 Selection Algorithm and Kinematical Properties

Proton candidates are searched among tracks that have not been classified as muon or pion by previous cuts. They have to originate in the same FGD as the muon candidate and have:

$$L_p > 0.5. \tag{3.10}$$

If the proton is contained in an FGD, the following condition has to be fulfilled:

$$Pull_p^{FGD} > -4. \tag{3.11}$$

The distributions of TPC likelihoods and FGD pulls are shown in Fig. 3.2[1].

Fig. 3.3 shows the true identity of a proton candidate. Most of the proton candidates are true protons, which is very encouraging. The misidentification occurs more often for $\cos\theta_\mu \sim 1$ and is primarily caused by DIS events, as can be seen in Fig. 3.4, which shows a similar distribution for misidentified proton candidates only, broken down by reaction. The $\cos\theta_\mu$ distributions are different for FGD1 and FGD2 samples, which is the consequence of the poorer reconstruction capabilities of FGD2 at higher angles.

Fig. 3.5 shows the numbers of reconstructed isoFGD and TPC-matched protons in CC0π-0γ samples. Few conclusions can be drawn from this plot. Firstly, there are more TPC-matched protons than isoFGD ones. Secondly, when looking at the reaction breakdown of events with one isoFGD or one TPC-matched proton (the second bin of the histogram), it is clear that events with one isoFGD proton have a higher fraction of CCQE interactions (60%) with respect to the TPC-matched protons (45%).

The CC0π-0p-0γ sample consists of events with the reconstructed muon only, as can be seen in Fig. 3.6 (A), whereas the situation is more complicated for CC0π-Np-0γ. A CC0π-Np-0γ event can consist of a muon with a very short isoFGD proton, a more energetic TPC-matched proton, or multiple protons.

The numbers of selected data events in proton-tagged samples are: 21329 (22935) for CC-0π-0p-0γ and 9257 (7373) for CC-0π-Np-0γ FGD1 (FGD2). The comparison with MC expectations will be discussed in the Chapter 6.

Fig. 3.7 shows the distributions of true momentum for the true highest momentum (HM) proton and reconstructed momentum for the HM proton candidate in CC0π FGD1 sample. By comparing those distributions, it can be observed that most protons are not reconstructed

---

[1] The Figure shows distributions for all particles, while in the selection the particles identified as muons will not be considered as proton candidates. However, the cuts on the likelihood were designed to work for general case.

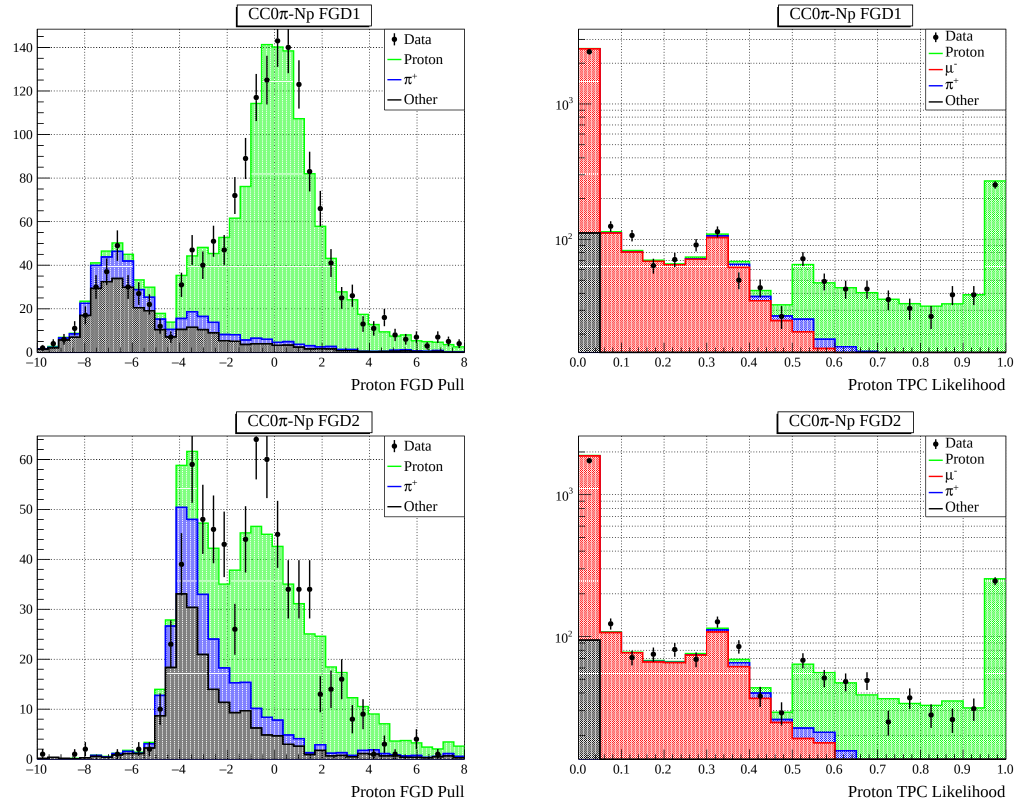

FIGURE 3.2: Proton pull for isoFGD tracks (left) and proton likelihood for tracks with a TPC segment (right) for CC-0π-Np-0γ selection. The top plots present FGD1, while the bottom ones FGD2 samples.

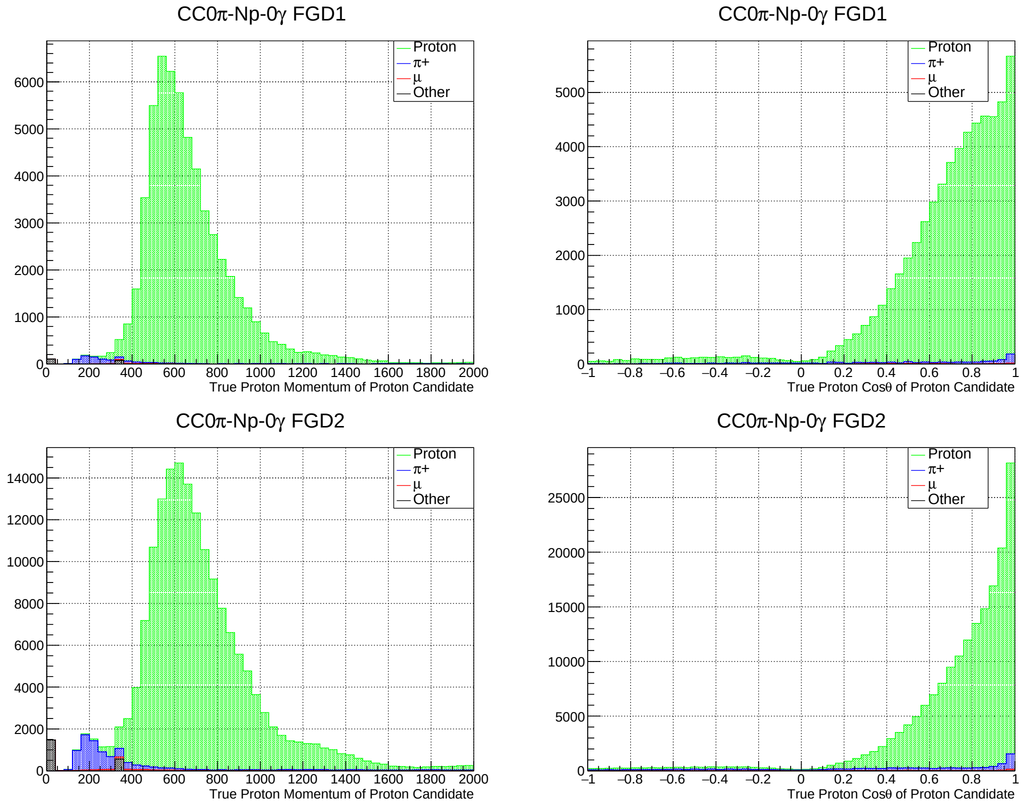

FIGURE 3.3: True identity of proton candidates as a function of p_{proton} (left) and $\cos\theta_{proton}$ (right). The top plots present FGD1, while the bottom ones FGD2 samples.

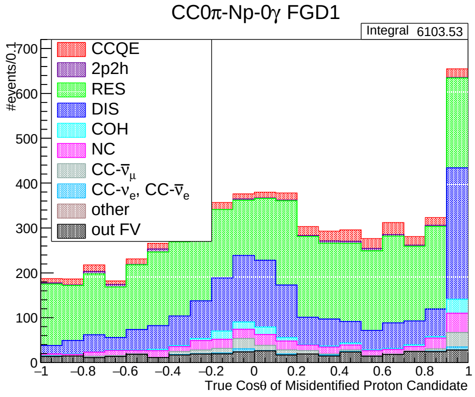

FIGURE 3.4: True $\cos\theta_\mu$ distribution of TPC-FGD1 matched proton candidates which are not true protons.

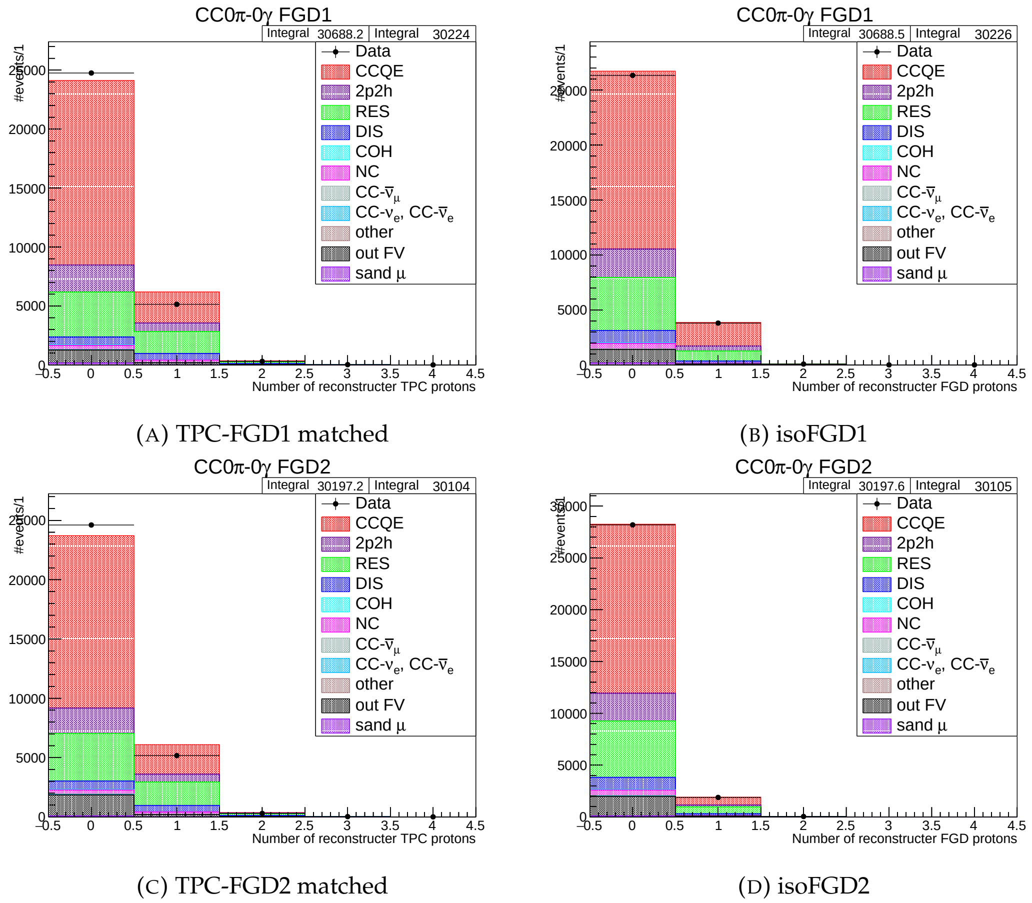

(A) TPC-FGD1 matched

(B) isoFGD1

(C) TPC-FGD2 matched

(D) isoFGD2

FIGURE 3.5: Number of reconstructed protons in CC0π-0γ samples. Most events have no reconstructed protons.

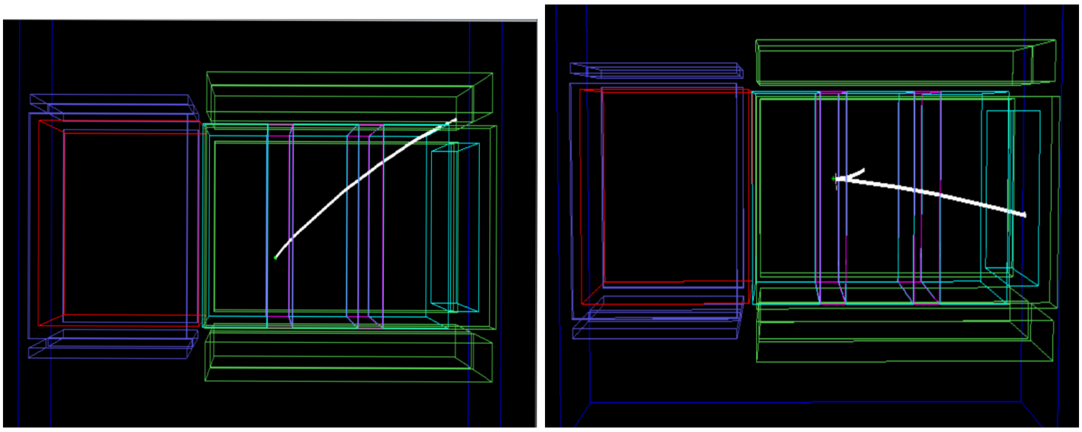

(A) CC0π-0p-0γ (B) CC0π-Np-0γ with TPC-matched proton

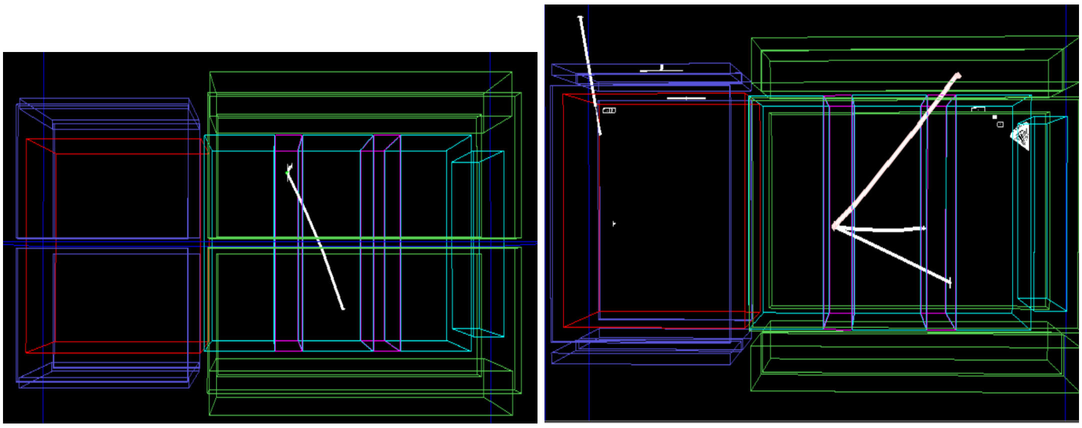

(C) CC0π-Np-0γ with isoFGD proton (D) CC0π-Np-0γ with multiple protons

FIGURE 3.6: Examples of ND280 event displays for proton-tagged samples. Three green frames represent the TPCs, while two purple ones show FGDs.

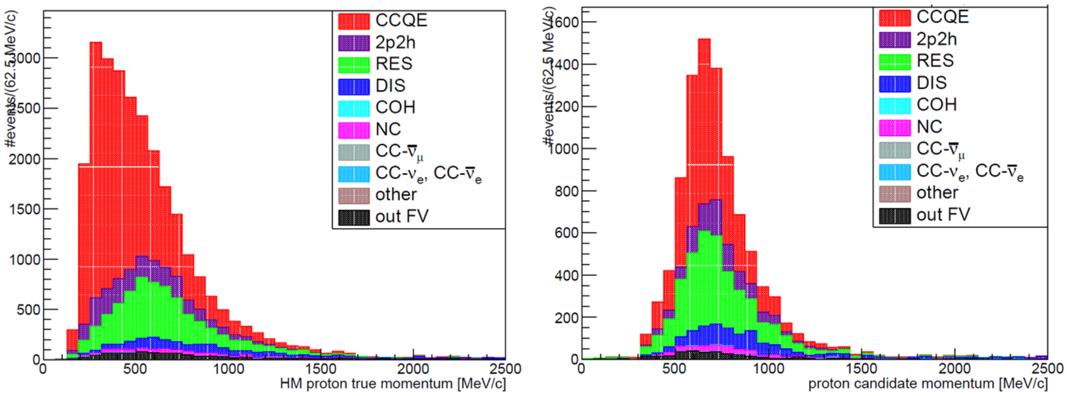

(A) True HM proton (B) HM proton candidate

FIGURE 3.7: Distributions of true momenta of true HM protons (left) and reconstructed momenta of HM proton candidates (right). Many events have a true proton that remains undetected; therefore, those plots cannot be directly compared.

because of their low momenta. Since most CCQE protons have rather low momenta (below 500 GeV/c), many observed protons originate from RES. That is the reason why the fraction of CCQE is higher for isoFGD protons.

By looking at the reconstructed momenta of isoFGD protons and TPC-matched protons separately (Fig. 3.8), we can see that TPC-matched protons have a much broader momentum distribution. This is expected, as a proton with higher momentum is more likely to pass to the TPC.

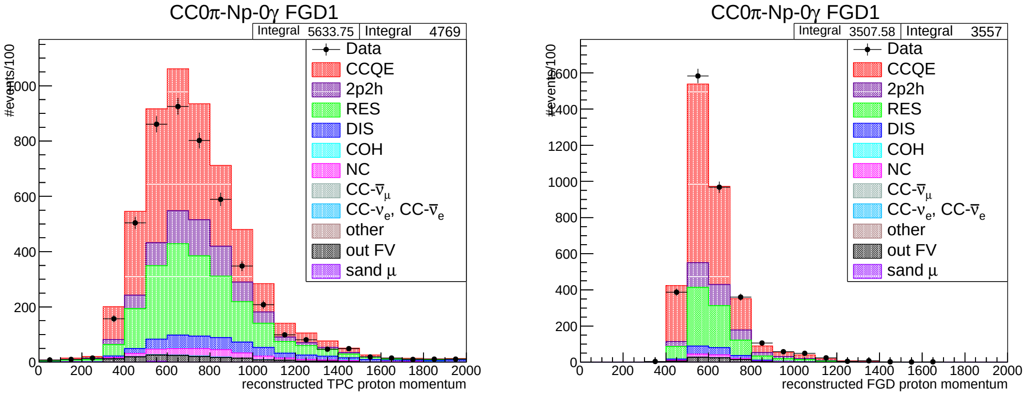

(A) TPC-matched FGD1 (B) isoFGD1

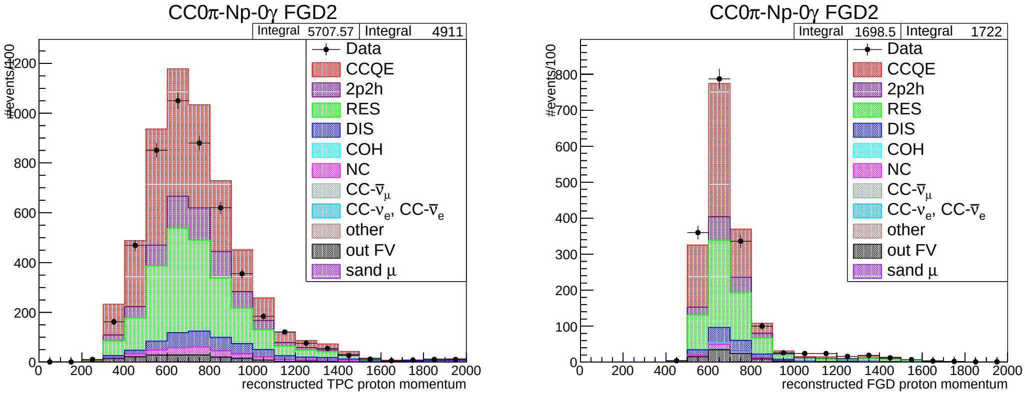

(C) TPC-matched FGD2 (D) isoFGD2

FIGURE 3.8: Momentum distributions of TPC-matched proton candidates and isoFGD proton candidates in CC0π-Np-0γ samples.

3.2.2 Physical Properties

For T2K analysis, the muon kinematics is very important, as the momentum and emission angle are the inputs to the ND280 fit. Fig. 3.9 shows the two-dimensional distributions of muon kinematics for CC0π-0p-0γ and CC0π-Np-0γ samples. Two notable differences can be observed. Firstly, the CC0π-Np-0γ muon momentum distribution reaches higher values. Secondly, CC0π-Np-0γ has much more muons emitted at high angles, whereas in CC0π-0p-0γ muons mostly travel forward. This can be easily understood in terms of the conservation of momentum in a two-body process. In a CC0π-Np-0γ event, there is at least one high momentum proton that can be emitted at a high angle (see Fig 3.3), so the muon has also to go at a higher angle to conserve the momentum. In a CC0π-0p-0γ event, there is usually a low momentum proton and the muon has to go in the same direction as the neutrino beam.

Tab. 3.2 shows the reaction breakdown for different samples. It can be observed that by splitting CC0π-0γ we can obtain a much higher fraction of CCQE in CC0π-0p-0γ, while

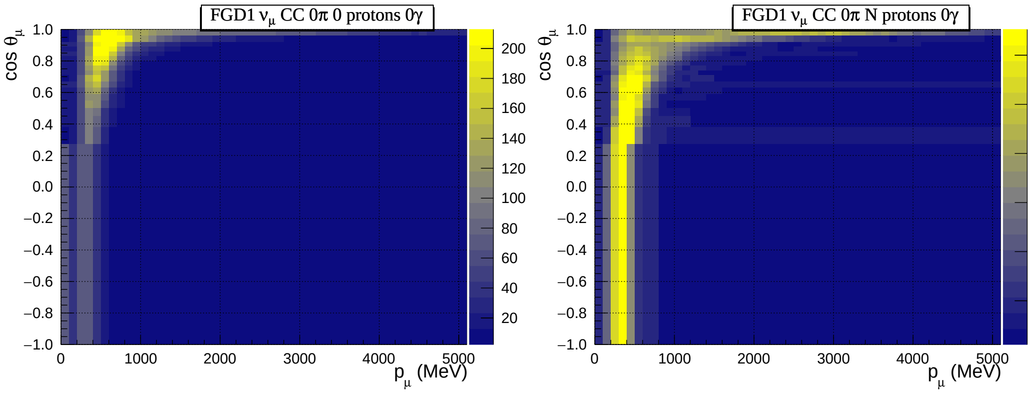

FIGURE 3.9: Two-dimensional distributions of reconstructed muon momenta and emission angles, for CC0π-0p-0γ (left) and CC0π-Np-0γ (right) FGD1 samples.

CC0π-Np-0γ contains a high fraction of non-CCQE modes. Since RES require higher energy neutrinos, high momentum protons are more likely to be produced in such reactions.

	CC0π-0γ	CC0π-0p-0γ	CC0π-Np-0γ
CCQE	51%	58%	38%
2p2h	11%	10%	11%
RES	23%	19%	30%
Other	15%	13%	21%

TABLE 3.2: Fractions of different reactions for three FGD1 FHC samples.

As can be seen in Fig. 3.10, proton-tagged samples have different distributions of four-momentum transfer Q^2. Events with low Q^2 transferred to the hadron system will have a proton with relatively low momentum and are very likely to be classified as CC0π-0p-0γ as such a proton is often below the reconstruction threshold. There are many effects dependent on Q^2, like Pauli blocking; hence, the new samples can help us probe those effects better.

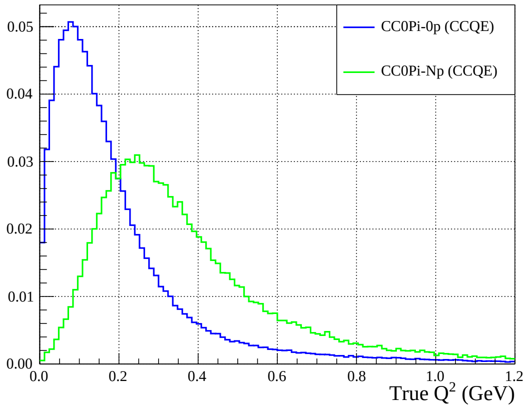

FIGURE 3.10: Distributions of true Q^2 for CCQE-only events for FGD1 proton-tagged samples.

Valencia model [81] is used by T2K to describe 2p2h interactions. The model has a very characteristic two-peak structure in phase space of energy and momentum transfer ($q_0/|\vec{q}_3|$), as shown in Fig. 3.11. Events from proton-tagged samples have different $q_0/|\vec{q}_3|$ distributions: CC0π-0p-0γ tends to occupy mostly the lower region, while CC0π-Np-0γ the upper one. It is worth mentioning that in general, 2p2h models predict unique distributions[2] of $q_0/|\vec{q}_3|$; hence, the proton-tagged samples can be used in model validation.

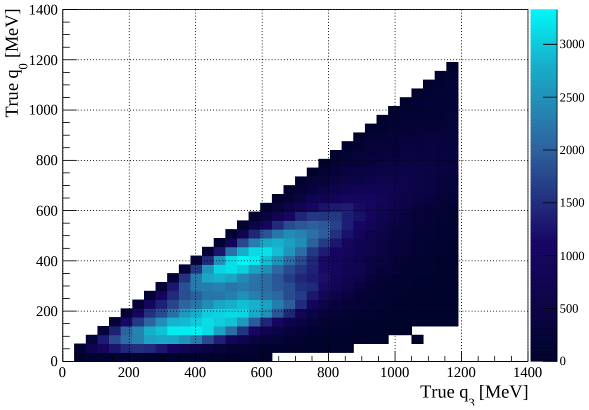

(A) Valencia Model 2p2h

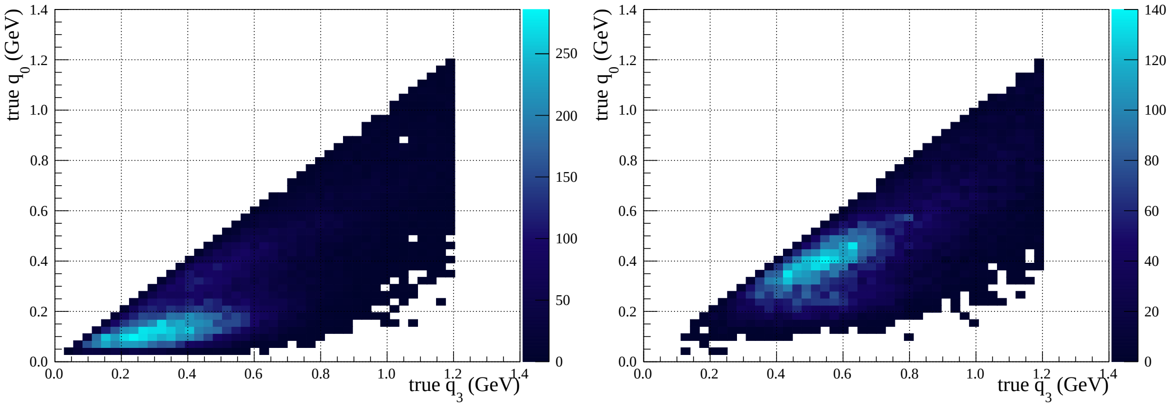

(B) CC0π-0p-0γ (2p2h only)

(C) CC0π-Np-0γ (2p2h only)

FIGURE 3.11: True $q_0/|\vec{q}_3|$ distributions for 2p2h channel for FGD1 proton-tagged samples.

Looking at Fig. 3.12, which depicts the true neutrino energy (E_ν) of 2p2h events for proton-tagged samples, we can see that the two samples have slightly different distributions, with CC0π-Np-0γ having higher E_ν values. This fact is important, as different models predict different cross-sections for low (below 0.6 GeV) and higher (above 0.6 GeV) neutrino energies.

The comparison of sensitivities for samples with and without proton and photon tagging is presented in Appendix A.2. We observe error reduction for many effects related to CCQE and 2p2h interactions.

3.2.3 Binning Study

Selecting the binning for each sample is an art in itself, with many requirements. Firstly, it is necessary to study the reconstruction accuracy and resolution of the detector. Fig. 3.13 top plot shows a two-dimensional comparison of true and reconstructed μ momentum, known as momentum reconstruction accuracy. The bottom left plot shows the mean and RMS of reconstructed p_μ projected onto true p_μ axis, while the bottom right one displays the errors from the left plot, corresponding to momentum resolution. We can observe that in the region between 200 and 900 MeV/c, the accuracy is very good. The resolution is reasonable in this

---

[2] For example, the SUSAv2 model [82].

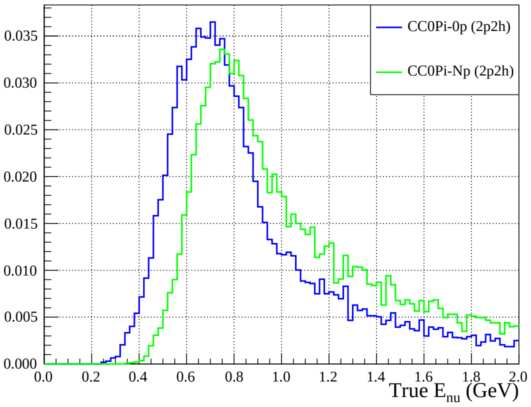

FIGURE 3.12: True neutrino energy for 2p2h channel for FGD1 proton-tagged samples.

momentum range as well. Below 200 MeV/c, both accuracy and resolution tend to be much worse, so it is better to include this region as one bin.

Fig. 3.14 shows an analogous study for $\cos\theta_\mu$. In this case, we observe that the reconstruction accuracy is very good in the forward-going region. Despite the fact that the plots were prepared for CC0π-0p-0γ, the resolution is a general property of the detector, and very similar results have been obtained for other samples.

Another criterion is to have at least 20 MC events in each bin. The number of MC events in a bin follows the Poisson distribution, so for such a number, it is unlikely to get a statistical fluctuation resulting in 0. We additionally require to have at least one data event.

After optimization, there are 650 bins for CC0π-0p-0γ and 352 for CC0π-Np-0γ. The same binning is assumed for FGD1 samples and their FGD2 counterparts. Since CC0π-0p-0γ is the most populated sample, it has the highest number of bins.

The final binning is presented in detail in Appendix B.2.

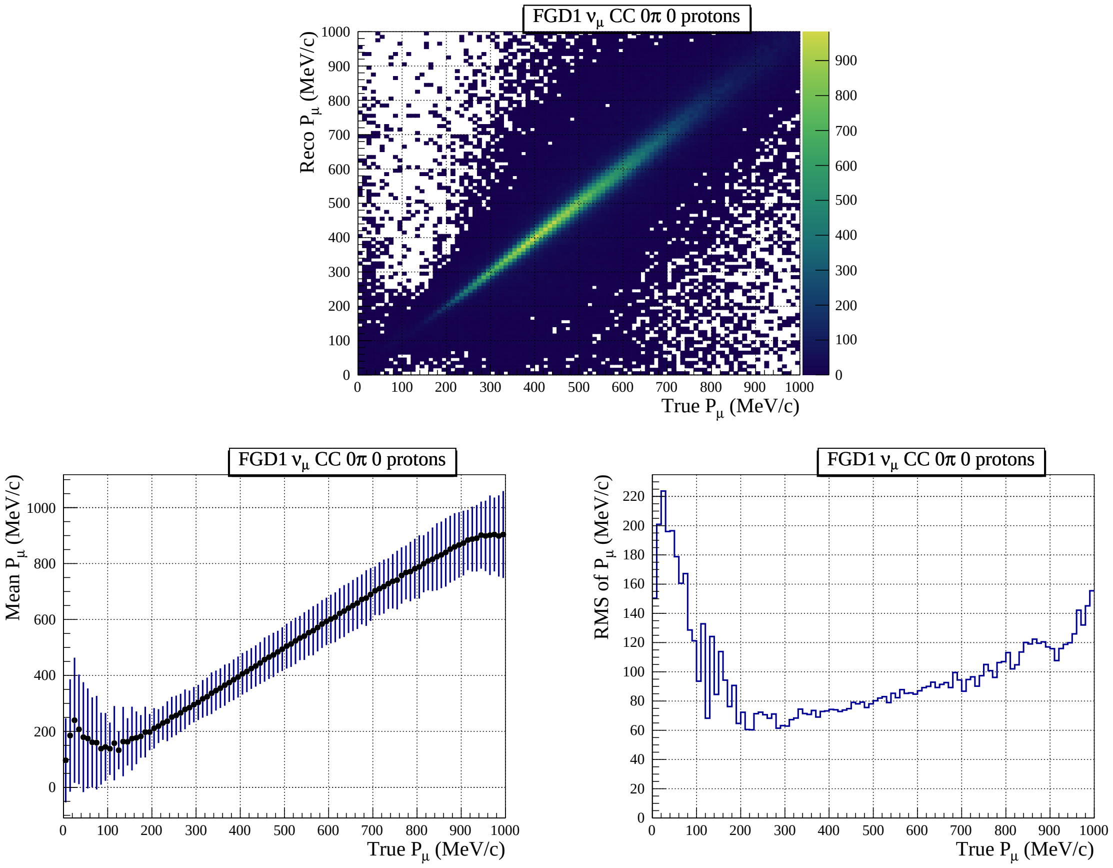

FIGURE 3.13: Muon momentum reconstruction accuracy and resolution.

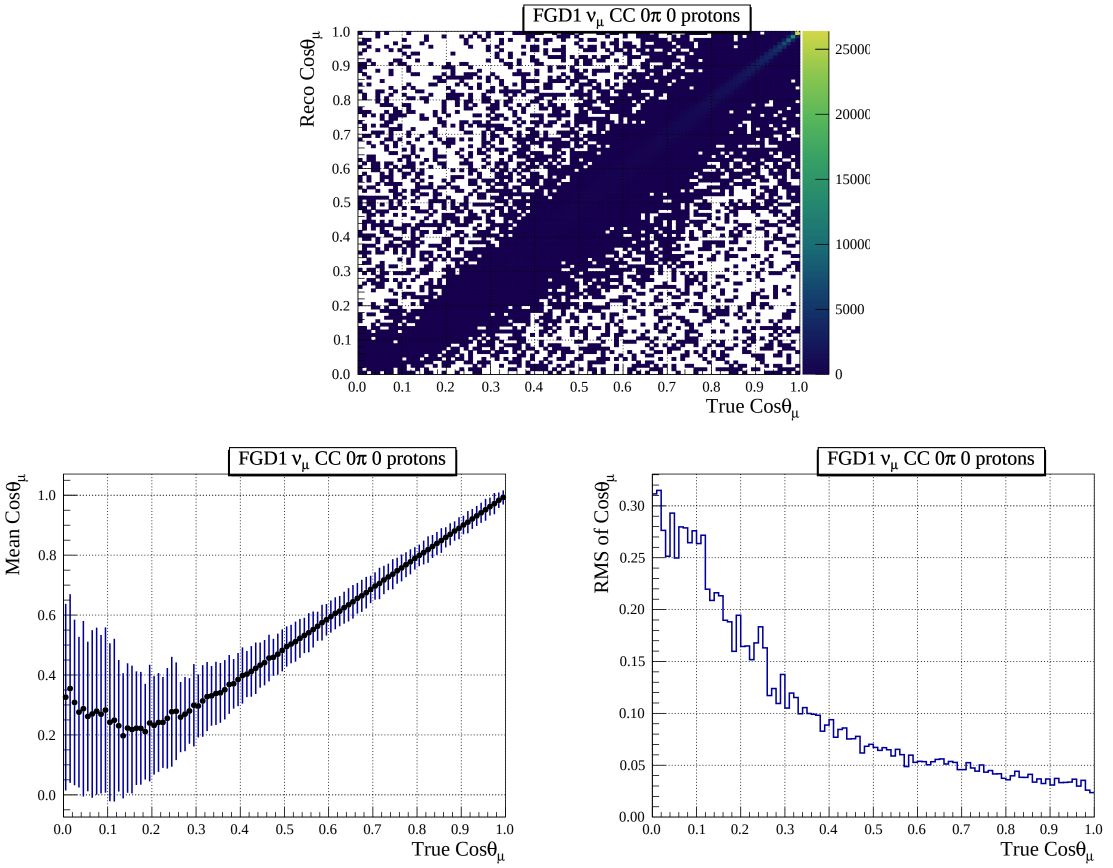

FIGURE 3.14: Muon angular reconstruction accuracy and resolution.

4

Systematic Model

> Men are always more inclined to pitch their estimate of the enemy's strength too high than too low, such is human nature.
>
> **Carl von Clausewitz**

In experiments, except for the statistical error, one has to take into account the systematic error as well. We can divide the sources of systematic uncertainties into three main categories: related to the detector, the flux, and the cross-section models. This Chapter discusses the systematic errors included in the ND280 analysis. The emphasis is placed on the systematic parameters developed by the Author or those that are most important for proton-tagged samples.

4.1 ND280 Detector Systematic Errors

ND280 is a complex detector with multiple sources of systematic uncertainties. The errors may originate from physical phenomena like secondary interactions (SI) of particles, or from the detection efficiency of each sub-detector used in the analysis, as well as from the matching of reconstructed track segments from different sub-detectors.

When it comes to the treatment of the detector systematic uncertainties and the estimation of their effect on the selected event samples, we can divide them into three categories [83, 84]:

- **Observable Variation Systematics** - The systematic error is applied as a smearing to the reconstructed event variables, for example p_μ. Therefore, it can change the reconstructed topology and lead to the direct migration of events between samples or bins.

- **Efficiency Systematics** - Concerns all the variables corresponding to a reconstruction or detection probability. In this case, the selection is run once, and a weight is computed from the probability. The errors are computed based on data/MC differences using studies with well-known control samples. Tracking and matching efficiencies can be estimated using the redundancy between detectors. For example, the TPC2 tracking efficiency can be computed using tracks with segments in FGD1 and FGD2.

- **Normalisation Systematics** - These are the systematic errors associated with the total event normalisation. Similarly as for efficiency systematics, weights are calculated for a whole category of events. A typical example is the uncertainty of an FGD mass.

Below, we list all sources of systematic uncertainties relevant to the analysis, along with short descriptions. For detailed explanations, see [79, 85].

- **Magnetic field distortions** uncertainty is caused by the lack of modelling of distortions in the TPC magnetic field and leads to biases in momentum measurements. The distortions are greater in TPC3, hence this systematic source affects FGD2 samples more. The error is applied based on a special map of the magnetic field that has been produced.

- **TPC momentum resolution** error describes how well the momentum resolution is modelled in MC. It was found that the resolution is underestimated as a function of the momentum, most probably due to the TPC electric field distortions. The uncertainty was calculated based on the data and MC difference between the momentum component transverse to the magnetic field.

- **TPC momentum scale** uncertainty is coming from the magnetic field map in ND280. Based on the data and MC comparison of the cosmic muon sample, the error was estimated to be 0.5%.

- **TPC PID** is based on pull distributions calculated from dE/dx. Dedicated control samples for muons, protons and electrons were created, and the uncertainties were estimated from data/MC differences. Since pions have a very similar energy loss to muons, the error for them is considered to be identical.

- **FGD PID** is calculated using particle pulls based on energy deposits in FGD. Pull distributions can be modelled by a Gaussian function and checked using control samples of particles stopping in FGD and having a TPC segment to use the TPC particle identification. Similarly as for TPC PID uncertainty, the same error is assumed for pions and muons.

- **Charge ID** uncertainty describes how effective the particle charge identification is, based on its curvature in the TPCs. If tracks have segments in multiple TPCs, the charge is computed for each segment individually and for the global track as a whole. If the charges for segments differ, the relative weight between the local charges is used in the determination of the global one.

- **TPC cluster efficiency** is the probability of finding a group of adjacent single TPC clusters (collection of contiguous pads with energy deposits) at a given column of pads, where charged particle crosses the gas volume of the TPC. It is evaluated separately for horizontal and vertical clusters. The *quality* cut requires a track to have at least 18 clusters, making this error relevant.

- **TPC tracking efficiency** includes an evaluation of the TPC pattern recognition algorithm and the likelihood fit. A reconstruction failure results in the misidentification of event topology, which can lead to fewer events being selected. This efficiency does not include the hardware efficiency, since the data quality checks guarantee that the TPCs were fully operational. The uncertainty was estimated using a control sample of muons going through two consecutive TPCs.

- **TPC-FGD matching efficiency** characterizes how well the reconstruction matches FGD tracks to TPC tracks. The control sample is created by selecting through-going muons passing through two consecutive TPCs. The efficiency is the ratio of events that also have a track in the FGD in between to all selected events.

- **FGD hybrid tracking efficiency** of reconstructing tracks contained in FGD in the presence of a longer track exiting to a TPC. For this study, see Appendix A.3.

- **Michel electron efficiency** describes how likely we are to identify such a delayed signal. Identification of the Michel electron will result in event classification as CC1π-0γ. Cosmic muons stopping in an FGD were used as a control sample.

- **ECal tracking efficiency** is related to the reconstruction of objects in the ECal. The control sample requires a good quality TPC track ending close to the edges of the ECal, where the end of the track points towards the ECal.

- **TPC-ECal matching efficiency** of track components coming from TPC and ECal. This systematic uncertainty is applied to any event that does not contain an isolated ECal object, covering the case where an ECal photon has been wrongly matched to a TPC track. TPC tracks entering the barrel and downstream ECals are used as control samples.

- **ECal PID EmHip** discriminates $e^{\pm}/\gamma$ from highly ionising particles like protons. ECal PID `EmHip` uncertainty has the potential to shift objects close to cut values. This shift will result in the event migration from CC Photon to another sample. Control samples of electrons, protons and forward-going and comics muons were used in the systematics evaluation.

- **ECal Photon Pile-Up** covers cases where any isolated ECal object is a product of a pile-up interaction in the ECal. The number of POT per spill increased over time, leading to more pile-up interactions, however, the data/MC agreement is comparable for all runs. Events with ECal photons and without FGD activity were used as control samples.

- **OOFV background** uncertainty is a normalisation of events coming from out of FGD fiducial volume, but selected as originating in it. OOFV rate for FGD1 (FGD2) has been found to be 5 (7.5)%. The background is separated into 9 samples using true MC information. The error is evaluated separately for each of these categories.

- **Sand muon background** is a special type of background events coming from the ND280 neighbourhood. A neutrino can interact in the pit containing ND280 or its surroundings, and some of the produced particles (usually called "sand muons", but in general any particle) can enter ND280. The error is estimated using charged particles entering through the front wall of P0D.

- **Pile-up** effect considered here is due to sand muons that are in coincidence with events originating in ND280. Similarly as for ECal Photon Pile-Up, the effect of increasing POT per spill over time leads to more pile-up events.

- **FGD mass** is related to the interaction targets and affects the overall number of neutrino interactions. MC overestimates the density of the FGD modules, and the uncertainty of the FGD1 (FGD2) mass is 0.6% (0.4%). The water mass uncertainty is not correlated with the scintillator mass uncertainty, hence the difference between FGD1 and FGD2 errors.

- **Proton secondary interactions**[1] systematic uncertainty is due to the modelling of proton SI. Each true proton is propagated through the volume of interest in the detector (corresponding mostly to FGD volume) in steps of 0.1 mm, and the interaction probabilities are calculated at each step. The final probability of interactions is varied to get the event weight. The inelastic cross-section is taken from the Wellisch-Axen parameterisation used by the GEANT4 Bertini cascade physics model.

---

[1] The Author adapted the existing SI proton implementation for proton-tagged samples. For events with more than two reconstructed protons, the error is not taken into account because it is very unlikely that the proton SI will cause a change in topology in such case.

- **Pion secondary interactions** uncertainty is related to π interactions after they leave the nucleus. Similarly as for proton SI, true pions are propagated through the volume of interest in steps of 0.1 mm. The systematic errors were calculated by comparing the GEANT4 cross-sections and external data for pion interactions.

The full set of systematic errors relevant for ND280 analysis is presented in Tab. 4.1 with respective fractional errors for the proton-tagged samples. As expected, the highest error comes from proton SI, with pion SI being the second most significant error source for CC0π-Np-0γ due to the high fraction of RES and DIS events. For a table with other FHC samples, see Appendix B.5. The fractional error for each ND280 detector systematic uncertainty as a function on μ momentum is presented on plots in Appendix B.6.

Systematic error source	**Total error in [%]**			
	CC0π-0p-0γ		CC0π-Np-0γ	
	FGD1	FGD2	FGD1	FGD2
Observable-like systematics				
Magnetic field distortions	0.0033	0.0074	0.0025	0.0087
TPC momentum resolution	0.0051	0.0036	0.0080	0.0082
TPC momentum scale	0.0147	0.0170	0.0109	0.0161
TPC PID	0.3145	0.4494	0.6191	0.7884
FGD PID	0.0890	0.0360	0.1801	0.0979
Efficiency-like systematics				
Charge ID efficiency	0.0814	0.2002	0.2440	0.3681
TPC cluster efficiency	0.0095	0.0096	0.0162	0.0165
TPC tracking efficiency	0.3036	0.7394	0.7527	1.3844
TPC-FGD matching efficiency	0.0767	0.1592	0.1898	0.3297
FGD hybrid track efficiency	0.2600	0.0512	0.8183	0.1560
Michel electron efficiency	0.0489	0.0759	0.0768	0.1671
ECal tracking efficiency	0.3414	0.3784	0.5168	0.6917
TPC-ECal matching efficiency	0.6082	0.3178	1.0097	1.0251
ECal PID `EmHip`	0.0790	0.0648	0.0597	0.0561
ECal photon pile-up	0.0689	0.0490	0.0423	0.0424
Normalisation systematics				
OOFV background	0.5425	0.7194	0.1389	0.1978
Pile-up	0.1782	0.1722	0.1789	0.1742
FGD mass	0.5651	0.3850	0.5757	0.3959
Pion secondary interactions	0.3605	0.3833	1.3837	1.3321
Proton secondary interactions	1.0580	1.2580	2.6137	3.0793
Sand muon background	0.0571	0.0280	0.0117	0.0113
All				
Total uncertainty	1.6808	1.9692	3.6612	4.2466

TABLE 4.1: Systematic error from different sources for proton-tagged samples.

4.2 ND280 Detector Error Propagation

Varying each ND280 detector systematic uncertainty in the main analysis would demand impossible computing resources; that's why the effect of ND280 systematic errors is taken into account as the covariance matrix. The number of the matrix row or column corresponds to a bin in the p_μ-$\cos\theta_\mu$ phase space for a given ND280 event sample. The ordering of the bins for each sample is such that the region of lowest $\cos\theta_\mu$ is selected first, which contains the bins of increasing p_μ (from 0 to 30 GeV), then comes the next region of $\cos\theta_\mu$ containing again the bins in p_μ starting from 0 GeV, an so on. Since the matrix is represented by a two-dimensional histogram, the diagonal elements are usually called bins. In the analysis, each bin is treated as a parameter that can be fitted.

The matrix is created by producing 2000 toy MCs with all the systematic uncertainties varied at the same time. Due to the systematic effects, the events can migrate between different bins and event samples, thus changing the number of events in a particular bin. Fig. 4.1 shows the example distributions of the number of events in given p_μ-$\cos\theta_\mu$ bins for selected ND280 samples. For each matrix element, the covariance is calculated based on the relative number of events in two bins in all toy MCs.

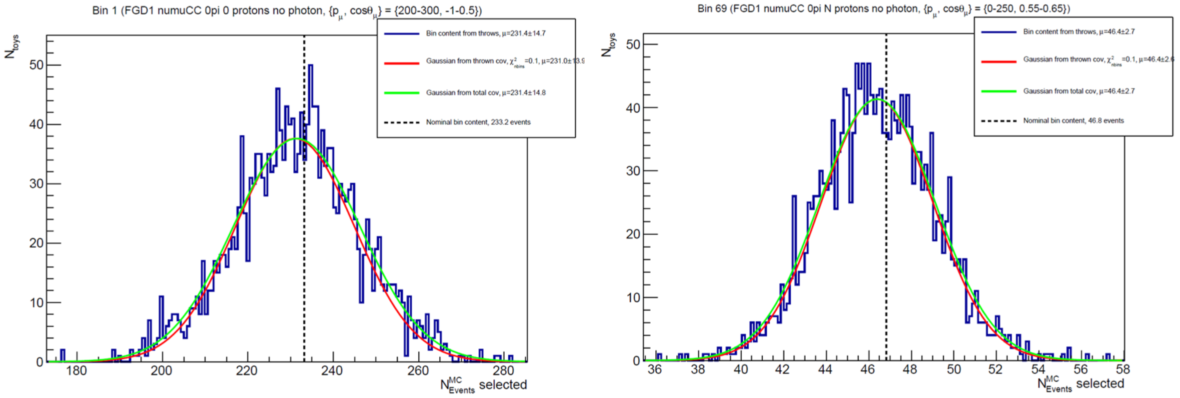

FIGURE 4.1: Distributions of the number of events in selected bins of p_μ and $\cos\theta_\mu$ from two ND280 event samples, for toy MCs built by varying the ND280 systematic parameters (marked with blue lines). The red line presents a Gaussian fit to the event distribution. The green line includes MC statistical uncertainty, although this is not used in the analysis. The black dotted line marks the nominal number of events in a bin.

The initial covariance matrix has identical binning as the one used in the fit (4952 bins, see Appendix B.2). Obviously, using such a huge matrix can be problematic; therefore a technique called bin merging has to be used, in which neighbouring bins having similar distributions are merged together. This allows to reduce the number of bins to 552 and such smaller matrix is used in the later part of the Thesis. An additional test was performed to confirm this operation did not bias the results (see Appendix A.4). The final detector covariance matrix used in the analysis can be seen in Fig. 4.2, while the details of its binning are given in Appendix B.3.

When looking at the covariance matrix, one might observe high values of covariance between CC0π-0p-0γ and CC0π-Np-0γ, which are expected, as, for example, Proton SI can lead to migration from one sample to the other.

Fig. 4.3 shows the diagonal element for each bin of the ND280 covariance matrix. The largest error is observed for the CC1π-0γ and CC0π-Np-0γ samples for high momentum bins and is primarily driven by pion and proton SI.

4.3 T2K Neutrino Flux

Production of the neutrino beam for T2K is a very complicated process and depends on many factors, which result in many sources of uncertainties in flux prediction. The most important ones are:

- hadron interactions in the target;
- proton beam profile and off-axis angle precision;

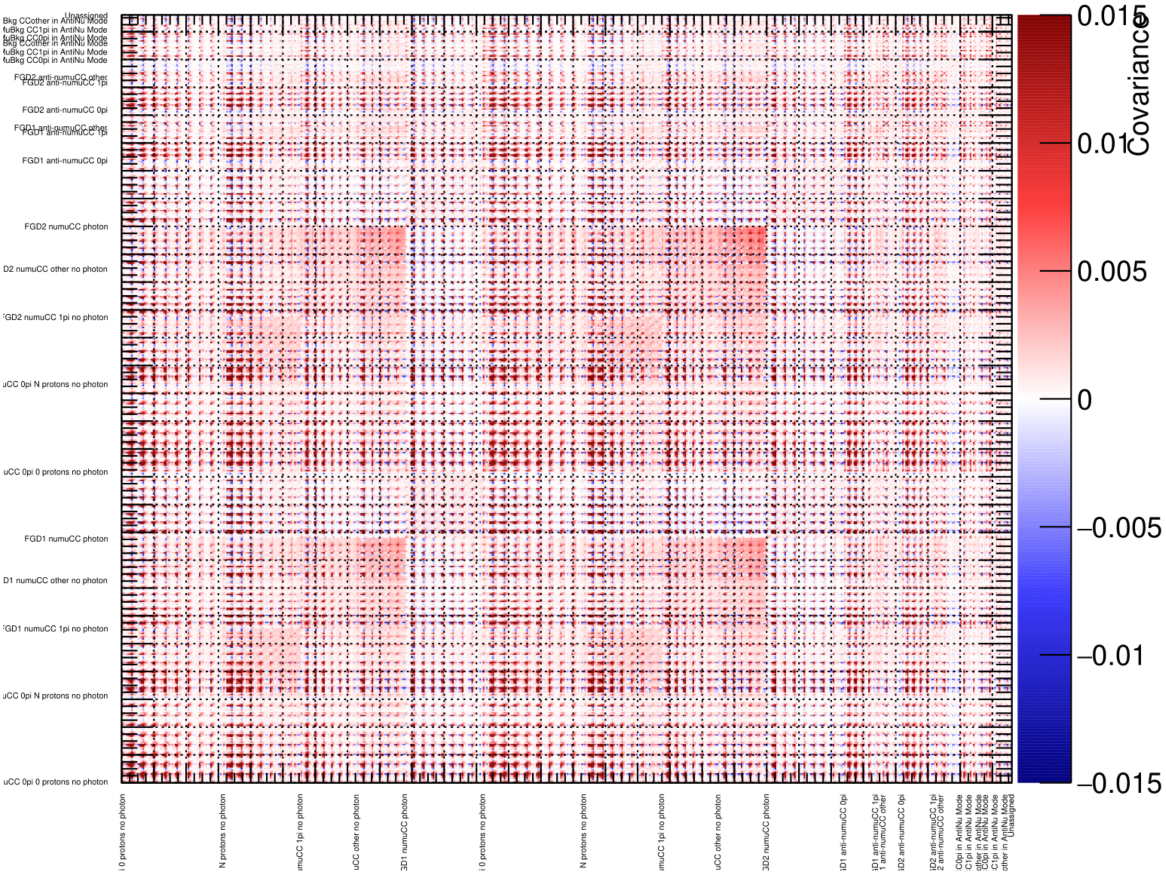

FIGURE 4.2: ND280 covariance matrix used in the fit. The rows and columns correspond to p_{μ}-$\cos\theta$ bins in the given ND280 samples.

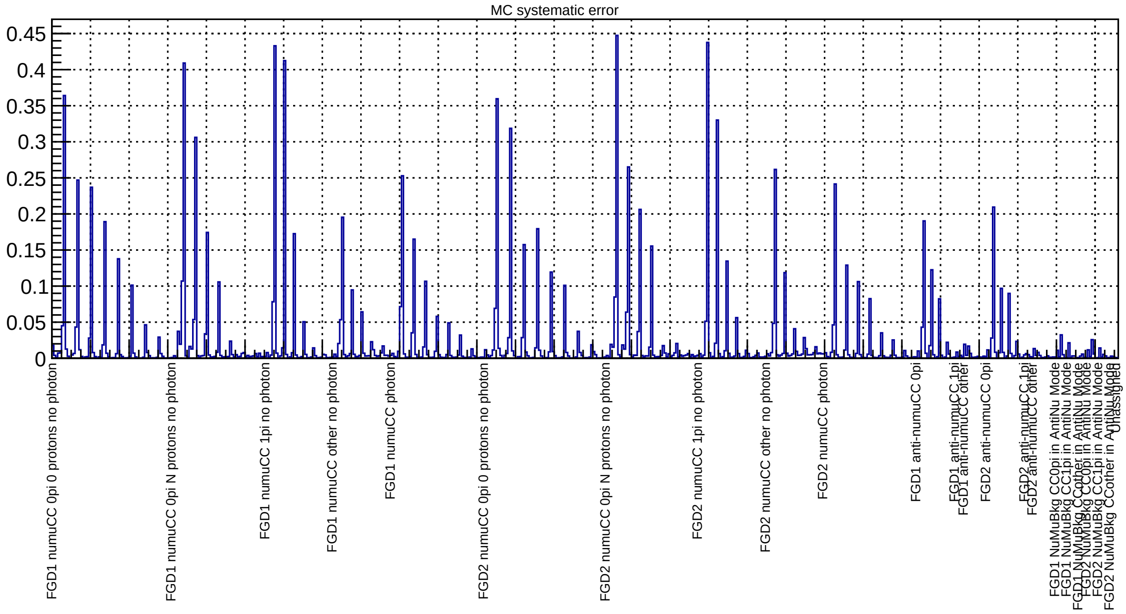

FIGURE 4.3: Diagonal elements for each bin of the ND280 covariance matrix.

- horn current and magnetic field;
- horn and target alignment;
- material modelling;
- number of protons on target.

Among the sources listed above, the dominant one is the modelling of hadron interactions, as can be seen in Fig. 4.4, showing the fractional error as a function of neutrino energy. To reduce the flux errors, T2K is using external hadron production data, most notably the T2K replica target measurements, performed in the NA61/SHINE experiment [86]. Compared to previous replica target data [87], using newer measurements allowed to reduce the error from 8% (black dotted line, `13av7.1`) to 5% (black solid line, `21vb2`). Furthermore, in some regions, hadron production is no longer the dominant source thanks to the NA61/SHINE tuning.

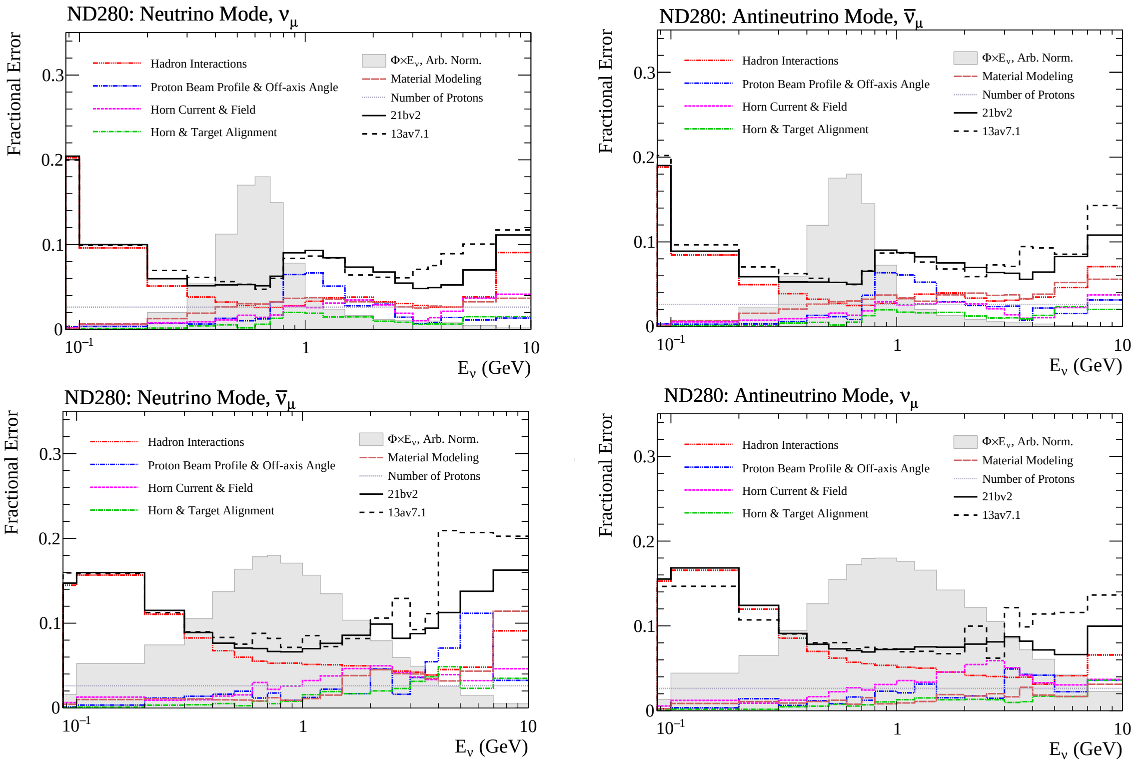

FIGURE 4.4: Total flux uncertainty and its main contributions for ND280 [88] as a function of neutrino energy. `21bv2` corresponds to the described analysis, while `13av7.1` to the previous one.

The flux systematic uncertainties are parametrized in true neutrino energy E_ν^{true} (GeV) and work as normalisation in a given bin of E_ν^{true}. The parameterization is done separately for each neutrino flavour (ν_μ, ν_e, $\bar{\nu}_\mu$, $\bar{\nu}_e$), each beam mode (FHC, RHC) and each detector (ND280, SK). In total, there are 100 flux parameters: 50 for ND280 and 50 for SK, as each detector has a different acceptance. Since the flux parameters for ND280 and SK are highly correlated, ND280 can indirectly constrain SK flux parameters. This can be seen in Fig. 4.5, which depicts the flux covariance matrix. Detailed flux binning can be found in Appendix B.4.

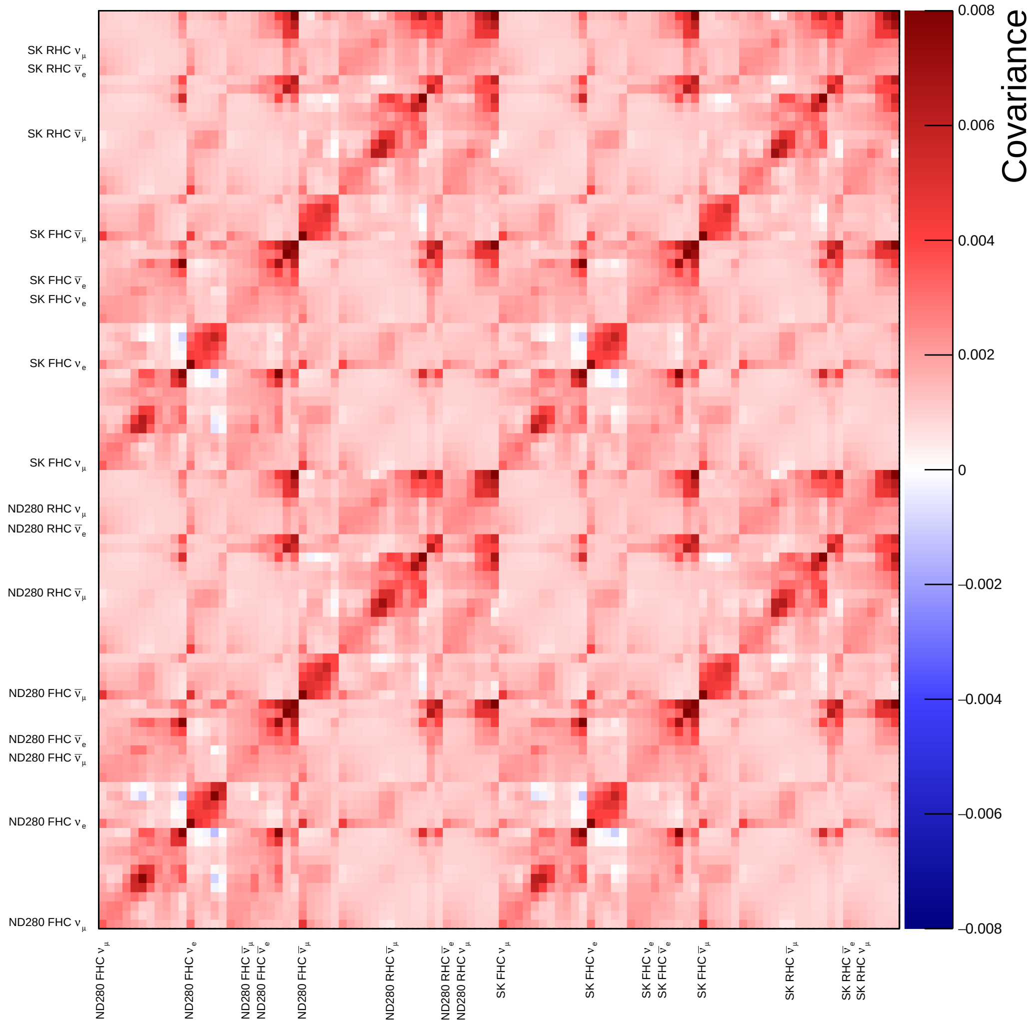

FIGURE 4.5: Prior flux covariance matrix. Each column and row corresponds to a neutrino energy bin for a particular beam mode and detector (ND280, SK).

4.4 Cross-section Systematic Model

Neutrinos can undergo various types of interactions, each described by a dedicated model. To accommodate for that, 75 of the cross-section parameters[2] are used in the Oscillation Analysis described in this Thesis. We can split them into two categories:

- Normalisation parameters - increase/decrease cross-section for a particular interaction channel or neutrino flavour. For example, there is separate normalisation for neutrino 2p2h and antineutrino 2p2h, as we know that both have different cross-sections.

- Shape parameters - those are meant to change kinematic distributions. An example is a dial that changes the ratio of events between the low and high Q^2, while preserving the total cross-section.

Dials are introduced by cross-section models describing particular interaction channels, initial nucleus state or nuclear effects (most of them were already mentioned in Section 1.6). Fig. 4.6 shows the neutrino cross-section for several reaction channels and T2K flux. We can see that for T2K flux, CCQE is the dominant reaction mode, and as a consequence a lot of the dials describe this channel.

T2K uses NEUT [40] event generator, which uses a particular model set and implementation, resulting in the choice of dials used in the analysis. All parameters are listed in Tab. 4.2, while the summary of them and some implementation details are presented below. We assign a Gaussian prior distribution for parameters for which we have measurements or several models with predictions, otherwise, we set a flat prior. The impact of this fact on the analysis is outlined in Section 5.2. Additionally, some parameters are fixed in ND280-only analysis as ND280 is not sensitive to those effects; however, they are not fixed in ND+FD joint analysis.

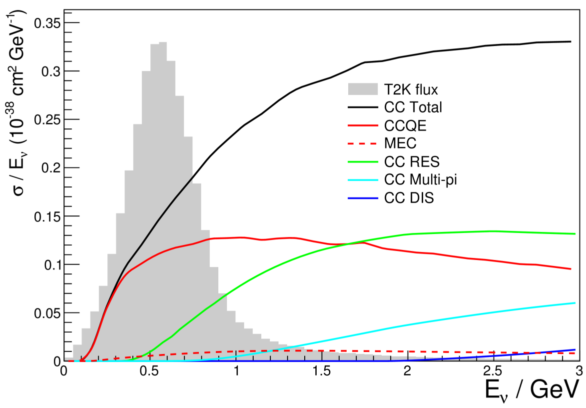

FIGURE 4.6: Cross-section for neutrino interactions in different channels and T2K flux.

CCQE - Since CCQE is the dominant T2K channel, the largest number of dials is related to this reaction mode. It includes parameters related to the CCQE dipole model and a number of dials describing the initial nucleus. The main CCQE dial is quasi-elastic axial mass M_A^{QE}, which modifies the form factor for quasi-elastic interaction (see Eq. 1.27) and has a huge impact on CCQE cross-section, as shown in Fig. 4.7 left.

It is known that for $Q^2 > 0.25$ GeV^2, the axial form factor parametrisation is not able to adequately describe the current data. Due to this fact, three normalisation parameters were introduced, each affecting different Q^2 regions (see Tab. 4.2). Two alternative models exist, namely the 3-component model and Z-expansion, but they cannot be used in the actual T2K

---

[2] Systematic parameters are often called "dials", because by changing parameter value we adjust the spectra of ND280 samples similarly to tuning a radio dial.

Parameter	Prefit	Type	Description
CCQE			
M_A^{QE}	1.03±0.06	Shape	Axial mass for CCQE
High Q^2 norm 1	1±0.11	Norm	for $0.25 < Q^2 < 0.5$
High Q^2 norm 2	1±0.18	Norm	for $0.5 < Q^2 < 1.0$
High Q^2 norm 3	1±0.40	Norm	for $1.0 < Q^2$
S-shell MF norm ^{12}C	0±0.45	Norm	
P-shell MF norm ^{12}C	0±0.2	Norm	
S shell MF norm ^{16}O	0±0.75	Norm	
$P_{1/2}$ shell MF norm ^{16}O	0±0.2	Norm	
$P_{3/2}$ shell MF norm ^{16}O	0±0.45	Norm	
SRC norm ^{12}C	1±2	Norm	
SRC norm ^{16}O	1±2	Norm	
S-shell MF p_{miss} Shape ^{12}C	0±1	Shape	Fixed at ND
P-shell MF p_{miss} Shape ^{12}C	0±1	Shape	Fixed at ND
S shell MF p_{miss} Shape ^{16}O	0±1	Shape	Fixed at ND
$P_{1/2}$ shell MF p_{miss} Shape ^{16}O	0±1	Shape	Fixed at ND
$P_{3/2}$ shell MF p_{miss} Shape ^{16}O	0±1	Shape	Fixed at ND
Pauli blocking ^{12}C ν	0±1	Shape	
Pauli blocking ^{16}O ν	0±1	Shape	
Pauli blocking ^{12}C $\bar{\nu}$	0±1	Shape	
Pauli blocking ^{16}O $\bar{\nu}$	0±1	Shape	
Optical Potential ^{12}C	0±1	Shape	Flat prior
Optical Potential ^{16}O	0±1	Shape	Flat prior
CCQE Binding Energy			
CCQE E_b ^{12}C ν	2±6	Shape	
CCQE E_b ^{12}C $\bar{\nu}$	0±6	Shape	
CCQE E_b ^{16}O ν	4±6	Shape	
CCQE E_b ^{16}O $\bar{\nu}$	0±6	Shape	
α correction (q_3)	0±1	Shape	Flat prior
2p2h			
2p2h norm ν	1±1	Norm	Flat prior
2p2h norm $\bar{\nu}$	1±1	Norm	Flat prior
2p2h norm ^{12}C to ^{16}O	1±0.2	Norm	
PNNN shape	0±0.33	Shape	
2p2h shape ^{12}C nn	0±3	Shape	
2p2h shape ^{12}C np	0±3	Shape	
2p2h shape ^{16}O nn	0±3	Shape	
2p2h shape ^{16}O np	0±3	Shape	
2p2h Edep low E_ν	1±1	Shape	Fixed at ND
2p2h Edep high E_ν	1±1	Shape	Fixed at ND
2p2h Edep low $E_{\bar{\nu}}$	1±1	Shape	Fixed at ND
2p2h Edep high $E_{\bar{\nu}}$	1±1	Shape	Fixed at ND
SPP			
C_A^5	1.06±0.1	Shape	Form factor norm.
M_A^{RES}	0.91±0.1	Shape	Axial mass for RES
Non-Res $I_{1/2}$	1.21±0.27	Shape	
Non-Res $I_{1/2}$ Low p_π	1.3±1.3	Shape	Fixed at ND
RS Δ Decay	1±1	Shape	Flat prior
SPP π^0 norm ν_μ	1±0.3	Norm	
SPP π^0 norm $\bar{\nu}_\mu$	1±0.3	Norm	
RES E_b ^{12}C ν_μ	25±25	Shape	
RES E_b ^{16}O ν_μ	25±25	Shape	
RES E_b ^{12}C $\bar{\nu}_\mu$	25±25	Shape	
RES E_b ^{16}O $\bar{\nu}_\mu$	25±25	Shape	
MPi and DIS			
Mπ Multi TotXSec	0±1	Shape	
Mπ BY Vector	0±1	Shape	
Mπ BY Axial	0±1	Shape	
Mπ Multi Shape	0±1	Shape	
CC BY DIS	0±1	Shape	
CC DIS Multπ Norm ν	1±0.035	Norm	
CC DIS Multπ Norm $\bar{\nu}$	1±0.065	Norm	
CC Misc	1±1	Norm	
FSI			
π FSI QE low E	1.069±0.313	Shape	For $p_\pi < 500$
π FSI QE high E	1.824±0.859	Shape	For $p_\pi > 500$
π FSI Prod.	1.002±1.101	Shape	
π FSI Abs.	1.404±0.432	Shape	
π FSI Cex low E	0.697±0.305	Shape	For $p_\pi < 500$
π FSI Cex high E	1.8±0.288	Shape	For $p_\pi > 500$
Nucleon FSI	0±0.3	Shape	
Other			
CC Coh ^{12}C	1±0.3	Norm.	
CC Coh ^{16}O	1±0.3	Norm.	
NC Coh	1±0.3	Norm.	Fixed at ND
NC 1γ	1±1	Norm.	Fixed at ND
NC other near	1±0.3	Norm.	
NC other far	1±0.3	Norm.	
CC norm ν	1±0.2	Norm.	
CC norm $\bar{\nu}$	1±0.1	Norm.	
ν_e/ν_μ	1±0.0282843	Norm.	
$\bar{\nu}_e/\bar{\nu}_\mu$	1±0.0282843	Norm.	

TABLE 4.2: Summary of all cross-section parameters used in the analysis.

analysis due to technical difficulties, as explained in Appendix A.5, which contains studies with alternative parametrisation. Fig. 4.7 right shows the impact of alternative parametrisation. Three normalisation parameters are meant to mimic this effect.

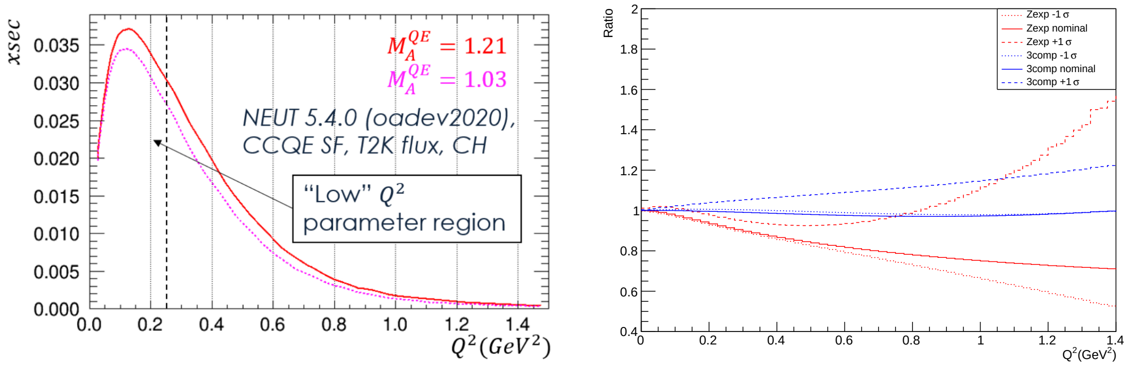

FIGURE 4.7: Left: The CCQE cross-section for two different values of M_A^{QE}. Right: The ratio to the dipole model for the alternative form factor fake data sets as a function of true Q^2. In each case, the solid line shows the effect of weighting to central value prediction of the alternative model, the upper dashed line represents the "+1σ" prediction, and the lower (fine) dashed line represents the "-1σ" prediction [89].

Ideally, the initial nucleus state model should be common for all interactions, however, each interaction mode is described with a different ground state model. For CCQE, it is a Spectral Function (SF, already described in Chapter 1.6), which can be divided into Mean Field (MF) and Short Range Correlations (SRC) regions. There are separate SF dials for ^{12}C and ^{16}O. Five parameters are used to normalise each nuclear shell in the MF region, and two others normalise the SRC region. Finally, five dials affect the shape of p_{miss} distribution for each shell; however, they are fixed in ND280-only analysis as they have negligible impact.

Pauli blocking dials modify the Fermi surface (see Eq. 1.31). When their values increase, the Fermi surface rises, which results in more events being rejected, while decreasing the values has the opposite effect. Changing the dial value by ±1 corresponds to a 30 MeV shift of the Fermi surface. Events with low Q^2 are close to the Fermi surface, hence only those will be affected by this dial. CC0π-0p-0γ is very sensitive to those parameters, see the Q^2 distribution in Fig. 3.10.

To account for FSI causing the outgoing wave function to be a distorted wave and not a plane wave, a dial called optical potential is introduced, as such an effect is not included in SF. It only modifies the outgoing lepton momentum for low Q^2 events.

Since FD uses reconstructed ν energy, the binding energy is important as it can bias this quantity. Based on a study using electron scattering data [41], it was decided to use a correction to binding energy which is momentum transfer ($|\vec{q}_3|$) dependent and given by

$$\Delta E_{\nu,T} = \delta_{\nu,T} + \alpha(a|\vec{q}_3| + b), \tag{4.1}$$

where $\delta_{\nu,T}$ are binding energy parameters depending on neutrino (ν or $\bar{\nu}$) and target nucleus T (^{12}C or ^{16}O), α is a correction factor with values ranging from 0 to 1, and a and b are constants obtained from a linear fit to external data. The higher is $\Delta E_{\nu,T}$, the lower p_μ is. The implementation of binding energy is unique, as a momentum shift (negative or positive) is applied to each event and can lead to the event being migrated to another histogram bin. It's worth noting that values of $\delta_{\nu,T}$ are relative to NEUT nominal values of 25 (27) MeV for ^{12}C (^{16}O).

Those are the only systematic parameters that lead to actual event migration, while all others use the reweighing method, explained later in Section 4.5.

2p2h - There are two 2p2h normalisation parameters, separately for ν and $\bar{\nu}$, and additional third normalisation of ^{12}C to ^{16}O.

Because of the introduction of proton-tagged samples, it was necessary to add a dial affecting the ratio of pn and nn pairs (see Fig. 1.4) in the target nucleus, namely `PNNN Shape`. This parameter is described in more detail in Section 4.7.

Other shape dials are related to the 2p2h Valencia model [81] used in T2K. They change the event ratio between two regions of $q_0/|\vec{q}_3|$ phase space, as can be seen in Fig. 4.8. There are separate dials for pn and nn pairs, as well as ^{12}C or ^{16}O, giving in total four parameters. The proton-tagged samples are sensitive to these dials because of different event distributions in the phase space; see Fig. 3.11.

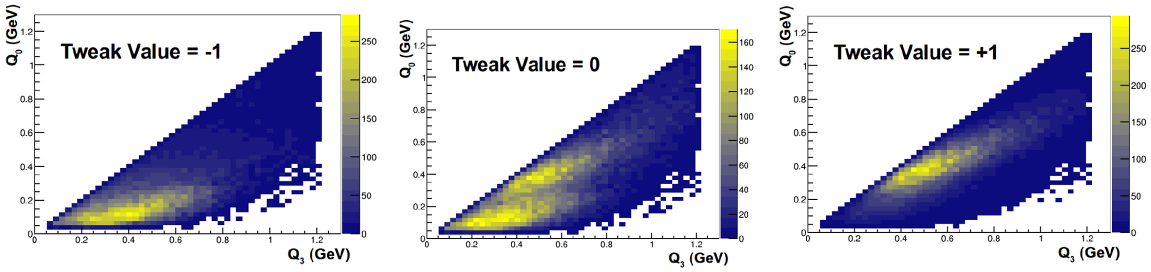

FIGURE 4.8: Impact of 2p2h shape dial on $q_0/|\vec{q}_3|$ distribution [90].

To account for the shape differences between 2p2h models (shown in Fig. 4.9), there are four dials affecting the cross-section below and above the arbitrarily set 600 MeV threshold. Those are also the dials, to which the proton-tagged samples are sensitive, as they have a different distribution of neutrino energy, see Fig. 3.12. Although, because of the T2K narrow band beam, the overall sensitivity is rather poor.

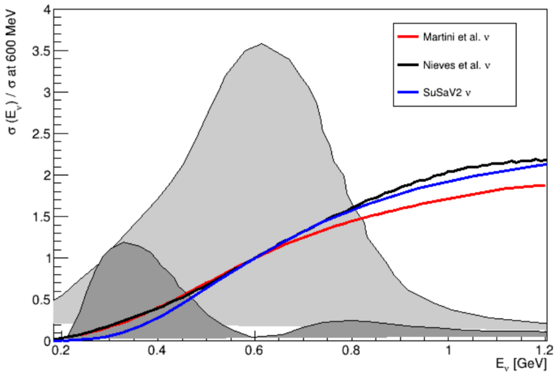

FIGURE 4.9: Energy dependence of the 2p2h cross-section for neutrinos for the 3 most advanced models. The grey bands show the oscillated (dark) and unoscillated (light) T2K μ_ν flux. The cross-section has been normalised such that it has the same value at 600 MeV in all three models [90].

SPP - Single Pion Production (SPP) consists of resonant and non-resonant reactions. The main dials affecting resonant interactions are M_A^{RES} and C_A^5, which are directly related to the form factor (Eq. 1.34).

Since in resonant interaction, there is a possibility to produce π^0, which decays to two photons, there are two normalisation dials for this process, one for ν_μ and one for $\bar{\nu}_\mu$, introduced due to the photon tagging.

The kinematics of outgoing hadrons can be described using either a simplistic isotropic (back-to-back in the center-of-mass frame) Δ decay, or a more sophisticated method calculating matrix elements for the $N \rightarrow \Delta$ transition. `RS Δ Decay` dial is used to switch from one model to the other, impacting pion and nucleon kinematic variables but not those of the muon. Fig. 4.10 shows how momenta predictions change as we go from the isotropic model (pink line) to the more sophisticated model (blue line). `RS Δ Decay` dial modifies only part of the resonant cross-section that is Adler angle-dependent (see Eq. 1.33). The main reason behind this dial was the introduction of the FHC ν_μCC1π sample in FD, but it is also relevant for proton-tagged samples in ND280 samples.

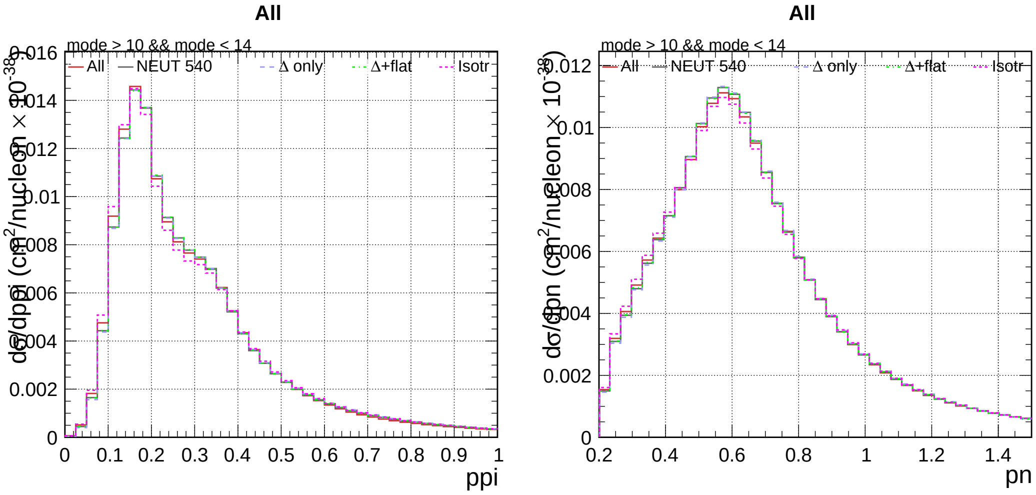

(A) Pion momentum [GeV/c]

(B) Nucleon momentum [GeV/c]

FIGURE 4.10: Changes of the cross-section for a carbon-hydrogen target without nuclear effects, showing the impact of the Δ decay model in resonant scattering. Colours represent different decay models (see text) [41].

Last but not least, four parameters are related to the binding energy for the resonant channel. When the binding energy is higher, the incoming neutrino has to transfer more energy to the hadron system for a kinematically allowed interaction. Therefore, at fixed E_ν, the average energy transfer q_0 is larger, which results in the Q^2 spectrum being shifted to lower values. This reduces the interaction cross-section and changes the shape of the lepton (and also hadron) kinematics spectra. NEUT generator doesn't simulate the binding energy for RES; hence, templates were prepared in another generator, NuWro [61]. The templates allow for altering NEUT-produced distributions to mimic the effect of binding energy. For CCQE, NEUT assumes E_b = 25 MeV, on the other hand the value of 0 MeV would correspond to no binding energy. Therefore, in the analysis the prior value has been set to 25 MeV with 25 MeV 1σ error to cover also 0 MeV, nevertheless such a big error is a very conservative assumption.

Additionally, there are iso-scalar non-resonant background parameters. `Non-Res I`$_{1/2}$ `Low` p_π covers anti-neutrino SPP events with a low momentum pion ($p_\pi < 200$) in the final state, while `Non-Res I`$_{1/2}$ all other cases. This division is mostly due to the desire to stabilise the parameters in the FD fit, where no data constraint is expected. The NEUT generator models a non-resonant process only for $\mathrm{I}_{1/2}$ interaction channels, and the lack of the $\mathrm{I}_{3/2}$ channel is still an outstanding issue. There is ongoing work to improve this [91], even though bubble chamber data suggest that $\mathrm{I}_{3/2}$ channel effects are small [48, 49].

DIS, Multi-π production - There are four parameters related to Multi-π production for $W < 2$ GeV/c^2. Two dials are related to Bodek-Yang (BY) parametrisation (see discussion on page 17), one describes the vector and the other the axial part, based on the formalism from [92]. Fig. 4.11 shows the impact of this correction as a function of Q^2 for T2K MC.

Additionally, there are Multi-π multiplicity dials that describe the probability of the number, charge and momenta of π being produced in an interaction. `TotXsec` dial increases or

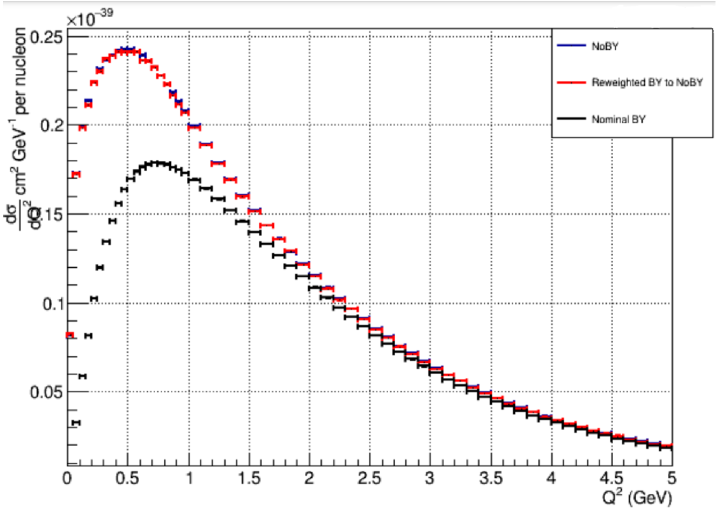

FIGURE 4.11: Comparison of the cross-sections with Bodek-Yang correction (black points, BY) and without BY correction (blue points, NoBY). The main difference in the cross-sections occurs at low Q^2 [90].

decreases the multiplicity. Since Multi-π mode specifically requires at least two π produced at the interaction vertex, a change to the multiplicity model will directly affect the fraction of events with two pions and thus the Multi-π cross-section. The `Multi π Shape` dial varies the invariant hadronic mass and π multiplicity between the NEUT default model and the AGKY model predictions (see discussion on page 17), while preserving the cross-section as a function of energy.

There are two normalisation parameters for Multi-π and DIS: one for ν and one for $\bar{\nu}$. Furthermore, there is the BY correction dial for DIS.

Lastly, the normalisation of other considered channels (called `CC Misc`), including: CC1K, CC1η and CC1γ, is introduced.

FSI - There are several pion FSI dials[3], which affect the probability of occurrence of a given FSI channel. For example, increasing the probability of pion absorption in the nucleus will result in the migration of events from CC-1π-0γ to CC-0π-Np-0γ, as more pions will not exit the nucleus, but protons produced in pion absorption might be reconstructed. The nucleon FSI is also considered because of proton-tagged samples, and it will be discussed in detail in Section 4.6.

Other - There are also several normalisation parameters related to the less important interaction channels. Two affect CC Coherent scattering for ^{12}C and ^{16}O. Additionally, one normalisation for the NC Coherent process and one for NC1γ are both fixed in ND280-only analysis, as ND280 is not able to constrain them due to small event statistics. Two separate parameters are related to the normalisation of NC interactions for near and far detectors, due to different processes contributing to NC background. For example, in μ-like samples at SK, NC reactions are dominated by NC1$\pi^{\pm}$, but that is not the case at ND. Furthermore, there are two more Coulomb Correction normalisation dials affecting only CC events between 300 and 600 MeV of true neutrino energy. Finally, there are relative normalisations of electron (anti)neutrino cross-section.

Fig. 4.12 shows the prefit covariance matrix for cross-section parameters. As can be seen, some dials have an initial correlation reflecting our current knowledge of the models. Probably most notable are the correlations between the CCQE E_b parameters, as here we can use electron scattering data that help to correlate them. ND280 fit introduces many correlations,

---

[3] See discussion in Section 1.7.

as numerous dials affect similar regions of the phase space. The so-called ND postfit correlation matrix is an important output from ND280 analysis.

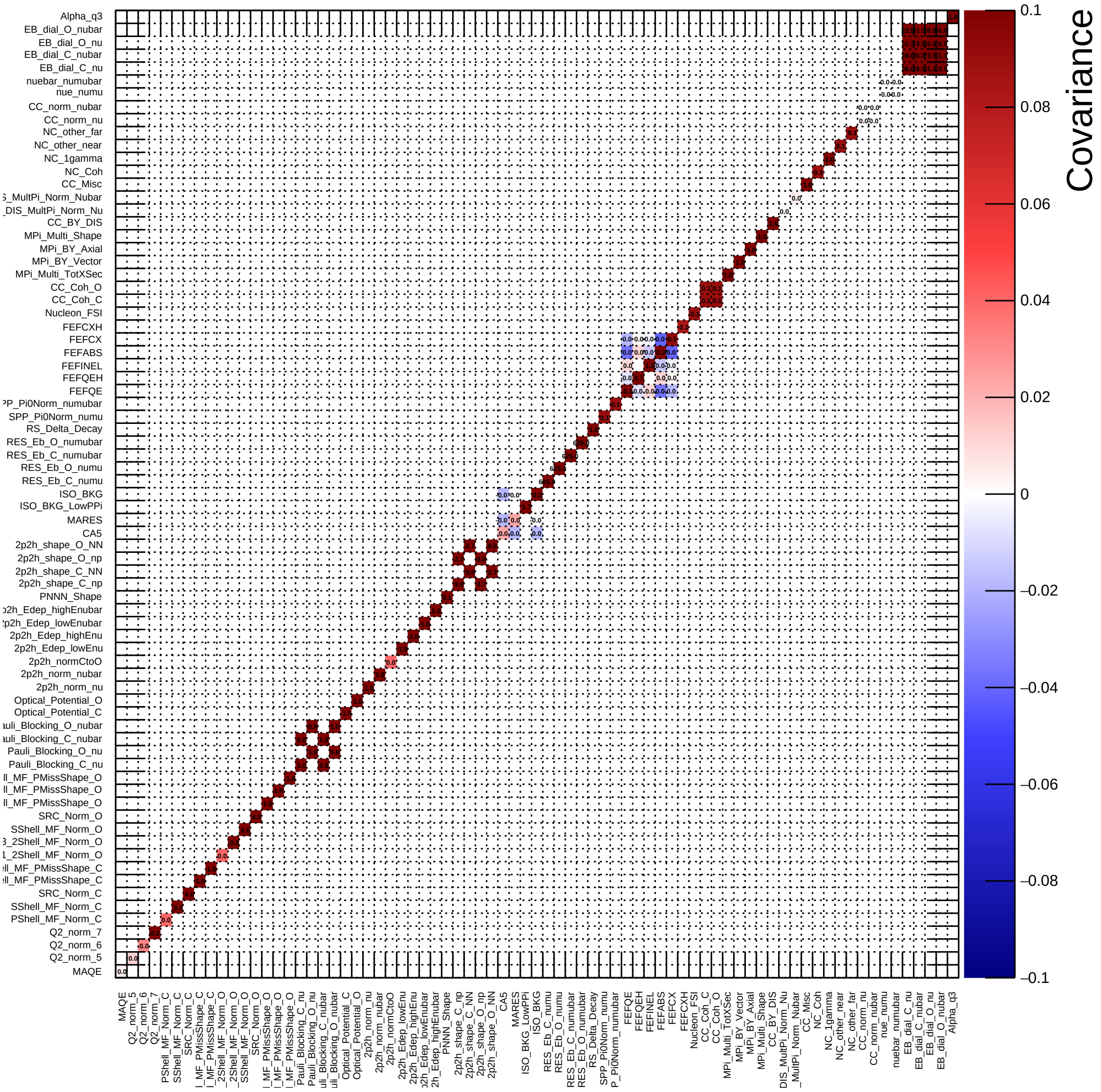

FIGURE 4.12: Prefit covariance cross-section matrix with the prior correlation between parameters.

4.5 Reweighting

Generating MC with different values of cross-section parameters (re-generation) is very time-consuming. There is an alternate method called reweighting, where we can assign a weight to a particular event depending on the values of cross-section parameters. In such a way, we can quickly modify existing MC without the need to generate it again. However, there are some limitations to this method: if there is a really low number of events in a particular phase space region (or even zero), then reweighting will not provide the same result as re-generation. Except for such boundary cases, reweighting and re-generating produce practically identical results. The biggest advantage of reweighting is the time scale, as reweighting of the full MC sample takes less than 0.1 second[4], while re-generating needs weeks or even months.

---

[4] The Author was involved in improving the code performance, and now this operation takes ~0.03s.

While filling a histogram, each MC event has an assigned weight, which is calculated as a ratio of the cross-section for the new parameter value to the generated cross-section ($weight = \sigma_{new}/\sigma_{gen}$). Then, the number of events in each bin is a weighted sum. Events with higher weights appear to be more frequent. Since weights may be different for each event, this would result in a change of the shape of kinematic distributions.

Calculating the weights during the fit would be very time-consuming, thus the weights are pre-calculated. In ND280 analysis, TSpline3 objects (defined in the ROOT framework [93]) are used to store the weights for several parameter values (knots). TSpline3 uses a 3rd-order polynomial to interpolate between knots because the dependence might not be linear. Examples of such splines are shown in Fig. 4.13, together with the linear interpolation between knots.

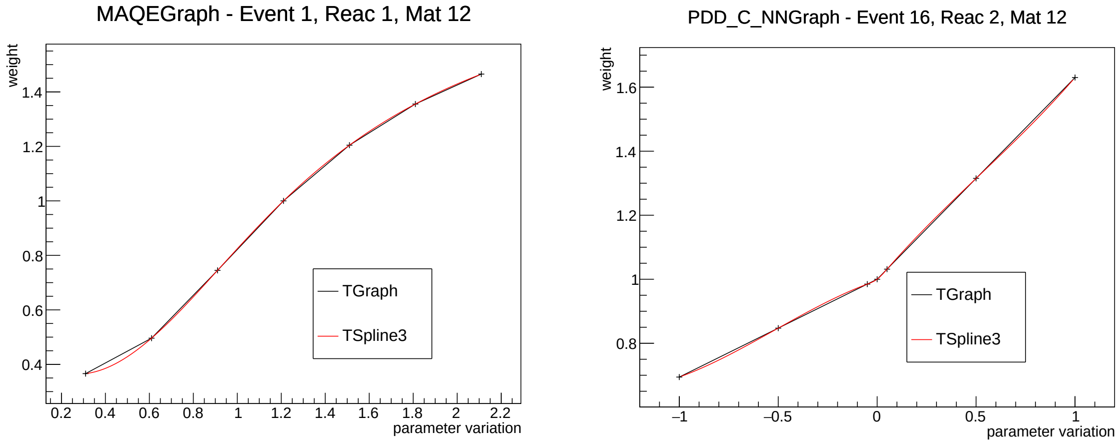

(A) M_A^{QE}

(B) 2p2h shape ^{12}C nn

FIGURE 4.13: Examples of splines used in the analysis compared to linear interpolation between knots (marked as TGraph).

Since we are using one-dimensional splines, it is assumed that the weight calculation for one dial is independent of the others; otherwise, multi-dimensional splines would be required[5].

Reweighting is used not only for the cross-section dials but also for flux or detector systematic parameters, as the weights are multiplicative. The total event weight in the ND280 analysis is a product of the following weights:

$$w_i = w_i^{POT} \cdot w_i^{flux} \cdot w_i^{beam} \cdot w_i^{NDdet} \cdot w_i^{NDcorr} \cdot w_i^{xsec}, \tag{4.2}$$

where:

- w_i^{POT} (POT weight) - Run-by-run correction, scaling generated MC to collected data POTs: $w_i^{POT} = N_{Data}^{POT}/N_{MC}^{POT}$. This weight is applied once and not varied in the fit.
- w_i^{beam} (Beam weight) - Run-by-run correction between the generated and measured primary beam. It is calculated using measurements from proton beam monitors, MUMON and INGRID. Not varied in the fit.
- w_i^{flux} (Flux weight) - Event-by-event weight as a function of E_ν^{true} and neutrino flavour (ν_μ, ν_e, $\bar{\nu}_\mu$, $\bar{\nu}_e$). It is parameterised using the flux covariance matrix; see Section 4.3. The prior value is always 1. Varied in the fit.

---

[5] This is the reason why there are `High` Q^2 `norm` parameters rather than physically motivated ones, see Appendix A.5.

- w_i^{NDcorr} (ND280 correction weight) - This weight is a result of many corrections (i.e. efficiency) applied to an ND280 event. This weight is applied once and not varied in the fit.
- w_i^{NDdet} (ND280 detector weight) - Event-by-event weight as a function of p_μ, $\cos\theta_\mu$ and the ND280 sample. This weight includes all ND280 systematic effects and is calculated using the ND280 covariance matrix (described in Section 4.2). Varied in the fit.
- w_i^{xsec} (Cross-section weight) - Event-by-event weight, related to cross-section and nuclear effects models. It is using the cross-section covariance matrix discussed in Section 4.4. Varied in the fit.

For FD samples, the detector weights are different, and additionally, there is a weight coming from the oscillation probability.

4.6 Nucleon FSI Systematic Uncertainty

For proton-tagged samples, it was important to introduce a new systematic error describing the probability of nucleon FSI occurrence. After undergoing FSI, the nucleons have smaller momenta and can leave the nuclei at the angles different from the original ones. This can result in the migration of events between CC0π-0p-0γ and CC0π-Np-0γ sample.

Fig. 4.14 (A) shows the fraction of events in which a nucleon FSI occurred and in which it did not. In roughly 60% of cases, there is no FSI. The prior error on this parameter has been set to 30% (Tab. 4.2), based on nucleon transparency studies [94].

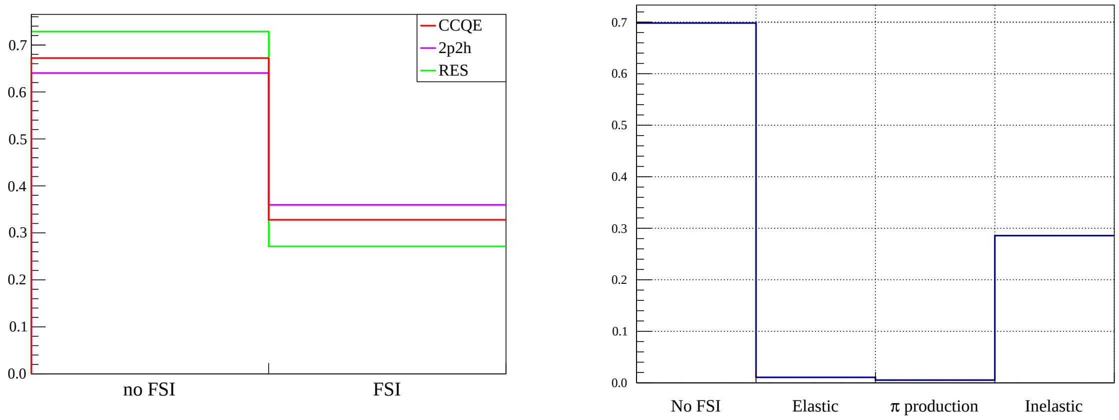

(A) For CCQE, 2-2h, RES

(B) For CCQE only

FIGURE 4.14: Fraction of nucleons undergoing FSI.

Fig. 4.14 (B) shows a more detailed breakdown of nucleon FSI processes for CCQE as an example. One can observe that FSI is dominated by inelastic scattering. Since elastic scattering or π absorption are negligible fractions, they can be grouped together with inelastic scattering for the purpose of the described analysis. It is quite possible that in the future, nucleon FSI will be further divided, since in the current analysis we are simply interested in the fact whether the proton was reconstructed or not.

The effect of variation of nucleon FSI dial on proton kinematics can be seen in Fig. 4.15. It can be observed that increasing the probability of FSI reduces true proton momentum and modifies the outgoing proton angle. This results in an increasing number of events in the CC0π-Np-0γ sample and a decrease in CC0π-0p-0γ, and vice versa.

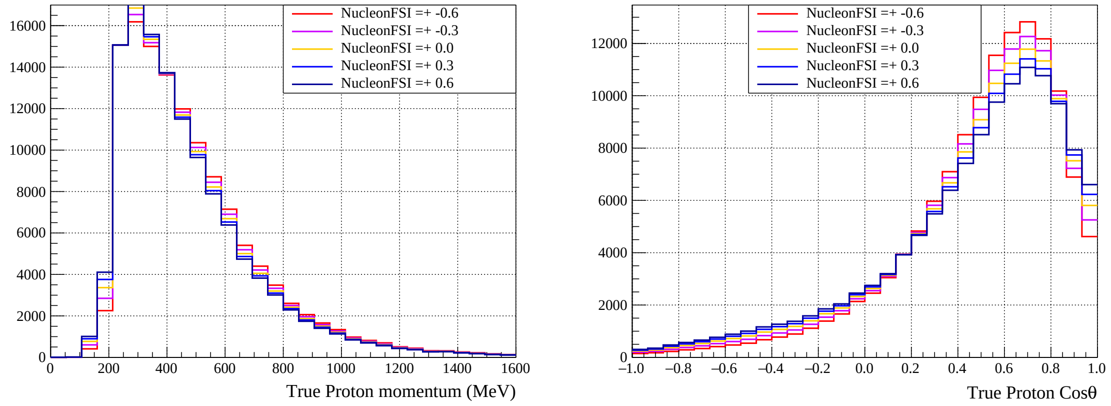

FIGURE 4.15: The effect of variation of nucleon the FSI dial on proton kinematic variables.

4.7 2p2h *pn* and *nn* Ratio Systematics

Neutrino interactions in 2p2h channel can occur on *pn* or *nn* pair (for more details, see Section 1.6). Currently, the ratio between those pairs is unknown, but different 2p2h models provide different predictions. After introducing proton-tagged samples, T2K may have enough sensitivity to start probing this effect.

NEUT, like many other neutrino interaction generators, uses an isotropic ejection model in a hadronic frame [95] to describe the kinematic properties of outgoing nucleons. Thus, the p-$\cos\theta$ distribution of the highest momentum proton coming from the *pn* pair will be different than in the *nn* case, as can be seen in 4.16. An increasing fraction of *pn* pairs results in the migration of events from CC0π-0p-0γ to CC0π-Np-0γ.

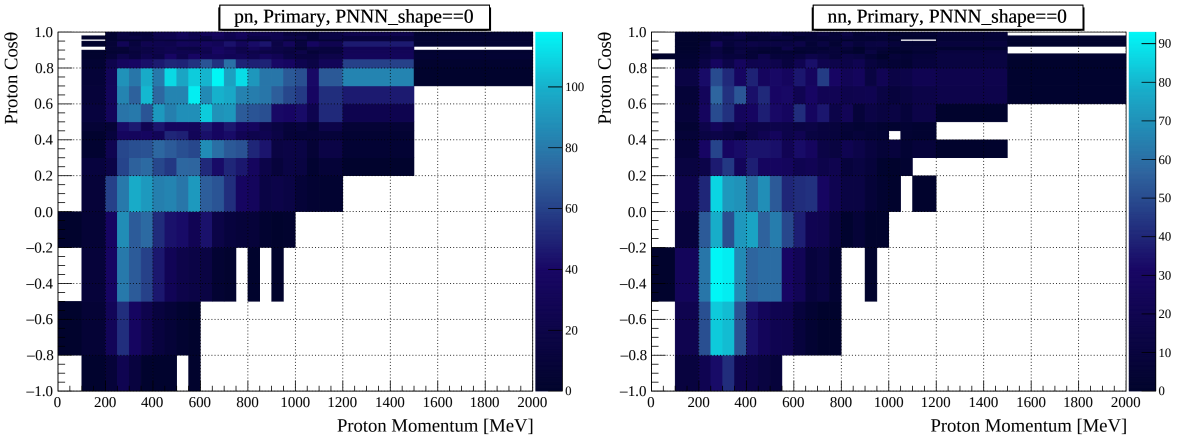

(A) *pn* pair

(B) *nn* pair

FIGURE 4.16: Distribution of true momentum and emission angle for the true highest momentum proton from a 2p2h interaction on a *pn* or *nn* pair.

The fraction of each pair for both ν and $\bar{\nu}$ predicted by NEUT is shown in Tab. 4.3. These fractions, however, are highly model dependent; for example, in the SUSAv2 model [82], *pn* pairs account for $\sim$ 80%, due to the inclusion of exchange interference terms in the calculation of the 2p2h cross-section [96]. Taking into account the model differences, the error on `PNNN Shape` dial has been set conservatively to 33% (Tab. 4.2).

In terms of implementation, a value of 0 corresponds to the NEUT default setting with the pn/nn ratio equal to 2/3, and a value $+1$ (-1) corresponds to the case of *pn* (*nn*) pairs

Pair	Fraction
Neutrino	
pn	66%
nn	34%
Antineutrino	
np	68%
pp	32%

TABLE 4.3: Fraction of different pairs in the Valencia model (NEUT) for neutrinos and antineutrinos.

only, as presented in Fig. 4.17. For the treatment of the ratio of 2p2h pairs in antineutrino interactions, the isospin symmetry was assumed, which means that nn (np) is replaced by pp (pn). Therefore, we have only one dial affecting both ν and $\bar{\nu}$.

4.8 Nominal MC Predictions

After applying all weights to MC events, we obtain the nominal MC predictions presented in Fig. 4.18 for FHC samples (full set of plots for other samples can be found in Appendix B.8). The nominal distributions are different from those shown in Fig. 3.1, which is mostly driven by applying the cross-section weight, particularly the one related to M_A^{QE}. M_A^{QE} has a prior value of 1.03 MeV/c^2, while MC was generated with 1.21 MeV/c^2 [6]; therefore, the reweighting leads to a lower predicted number of CCQE events.

---

[6] The choice of prior value is mostly due to historical reasons, but as will be presented in the later part of the Thesis, the value preferred by T2K data is in between the nominal and generated one.

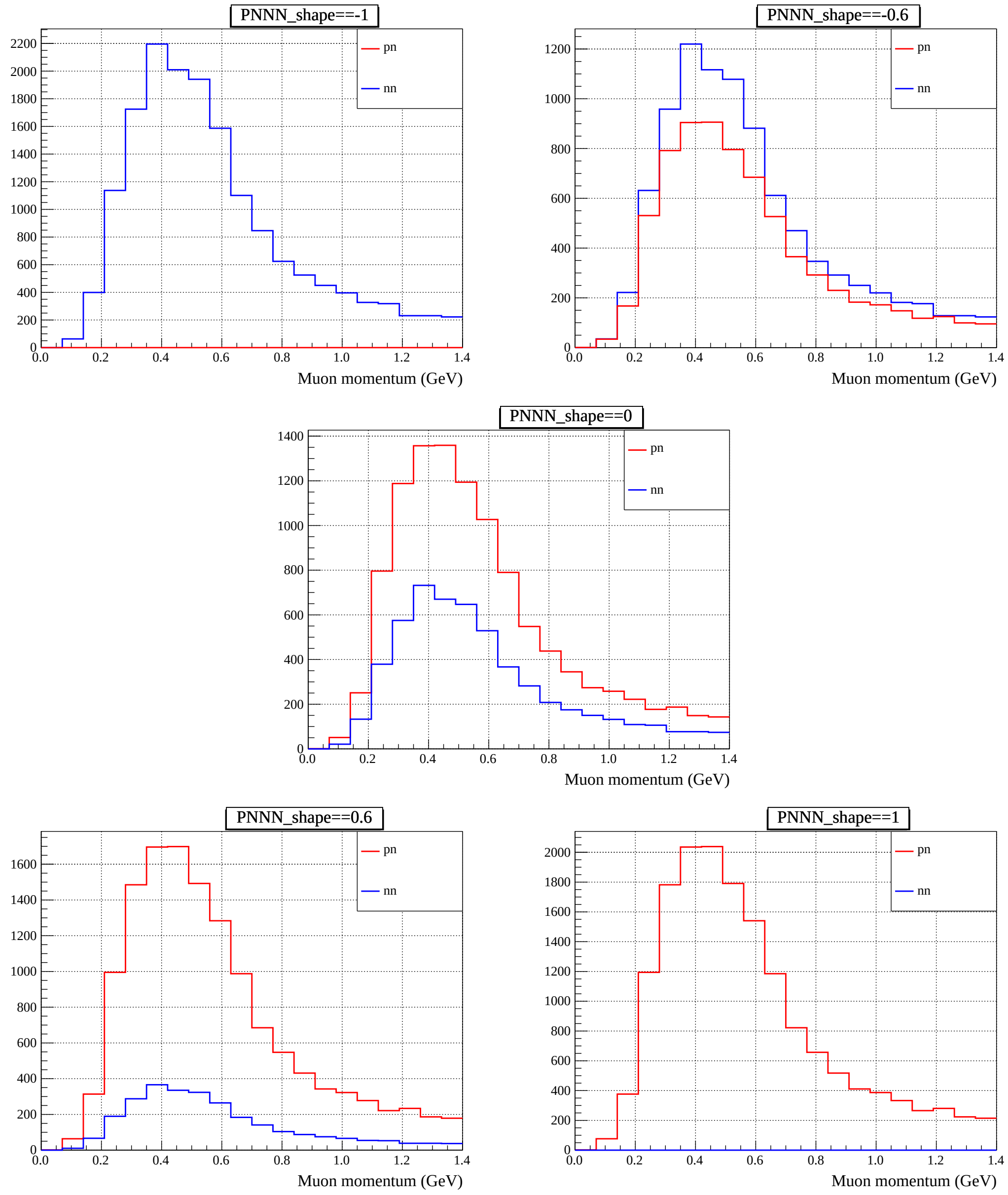

FIGURE 4.17: Distributions of muon momentum for ν_μ 2p2h interactions, split by pair type. Each plot shows the relative contributions of both pairs for different values of the `PNNN Shape` dial.

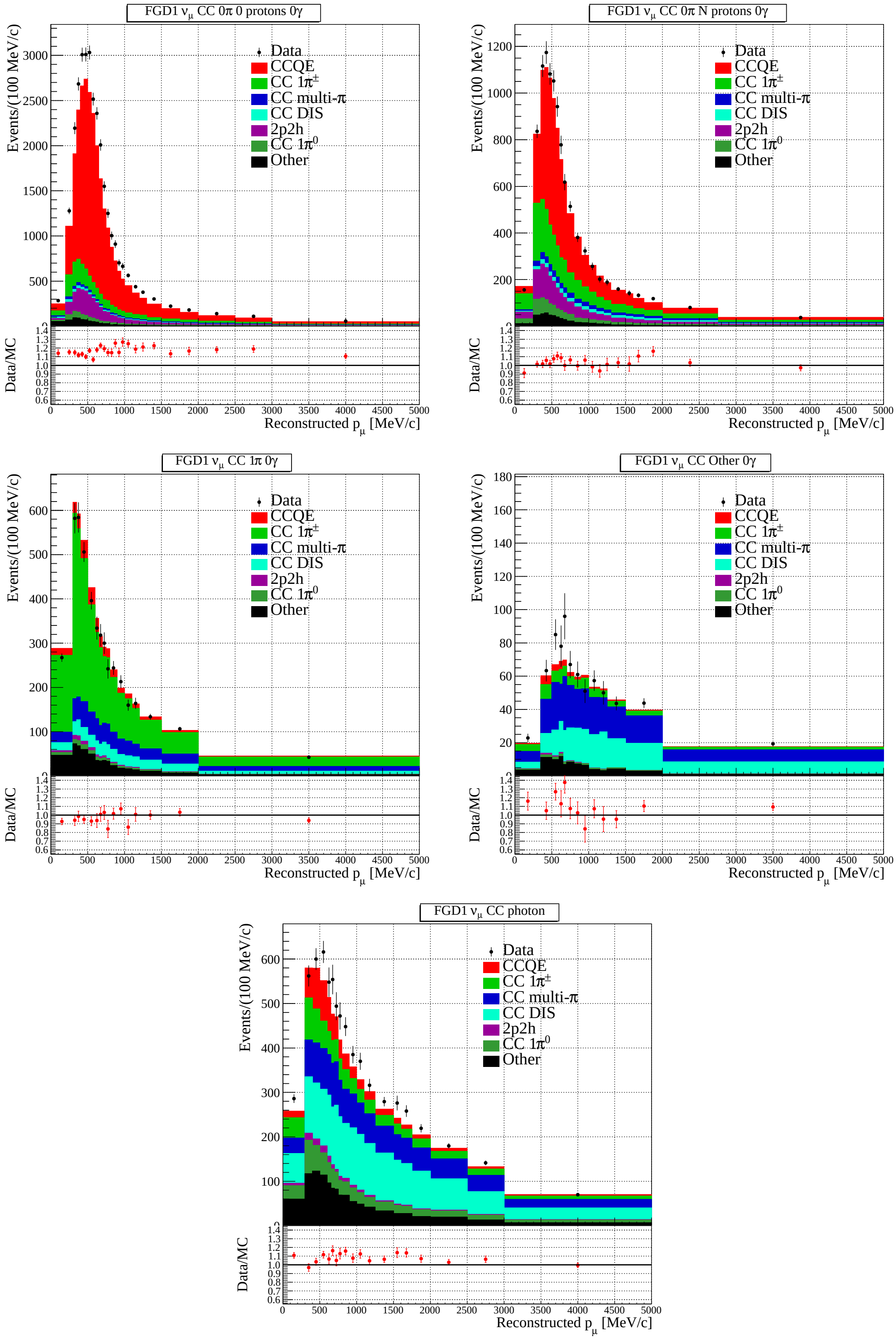

FIGURE 4.18: Nominal MC predictions for FHC samples after applying all weights, with overlayed data points.

5

Oscillation Analysis in the T2K

> Everything in war is simple, but the simplest thing is difficult.
>
> **Karl von Clausewitz**

5.1 Introduction

The main aim of oscillations analysis (OA) is to extract the PMNS matrix parameters by comparing MC-predicted event rates to the collected data. The expected number of events in SK is given by:

$$N(E_{\nu}^{rec}) = \Phi_{SK}^{exp}(E_{\nu}^{true}) \cdot \sigma(E_{\nu}^{true}) \cdot P_{osc}(E_{\nu}^{true}) \cdot \epsilon_{SK}(E_{\nu}^{true}) \cdot f(E_{\nu}^{true}, E_{\nu}^{rec}), \tag{5.1}$$

where Φ_{SK}^{exp} is the expected unoscillated neutrino flux at SK, $\sigma(E_{\nu}^{true})$ the neutrino cross-section, $P_{osc}(E_{\nu}^{true})$ the oscillation probability, $\epsilon_{SK}(E_{\nu}^{true})$ the efficiency to detect a neutrino at SK and $f(E_{\nu}^{true}, E_{\nu}^{rec})$ is the energy response function. ND280 helps to constrain Φ_{SK}^{exp} and $\sigma(E_{\nu}^{true})$, as previously mentioned in Sections 4.3 and 4.4.

To obtain the best agreement between data and MC, we change the values of the systematic parameters described in Chapter 4 and the oscillation parameters. The agreement is measured by using $\Delta\chi^2$ (the definition will be given later), and the purpose of the fit is to find the minimum value of $\Delta\chi^2$.

There are two different approaches how to perform ND280 analysis in OA. The first one, called BANFF [97], is a MINUIT-based [98] fitter and uses a frequentist approach. BANFF performs the fit for ND280 MC and data only, and then the best-fit values of cross-section and flux parameters, together with their uncertainties, are propagated to FD. Then another fit is performed for SK data and corrected predictions, using another fitter, from which the oscillation parameters are obtained. Furthermore, BANFF calculates the frequentist p-value which determines whether the prefit model is sufficiently flexible to accommodate the ND280 data.

The second approach uses MaCh3 [99], a Bayesian framework based on the Markov chain Monte Carlo, to find Posterior Distribution Functions (PDF) of cross-section, flux and detector parameters. Using PDFs instead of best-fit values with errors allows us to not make any assumptions of underlying distributions. MaCh3 is also capable of doing so-called joint-fit, where the fit is performed simultaneously to ND280 and SK data. MaCh3 calculates the Bayesian p-value which has a different interpretation than the BANFF p-value and will be discussed further. Since the Author worked mostly with MaCh3, the following Sections will describe the Markov chain Monte Carlo in detail.

BANFF and MaCh3 ND280 analysis outcomes are cross-checked to give more robust results. The fitters' validation is presented in Appendix A.6.

5.2 Likelihood Fit

The ND280 (and oscillation in extent) analysis is basically a counting experiment where event rates in a particular bin are compared between data and MC prediction. The probability distribution describing the counting experiment is given by a discrete Poisson distribution:

$$p(x) = \frac{\lambda^x e^{-\lambda}}{x!}, \tag{5.2}$$

where λ is the expected number of events, which in our case depends on a set of systematic parameters $\vec{\theta}$: $\lambda = \lambda(\vec{\theta})$. In general, we can describe the model by the *prior probability distribution* $p(\vec{\theta})$, often referred to just as "prior". Most parameters have a Gaussian probability distribution, but some have flat (in general, it can be any distribution).

The goal of experiments is to determine if (or which) model represents accumulated data best. In the language of statistical analysis, this can be expressed by the *posterior probability distribution* $p(\vec{\theta}|Z)$, also known as the likelihood ($\mathcal{L}$) [100]. To relate $p(\vec{\theta}|Z)$ with $p(\vec{\theta})$ let's remind Bayes' theorem, which states:

$$p(\vec{\theta}|Z) = \frac{p(Z|\vec{\theta})p(\vec{\theta})}{p(Z)}, \tag{5.3}$$

where $p(Z|\vec{\theta})$ exhibits the probability of taking the measurement Z with the assumption that the model with parameters $\vec{\theta}$ is a correct description of our experiment, while $p(Z)$ works as a normalisation term and can be expressed alternatively as $\sum_i p(Z|\vec{\theta}_i)p(\vec{\theta}_i)$, which will later cancel out.

In the ND280 analysis, we have almost 5000 bins, and each is described by its own Poisson probability distribution. Therefore, we can write the likelihood as a product of Poisson distributions in each bin:

$$\mathcal{L}(Z|\vec{\theta}) = \prod_i \frac{\left(N_i^{\mathrm{MC}}(\vec{\theta})\right)^{N_i^{\mathrm{data}}} e^{-N_i^{\mathrm{MC}}(\vec{\theta})}}{N_i^{\mathrm{data}}!}, \tag{5.4}$$

where i enumerates bins of p_μ and $\cos\theta_\mu$, N_i^{data} is the number of data events in i-th bin, while $N_i^{\mathrm{MC}}(\theta)$ is the number of events predicted by MC, and $\vec{\theta}$ is a vector of parameters describing our model. For the sake of brevity we will replace $\mathcal{L}(Z|\vec{\theta})$ with $\mathcal{L}(\vec{\theta})$.

To perform the test of the hypothesis that our data is described by a set of parameters $\vec{\theta}$, the likelihood ratio is used. According to Wilks' theorem [101], the logarithm of the likelihood ratio (-2LLH) approaches asymptotically[1] $\Delta\chi^2$:

$$\Delta\chi^2 = -2\ln\left(\frac{\mathcal{L}(\vec{\theta})}{\mathcal{L}_0(\vec{\theta}_0)}\right), \tag{5.5}$$

where $\mathcal{L}_0(\vec{\theta}_0)$ is the likelihood of a null hypothesis (in this case, an ideal situation in which expected values are in perfect agreement with data, which can be written as $N_i^{MC}(\vec{\theta}_0) =$

---

[1] For a number of bins approaching infinity.

N_i^{data}). Using the likelihood definition from Eq. 5.4, we derive:

$$\begin{aligned}\Delta\chi^2 &= -2\ln\left(\prod_i \left(N_i^{\text{MC}}(\vec{\theta})\right)^{N_i^{\text{data}}} e^{-N_i^{\text{MC}}(\vec{\theta})}\right) + 2\ln\left(\prod_i \left(N_i^{\text{MC}}(\vec{\theta}_0)\right)^{N_i^{\text{data}}} e^{-N_i^{\text{MC}}(\theta_0)}\right) \\ &\xrightarrow{N_i^{MC}(\vec{\theta}_0)=N_i^{data}} 2\sum_i\left[-\ln\left(\left(N_i^{\text{MC}}(\vec{\theta})\right)^{N_i^{\text{data}}} e^{-N_i^{\text{MC}}(\vec{\theta})}\right) + \ln\left(\left(N_i^{\text{data}}\right)^{N_i^{\text{data}}} e^{-N_i^{\text{data}}}\right)\right],\end{aligned} \tag{5.6}$$

where terms with factorials cancel each other. Finally, we obtain:

$$\Delta\chi^2 = -2\log\mathcal{L}_{\text{Stat}} = 2\sum_i\left[N_i^{\text{MC}}(\vec{\theta}) - N_i^{\text{data}} + N_i^{\text{data}}\ln\left(\frac{N_i^{\text{data}}}{N_i^{\text{MC}}(\vec{\theta})}\right)\right]. \tag{5.7}$$

Since this term was derived from the Poisson distribution, it will be referred to as a statistical term or simply $-2\log\mathcal{L}_{\text{Stat}}$.

The quantity in Eq. 5.7 follows the χ^2 distribution under assumption that all parameters $\vec{\theta}$ are uncorrelated and have no prior uncertainties. This, in general, is not the case, and one must consider prior uncertainties and correlations of parameters that are not included in $\Delta\chi^2$. Model parameters are described by multivariate normal distributions with a covariance matrix V_θ (the treatment of flat priors will be discussed later):

$$\pi(\vec{\theta}) = \prod_{ij}\frac{1}{(2\pi)^{k/2}|(V_\theta)_{ij}|^{1/2}} e^{-\frac{1}{2}\Delta\vec{\theta}_i\left(V_\theta^{-1}\right)_{ij}\Delta\vec{\theta}_j^T}, \tag{5.8}$$

where k is the dimension of parameter vector $\vec{\theta}$ and $\Delta\vec{\theta} = \vec{\theta} - \vec{\theta}_0$, with $\vec{\theta}_0$ being the prior value.

Knowing this, we can modify Eq. 5.5 to include a probability distribution describing the systematic model. One important feature of -2LLH is that it is additive, so we can introduce separate contributions from data/MC comparison ($-2\log\mathcal{L}_{\text{Stat}}$) and systematic parameters ($-2\log\mathcal{L}_{\text{Sys}}$).

$$\begin{aligned}\Delta\chi^2 &= -2\ln\left(\frac{\pi(\vec{\theta})\mathcal{L}(\vec{\theta})}{\pi_0(\vec{\theta}_0)\mathcal{L}_0(\vec{\theta}_0)}\right) \\ &= -2\ln\left(\frac{\mathcal{L}(\vec{\theta})}{\mathcal{L}_0(\vec{\theta}_0)}\right) - 2\ln\left(\frac{\pi(\vec{\theta})}{\pi_0(\vec{\theta}_0)}\right) = -2\log\mathcal{L}_{\text{Stat}} - 2\log\mathcal{L}_{\text{Sys}}.\end{aligned} \tag{5.9}$$

It's worth noting that we assumed all parameters to have Gaussian prior probability distributions. As was mentioned in Section 4.4, for some parameters we assume flat priors. In this case, the corresponding part of $-2\log\mathcal{L}_{\text{Sys}}$ is 0, as the nominator and denominator cancel out, yielding $\approx \ln(1)$.

After substitution 5.8 into 5.9 and accounting for the systematic uncertainties from the three sources described previously, our likelihood takes the following form:

$$\begin{aligned}\Delta\chi^2 = 2\sum_i^{\text{Nbins}} N_i^{\text{MC}}(\vec{f},\vec{x},\vec{d}) - N_i^{\text{data}} + N_i^{\text{data}}\ln\left(\frac{N_i^{\text{data}}}{N_i^{\text{MC}}(\vec{f},\vec{x},\vec{d})}\right) \\ \left.\begin{array}{ll} + & \sum_i^{E_\nu bins}\sum_j^{E_\nu bins}\Delta\vec{f}_i\left(V_f^{-1}\right)_{i,j}\Delta\vec{f}_j \\ + & \sum_i^{\text{xsecpars}}\sum_j^{\text{xsecpars}}\Delta\vec{x}_i\left(V_x^{-1}\right)_{i,j}\Delta\vec{x}_j \\ + & \sum_i^{\text{ND280det}}\sum_j^{\text{ND280det}}\Delta d^{\vec{ND}}{}_i\left(V_d^{-1}\right)_{i,j}\Delta d^{\vec{ND}}{}_j \end{array}\right\} -2\log\mathcal{L}_{\text{Sys}}\end{aligned} \tag{5.10}$$

where $\vec{f}$ refers to neutrino flux, $\vec{x}$ to cross-section and $d^{\vec{N}D}$ to ND detector parameters. By looking at $-2\log\mathcal{L}_{\mathrm{Sys}}$ one can see, that if a parameter stays at the prior value ($\vec{\theta} = \vec{\theta}_0$) it will not contribute to -2LLH and the further away a parameter is from the prior value, the greater -2LLH will be. For example, parameters with tight prior are getting larger contributions than parameters with loose prior. This part of -2LLH is often referred to as penalty term.

The generation of MC is a stochastic process, so even identical settings can lead to different outputs[2]. This fact introduces uncertainty in the MC distributions, especially for phase space regions with a low number of events. Because of that, the ND280 fit uses a correction to Poissonian likelihood described by Barlow-Beeston [102] which accounts for MC statistical uncertainty and is as follows:

$$
\begin{aligned}
-2\log\mathcal{L}_{\mathrm{Stat}} &= -2\log\mathcal{L}_{\mathrm{Poisson}} - 2\log\mathcal{L}_{\mathrm{MC_{stat}}} = \\
&= 2\sum_i \left[N_i^{\mathrm{MC}}(\vec{\theta}) - N_i^{\mathrm{data}} + N_i^{\mathrm{data}} \ln\left(\frac{N_i^{\mathrm{data}}}{N_i^{\mathrm{MC}}(\vec{\theta})} \right) + \frac{(\beta_i - 1)^2}{2\sigma_{\beta_i}^2} \right],
\end{aligned}
\tag{5.11}
$$

where β_i is a scaling parameter between ideal ("true") and generated MC in a bin ($N_{\mathrm{MC},i}^{\mathrm{true}} = \beta_i N_i^{\mathrm{MC}}$), and $\sigma_{\beta_i}^2 = \sqrt{\sum w_i^2 / N_i^{\mathrm{MC}}}$, $\sum w_i^2$ being the sum of the squares of the weights in the bin i. Additionally, N_i^{MC} has been replaced by $N_{\mathrm{MC},i}^{\mathrm{true}}$. Assuming β_i has a Gaussian distribution, we can find its mean value by solving following equation derived by Conway [103]:

$$
\beta_i^2 + (N_i^{\mathrm{MC}}\sigma_{\beta_i}^2 - 1)\beta_i - N_i^{\mathrm{data}}\sigma_{\beta_i}^2 = 0. \tag{5.12}
$$

An example of β_i parameter can be seen in Fig. 5.1, which demonstrates that they are in fact Gaussian.

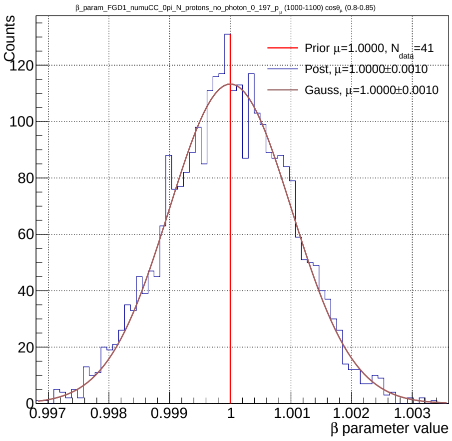

FIGURE 5.1: Example of the Barlow-Beeston β parameter for a bin with 41 data events. The red line marks the mean value of β, the blue histogram shows the distribution obtained by varying $\vec{\theta}$ parameters, and the brown line is a Gaussian fit to the histogram.

There is an alternative likelihood proposed by the IceCube collaboration that works spectacularly well for low-statistics cases. Because of it and to check if the choice of likelihood doesn't bias results, an additional test was done, presented in Appendix A.7.

As previously discussed, in the MaCh3 framework, we can perform a simultaneous fit of ND280 and SK event samples. In such an analysis, we need to include -2LLH and penalty terms for both ND280 and SK samples and systematic uncertainties. It is important to note

---

[2] Assuming that the seeds of the random number generator are different.

that the Barlow-Beeston correction is only used for ND280 samples. Due to the small number of data events at FD, the impact of MC statistics is small, if not negligible.

In the joint-fit, we have to account for oscillation probabilities. T2K is sensitive to $\sin^2\theta_{23}$, Δm^2_{32} and δ_{CP}, for which we assume flat priors. On the other hand, $\sin^2\theta_{12}$, Δm^2_{21} and $\sin^2\theta_{13}$[3] have Gaussian priors based on the results of other experiments, and we need to include a penalty term related to them.

Finally, we obtain the equation for -2LLH used in the oscillation fit:

$$\begin{aligned}
-2\ln\mathcal{L} =& 2\sum_{i}^{\text{ND280bins}} N_i^{\text{ND,MC}}(\vec{f},\vec{x},d^{\vec{ND}}) - N_i^{\text{ND,data}} + N_i^{\text{ND,data}}\ln\left(\frac{N_i^{\text{ND,data}}}{N_i^{\text{ND,MC}}(\vec{f},\vec{x},d^{\vec{ND}})}\right) + \frac{(\beta_i-1)^2}{2\sigma^2_{\beta_i}} \\
&+2\sum_{i}^{\text{SKbins}} N_i^{\text{SK,MC}}(\vec{f},\vec{x},d^{\vec{SK}}) - N_i^{\text{SK,data}} + N_i^{\text{SK,data}}\ln\left(\frac{N_i^{\text{SK,data}}}{N_i^{\text{SK,MC}}(\vec{f},\vec{x},d^{\vec{SK}})}\right) \\
&+\sum_{i}^{E_\nu bins}\sum_{j}^{E_\nu bins}\Delta\vec{f}_i\left(V_f^{-1}\right)_{i,j}\Delta\vec{f}_j \\
&+\sum_{i}^{\text{xsecpars}}\sum_{j}^{\text{xsecpars}}\Delta\vec{x}_i\left(V_x^{-1}\right)_{i,j}\Delta\vec{x}_j \\
&+\sum_{i}^{\text{ND280det}}\sum_{j}^{\text{ND280det}}\Delta d^{\vec{ND}}{}_i\left(V_{d^{ND}}^{-1}\right)_{i,j}\Delta d^{\vec{ND}}{}_j \\
&+\sum_{i}^{\text{SKdet}}\sum_{j}^{\text{SKdet}}\Delta d^{\vec{SK}}{}_i\left(V_{d^{SK}}^{-1}\right)_{i,j}\Delta d^{\vec{SK}}{}_j \\
&+\sum_{i}^{\text{oscpars}}\sum_{j}^{\text{oscpars}}\Delta\vec{o}_i\left(V_o^{-1}\right)_{i,j}\Delta\vec{o}_j.
\end{aligned} \tag{5.13}$$

5.3 Markov Chain Monte Carlo - MCMC

Markov chain [104] is a type of stochastic process in which we consider a number of states that the chain can enter, and the transition between states is possible with a given probability known as the transition probability. The most common example of a Markov chain is a random walk. The transition between two states is called a step.

Markov chains have the property that the transition probability depends only on the current state, in other words, it does not depend on what happened in the past steps. Such a feature is called "memorylessness" or "Markovian property". A Markov chain can converge to a stationary state when the probabilities of occupying each state are constant in time (do not change after a step). It is crucial to understand that the stationary chain can still transit between its states; it is only the probability of occupying each state that stays constant. Intuitively, we can think that the stationary state is located near a minimum of $\Delta\chi^2$ and the chain is transitioning to different states $X_{\vec{\theta}}$ corresponding to parameters $\vec{\theta}$ (details will be explained later).

A Markov chain has to satisfy the following conditions to have a stationary state:

---

[3] T2K is sensitive to this parameter, although not as much as reactor neutrino experiments. Therefore, two analyses are performed: one with the reactor constraint applied and another one without it. In the Thesis only the former is presented.

- Aperiodic - chain steps cannot be periodic. A very simple example of a periodic chain is shown in Fig. 5.2 (A). In this example, we can move from a hot to a cold room, and there is always 100% probability of changing room. In this case, the probabilities of occupying each state are equal to $\begin{pmatrix}1 & 0\end{pmatrix}$ for even steps, and $\begin{pmatrix}0 & 1\end{pmatrix}$ for odd steps. As was mentioned, in the stationary state, the probability of occupying a given state is constant, which clearly is not fulfilled by a periodic chain.
- Irreducible - any state can be reached with non-zero probability from any other state in a finite number of steps. Thus, the stationary state will not depend on the starting position of the chain. An example of an irreducible as well as a non-irreducible chain is shown in Fig. 5.2 (B).

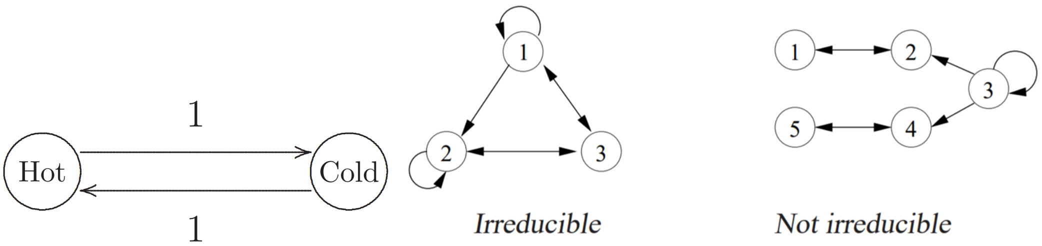

(A) Example of a periodic chain.

(B) Example of an irreducible and not irreducible chain.

FIGURE 5.2: Examples of Markov chain properties [105].

Additionally, there is the Detailed Balance principle, which states that:

$$\pi(\vec{\theta})p(\vec{\theta}'|\vec{\theta}) = \pi(\vec{\theta}')p(\vec{\theta}|\vec{\theta}'), \tag{5.14}$$

where $\pi(\vec{\theta})$ is the probability distribution (in the stationary state) of a state $X_{\vec{\theta}}$ and $p(\vec{\theta}'|\vec{\theta})$ is the probability of the transition from state $X_{\vec{\theta}}$ to $X_{\vec{\theta}'}$. One can notice that the probability distribution in the stationary state represents the posterior probability distribution from Bayes' theorem (Eq. 5.3), therefore we will usually use the latter name. The Detailed Balance equation has an easy interpretation in the fluid theory: we can think of $\pi(\vec{\theta})$ as the fluid density and $p(\vec{\theta}'|\vec{\theta})$ as the probability of liquid flow from one reservoir to another.

Now let's derive the basic equation for Markov chain Monte Carlo (MCMC). We are interested in finding the posterior distribution, which describes the joint probability of all parameters used in the analysis. Therefore, our algorithm has to satisfy the aforementioned conditions. Since it is simple to construct a chain that is irreducible and aperiodic, the derivation of MCMC begins with the Detailed Balance equation 5.14. The transition probability is divided into the proposal (or auxiliary) distribution $g(\vec{\theta}'|\vec{\theta})$ and the acceptance probability $A(\vec{\theta}',\vec{\theta})$, being the probability of accepting a new state:

$$p(\vec{\theta}'|\vec{\theta}) = g(\vec{\theta}'|\vec{\theta})A(\vec{\theta}',\vec{\theta}). \tag{5.15}$$

There is a large freedom in choice of the proposal distribution $g(\vec{\theta}'|\vec{\theta})$. The most popular choices are uniform or normal distributions. The proposed step leading to state $X_{\vec{\theta}'}$ can be expressed as $X_{\vec{\theta}'} = X_{\vec{\theta}} + rand_{proposal}(\vec{\theta})$, where $rand_{proposal}(\vec{\theta})$ used in MaCh3 is a vector of random numbers drawn from Gaussian distributions with mean values equal to 0 and standard deviations corresponding to prior errors of given parameters.

The acceptance probability simply tells whether the proposed step is accepted or not, as MCMC is a directed random walk following the regions of low -2LLH. To increase the probability of accepting a step, MaCh3 uses correlated throws [106] (via the Cholesky decomposition of the covariance matrix). When proposing a step, $rand_{proposal}(\vec{\theta})$ is multiplied by the aforementioned Cholesky matrix. Thanks to including correlated throws, the proposed values for two correlated parameters should be more likely to change in the same way. If we imagine the step as a vector in N-dimensional space, then taking into account the correlations results in some directions being preferred. A chain without correlated throws will still converge, but slower and demanding more computing resources.

After substituting Eq. 5.15 into the Detailed Balance equation 5.14 we obtain:

$$\pi(\vec{\theta})g(\vec{\theta}'|\vec{\theta})A(\vec{\theta}',\vec{\theta}) = A(\vec{\theta},\vec{\theta}')\pi(\vec{\theta}')g(\vec{\theta}|\vec{\theta}'). \tag{5.16}$$

After minor operations, we obtain the main MCMC equation [107]:

$$\frac{A(\vec{\theta}',\vec{\theta})}{A(\vec{\theta},\vec{\theta}')} = \frac{\pi(\vec{\theta}')g(\vec{\theta}|\vec{\theta}')}{\pi(\vec{\theta})g(\vec{\theta}'|\vec{\theta})}. \tag{5.17}$$

The main scheme of MCMC is as follows: a chain explores the phase space in steps and $A(\vec{\theta}',\vec{\theta})$ tells whether or not to accept the next step. Each accepted state $X_{\vec{\theta}}$ contributes to the posterior distribution which is the main result of MCMC.

Up to this point, the derivation was common for all MCMC algorithms, and from now on we will focus on a very popular algorithm known as the Metropolis-Hastings algorithm [108], used in MaCh3[4]. The basic assumption is that the acceptance probability of the next step $A(\vec{\theta}',\vec{\theta})$ takes the following form:

$$A(\vec{\theta}',\vec{\theta}) = min\left(1, \frac{\pi(\vec{\theta}')g(\vec{\theta}|\vec{\theta}')}{\pi(\vec{\theta})g(\vec{\theta}'|\vec{\theta})}\right). \tag{5.18}$$

As previously stated, $\pi(\vec{\theta})$ is $p(\vec{\theta}|Z)$ from Bayes' theorem (Eq. 5.3), so after substituting we obtain:

$$A(\vec{\theta}',\vec{\theta}) = min\left(1, \frac{g(\vec{\theta}|\vec{\theta}')p(Z|\vec{\theta}')p(\vec{\theta}')}{g(\vec{\theta}'|\vec{\theta})p(Z|\vec{\theta})p(\vec{\theta})}\right). \tag{5.19}$$

Then we can replace $p(Z|\vec{\theta}') = \mathcal{L}(\vec{\theta}')$ and $p(Z|\vec{\theta}) = \mathcal{L}(\vec{\theta})$. Since we know the other terms, we can rewrite the equation as:

$$A(\vec{\theta}',\vec{\theta}) = min\left(1, \frac{\mathcal{L}(\vec{\theta}')}{\mathcal{L}(\vec{\theta})}\right) = min\left(1, e^{log\mathcal{L}(\vec{\theta}')-log\mathcal{L}(\vec{\theta})}\right). \tag{5.20}$$

Here, $\mathcal{L}$[5] can be either Eq. 5.10 (with Barlow-Beeston correction from Eq. 5.11) for ND280-only fit, or Eq. 5.13 for ND+FD joint-fit.

Eq. 5.20 can be understood as follows: if the likelihood after the proposed step $\mathcal{L}(\vec{\theta}')$ is greater than the likelihood in the current state $\mathcal{L}(\vec{\theta})$, the acceptance probability $A(\vec{\theta}',\vec{\theta})$ is equal to 1. In other words, if MC would better represent data after the proposed step, we always accept such a step. If $A(\vec{\theta}',\vec{\theta}) < 1$, we draw a random number from the flat distribution ($0 \leqslant u \leqslant 1$) and if $A(\vec{\theta}',\vec{\theta}) \geqslant u$, we accept the proposed step. In the case of $A(\vec{\theta}',\vec{\theta}) < u$, the chain stays in the same state, and a new proposal is made that is evaluated in the same manner. It is worth noting that if the chain remains in the same state, the state $X_{\vec{\theta}}$ contributes to the posterior distribution.

We allow the chain to accept steps that would result in a lower $\mathcal{L}$, as this allows to sample the parameter space instead of searching just for a single point. In other words, the goal of

---

[4] Other algorithms were also tested in the MaCh3 framework, including Hamilton MCMC [109].

[5] In the MaCh3 fitter, we use $log\mathcal{L}$ rather than $\mathcal{L}$, in the form presented in the second part of the equation.

MCMC is to find the posterior probability distributions, not just the maximum of the distribution.

Fig. 5.3 shows the value of $-$LLH after each step of an example MCMC. It can be observed that at first $-$LLH was decreasing, and after $\sim$400 steps $-$LLH started to oscillate around some value, which can indicate that the chain achieved the stationary state.

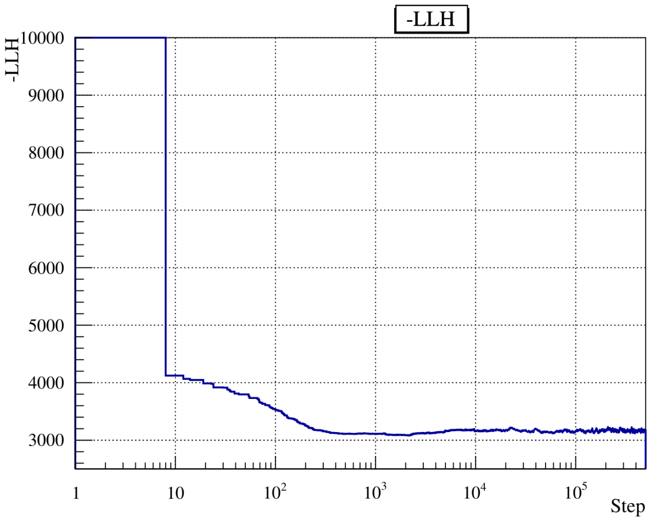

FIGURE 5.3: Values of $-$LLH after each step of an example MCMC. One can see $-$LLH decreasing until the stationary state is achieved.

5.4 MCMC Diagnosis and Analysis

Observing when a Markov chain achieves the stationary state is important in MCMC diagnosis. Since before reaching the stationary state the probabilities of transitions to different states are not constant, it is a good practice to remove (not include in the analysis) the steps, which were taken before reaching the stationary state. Such process is commonly referred to as *burn-in*.

There are several studies we can perform to diagnose a chain. Examples of them are shown in Fig. 5.4 for four independent chains which had different, randomly chosen, starting parameter values. We want our steps to be more random and weakly correlated to quickly converge, so firstly, we can study chain autocorrelations. Therefore, we introduce the variable $Lag(n)= corr(X_i, X_{i-n})$ which tells us how much correlated are states that are n steps apart, where i is the maximal considered distance (here $i = 25000$)[6]. Fig. 5.4 (A) shows the autocorrelations for the M_A^{QE} parameter. The rule of thumb for autocorrelations is that they should fall below 0.2 for $Lag(n = 10000)$, which in fact happens in our case. However, this isn't a strict criterion so if autocorrelations drop sometimes slightly slower than the blue line in the presented plot, it is not a problem.

Fig. 5.4 (B) shows the trace which represents the value of a chosen parameter (here M_A^{QE}) in each subsequent state. It can be seen, that at first the chains have different traces, but after $\sim$90 thousands steps they start to stabilise and oscillate around a very similar value, indicating that the chain converged and the stationary state was achieved.

Finally, Fig. 5.4 (C) shows the mean value of acceptance probability $A(\vec{\theta}', \vec{\theta})$ in the intervals of 5 thousands steps (batched mean). In the beginning, before achieving the stationary

---

[6] The computation time of $Lag(n)$ increases significantly as i increases; thus, we choose a value that produces satisfactory results in a reasonable amount of time.

state, the data/MC agreement is usually poor and the proposed step is more likely to improve the agreement, resulting in a high acceptance rate. When the chain gets close to the stationary state, the probability starts to stabilise. The acceptance probability for the chain marked with orange falls the fastest, while those marked with blue and green are decreasing gradually, but the one marked red has not converged yet.

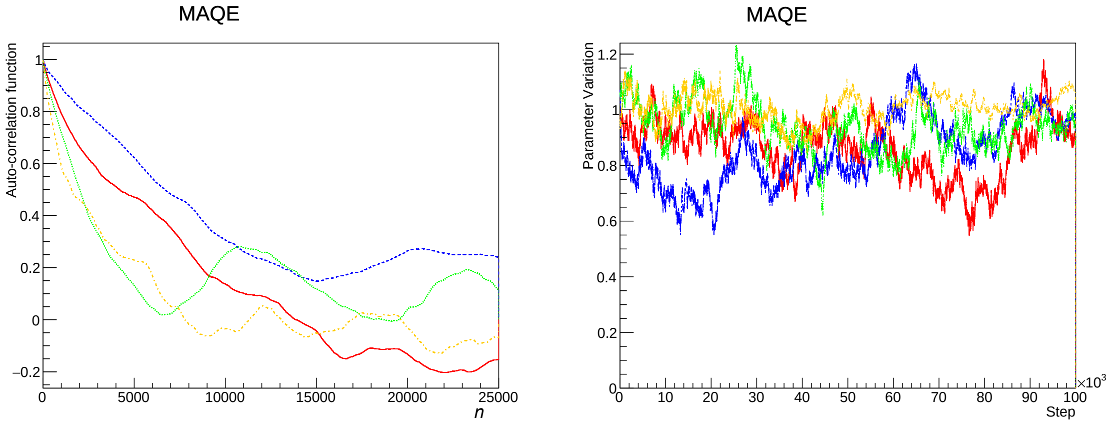

(A) Autocorrelation for a M_A^{QE} parameter (B) Trace for a M_A^{QE} parameter

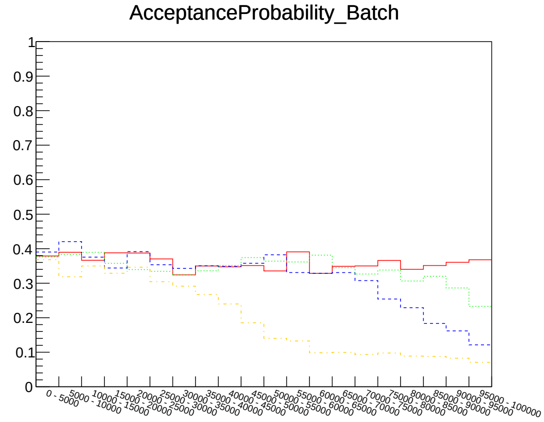

(C) Batched mean of acceptance probability

FIGURE 5.4: Examples of MCMC diagnostic tests for four chains (marked with different colours) that had different randomly selected starting positions. Plot (A) shows how autocorrelations change for states that are n-steps apart, plot (B) how the value of a selected parameter changes as a function of step number, and plot (C) presents the batched mean of the probability of accepting step $A(\vec{\theta}', \vec{\theta})$. All chains used the same Metropolis-Hastings algorithm, set of parameters, and event samples.

Fig. 5.5 displays examples of posterior distributions for two parameters after 8,000,000 MCMC steps (including 1,600,000 steps *burn-in* period). The red line marks the prior value of the parameter, and we can observe that the mean of the posterior distribution is shifted. For comparison with BANFF and to estimate how the parameter error decreased after the fit, it is important to choose the method used to extract the postfit parameter value. One option is to take the mean of the distribution with RMS error (marked as PDF in the Figures) or to fit a Gaussian function (orange line). Lastly, we can take the Highest Posterior Density (marked as HPD, vertical black line) which is just the maximum of the distribution. In this case, we calculate the error by integrating over the distribution, starting from the HPD point and doing it symmetrically until the integral of 0.6827 is reached. If a physical boundary of a parameter is reached on one side, then the integration continues only on the other side. For the posterior distribution on the left plot, we can see that all three methods give the same result ($\mu = 1.13$), which is expected, given the Gaussian-like shape of the distribution. On the other hand, the posterior distribution on the right plot is definitely not Gaussian[7] and here the three methods give different results. In this case, the most reasonable way of extracting the parameter postfit value and error is to use the HPD method.

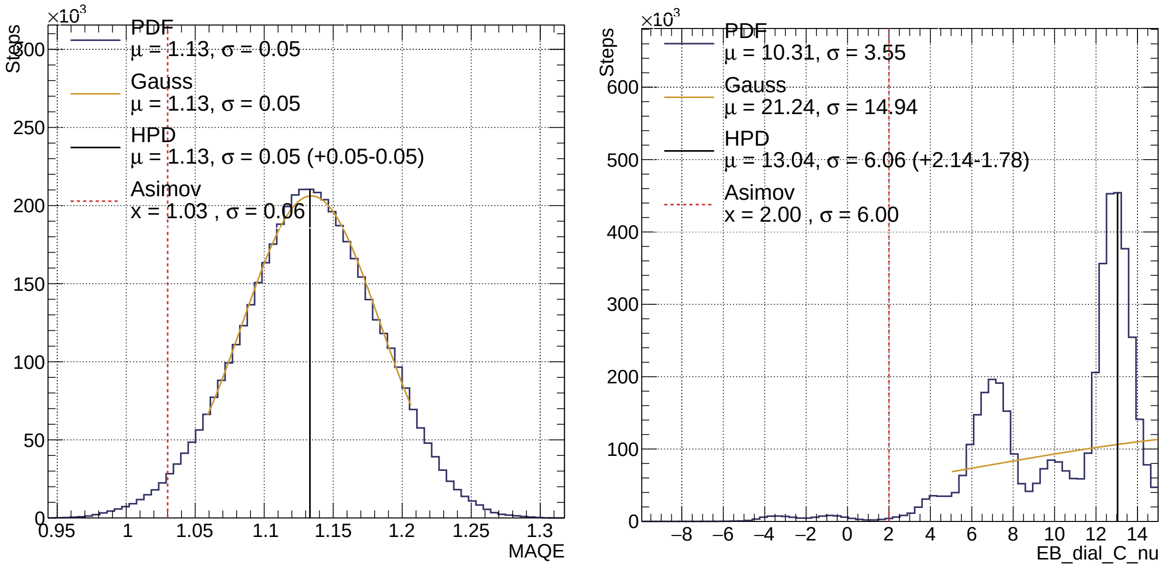

(A) M_A^{QE} (B) CCQE E_b ^{12}C

FIGURE 5.5: Posterior distributions for two dials used in T2K fit.

5.5 Fitter Validations - Asimov Fit and LLH Scan

OA is a complex analysis and one needs good validation methods, one of them being commonly known as Asimov fit. In this case, we use the full set of MC with prior values of parameters that mimic data, and we fit this fixed MC with the identical MC where the parameters are allowed to vary. As a result, we obtain the parameters distributions with the HPDs which should be close to the prior values. If they are not, this might indicate a problem with the fitter, parameter implementation etc. An example of the Asimov MCMC fit result is shown in Fig. 5.6 (A). For highly correlated parameters, it is better to examine joint two-dimensional distributions rather than one-dimensional distributions separately for each parameter. Such a two-dimensional distribution is presented in Fig. 5.6 (B) for two P and S shell normalisation parameters. Since both parameters affect the normalisation of the CCQE interaction, they should be strongly anticorrelated, and that's exactly what we observe. By extracting the correlation coefficient from such a distribution for any combination of parameters, we can create the postfit correlation matrix.

Another important test is the LLH scan, which uses a similar idea to the Asimov fit. The conceptual outline of this method is as follows: two identical sets of MC are prepared (Asimov set). For such two sets, the -2LLH is 0. Then, in the scan process, we modify the value of a dial in only one of the MCs. After changing the dial value, the MCs should not agree anymore[8], and this is observed as the change of -2LLH. In most cases, an LLH scan is performed in the range of $\pm\sigma$ of a given parameter.

---

[7] Non-Gaussian shape is most often a consequence of degenerate solutions.

[8] If the particular dial has no impact on used MC samples, then -2LLH is still 0. An example would be an FD-only dial in ND280-only analysis.

The LLH scan allows to test how sensitive the analysis is to a particular dial. For example, we include new samples to the fit and compare −2LLHs to check if the new samples provide better constraints. In Fig. 5.6 (C) we can see an example of such a study: faster-rising −2LLH indicate greater sensitivity and, in consequence, stronger constraints on a given parameter.

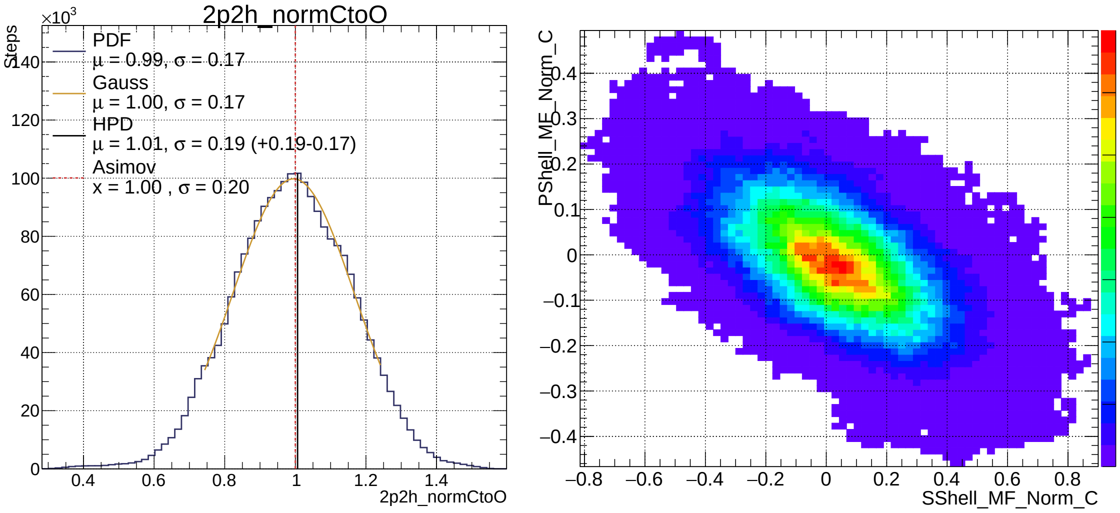

(A) Posterior distribution from Asimov fit

(B) Correlation between two parameters

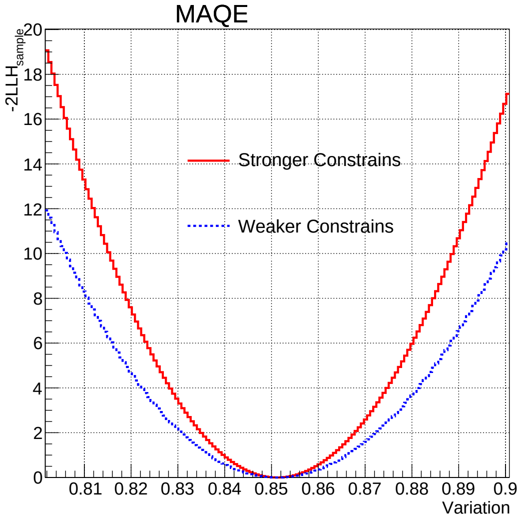

(C) LLH scan

FIGURE 5.6: Examples of posterior distributions from Asimov fit and an LLH scan, demonstrating how stronger and weaker constraints can be studied.

Usually, the results of the fit are shown as an overlay of prefit and postfit parameter values and uncertainties. An example is shown in Fig. 5.7, where the red band shows the prefit values with 1σ errors (which can be found in Tab. 4.2), while the black dots with error bars are the postfit values, or more precisely, the HPD values for posterior distributions, such as that in Fig. 5.6 (A).

Such plots are only illustrative, as the MCMC fitter is not using the HPD values in the actual analysis. In the next Section, we shall discuss how to produce predicted event spectra using posterior distributions.

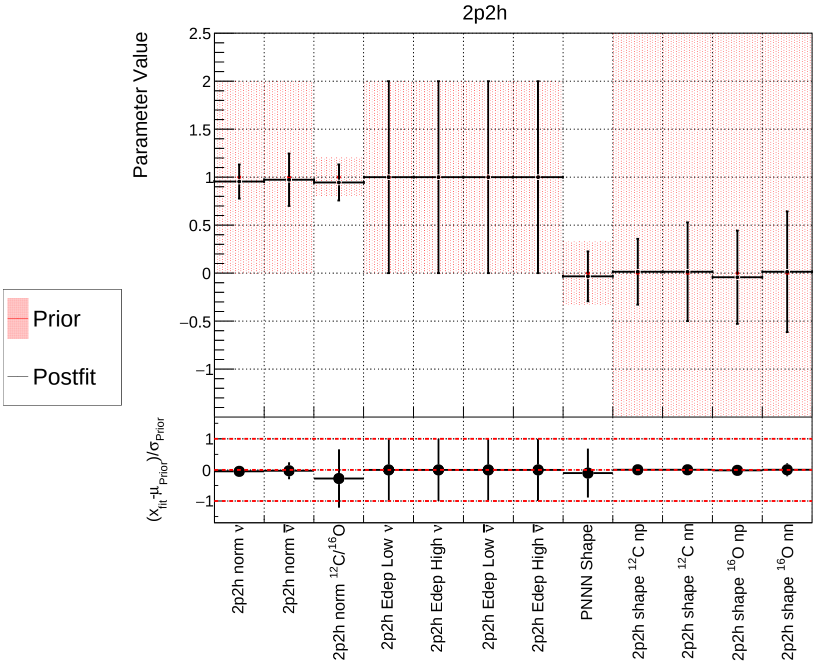

FIGURE 5.7: Example of Asimov prefit/postfit parameter overlay. The central value and error are obtained using the HPD method.

5.6 Prior and Posterior Predictive Distributions

In the other framework used in T2K (BANFF, see Section 5.1), one gets best-fit spectra simply by reweighting MC to the best-fit values of the parameters, but in the Bayesian framework we use prior and posterior predictive distributions. In this example, we will consider the predictive distributions of the number of events Z. The prior predictive distribution of Z is given by [110]:

$$p(Z) = \int_{\vec{\theta}} p(\vec{\theta})p(Z|\vec{\theta})d\vec{\theta}, \tag{5.21}$$

where $p(\vec{\theta})$ is the same prior probability as in Bayes' theorem (see Eq. 5.3). We use the following procedure to obtain the prior predictive distribution:

1. Throw values of the parameters using their prior distributions.
2. Reweight MC to the selected parameters values. Reweighted MC is usually called a toy MC.
3. From multiple toy MCs, we obtain the mean value of the number of events Z[9].

After ND280 fit, we can predict the observable Z_{pred}, which estimates the expected measurement of the same physical process as Z. This is knows as posterior predictive distribution $p(Z_{pred}|Z)$ and can be expressed as [110]:

$$p(Z_{pred}|Z) = \int_{\vec{\theta}} p(Z_{pred}|\vec{\theta})p(\vec{\theta}|Z)d\vec{\theta}, \tag{5.22}$$

where $p(\vec{\theta}|Z)$ is the posterior probability (see Eq. 5.3). We obtain the posterior predictive distribution with the following steps:

---

[9] In the analysis, we also do checks with the median; both methods give consistent results.

1. Sample the posterior probability distribution by randomly selecting steps, to get $\vec{\theta}$ associated with the selected step.
2. Reweight MC to the selected parameters values.
3. From multiple toy MCs, we obtain the mean value of the number of events Z_{pred}.

Fig. 5.8 shows the prior and posterior predictive distributions of the number of events for CC0π-0p-0γ. The prior predictive distribution is very wide compared to the posterior predictive distribution, and the relative error on the number of events for this sample has been reduced from 14% to 0.7%, which confirms that the ND280 fit greatly constrains the uncertainties in the analysis.

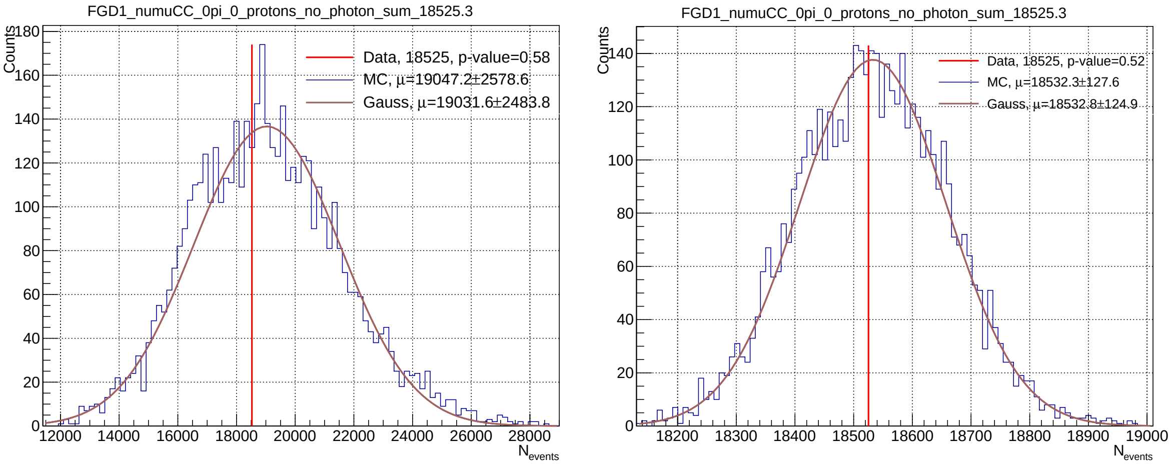

(A) Prior predictive

(B) Posterior predictive

FIGURE 5.8: Prior and posterior predictive distributions for the CC0π-0p-0γ sample, obtained using 5000 toy MCs. Note the different ranges on the horizontal axis.

The number of events is a good metric for the goodness of fit, but it is needed to compare the distributions of muon kinematic variables used in the fit. Fig. 5.9 shows the posterior predictive distributions of p_μ and $\cos\theta_\mu$ for CC0π-0p-0γ, produced by repeating the aforementioned steps for each kinematic bin.

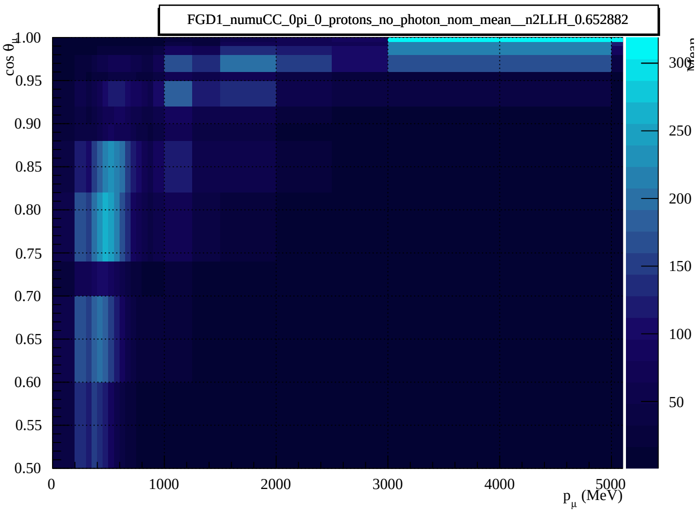

FIGURE 5.9: Posterior predictive distribution of muon kinematic variables for the CC0π-0p-0γ sample, obtained using 5000 toy MCs by sampling the posterior distribution obtained from the Asimov fit.

The presented methods are a great tool for studying fit stability etc. To evaluate the goodness of fit, we can calculate the posterior predictive p-value, which is discussed in Appendix A.8. In the next Chapter, we will show the posterior predictive distributions obtained from the actual fit to the data.

6

Fit Results

> If the tanks succeed, then victory follows.
>
> **Heinz Guderian**

This Chapter summarises the results of the official T2K oscillation analysis which uses in total 202.12×10^{19} POT for ND280 and 360.1×10^{19} POT for FD (see Section 2.6). Firstly, validations with Asimov fits are discussed, followed by the official ND280 data fit. The emphasis is placed on the latter results and discussions, as the Author was responsible for this part of the analysis. Even though the Author was not directly involved in the preparation of the neutrino oscillation results, they will be discussed here shortly for completeness. The official results have been presented at the Neutrino 2022 and ICHEP 2022 conferences [4] and are prepared to be published in the Physical Review Letter in 2023.

6.1 ND280 Asimov Fit

The results of the Asimov fit based on only ND280 samples are presented in Fig. 6.1. It shows the overlay of prior and postfit parameter values for CCQE and 2p2h-related dials. The postfit values are extracted using the HPD method, as was explained in Section 5.5. Prior and postfit values overlay very nicely, so we can conclude that the Asimov fit converged correctly. Although, on the leftmost plot, we see that the Pauli blocking dials do not fully match their prior values, as they have been shifted (or pulled, both terms will be used interchangeably) to the negative values. We have to remember that those are one-dimensional projections from an N-dimensional probability distribution. When looking at Fig. 6.2 which depicts the posteriors for Pauli blocking and optical potential dials as well as their joint two-dimensional distribution, we observe that they are strongly correlated. In addition, optical potential has a prior value on the physical boundary, as it is only valid between 0 and 1. This leads to the so-called marginalisation problem, which does not impact analysis in any way, only the projection of an N-dimensional distribution is biased. We shall emphasize again that the one-dimensional projections are only meant to help with the presentation of the results.

The results for other cross-section parameters are shown in Fig. 6.3. Here, we do not observe any problems as in the case of Pauli blocking. We can see significantly reduced errors. In general, the fitting framework has been validated successfully and is producing sensible results, so we can proceed with the data fit.

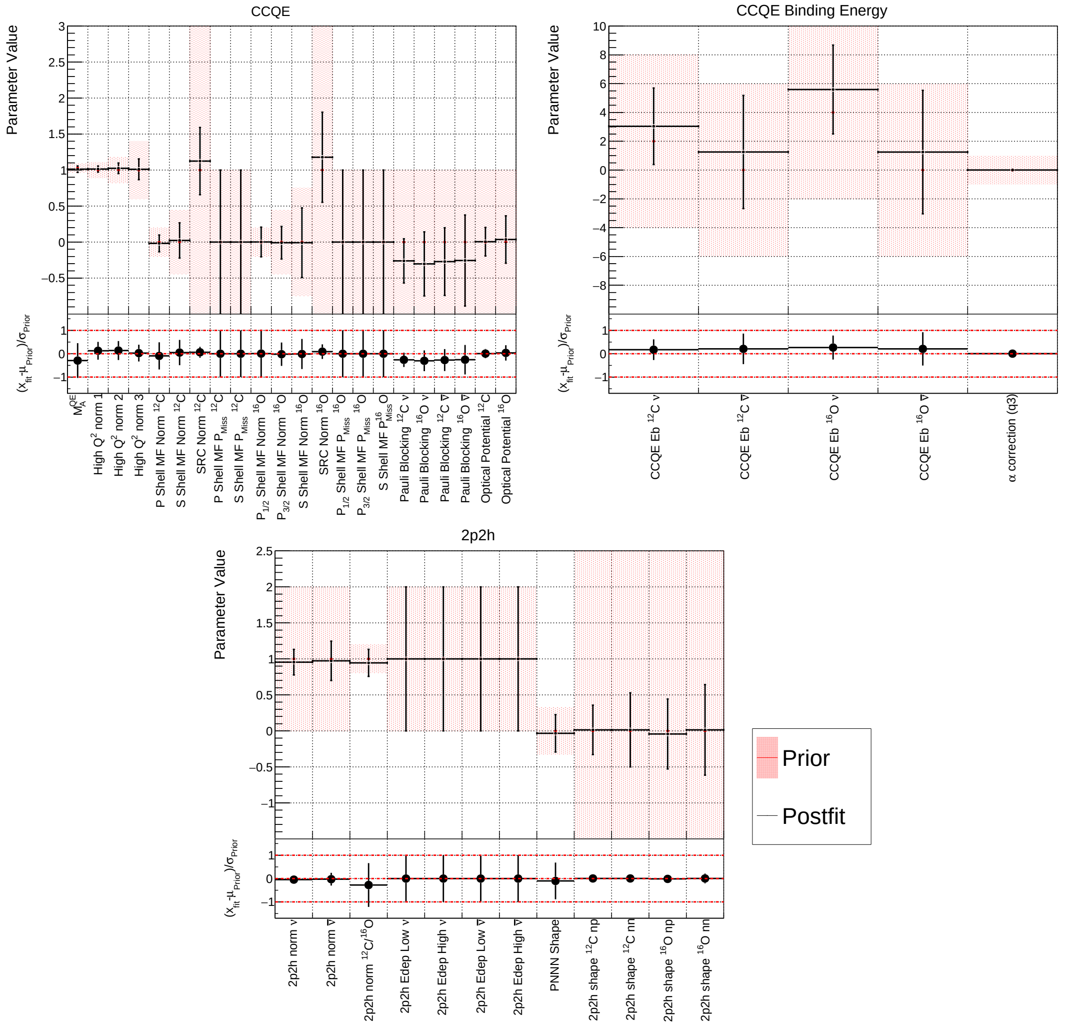

FIGURE 6.1: Overlay of parameter values from the Asimov fit for CCQE and 2p2h dials.

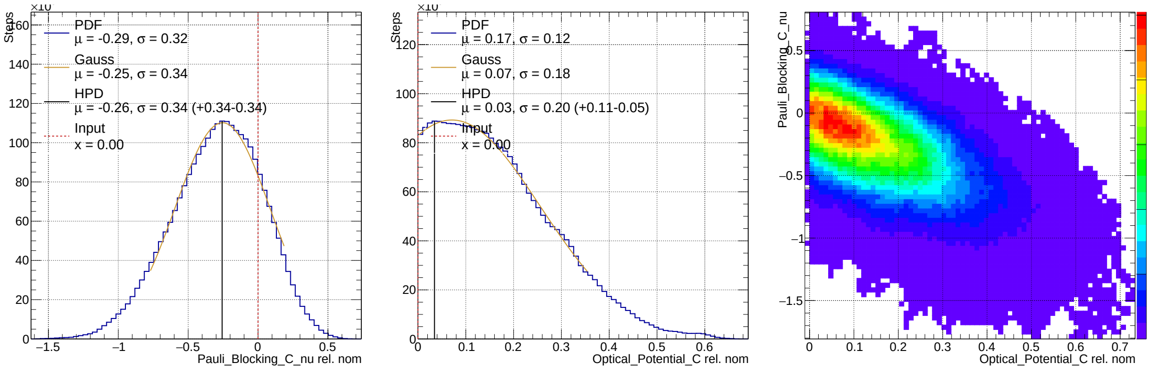

FIGURE 6.2: Asimov posterior distributions for Pauli blocking (left) and optical potential (middle) parameters, and their joint two-dimensional distribution (right), showing that both dials are strongly anticorrelated, which results in marginalisation problem.

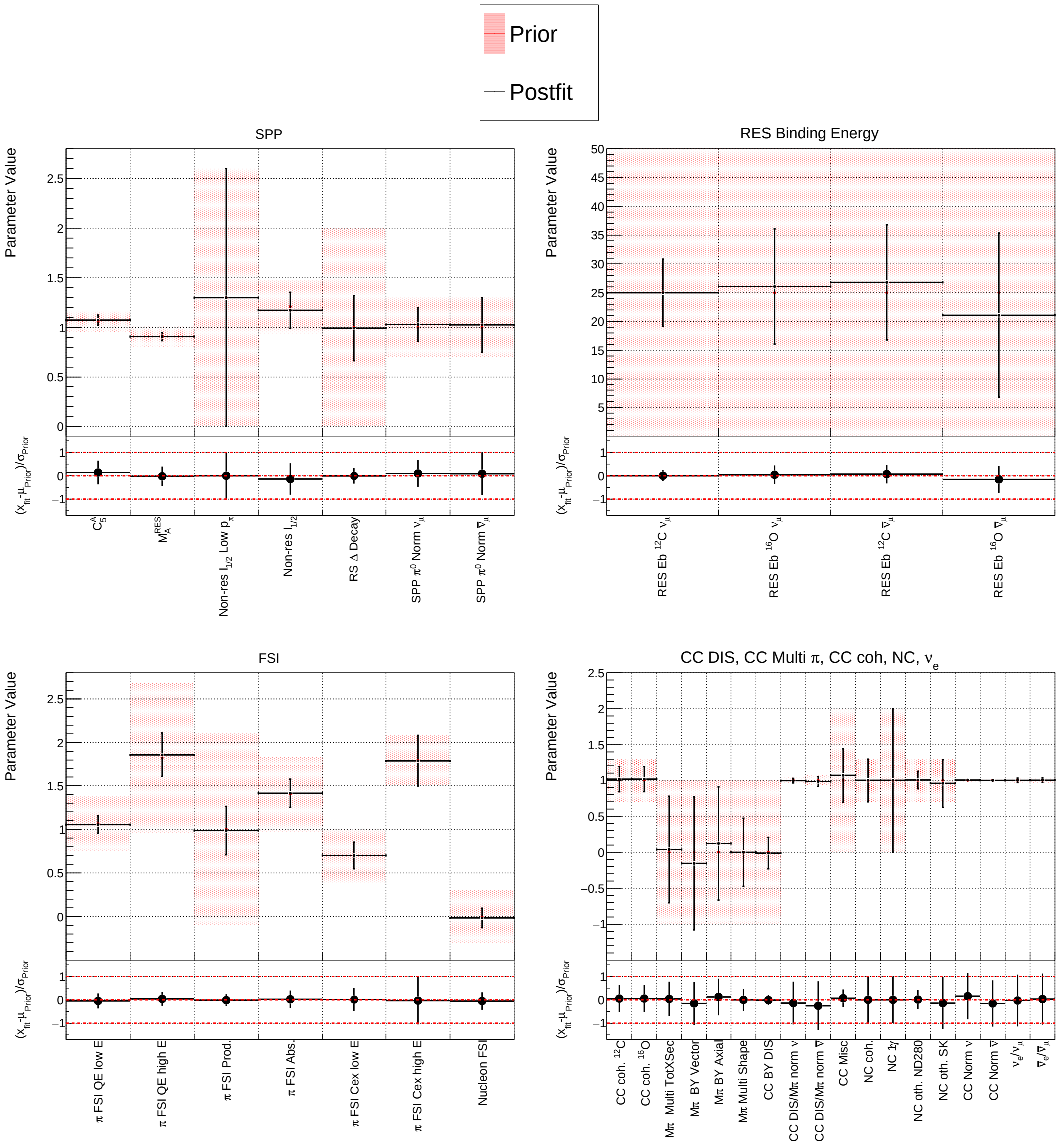

FIGURE 6.3: Overlay of parameter values from the Asimov fit for non-CCQE and non-2p2h dials.

6.2 ND280 Data Fit

After applying the selection outlined in Section 3, we obtain the event rates for each sample, which are presented in Tab. 6.1. We can observe that there is a disagreement between the initial model predictions and data, especially for FHC CC0π-0p-0γ. Because of that, we can expect that some of the CCQE parameters will be significantly pulled away from their prior values after the fit.

Sample	Data	Nominal MC
FGD1 FHC CC0π-0p-0γ	21329	18525.3
FGD1 FHC CC0π-Np-0γ	9257	9055.7
FGD1 FHC CC1π-0γ	6224	6493.6
FGD1 FHC CC-Other-0γ	1737	1621.3
FGD1 FHC CC-Photon	11156	10530.0
FGD2 FHC CC0π-0p-0γ	22935	19600.1
FGD2 FHC CC0π-Np-0γ	7373	7411.2
FGD2 FHC CC1π-0γ	5099	5312.4
FGD2 FHC CC-Other-0γ	1620	1560.6
FGD2 FHC CC-Photon	10460	9542.8
FGD1 RHC CC0π	8676	8283.3
FGD1 RHC CC1π	719	699.9
FGD1 RHC CC-Other	1533	1372.3
FGD2 RHC CC0π	8608	7910.3
FGD2 RHC CC1π	660	654.3
FGD2 RHC CC-Other	1396	1231.5
FGD1 RHC BKG CC0π	3714	3460.4
FGD1 RHC BKG CC1π	1147	1212.7
FGD1 RHC BKG CC-Other	1425	1164.4
FGD2 RHC BKG CC0π	3537	3375.3
FGD2 RHC BKG CC1π	955	974.9
FGD2 RHC BKG CC-Other	1334	1101.9
Total	130894	121094.0

TABLE 6.1: Data and nominal MC predictions for each ND280 sample used in the analysis.

Here, we only present the parameter overlays, while the full set of posterior distributions for each dial can be found in Appendix B.10. ND detector systematic parameters have no direct impact on FD predictions. However, as demonstrated in Appendix A.9, they affect FD predictions indirectly via correlations with flux and cross-section parameters, though the effect is negligible. Therefore, the overlay plots for ND detector dials are not presented here and can be found in Appendix B.11. We shall only note that most postfit values of ND detector parameters are within the prior 1σ error.

The results of the data fit for CCQE and 2p2h parameters are shown in Fig. 6.4. M_A^{QE} is pulled 2σ above its prior value, much closer to the generated value (equal to 1.21 GeV/c^2), which is consistent with the results from the previous ND280 fit [80]. The Q^2 parameters are also pulled away from their priors, with `high` Q^2 `norm 1` (relevant for the region of $0.25 < Q^2 < 0.5$ GeV^2) being pulled most significantly.

The `S-shell MF Norm` ^{12}`C` parameter is pulled in the opposite direction to the `P-shell MF Norm` ^{12}`C` parameter, resulting in an increase of S-Shell contribution, while the P-Shell contribution is weakened. However, both parameters are within their prior uncertainty bands. The oxygen-related shell dials, $P_{1/2}$ and $P_{3/2}$ `Shell MF Norm` ^{16}`O`, are very close to their priors;

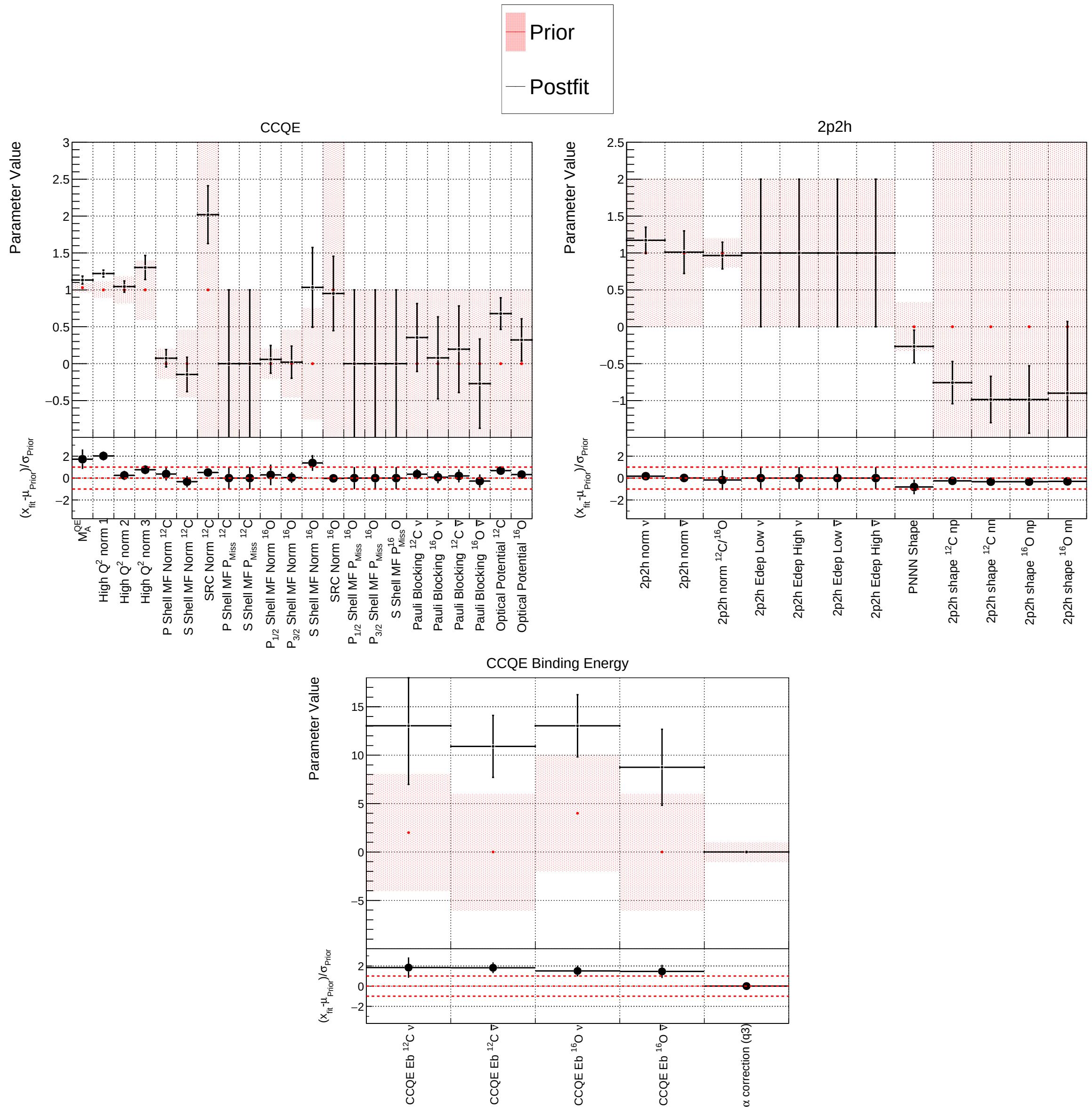

FIGURE 6.4: Postfit values for CCQE and 2p2h cross-section parameters from the data fit.

however, `S-Shell MF Norm` ^{16}`O` is pulled 1σ away from the prior, increasing the contribution from this shell. `SRC Norm` ^{12}`C` is strongly pulled away from the prior, increasing the relative strength of the SRC region in carbon, while `SRC Norm` ^{16}`O` is pulled very gently in the opposite direction, decreasing the number of SRC in oxygen.

Almost all of the Pauli blocking dials are pulled to higher values with respect to their prior central values. This translates to an increased probability of events being Pauli blocked, leading to suppression in the low Q^2 CCQE region. Furthermore, the values of the optical potential dials are increased, which corresponds to increased FSI for leptons, further suppressing the low Q^2 region. Additionally, Fig. 6.5 shows that the Pauli blocking dials do not have Gaussian posterior distributions. Fig. 6.6 presents posterior distributions for the CCQE binding energy parameters, which are also highly non-Gaussian. Since the frequentist ND280 fit (BANFF) assumes all parameters have Gaussian distributions, additional tests were performed where the binding energy parameters were fixed, and a dependence between the non-Gaussian structure of the binding energy and Pauli blocking parameters was observed.

The tests are discussed in detail in Appendix A.10 and we conclude that non-Gaussian structure doesn't impact FD analysis.

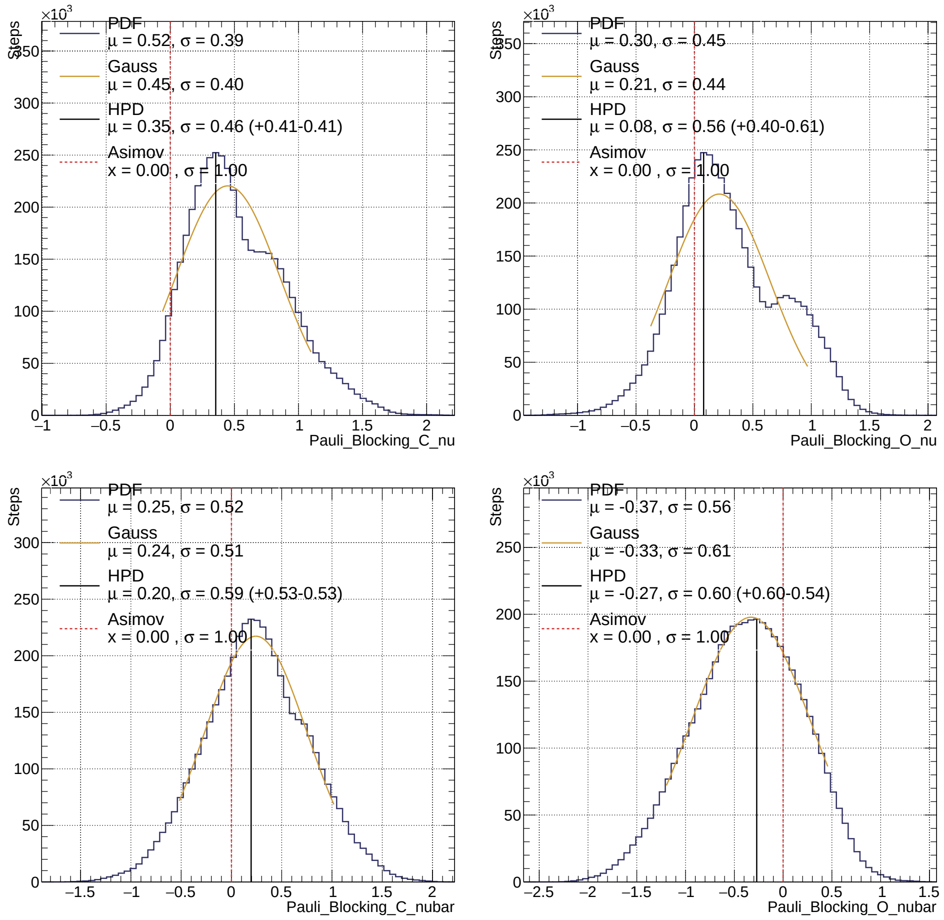

FIGURE 6.5: Posterior distributions of the Pauli blocking parameters from the data fit.

Slightly different postfit values for ν and $\bar{\nu}$ 2p2h normalisations are observed, but these are just within each others' postfit uncertainties. All 2p2h shape parameters are shifted toward value of -1, which corresponds to the lower lobe in the $q_0/|\vec{q}_3|$ phase space of Valencia model (see Fig. 4.8 on page 58). The `PNNN Shape` dial favours an increase of the number of nn pairs. Apparently, 2p2h dials were shifted to such parameter values, which result in an increased number of events in CC0π-0p-0γ and a decrease in CC0π-Np-0γ. One needs to remember that the prior value of 0 corresponds to the ratio pn/nn equal to $2/3$. The ratio value preferred by the fitter is close to $1/2$. Even though the impact of this dial is rather small, ND280 is sensitive to the 2p2h pair ratio.

The non-CCQE, non-2p2h parameters are shown in Fig. 6.7. C_A^5 is pulled almost 2σ away from the prior, whereas M_A^{RES} remains at the prior value. `RS` Δ `Decay` prefers delta-like decay, meaning the data suggest physically motivated decay, contrary to simplistic isotropic one. The π^0 normalisation for ν is pulled by 1σ, whereas it remains at the prior value for $\bar{\nu}$. The parameter for $\bar{\nu}$ is constrained weaker than the parameter for ν, which is not surprising given that the new photon tagging is only applied in FHC.

The resonant binding energy parameters have been strongly pulled towards 0, which is the generated value. As was already mentioned, the prior values for those dials have been set very conservatively to 25 MeV, so a smaller binding energy is consistent with previous results [80], where there was effectively no binding energy for resonant interactions. Most of

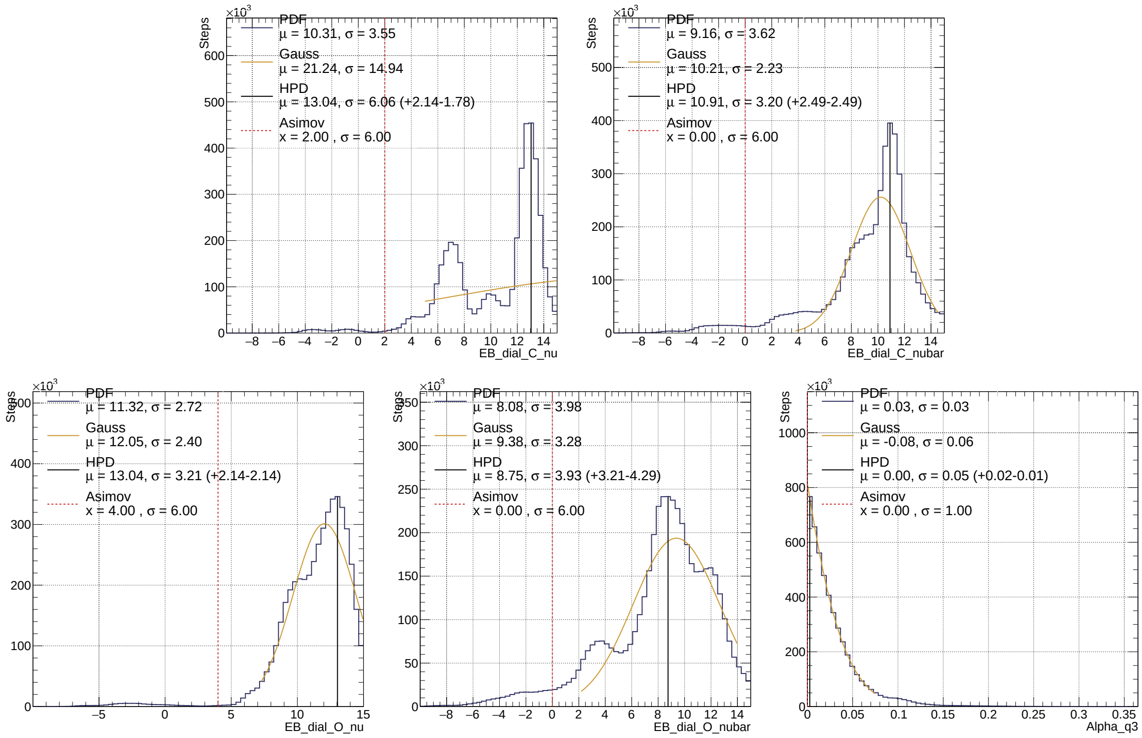

FIGURE 6.6: Posterior distributions of the E_b parameters from the data fit.

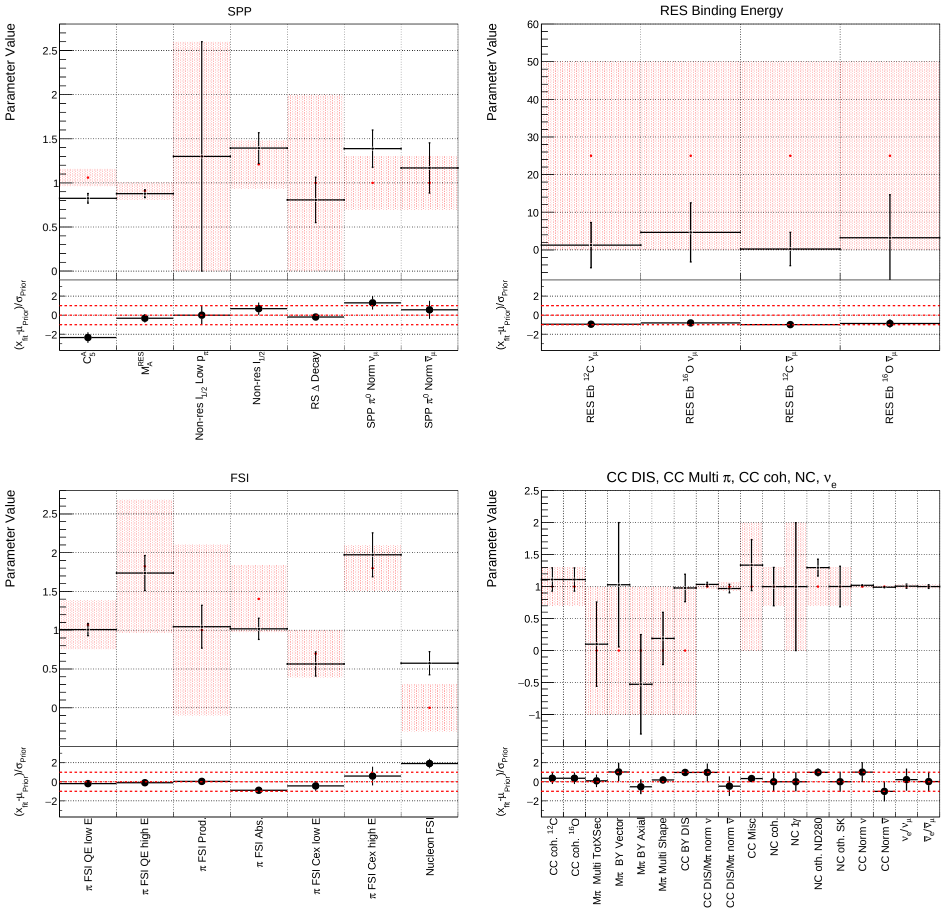

FIGURE 6.7: Non-CCQE, non-2p2h interaction parameters from the data fit.

the pion FSI dials are not shifted, except for the absorption, which was pulled by 1σ, reducing the probability of absorption and resulting in fewer events in CC0π-Np-0γ, but more in CC1π-0γ. However, the nucleon FSI parameter is pulled by almost 2σ, increasing the strength of nucleon FSI. This may come from the poor agreement with the data before the fit seen in the CC0π-0p-0γ sample but very good agreement in the CC0π-Np-0γ sample.

There is some tension between the Multiπ dials, as `BY Vector` parameter prefers a stronger correction compared to BY Axial, which is pulled to the value giving a smaller correction. `CC BY DIS` is also strongly pulled but is still in the range of the prior error. Multiplicity Shape dial is closer to the prior value, meaning the data suggest the nominal NEUT model rather than AGKY. The `CC Misc` parameter is also pushed by 1σ, but this parameter has a large prior uncertainty.

The postfit ND280 flux parameters are shown in Fig. 6.8. Due to strong prefit correlations between the ND280 and SK flux parameters, both sets of dials behave very similarly; thus, we present only the ND280 flux parameters. For FHC ν_μ, $\bar{\nu}_\mu$ and RHC ν_μ there is a pull of about 10% for neutrino energies below 1 GeV. This effect decreases as the energy increases. For energies above $E_\nu = 4$ GeV, the postfit values fall below the priors. A similarly high pull is observed for FHC ν_e and RHC $\bar{\nu}_\mu$ parameters. The RHC $\bar{\nu}_e$ parameters are 6% above the priors for energies below 1.5 GeV, but they go closer to the priors at higher energies. For FHC $\bar{\nu}_e$ and RHC ν_e the pull is 5% for the low energy parameter, but the high energy parameter is close to its prior value.

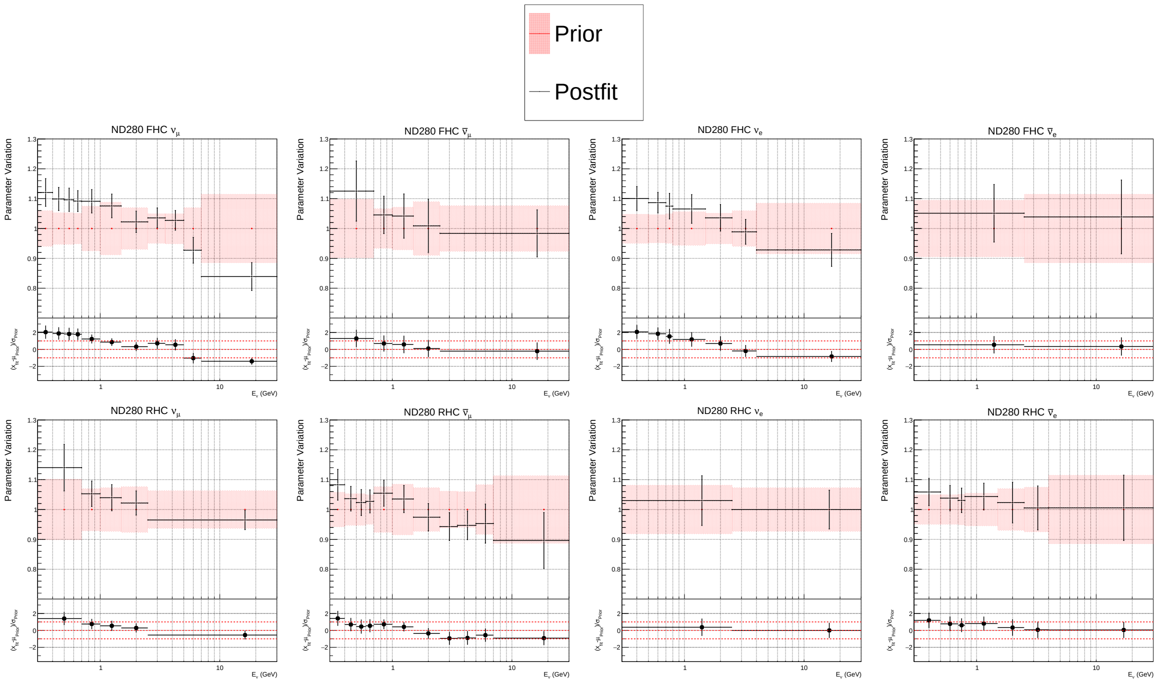

FIGURE 6.8: Prefit and postfit values for flux parameters from the data fit.

Although many of the flux parameters are pulled away from their prior values and beyond the prefit $\pm 1\sigma$ ranges (without accounting for the strong correlations between the parameters), they do not contribute significantly to the penalty term in the likelihood. As the flux parameters are strongly correlated, a pull in one can lead to many of them moving in a similar way. The flux penalty contribution to the $-$LLH at each step in the Markov chain is shown in Fig. 6.9. The stationary state corresponds to $-\log \mathcal{L}_{flux} = 50$–$60$, which for 100 flux parameters can be translated to $\mathcal{O}(1)$ χ^2 per parameter. To better understand the impact of correlations between flux parameters, an additional study using Principal Component Analysis was performed and is presented in Appendix A.11.

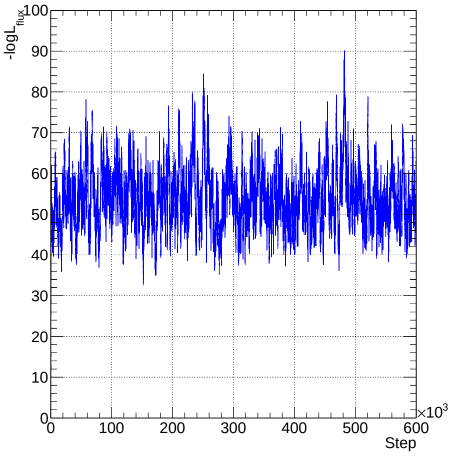

FIGURE 6.9: Flux penalty term in the MCMC data fit as a function of the step number. There are 100 flux parameters and $-$LLH$\approx$ 50–60, so $\chi^2 \approx$ 100–200 / 100 degrees of freedom.

Fig. 6.10 shows the postfit flux+cross-section correlation matrix. It is worth reminding that many of the cross-section parameters did not have initial correlations, but now correlations can be clearly seen. To better understand this outcome, let's look at the correlations between `S` and `P-Shell Norm` parameters. Both of them significantly affect the normalisation of CCQE interactions. Since they affect it so strongly, if one increases, the other has to decrease; otherwise the data-MC disagreement would be huge. Another good example is the anticorrelation of Pauli blocking and optical potential, which is expected given that both sets of dials affect low Q^2 phenomena.

The next important point is the strong correlations between flux and cross-section parameters, especially for normalisation dials. Since we have no prior knowledge of how the flux and cross-section parameters should be correlated, this demonstrates the importance of the ND280 fit.

After showing that the results are qualitatively good, we will evaluate quantitatively the goodness of fit using the posterior predictive distributions.

6.3 ND280 Posterior Predictive Distributions

Using the posterior distributions and the method described in Section 5.6, the prior and posterior predictive distributions were obtained and are shown in Fig. 6.11 for the FGD1 proton-tagged samples, and in Appendix B.9 for other ND280 samples. As expected, the posterior predictive distributions agree much better with the data than the prior predictive distributions, particularly for the FGD1 FHC CC0π-0p-0γ sample. Furthermore, the systematic error in each bin is significantly smaller. In the bottom plots of Fig. 6.11, we also show the reaction breakdown. Since we do not observe any unexpected and significant changes in fractions of interaction modes, we have further proof of the analysis' robustness. Still, the postfit model does not perfectly describe the data; for example, at high p_μ there are regions with an underestimated number of events in MC.

The improvement of data and MC agreement is further confirmed by the reduction in $-2\log\mathcal{L}_{\text{Stat}}$ for the posterior prediction compared to the prior prediction, as shown in Tab. 6.2. The uncertainties on the event rates for all samples are also reduced significantly. The fractional systematic errors in Tab. 6.3[1] show that the total ND280 event rate systematic uncertainty has been reduced from 9.07% to 0.28% after the fit. The CC0π-0p-0γ sample has the

---

[1] A similar table showing the errors from different systematic sources can be found in Appendix B.7.

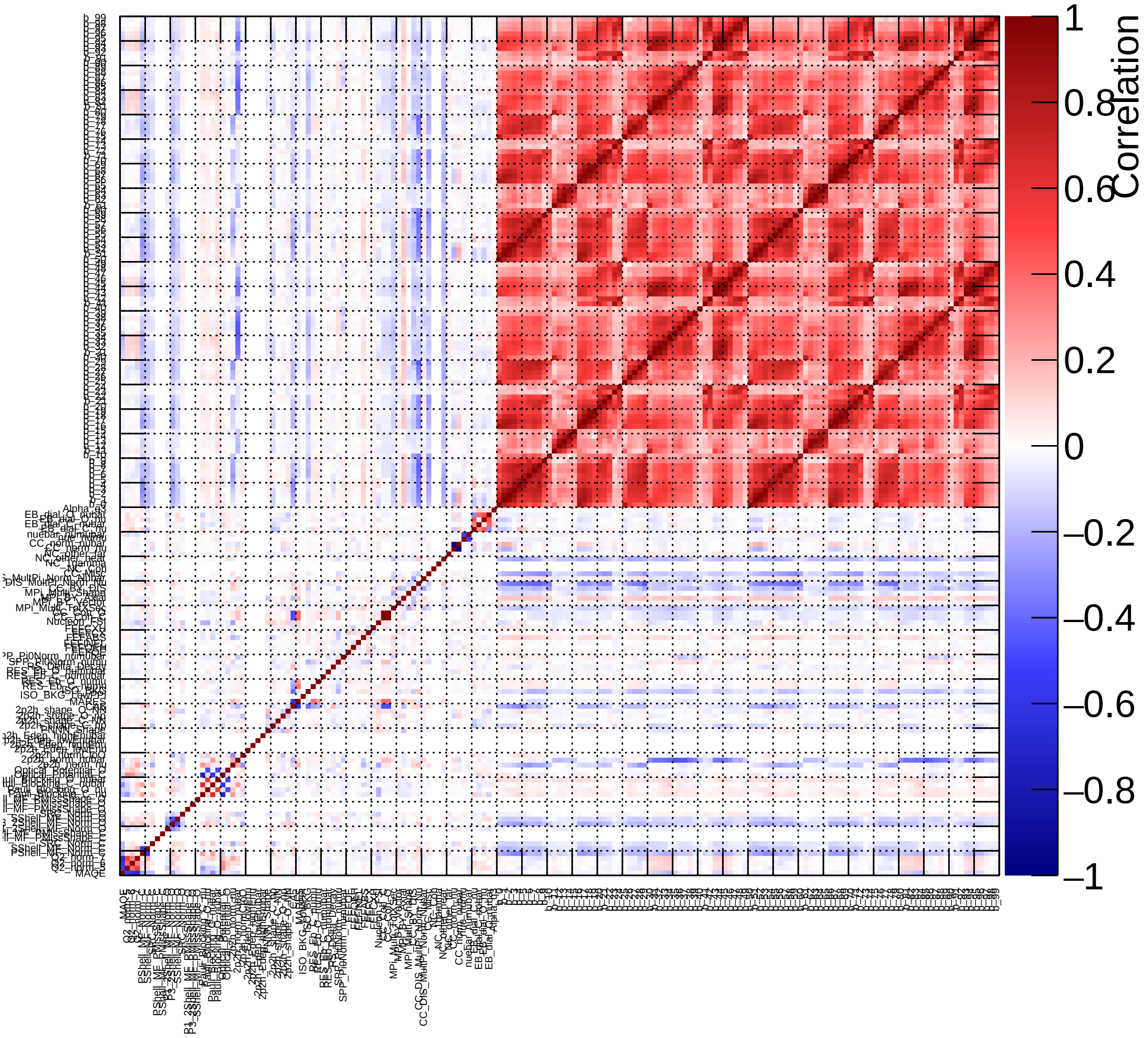

FIGURE 6.10: Postfit cross-section and flux correlation matrix from the data fit.

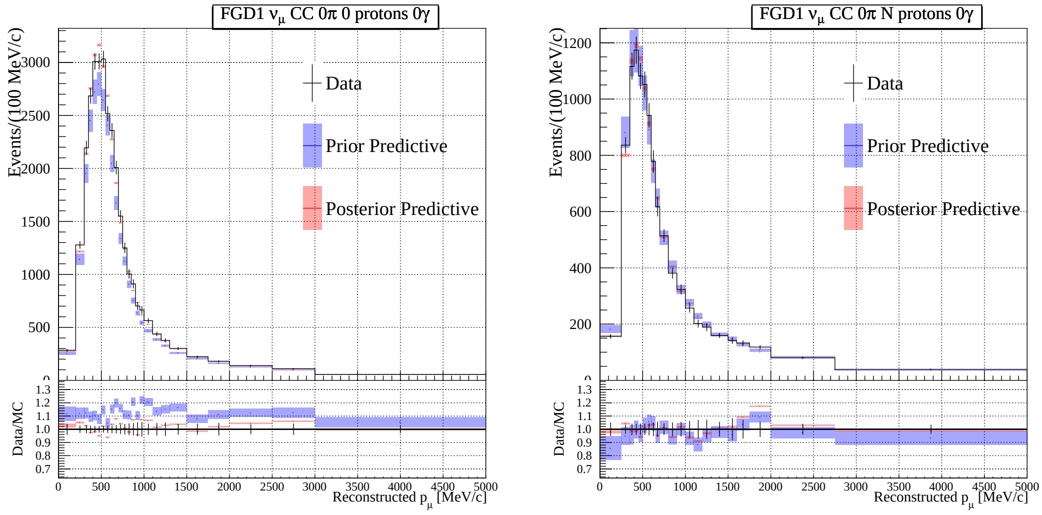

(A) FGD1 FHC CC0π-0p-0γ (B) FGD1 FHC CC0π-Np-0γ

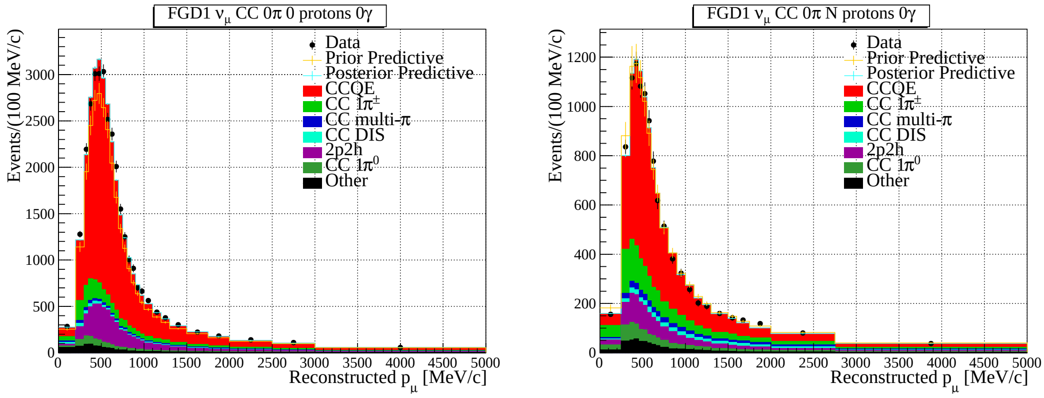

(C) FGD1 FHC CC0π-0p-0γ (D) FGD1 FHC CC0π-Np-0γ

FIGURE 6.11: Prior and posterior predictive distributions for FGD1 proton-tagged samples. Top plots include the comparison of the prior and posterior systematic errors and contain panels with the data to MC ratios. Bottom plots show the reaction breakdown.

lowest postfit systematic uncertainty, while the CC-Other-0γ sample has the largest. This is reassuring, as the CC0π-0p-0γ sample has the highest fraction of CCQE events, which are the dominant signal at SK, while the CC-Other-0γ sample is much less important in the analysis, and similar issues were noticed in the past analysis [80].

As it was shown, the ND280 fit significantly reduced the uncertainties of systematic parameters, which resulted in much more precise predictions for ND280 event samples. We expect that a similar reduction should be observed for FD samples.

Sample	Data	Event Rates		$-2\log\mathcal{L}_{\text{Stat}}$	
		Prior	Post.	Prior	Post.
FGD1 FHC CC0π-0p-0γ	21329	18742.2 ± 2191.3	21123.5 ± 136.2	1506.84	707.32
FGD1 FHC CC0π-Np-0γ	9257	9280.5 ± 1074.2	9262.7 ± 85.3	536.63	387.59
FGD1 FHC CC1π-0γ	6224	6542.9 ± 651.2	6310.2 ± 62.7	338.70	316.62
FGD1 FHC CC-Other-0γ	1737	1640.9 ± 172.6	1727.2 ± 26.7	158.00	143.63
FGD1 FHC CC-Photon	11156	10751.9 ± 1083.9	11305.7 ± 94.4	533.50	487.71
FGD2 FHC CC0π-0p-0γ	22935	20144.9 ± 2183.8	22776.7 ± 139.7	1297.96	698.65
FGD2 FHC CC0π-Np-0γ	7373	7653.5 ± 847.0	7497.7 ± 76.0	553.7	339.9
FGD2 FHC CC1π-0γ	5099	5345.9 ± 527.1	5085.7 ± 48.4	312.5	286.6
FGD2 FHC CC-Other-0γ	1620	1571.3 ± 173.1	1592.7 ± 30.3	162.4	151.2
FGD2 FHC CC-Photon	10460	9765.6 ± 974.2	10235.8 ± 86.3	481.2	427.3
FGD1 RHC CC0π	8676	8493.9 ± 915.5	8671.1 ± 78.3	470.3	368.7
FGD1 RHC CC1π	719	712.4 ± 76.3	718.5 ± 13.6	72.0	68.6
FGD1 RHC CC-Other	1533	1408.3 ± 141.8	1479.7 ± 21.9	106.3	100.2
FGD2 RHC CC0π	8608	8187.0 ± 837.9	8505.4 ± 76.3	451.2	368.1
FGD2 RHC CC1π	660	668.0 ± 70.8	681.7 ± 12.9	56.6	56.7
FGD2 RHC CC-Other	1396	1263.3 ± 128.3	1331.0 ± 19.1	102.3	98.0
FGD1 RHC BKG CC0π	3714	3568.4 ± 370.7	3791.4 ± 40.7	167.4	143.2
FGD1 RHC BKG CC1π	1147	1235.9 ± 120.0	1227.4 ± 15.4	63.3	58.9
FGD1 RHC BKG CC-Other	1425	1189.3 ± 120.6	1293.0 ± 18.2	93.7	68.6
FGD2 RHC BKG CC0π	3537	3511.5 ± 350.1	3715.6 ± 40.0	141.36	144.1
FGD2 RHC BKG CC1π	955	987.6 ± 94.9	968.6 ± 12.3	61.30	60.2
FGD2 RHC BKG CC-Other	1334	1124.8 ± 113.6	1200.00 ± 16.5	81.11	61.4
Total	130894	125304.3 ± 11374.4	130502.1 ± 370.0	7748.1	5542.9

TABLE 6.2: Prior and posterior predictive event rates and $-2\log\mathcal{L}_{\text{Stat}}$ based on the data fit.

Sample	$\delta N/N(\%)$ FGD1		$\delta N/N(\%)$ FGD2	
	Prior	Posterior	Prior	Posterior
FHC CC0π-0p-0γ	12.82	0.64	11.50	0.61
FHC CC0π-Np-0γ	12.94	0.92	12.21	1.01
FHC CC1π-0γ	10.62	0.99	10.50	0.95
FHC CC-Other-0γ	11.03	1.55	11.45	1.91
FHC CC-Photon	10.49	0.84	10.35	0.84
RHC CC0π	12.15	0.90	10.87	0.90
RHC CC1π	11.36	1.90	11.28	1.89
RHC CC-Other	10.51	1.48	10.60	1.44
RHC BKG CC0π	11.21	1.07	10.66	1.08
RHC BKG CC1π	10.13	1.25	10.02	1.27
RHC BKG CC-Other	10.42	1.41	10.55	1.37

TABLE 6.3: Fractional uncertainties on the prior and posterior predictive event rates. The total prior uncertainty 9.07% is reduced to 0.28% after the fit.

6.4 Constraining Far Detector Predictions

So far, the posterior predictive distributions for ND280 samples have been discussed, but an identical procedure can be used to build distributions for FD samples, as introduced in Section 2.5. Fig. 6.12 shows the FD spectra of reconstructed neutrino energy before and after applying ND constraints. The error marked by colour bands represents 1σ uncertainty on event rates, originating from ND constrainable systematic errors. However, it does not include the SK detector systematic uncertainties, as here we are interested only in the impact of the ND280 fit. We can see that error reduction is significant. Moreover, we observe changes in the shape of the distributions, in particular, the number of expected events increased in most samples. This is mostly the consequence of the 2σ pull from the prior value for M_A^{QE}.

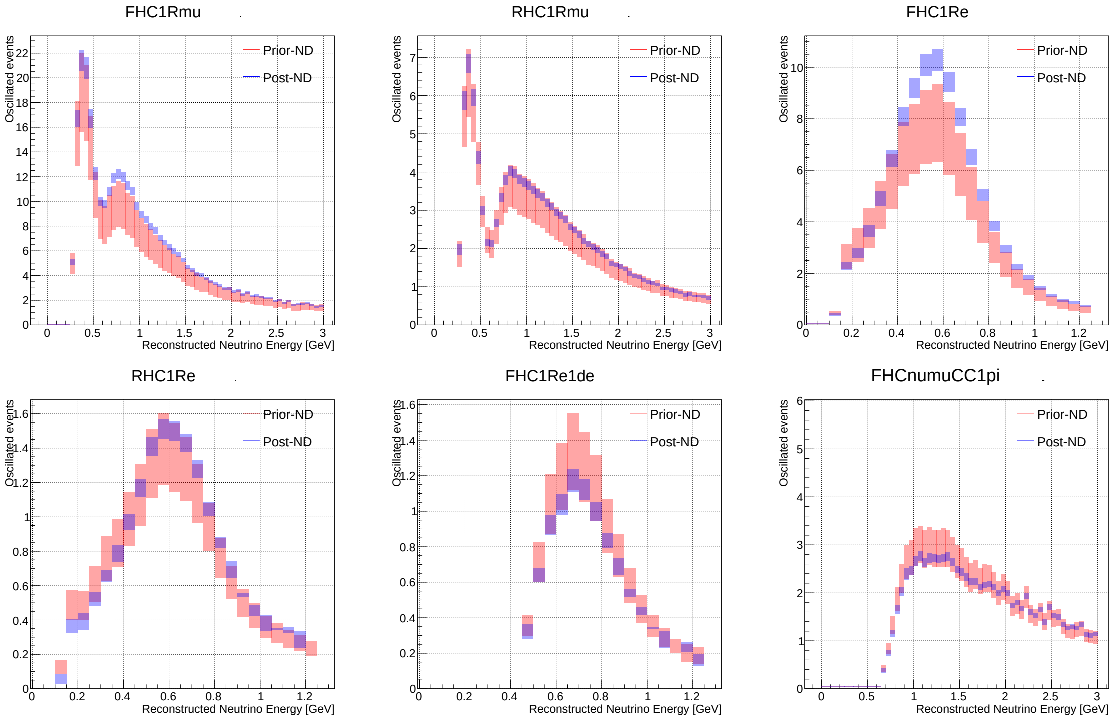

FIGURE 6.12: FD prior predictive (before the ND280 fit, pink) and posterior predictive distributions (after using results from the ND280-only fit, blue). The presented errors come only from ND constrainable parameters.

In Fig. 6.13 we show also the FD spectra but with the SK detector error included. One can notice that there are kinematic regions where the SK systematic error is dominant, such as the low energy region of the 1Rμ samples, while the ND constrainable errors dominate in the tail of those distributions. In other words, in the region where the oscillation effects are most apparent, the ND constraints play a crucial role. Different behaviour is observed for the FHC 1Re1de and ν_μCC1π samples, for which pion secondary interactions in SK become important.

In addition, Tab. 6.4 summarises the errors on predicted event numbers before and after applying ND280 constraints. For example, thanks to ND280 constraints it was possible to reduce the 1Rμ FHC sample uncertainty from 16.7% to 3.4%.

Some cross-section parameters are fixed in the ND280-only fit (like `2p2h Edep`) or have no effect on the ND280 samples, and such are labelled in the Table as *ND unconstr* (unconstrainable by ND280). Among them, the largest uncertainty comes from the ν_e/ν_μ and $\bar{\nu}_e/\bar{\nu}_\mu$ parameters (relative normalisations of electron (anti)neutrino cross-section), since ND280 doesn't have dedicated $\nu_e(\bar{\nu}_e)$ samples.

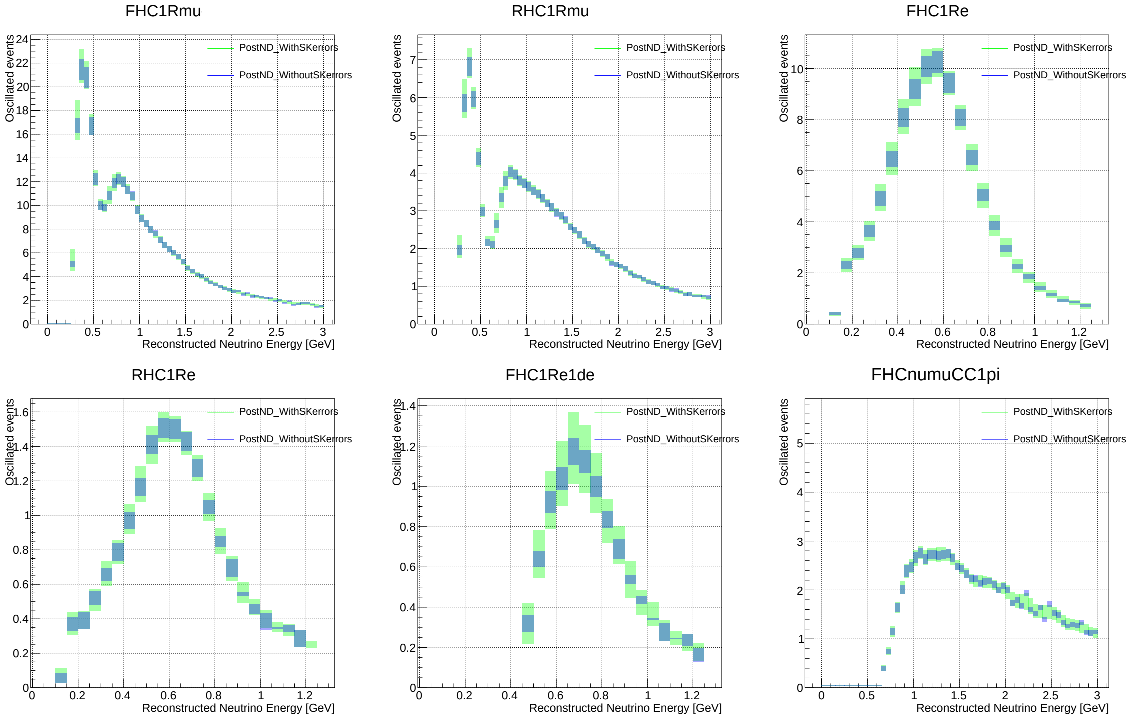

FIGURE 6.13: FD posterior predictive distributions after using results from the ND280-only fit. The green boxes mark the distributions with SK detector errors included additionally.

6.5 Results of ND and FD Joint-Fit

Standalone ND280 fit was validated, and it was shown that it can greatly constrain FD predictions. Now we shall discuss the results of the ND+FD joint analysis.

Appendix A.12 compares the cross-section and flux parameters obtained from the ND280-only and ND+FD fit. The primary conclusion is that including FD samples does not change the results for the parameters to which ND280 is sensitive, so all ND280-based studies are still valid for the ND+FD joint-fit.

Firstly, Fig. 6.14 shows the posterior predictive distributions with overlayed data, after the joint-fit. The overall agreement is quite good; however, the small event statistics at FD is currently the main problem.

Fig. 6.15 (A) shows the posterior probability distribution for δ_{CP} parameter with credible intervals marked by shades of grey. Credible intervals in Bayesian statistics correspond to the probability that the true value of the measured quantity lies within a given interval. We calculate them similarly to HPD by integrating over the distribution until a given percentage is obtained. The main conclusions are that T2K shows preference for maximal CP violation with δ_{CP} close to $-\pi/2$ and excludes the CP conserving values of $\delta_{CP} = 0$ and π with 90% credible intervals.

An additional test was performed to determine the possible CP violation. There are several parameterizations of the neutrino mixing matrix, which lead to different priors on the oscillation parameters. On the other hand, the Jarlskog invariant $J_{CP,l}$ (see Eq. 1.15 on page 9) is independent of the chosen parametrisation, therefore it can demonstrate that the results are driven by the data and not the choice of the prior. We present the results for $J_{CP,l}$ in Fig. 6.15 (B). Two fits were performed, with a flat prior assumed for δ_{CP} or for $\sin \delta_{CP}$, as both choices are equally valid. We observe that the choice of the prior impacts the sensitivity; however, it does not change the physical conclusion, which is T2K preference for maximal CP violation in the lepton sector.

Error source (%)	1Rμ		ν_μCC1π	1Re		1R1de
	FHC	RHC	FHC	FHC	RHC	FHC
Before ND280						
Flux	5.0	4.6	5.2	4.9	4.6	5.1
Cross-section (all)	15.8	13.6	10.6	16.3	13.1	14.7
SK detector	2.6	2.2	4.0	3.1	3.9	13.6
Total	16.7	14.6	12.5	17.3	14.4	20.9
After ND280						
Flux	2.8	2.9	2.8	2.8	3.0	2.8
Xsec (ND constr)	3.7	3.5	3.0	3.8	3.5	4.1
Flux+Xsec (ND constr)	2.7	2.6	2.2	2.8	2.7	3.4
Xsec (ND unconstr)	0.7	2.4	1.4	2.9	3.3	2.8
SK detector	2.0	1.7	4.1	3.1	3.8	13.6
Total	3.4	3.9	4.9	5.2	5.8	14.3

TABLE 6.4: Uncertainty on the expected number of events in each SK sample broken down by error source, before and after the ND280 fit.

Fig. 6.16 outlines credible regions for Δm^2_{32} and $\sin^2\theta_{23}$. As can be seen, T2K has a preference for the upper octant (UO, $\theta_{23} > 0.45°$), but the lower octant (LO) is still within 68% credible intervals. This is currently the most precise measurement of $\sin^2\theta_{23}$. In addition, T2K results weakly prefer the normal mass hierarchy (NH).

To quantify T2K preferences, the Bayes factors were calculated. Bayes factors estimate how one model or hypothesis is more probable with respect to another. In the case of MCMC posterior distributions, one can easily obtain the Bayes factor by calculating the ratio of the number of accepted steps for two hypotheses. The Bayes factors were calculated for θ_{23} upper/lower octant and normal/inverted mass hierarchy hypotheses, and are equal to $\mathfrak{B}(UO/LO) = 3.00$ and $\mathfrak{B}(NH/IH) = 2.85$, respectively. On Jeffrey's scale of Bayes factor interpretation, both would be classified as "barely worth mentioning" [112]. The posterior probability for the normal mass hierarchy is 74%, and the probability of the upper octant is 75%, as can be seen in Tab. 6.5.

	$\sin^2\theta_{23} < 0.5$	$\sin^2\theta_{23} > 0.5$	Sum
NH ($\Delta m^2_{32} > 0$)	0.20	0.54	0.74
IH ($\Delta m^2_{32} < 0$)	0.05	0.21	0.26
Sum	0.25	0.75	1.00

TABLE 6.5: Comparison of posterior probabilities for normal and inverted hierarchies, as well as upper and lower octant hypotheses [111].

To summarize, T2K data indicate a strong preference for maximal CP violation. Also, the results suggest the upper octant for the θ_{23} mixing angle and normal mass hierarchy.

T2K plans to collect more data till 2027; additionally, there is an ongoing development of the NEUT generator. As it was mentioned in Chapter 2.7, the upgrade of the ND280 facility is being conducted and will be completed in 2023. Those improvements will enable new studies that were not possible before.

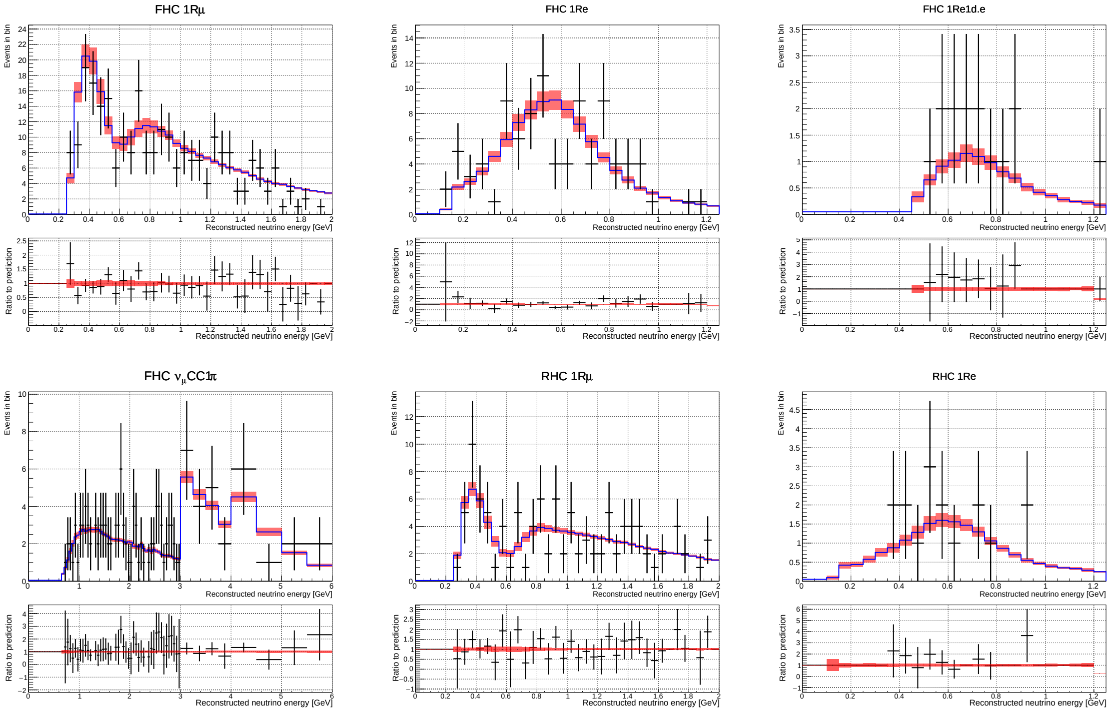

FIGURE 6.14: FD posterior predictive distributions after the ND+FD joint-fit, with overlayed data points. The bottom panels show the data to MC ratios [111].

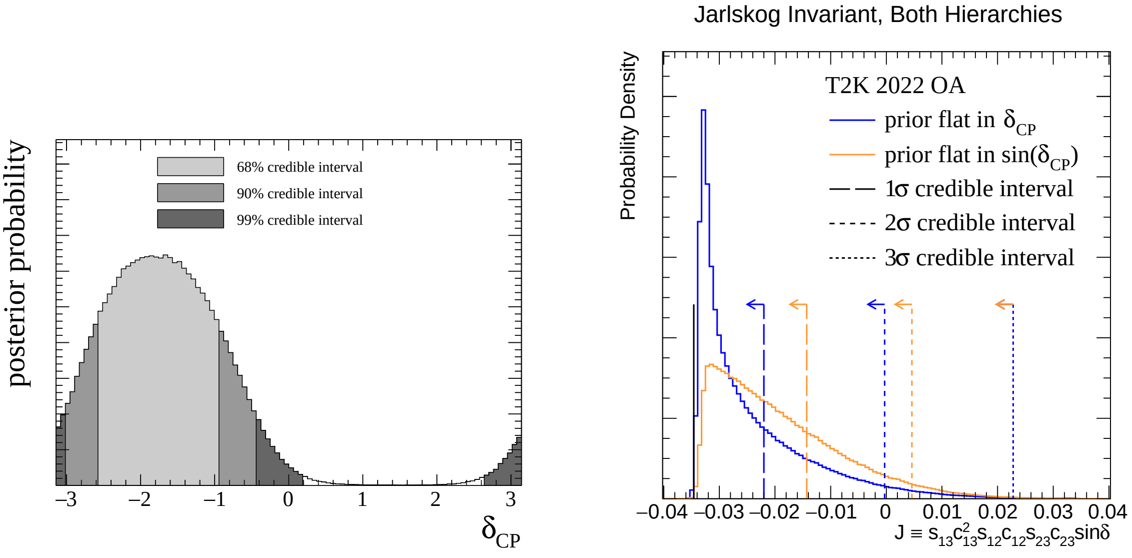

(A) δ_{CP}

(B) $J_{CP,I}$

FIGURE 6.15: Posterior distributions for the δ_{CP} parameter and the Jarlskog invariant with credible intervals [111].

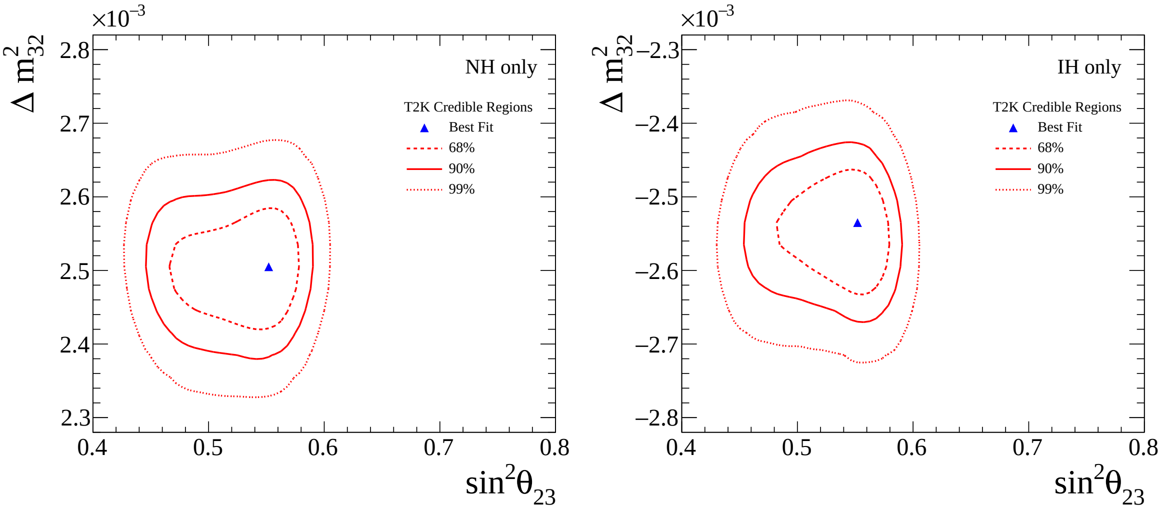

(A) Normal hierarchy

(B) Inverted hierarchy

FIGURE 6.16: Credible regions for Δm^2_{32} and $\sin^2\theta_{23}$ for both hierarchies [111].

7

Future Sensitivity Studies for Proton-Tagged Samples

> At the beginning of a campaign, it is important to consider whether or not to move forward, but when one has taken the offensive it is necessary to maintain it to the last extremity.
>
> **Napoléon Bonaparte**

T2K OA is currently focused on the lepton kinematics. As the neutrino field is moving into the era of precise measurements, it is important to push our understanding of nucleons and neutrino interactions. This Chapter presents the sensitivity studies using proton properties as well as the first look at new event samples from the upgraded ND280. These studies are not part of the official T2K oscillation analysis; however, they are interesting and may pave the way forward for what will be used or performed to make OA more robust.

7.1 Proton Kinematics in ND280

7.1.1 Predictions of Proton Kinematic Variables

The studies presented here use the same event samples, cross-section model, etc. as in previous Chapters; however, the emphasis is placed on protons rather than muons.

Fig. 7.1 shows the posterior predictive distributions of proton momentum and $\cos\theta$[1], obtained by sampling the posterior distribution from the ND280-only data fit, as described in the previous Chapter. Even though the proton kinematics was not used directly in the fit, the posterior predictive distributions are much closer to the data than the prior predictive ones. This indicates that by using the proton-tagged samples, we can probe the kinematical properties of protons indirectly.

By looking at $\cos\theta_{proton}$ distribution, we can observe a data/MC discrepancy, which suggests either a problem with the reconstruction or modelling.

To check if the problem is due to the reconstruction, the posterior predictive distributions for either TPC-matched or isoFGD protons were prepared and are shown in Fig. 7.2. As can be seen, the discrepancy in angular distribution originates from TPC-matched protons. Since TPCs have better granularity than FGDs, we do not expect any major issues with the reconstruction. This might indicate that the problem lies in the modelling of outgoing protons.

Most models include proper theoretical description of outgoing lepton, but the proton kinematics is poorly modelled for several reasons. For example, in the SF model, SRC are

---

[1] Hereafter, often referred to as proton kinematics.

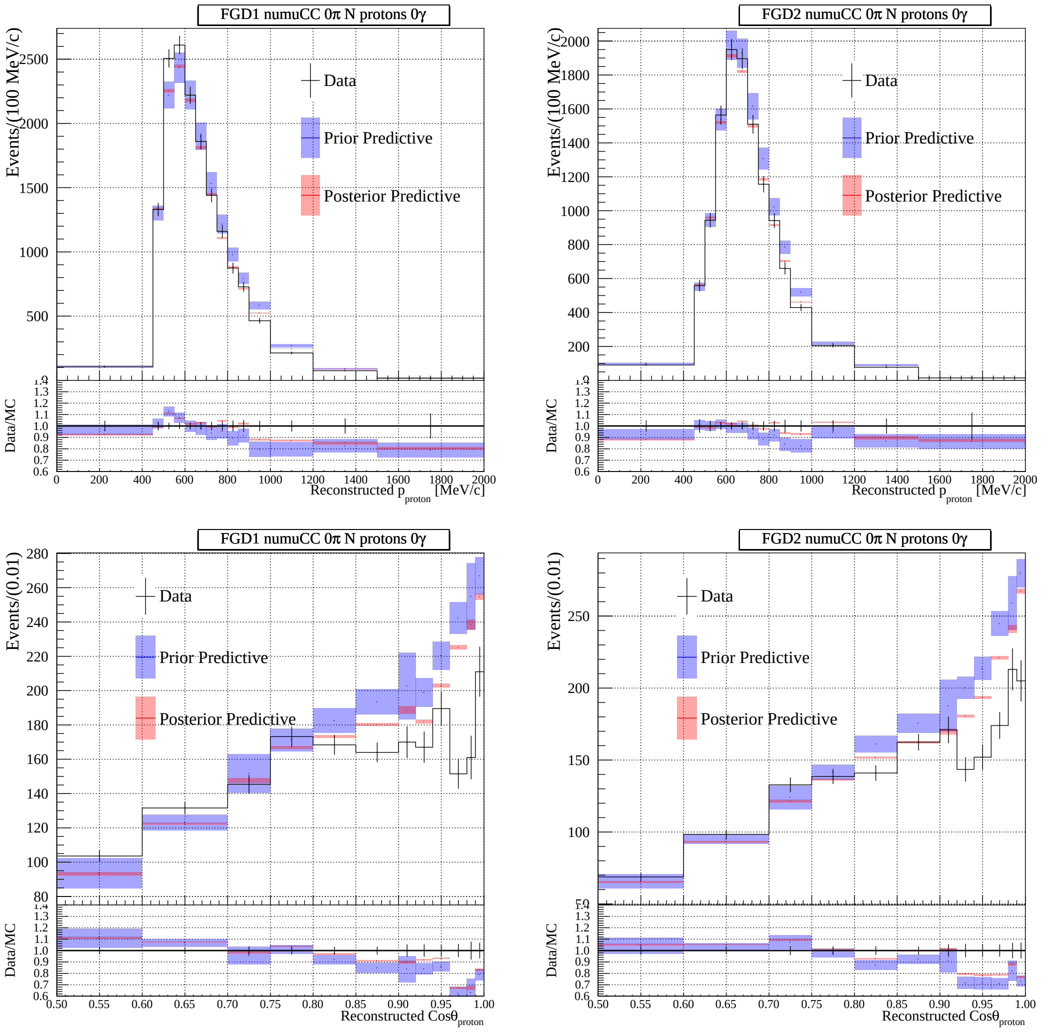

FIGURE 7.1: Prior and posterior predictive distributions of proton kinematics obtained by sampling the posterior distribution from the ND280-only data fit that used only the muon kinematics.

simulated in a back-to-back manner, so correlated nucleons have the same momentum but travel in opposite directions. There is ongoing work by many theorists to improve the state of affairs [57]. Similarly, in 2p2h interactions, the nucleon kinematics is calculated using an isotropic model, which is a good approximation but may not be good enough for high-precision measurements. Finally, 3p3h interactions [36] are not simulated in NEUT at all. In addition, current FSI are simulated using a cascade model. However, recent studies suggest that it only provides reliable predictions for nucleons with momentum above 200 MeV/c and the optical potential approach produces more sensible results [113]. Since the effect of optical potential is only dominant for low momentum nucleons, current ND280 samples are not affected significantly. When it comes to FSI relevant for higher energies, currently deuterons and other heavier nuclear fragments are not included, although there is ongoing work to improve this as well [58]. All the issues mentioned above should be resolved in the future; however, they are not covered by the models used currently.

Nevertheless, we expect that the inclusion of proton kinematics information in the fit can enhance sensitivity to effects like FSI, better probe the SF structure, or improve the understanding of 2p2h. Therefore, in spite of imperfect modelling, the next Section is devoted to the prospects of using proton kinematics in the ND280 fit, as we expect that models will be improved in the future.

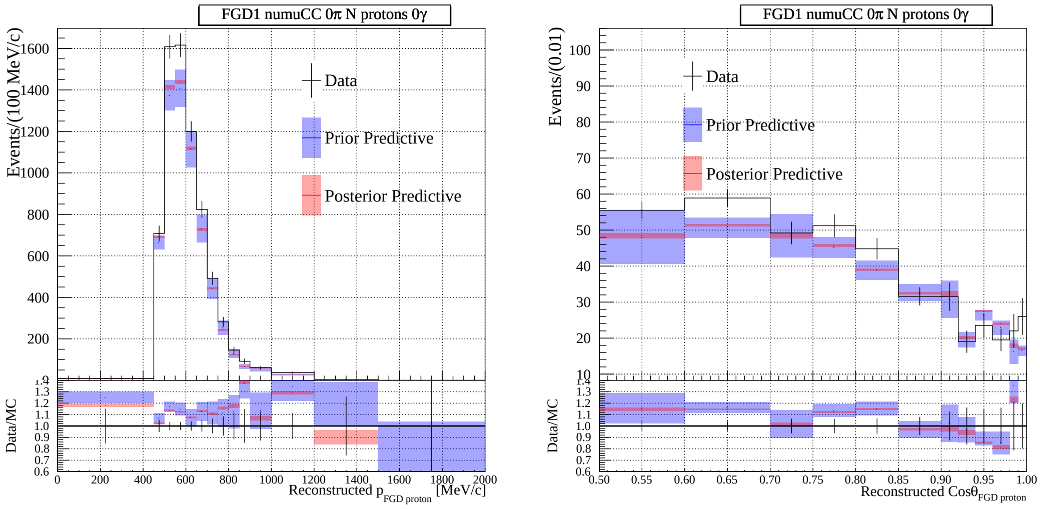

(A) isoFGD proton (B) isoFGD proton

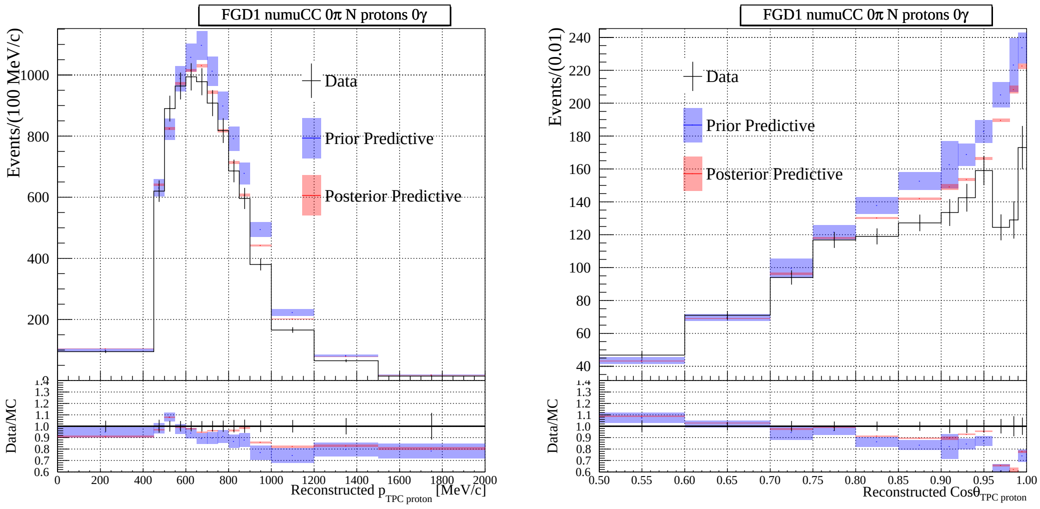

(C) TPC-matched protons (D) TPC-matched protons

FIGURE 7.2: Prior and posterior predictive distributions of proton kinematics (of either isoFGD or TPC-matched protons) obtained by sampling the posterior distribution from the ND280-only data fit that used only the muon kinematics.

7.1.2 Binning, Transverse Kinematic Variables and Preliminary Sensitivity

Adding even a single variable to the fit requires significant framework changes as well as demands the construction of a multidimensional binning. Thus, it was decided to use three-dimensional binning for FGD1 (FGD2) CC0π-Np-0γ, with muon momentum, $\cos\theta_\mu$, and a third additional variable, while keeping the variables and the binning for the remaining samples unchanged. By using the same muon-related variables, it is possible to make the comparison with the official ND280 analysis.

The natural candidate for a proton-related variable is the proton momentum. However, to produce a proper binning for this variable, it was necessary to study the momentum reconstruction accuracy, as it was performed for proton-tagged samples (see Section 3.2.3). The comparison of true and reconstructed proton momentum can be seen in Fig. 7.3. As can be observed, the reconstruction accuracy is quite stable, but only above 400 MeV/c; as below this threshold, proton reconstruction is unreliable.

As a consequence, we decided to consider another variable. Based on the study presented

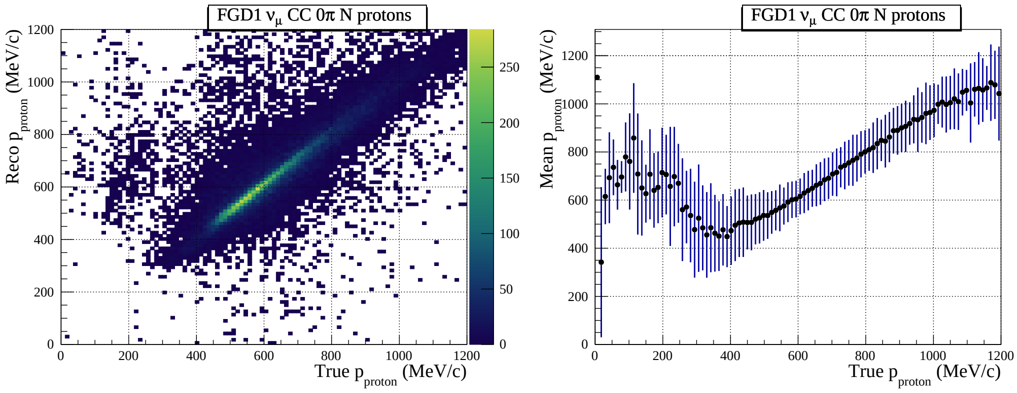

FIGURE 7.3: Reconstruction accuracy of proton momentum in CC0π-Np-0γ FGD1 sample.

in [114], transverse kinematic variables, in particular the transverse kinematic imbalance δp_T (see Fig. 7.4 for definition), seemed promising. This variable is sensitive to FSI. If energy and momentum are conserved, δp_T should be close to 0 for CCQE, while FSI distort final proton kinematics and pull this variable away from 0.

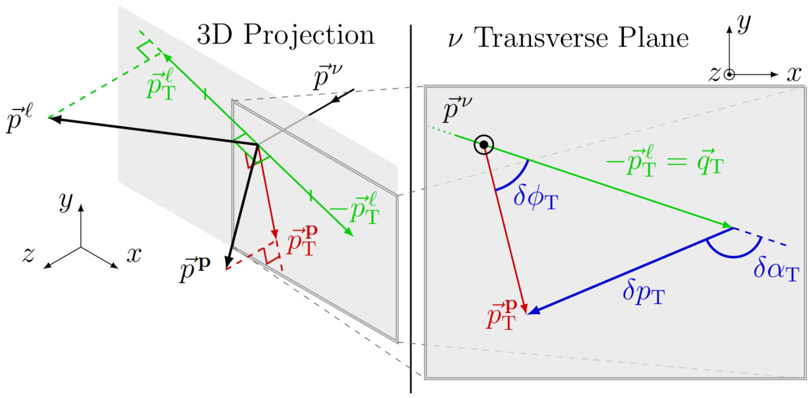

FIGURE 7.4: Schematic definition of transverse kinematic variables, most notably δp_T (blue), in CCQE neutrino interaction [115].

Fig. 7.5 shows the reconstruction accuracy for δp_T, and it is very stable, without any significant drop, only minor fluctuations can be seen above 1000 MeV/c, where we have much smaller event statistics. Since there are no problems with δp_T reconstruction accuracy, it can be used in the analysis.

Fig. 7.6 presents the prior predictive distribution for δp_T. We can see some data/MC disagreement, although not as striking as for $\cos\theta_{proton}$. In addition, we can notice that the highest fraction of CCQE events is close to $\delta p_T = 0$, while other reactions become more apparent at higher δp_T values.

Since δp_T has a characteristic stairs-like structure, only four bins (the last bin goes from 1200 to 20000 MeV/c) should be enough to describe its variation. Increasing the number of δp_T bins would result in decreasing the number of bins for p_μ and $\cos\theta_\mu$, as each bin must contain at least 1 data and 20 MC events. Fig. 7.7 shows the one-dimensional projections from the three-dimensional kinematic distribution for the FGD1 CC0π-Np-0γ sample for data. The same binning is used for FGD1 and FGD2 samples.

Fig. 7.8 displays the LLH scan comparison and overlay of posterior distributions from the Asimov fit using only muon kinematic variables and another one using additionally δp_T

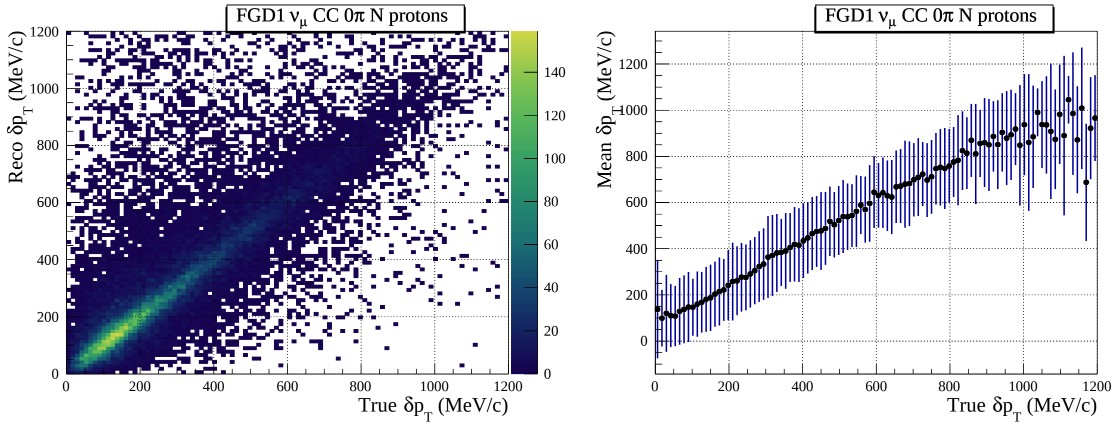

FIGURE 7.5: Reconstruction accuracy of the δp_T variable in FGD1 CC0π-Np-0γ sample.

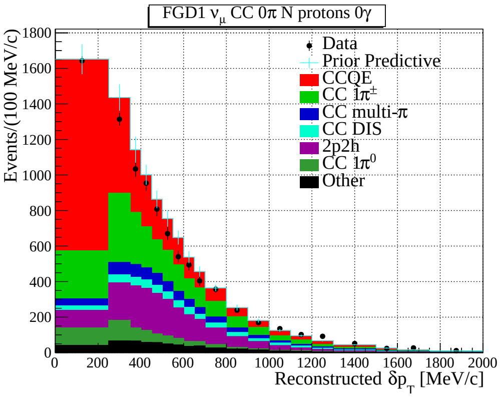

FIGURE 7.6: Prior predictive distribution for δp_T with colours marking different reactions.

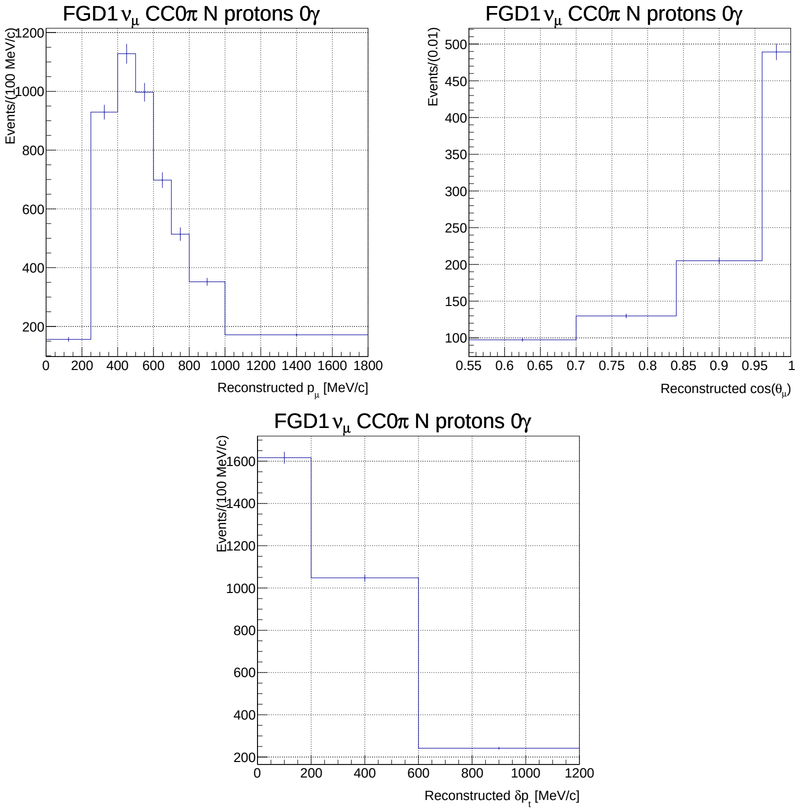

FIGURE 7.7: One-dimensional projection of three-dimensional kinematic distribution for FGD1 CC0π-Np-0γ for data.

variable for N-proton samples. Here, as well as in the following studies, only selected parameters are shown, for which we expect a change or, for cross-check, which should remain unaffected. Firstly, plots (A) and (D) show results for the Pauli blocking parameter, for which we do not observe almost any improvements when using δp_T, both in the LLH scan and posterior distributions. As we don't expect an increased sensitivity to that parameter, this confirms the validity of the results. Plots (B) and (E) show analogous results for nucleon FSI. It can be noticed that using δp_T increases the sensitivity to the nucleon FSI parameter, which is true both for LLH and Asimov fit results. As demonstrated by plots (C) and (F), using δp_T enhances slightly also the sensitivity to 2p2h-related parameters, as when calculating δp_T we include only the highest momentum proton, which can be interpreted as a distortion of this variable distribution.

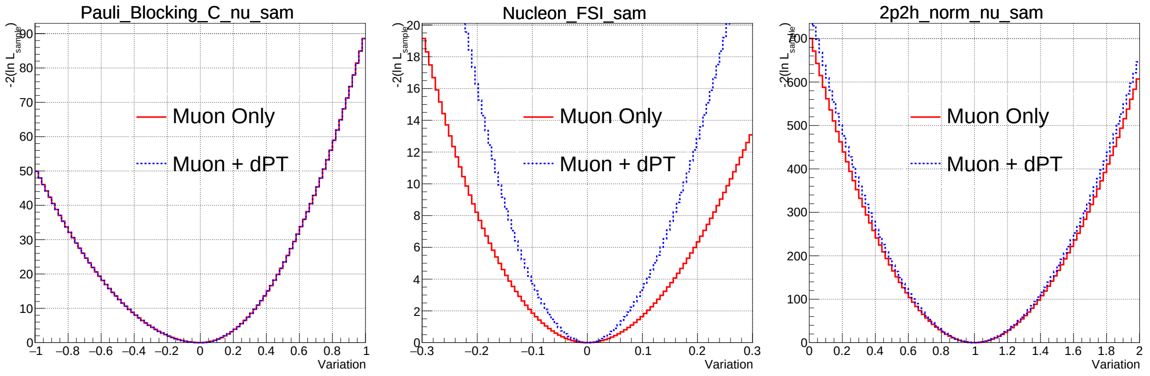

(A) Pauli blocking ^{12}C ν (B) Nucleon FSI (C) 2p2h norm ν

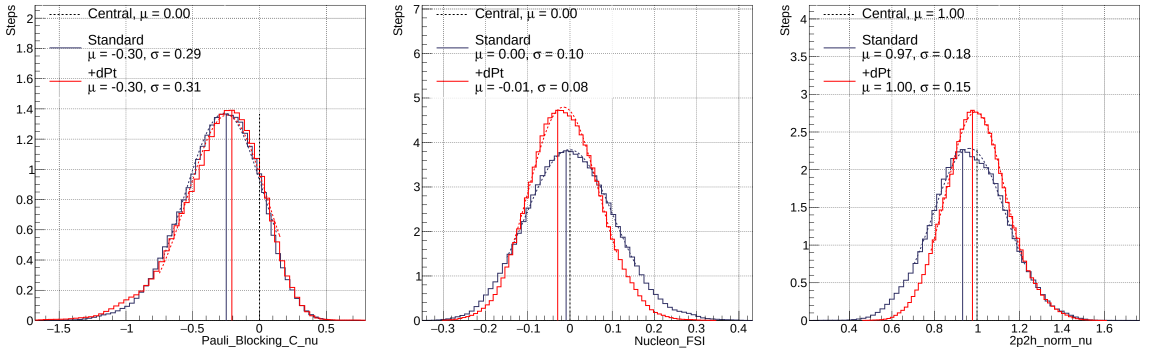

(D) Pauli blocking ^{12}C ν (E) Nucleon FSI (F) 2p2h norm ν

FIGURE 7.8: Selected LLH scans and Asimov fit posterior distributions using the standard fit with muon kinematics only and the improved one with additional δp_T variable.

Since the LLH scans and Asimov fits are sensible and show an increase in sensitivity, we can proceed with the data fit.

7.1.3 Data Fit Results and Impact of Proton Kinematic

Data fit results for selected parameters are presented in Fig. 7.9. When looking at (A), it can be observed that for Pauli blocking, the results have not changed. Since Pauli blocking affects mostly CC-0π-0p-0γ samples and an additional variable is used only in CC-0π-Np-0γ samples, we would not expect a change in the posterior distribution of this parameter. On the other hand, the posterior distributions for nucleon FSI, `2p2h norm` or `PNNN shape` dials, which affect proton kinematics, are shifted with respect to the official ND280 analysis. Moreover, we observe the error reduction for these parameters, in case of nucleon FSI it is reduced further from $\sigma = 0.13$ to $\sigma = 0.08$. The differences in posterior distributions are expected because of the inclusion of δp_T information and the data/MC disagreement in the $\cos\theta_{proton}$ (related to δp_T) distribution shown in Fig. 7.1, which the fitter is trying to reduce. Nevertheless, the posterior distributions partially overlap in all cases, so we can conclude that the results are still compatible.

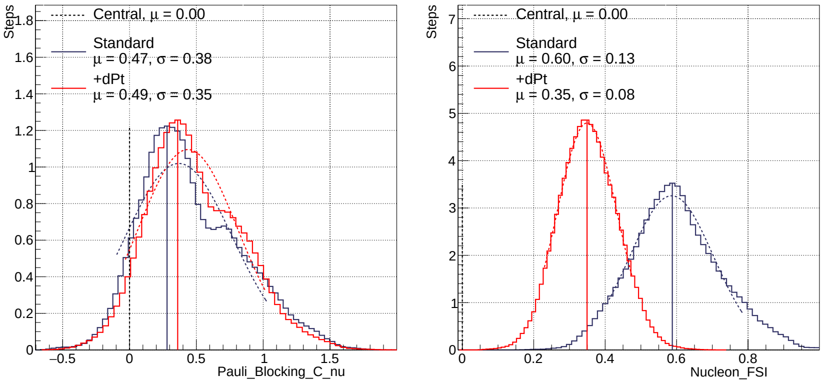

(A) Pauli blocking ^{12}C ν

(B) Nucleon FSI

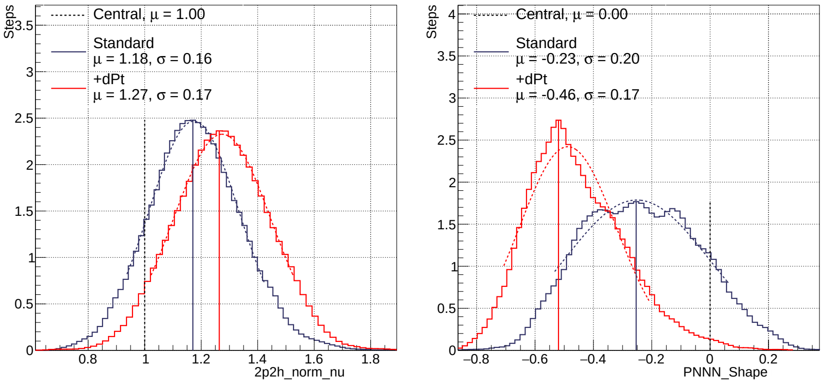

(C) 2p2h norm ν

(D) PNNN shape

FIGURE 7.9: Selected posterior distributions from the standard data fit with muon kinematics only and the improved one with additional δp_T variable.

Fig. 7.10 presents the overlay of prior and posterior predictive distributions for FGD1 CC-0π-Np-0γ sample. We can see better agreement in most bins.

The posterior predictive distributions for the same sample from the official ND280 analysis and from the fit using δp_T are compared in Fig. 7.11. We can see that the p_{proton} data/MC agreement is comparable for the two fits. Since the agreement was satisfactory after the official ND280 fit, we didn't expect much improvement here. However, the agreement for $\cos\theta_{\text{proton}}$ is significantly better. This naively demonstrates that using proton kinematics can help to constrain the nuclear effects; however, due to current poor modelling of proton kinematics and not available sufficient systematic model, it is not possible to fully exploit this fact.

Better understanding and utilisation of nucleon information is important for the gadolinium-doped SK detector, as the nucleon information will become an important input. Since the upgraded ND280 with improved reconstruction capabilities will be able to detect protons with much lower momentum, we can expect much more precise measurements of interactions with proton production. In particular, there are already plans to perform dedicated cross-section measurements using the upgraded ND280, which should aid theorists with model development.

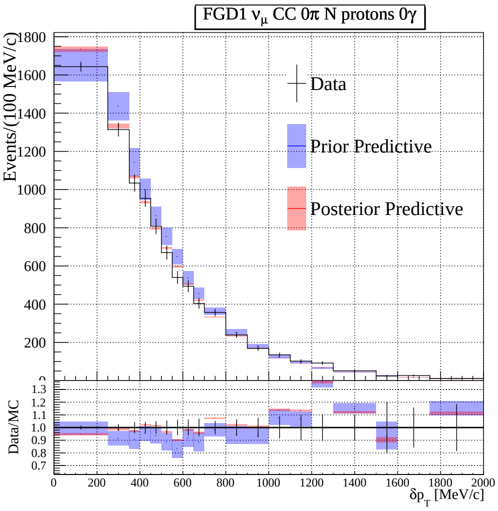

FIGURE 7.10: Overlay of prior and posterior predictive distributions for FGD1 CC-0π-Np-0γ sample, based on the fit with additional δp_T variable.

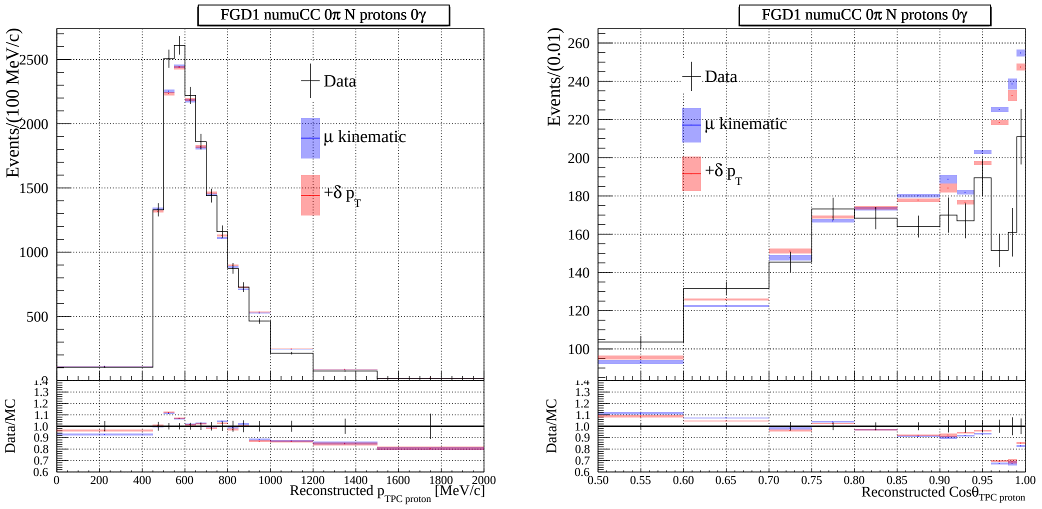

FIGURE 7.11: Posterior predictive distributions of proton kinematics for FGD1 CC-0π-Np-0γ sample from official ND280 analysis and the fit with additional δp_T variable.

7.2 Sensitivity Study Using Preliminary Simulation of Upgraded ND280

7.2.1 SFGD Samples

As discussed in Section 2.7 on page 29, there is an ongoing upgrade of the beam and, more importantly, of the ND280 detector. Here we will discuss the expected sensitivity of the upgraded ND280. By the time the Thesis was complete, the full detector simulation was not yet available. A GEANT4-based simulation of the new detector already exists, and, thanks to various measurements of the new detector components at test beams at CERN [77, 116] and DESY [117], the preliminary expected detector response can be assumed. The main reconstruction effects, such as momentum smearing and resolution, have been parameterised and applied to NEUT simulated true variables used in the following analysis[2].

For the beginning, we will consider only two samples of events originating from the SFGD sub-detector, namely CC0π-0p and CC0π-Np, as due to the incomplete reconstruction algorithm, they are most reliable. Later, we will discuss other samples as well. In the previous Sections, it was shown that the current cross-section models are not able to reliably predict proton kinematics; hence, in the presented SFGD study, we use only muon kinematics for all samples.

Fig. 7.12 shows the expected spectra for two SFGD samples. If we compare them with analogous distributions for FGD1 and FGD2 samples (see Fig. 6.11), we can see that the breakdown of interactions is similar and the momentum distributions look sensible. Thus, using a simplified reconstruction should be sufficient for such studies.

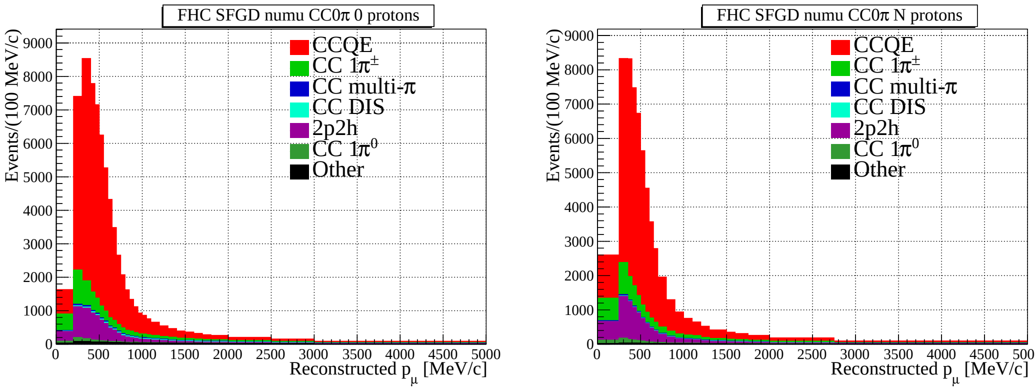

FIGURE 7.12: Expected momentum distributions for SFGD samples as a function of p_μ. Colours denote different reaction modes.

Tab. 7.1 presents the expected event rates depending on accumulated POT. As can be observed, the upgraded ND280 will significantly increase ND280 data statistics (compare to Tab. 6.2), as SFGD FHC CC0π-0p is expected to collect $\sim$50112 events, whereas its FGD1 counterpart, FHC CC0π-0p-0γ, currently contains 21329 data events. Such event rates are the consequence of the SFGD mass being twice as big as that of one FGD. Additionally, SFGD has better acceptance for particles travelling at high and backward angles with respect to the neutrino beam; thus, we expect more than doubling of data statistics with a comparable number of POT. Another important conclusion is that the event rates for the SFGD CC0π-0p and CC0π-Np samples are much more alike, while in the case of FGD1 and FGD2, there

---

[2] The simulated events are exactly the same as used and described in [114].

are roughly two times more events in CC0π-0p samples than in CC0π-Np. This is the consequence of the lower threshold for proton reconstruction in SFGD with respect to FGD1(2) (see Fig. 2.19 on page 31).

Sample	POT 1.08×10^{21}	 2.4×10^{21}
SFGD FHC CC0π-0p	50111.8	94655.7
SFGD FHC CC0π-Np	47337.2	89414.7

TABLE 7.1: Expected event rates for SFGD proton-tagged samples with different assumed POT numbers.

7.2.2 Angular Acceptance and Binning for Upgraded ND280 Samples

Since we are going to use new samples with improved acceptance, it is necessary to repeat the study of momentum and angular reconstruction accuracy. Fig. 7.13 presents the reconstruction accuracy for the SFGD sample. As already mentioned, the final reconstruction is not ready yet (when the Thesis was written), so the reconstruction accuracy might be over-optimistic in some regions. Nevertheless, it should be sufficient for the study presented here and give an idea of the improvement we can expect from the new sub-detectors. For comparison, the reconstruction accuracies for the FGD1 sample are presented in Fig. 3.13 on page 45.

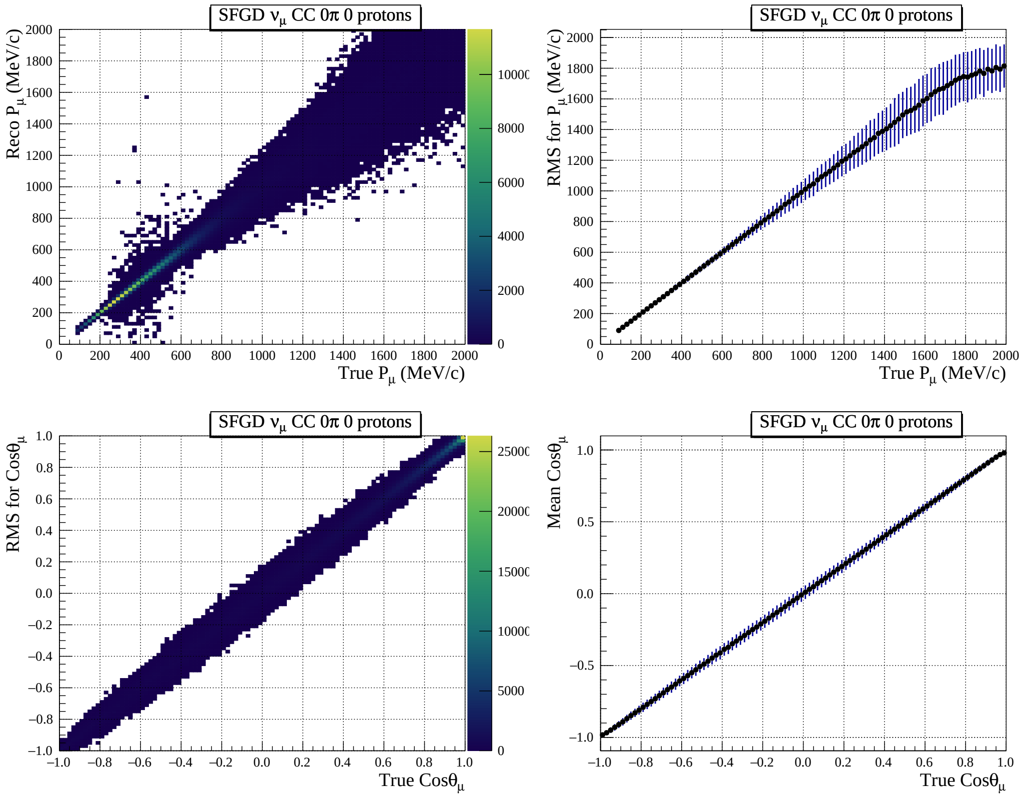

FIGURE 7.13: Reconstruction accuracy of SFGD for muon momentum and emission angle.

The upgraded ND280 will have much better capability to reconstruct particles travelling at high scattering angles. Therefore, it is necessary to use different binning than for the FGD samples. Fig. 7.14 compares the standard FGD binning with uniform and coarse bins in backward region (A) and the improved binning designed for the SFGD samples[3] with non-uniform bins (B). Backward going muons tend to have in general much lower momentum, as can be seen in Fig. 7.15, showing muon kinematics distributions for the SFGD samples using non-uniform binning. In the same Figure, we can see Q^2 lines visually marking the value of true Q^2 and demonstrating that in the region of backward going muons, we have mostly events with higher Q^2, therefore we could expect enhanced sensitivity to high Q^2 physics.

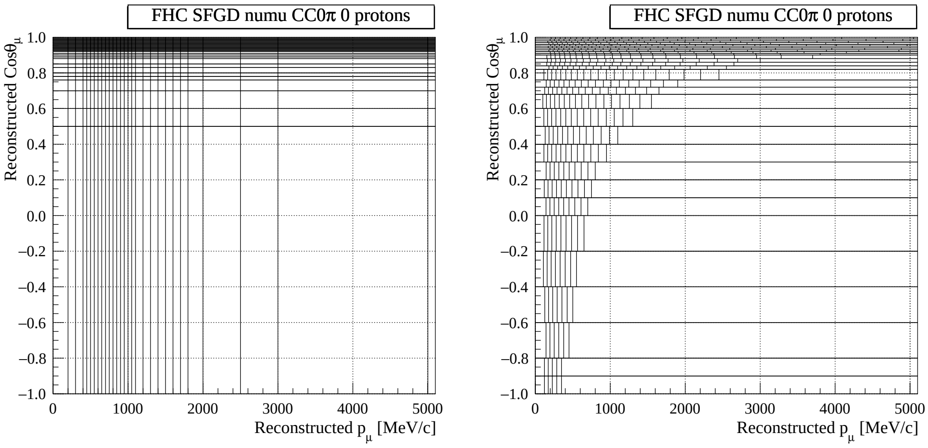

(A) Uniform binning (B) Non-uniform binning

FIGURE 7.14: Examples of uniform and non-uniform binning, the latter giving much more freedom in the backward going muon region.

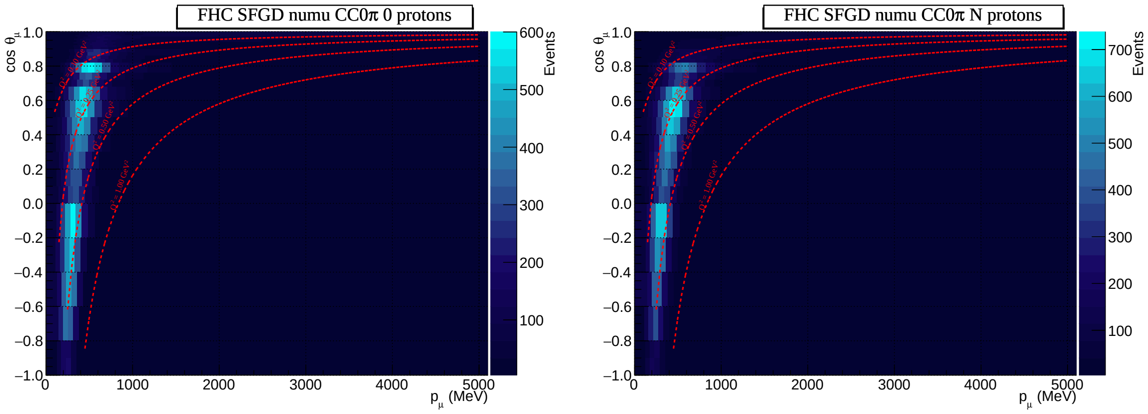

FIGURE 7.15: Event rate distribution for SFGD samples using non-uniform binning. The colour scale represents the number of events in one bin. The effect of the discontinuity in the low momentum region at $cos\theta \approx -0.2$–0 is related to the change in bin size.

To better understand the impact of events with muons scattered at high angles, a special test was performed, in which we extracted the event kinematic distribution for prior values of parameters and another distribution with one parameter moved by 3σ from the prior value, and calculated the ratio of both distributions. Examples of such plots can be seen in Fig. 7.16. Two top plots show the impact of the same dial (`High` Q^2 `norm 2`): the left one for events in FGD1 and the right one for events in SFGD. At least two conclusions can be drawn. Firstly, in the backward going muon region, the shape is much smoother for SFGD, so it should be possible to probe not only the normalisation changes but also the shape changes, which is

---

[3] Using TH2Poly implementation from the ROOT package [93].

much more difficult with FGD samples. Secondly, on the top right plot, in the case of SFGD there are barely any changes, while for the FGD1 sample there are visible differences. This is because the `High` Q^2 `norm 2` parameter affects the event rates based on the true Q^2 of an event, whereas the plots show the effect as a function of reconstructed variables. Since SFGD has much better reconstruction accuracy, the affected region is much more condensed.

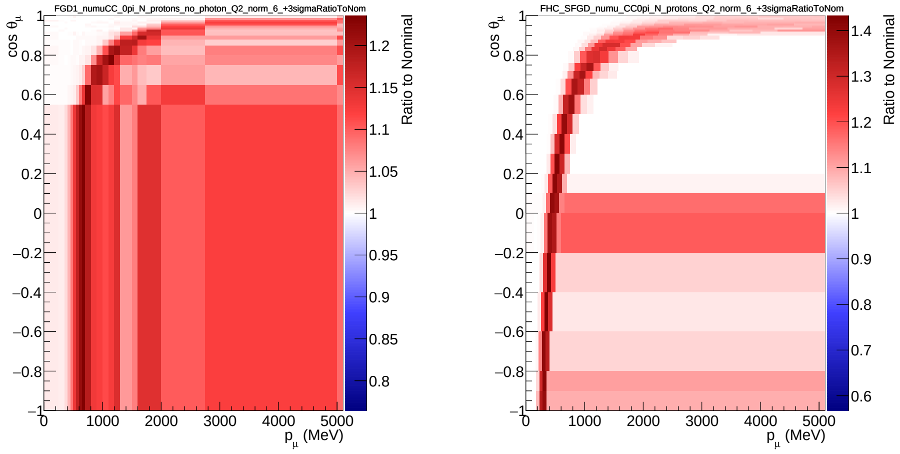

(A) High Q^2 norm 2 at FGD1

(B) High Q^2 norm 2 at SFGD

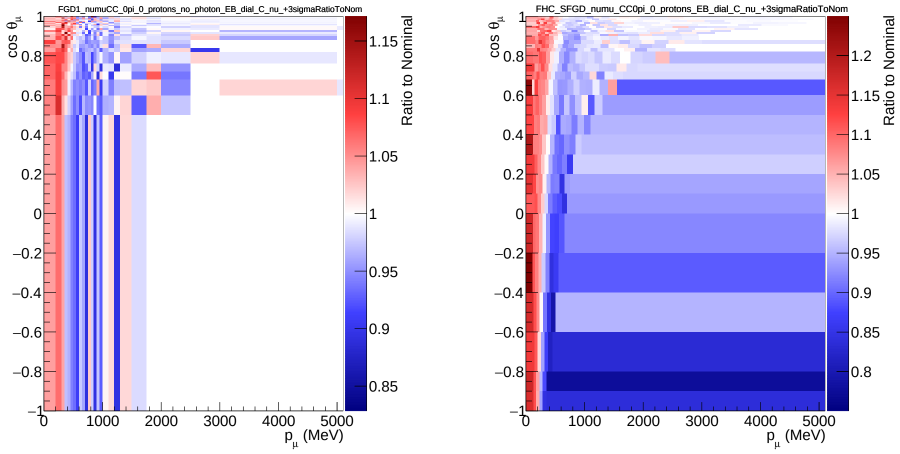

(C) CCQE E_b ^{12}C at FGD1

(D) CCQE E_b ^{12}C at SFGD

FIGURE 7.16: Impact of +3σ variation for selected FGD1 and SFGD samples for two dials benefitting from the enhanced acceptance for backward going muons.

Furthermore, the bottom plot on Fig. 7.16 demonstrates the impact of the CCQE E_b dial. This dial is shifting events from the region of higher momentum to that of lower momentum; hence, we observe the reduction of events above 600 MeV/c and the increase below it. For the SFGD sample, thanks to finer binning and resolution, more distinct separation is observed, manifesting as a white band. It clearly demonstrates visually what sensitivity enhancements we can expect from the upgraded ND280.

7.2.3 Evaluating Upgraded ND280 Sensitivity

In this Section, we further demonstrate the improvements from the upgraded ND280. The assumption in these studies is that the FGD samples remain the same (as in Chapter 6, and only the SFGD samples are added with different POT values, corresponding to those in Tab. 7.1.

LLH scans for selected parameters are presented in Fig. 7.17. Here, as well as in the following studies, only selected parameters are shown, for which we expect a change or, for cross-check, which should remain unaffected. Thanks to better reconstruction accuracy, the region affected by Pauli blocking is more condensed, resulting in better constraints. We can see a significant improvement for the `High` Q^2 `norm 2` dial, which is an expected result given the discussion of sigma variation in Fig. 7.16. No improvement is observed for the `M`π `Multi TotXSecFor` dial, which is also expected given the DIS-enriched samples are not used so far. Lastly, for the `SRC Norm` ^{16}`O` parameter, there is no difference, since SFGD is a purely carbon-based detector and we do not foresee any constraints on parameters related to ^{16}O, which is an important result from the validation point of view.

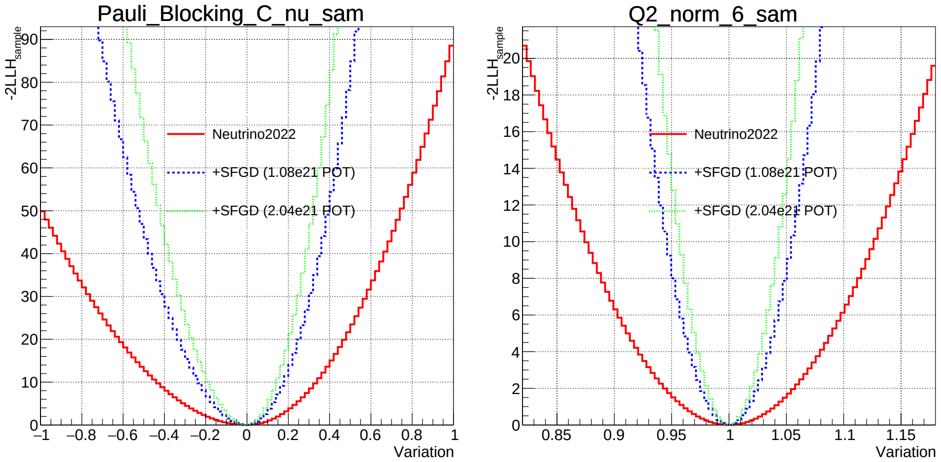

(A) Pauli blocking ^{12}C ν (B) High Q^2 norm 2

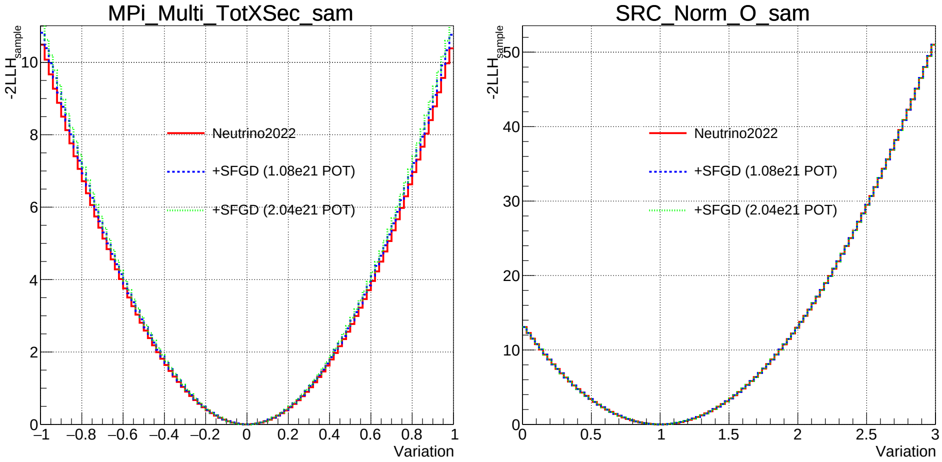

(C) Mπ Multi TotXSec (D) SRC Norm ^{16}O

FIGURE 7.17: LLH scans comparing the sensitivities obtained using samples the from official ND280 analysis and after including SFGD samples with two POT assumptions.

A question arises, how much of the improved sensitivity comes from bigger event statistics and how much from better capabilities of SFGD. To answer that, the following study was conducted: an LLH scan was performed using only FHC samples for FGD1 and FGD2, while in the second one only SFGD samples were used, with the same POT number as that of FGD samples. The results are presented in Fig. 7.18. For CCQE parameters (in this case, Pauli blocking and `High` Q^2 `norm 2`), the SFGD samples show better performance, which is a consequence of better acceptance and resolution. However, the results for RES and FSI-related parameters (C_A^5, π `FSI QE low E`) demonstrate that the FGD samples give better results. As previously stated, only the CC0π SFGD samples are used in this study; hence, the lower sensitivity is expected, in addition confirming the validity of the analysis. Nevertheless, the final sensitivity should not be judged negatively based on those results.

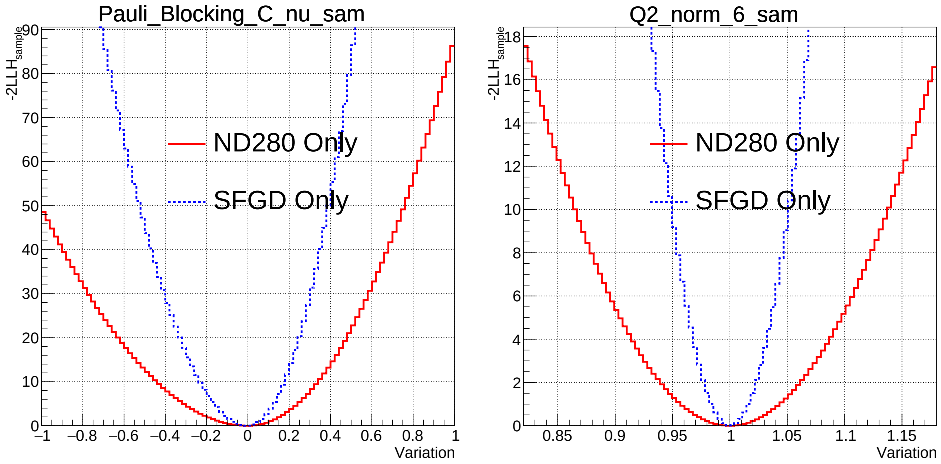

(A) Pauli blocking ^{12}C ν

(B) High Q^2 norm 2

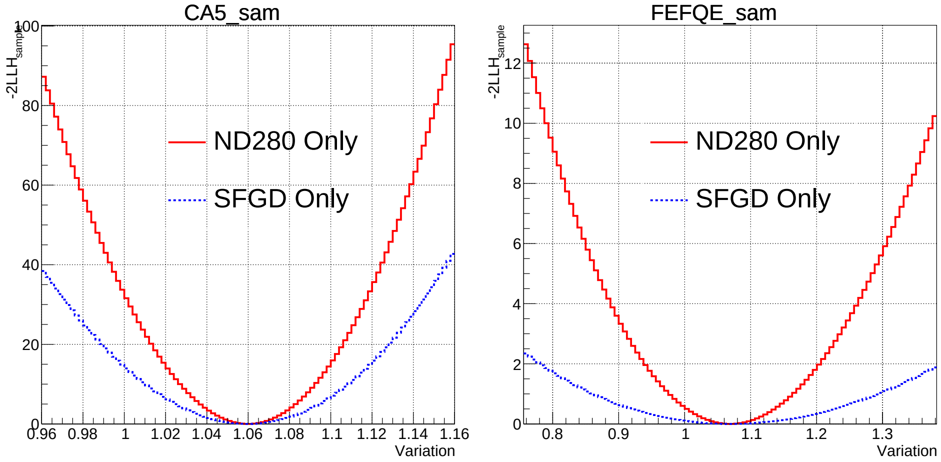

(C) C_A^5

(D) π FSI QE low E

FIGURE 7.18: LLH scans comparing the sensitivities obtained using only FGD1 and FGD2 FHC samples and using only SFGD samples with the same POT number as in the official ND280 analysis.

LLH scans in Fig. 7.18 show significant improvement; however, as always, the best way to have a complete picture is to run a fit. Based on the Asimov fit results, the FD predicted spectra were produced, which can be seen in Fig. 7.19. The effect may look slightly disappointing at first. To better understand it, one has to look at individual posterior distributions from the Asimov fit, which are shown in Fig. 7.20. It can be seen that the Pauli blocking parameter for ^{12}C is significantly constrained, while the analogous parameter for ^{16}O is not. As was already mentioned, SFGD is carbon-based; hence, it does not constrain dials related to ^{16}O. Since SK is a water-based detector, it is no surprise that we do not see such great improvement in the spectra in Fig. 7.19. On the other hand, Fig. 7.20 presents also the posterior distributions for CCQE E_b parameters, and the dial for ^{16}O is better constrained in the Asimov fit, which used the SFGD samples. As discussed in Section 4.4[4], CCQE E_b parameters have high initial correlations. In consequence, the increase in the sensitivity for `CCQE` E_b ^{16}`O` ν is driven purely by strong ^{12}C/^{16}O correlations.

Since the results suggest that the correlations can help better utilise the upgraded ND280 for oscillation analysis, it is worth considering that more thoroughly.

---

[4] See Fig. 4.12 on page 61.

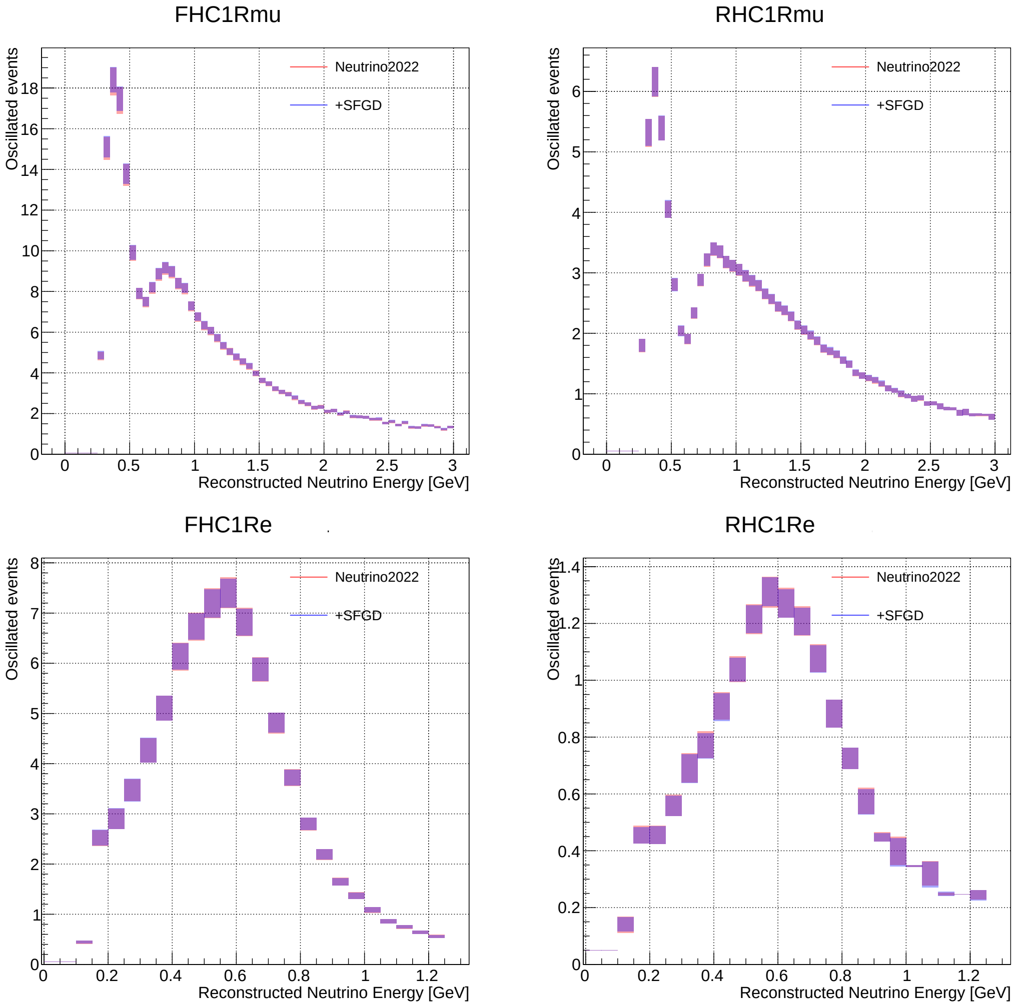

FIGURE 7.19: Selected FD posterior predictive distributions before and after adding SFGD constraints from the Asimov fit.

7.2.4 Carbon-Oxygen Correlation Study

First, let's discuss how the correlations are obtained. They come from external measurements; for example, the correlations for SPP dials like C_A^5 and M_A^{RES} are extracted from a fit to ANL and BNL data [46], while for CCQE E_b parameters electron scattering data are used [118].

In the first instance, let's consider if it is a viable option to use the postfit correlations from the ND280-only analysis in the upgraded ND280 Asimov fit. Fig. 7.21 shows the correlations for blocks of cross-section parameters that are split into those related to ^{12}C and ^{16}O, from the data fit discussed in Chapter 6. The ND280 fit is clearly able to find correlations, but the ^{12}C to ^{16}O ones are mostly weak, with the exception of the last plot, showing the correlations for CCQE E_b parameters, which are mostly driven by the initial correlations. This shows that current FGD2 samples are not able to strongly correlate those parameters. As a consequence, using the postfit correlations will not be enough to better demonstrate the impact of the SFGD samples.

Currently, there is a lot of ongoing work on new detectors or experiments using the same J-PARC neutrino beam. Therefore, it is quite likely that our knowledge of the initial state will improve. To name a few:

1. WAter-Grid-And-SCIntillator (WAGASCI) - the detector consists of a three-dimensional grid structured plastic scintillator target filled with water [119]. It is located in the same pit as ND280, but at 1.5° off-axis angle. The motivation of the WAGASCI experiment

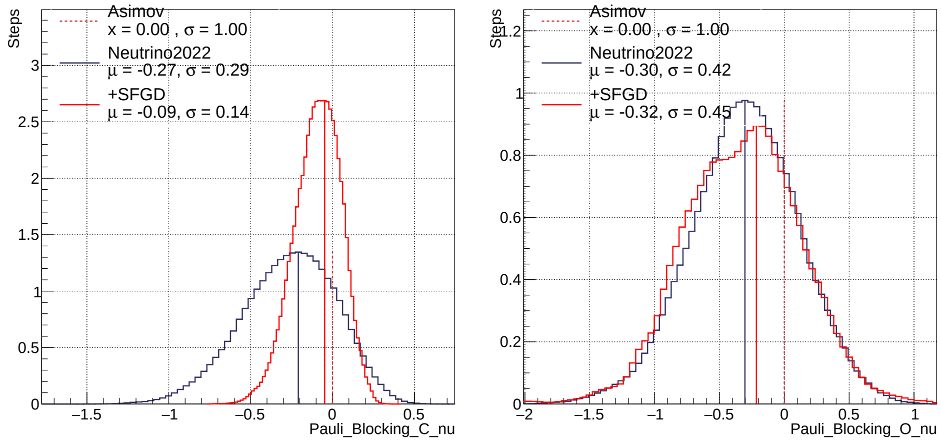

(A) Pauli blocking ^{12}C ν (B) Pauli blocking ^{16}O ν

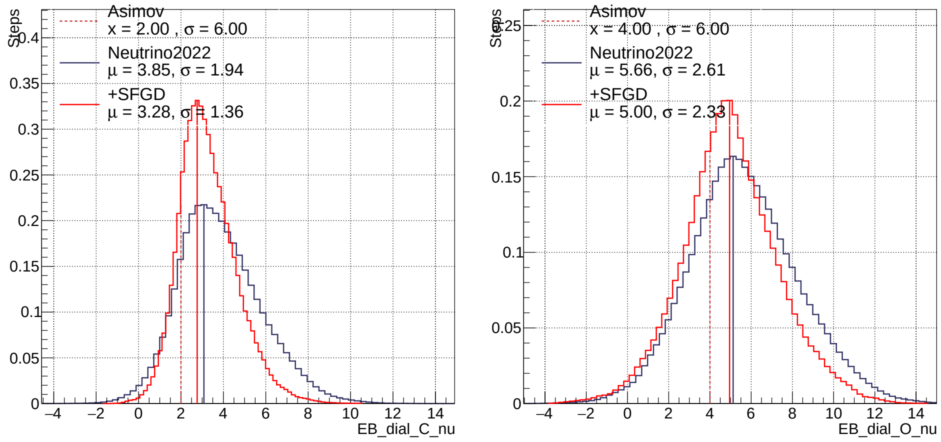

(C) CCQE E_b ^{12}C ν (D) CCQE E_b ^{16}O ν

FIGURE 7.20: Posterior distributions for several parameters from the ND280-only fit (marked as Neutrino2022, black) and the fit including SFGD samples (red).

is to reduce the systematic uncertainty on the neutrino cross-section with the same target and acceptance as SK. There is potential for joint ND280-WAGASCI cross-section measurement.

2. Intermediate Water Cherenkov Detector (IWCD) - a planned water detector in between ND280 and FD (in this case, a successor of SK) at a distance of $\approx$1-2 km [120]. In the future, a joint-fit using ND, FD and IWCD samples will help to better understand ^{12}C and ^{16}O correlations.

Thanks to those projects, in the future we will be able to better correlate ^{12}C and ^{16}O parameters.

In the next short study, we assume that the correlations for the Pauli blocking parameters are identical as for CCQE E_b. Since both effects are related to low Q^2 physics, we can naively expect the correlation to be to some extent similar, although this assumption is made only for the purpose of this study. In Fig. 7.22, we can see that the ^{12}C-related parameter error did not change significantly. Since ^{12}C ν is the best constrained Pauli blocking dial, this is expected. However, thanks to changing only the initial correlations for Pauli blocking ^{16}O ν, we observe the error reduced from $\sigma = 0.45$ to $\sigma = 0.35$, which is more than 20%. This demonstrates how important it is to study the ^{12}C and ^{16}O correlations, using both internal and external data.

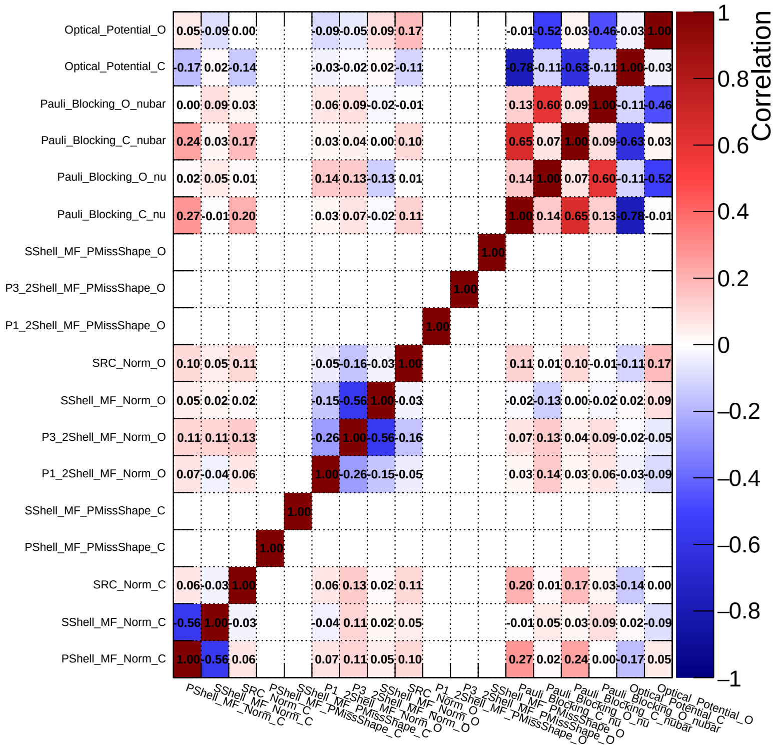

(A) CCQE SF dials

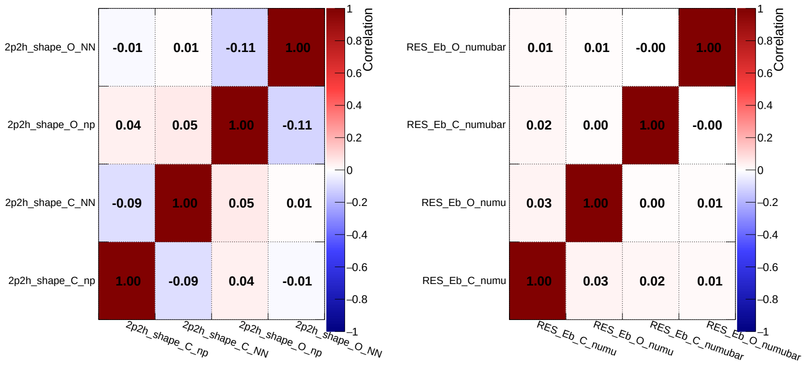

(B) 2p2h shape dials (C) RES E_b dials

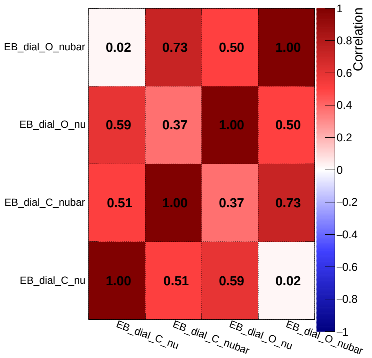

(D) CCQE E_b dials

FIGURE 7.21: Correlations after the ND280-only data fit for the cross-section parameters that are separated for carbon and oxygen.

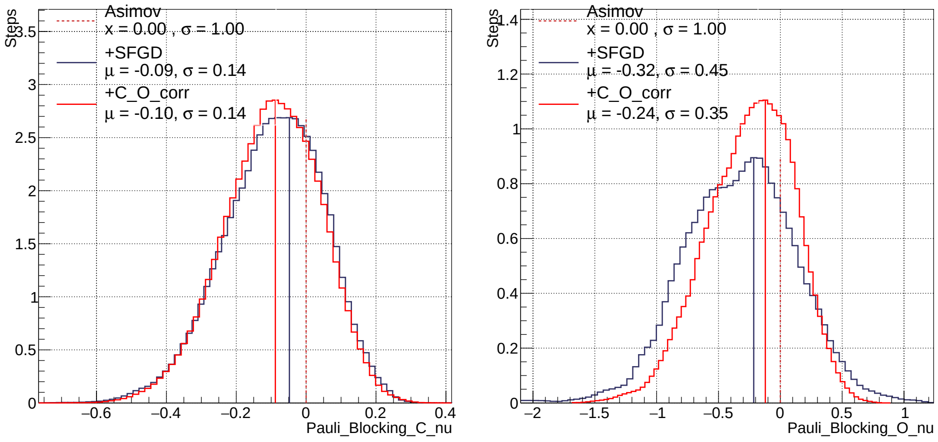

(A) Pauli blocking ^{12}C ν

(B) Pauli blocking ^{16}O ν

FIGURE 7.22: Posterior distributions for Pauli blocking parameters showing the impact of ad-hoc carbon-oxygen correlations.

7.2.5 Fit with All SFGD FHC Samples

Until now, only the CC0π event samples from SFGD have been considered. Here, we add the CC1π and CC-Other samples, both split based on proton presence (6 samples in total). Tab. 7.2 shows the expected event rates. It can be observed that the inclusion of additional samples increases overall event rates by one-third.

Sample	POT = 1.08×10^{21}
SFGD FHC CC0π-0p	50111.8
SFGD FHC CC0π-Np	47337.2
SFGD FHC CC1π-0p	14506.1
SFGD FHC CC1π-Np	8683.31
SFGD FHC CC Other-0p	16254.7
SFGD FHC CC Other-Np	9107.52

TABLE 7.2: Expected event rates for all SFGD samples.

As was mentioned in Section 7.2.1, those samples have not been included before because they are not fully reliable. Fig. 7.23 shows the reaction breakdown for the SFGD CC1π and CC Other samples and the RES and DIS fractions are improbably high, as there are barely any CCQE/2p2h events. Nevertheless, due to the lack of better simulation, additional studies were performed to evaluate the impact of those samples.

Another Asimov fit was performed, including all available SFGD samples as well as FGD1 and FGD2 samples, and without ad-hoc ^{12}C/^{16}O correlations. Fig. 7.24 summarizes the posterior distributions for parameters that are strongly affected by adding the SFGD CC1π and CC Other samples. That includes parameters related to SPP and DIS, clearly indicating that SFGD samples have the potential to introduce additional constraints.

When looking at the impact for selected FD samples in Fig. 7.25, it may appear quite surprising that for RHC 1Rμ (plot B) the largest effect is observed for lower energies. One has to keep in mind that this is the distribution of reconstructed energy, and there is higher contamination of DIS and π production in this region (see plot A). As for 1Re1de and ν_μCC1π samples, the interpretation is simpler as both samples contain a high fraction of RES, thus the greater constraints.

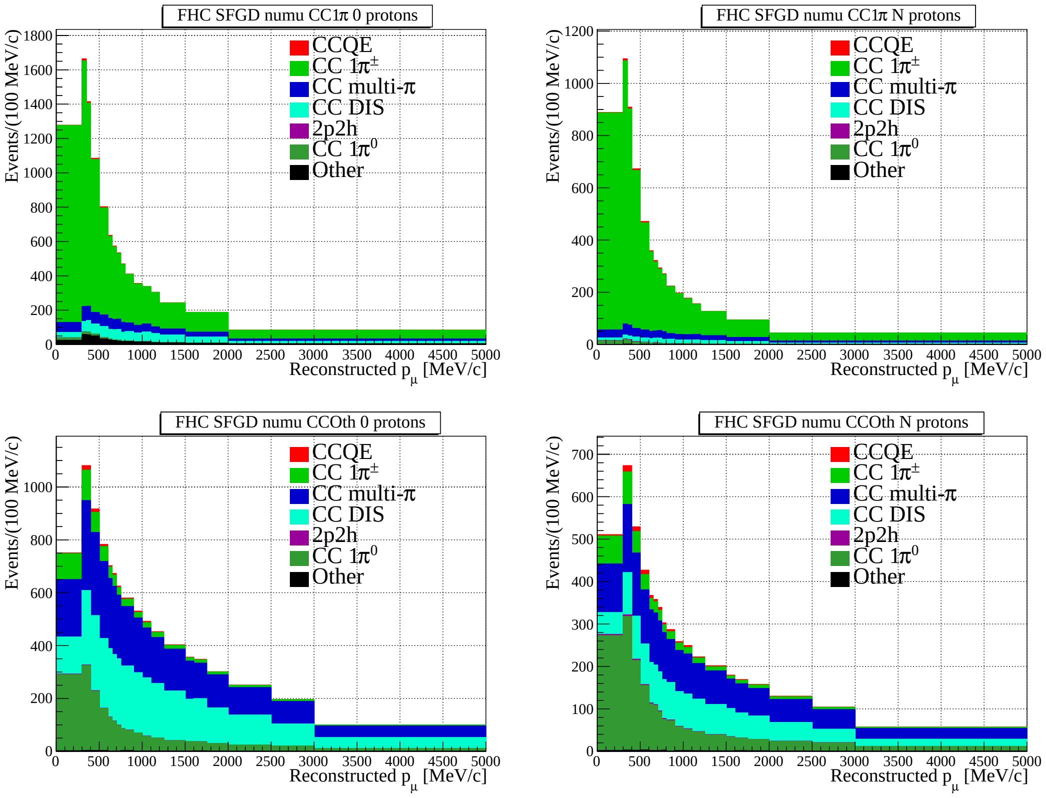

FIGURE 7.23: Momentum distributions for SFGD CC1π and CC Other samples, with colours indicating different reactions.

Summarizing, the upgraded ND280 will be a great addition to future oscillation analysis. Current sensitivity studies have shown that the errors for many parameters can be reduced even by half. Still, a lot of work is required on the systematic model, related in particular to predictions of nucleon kinematics.

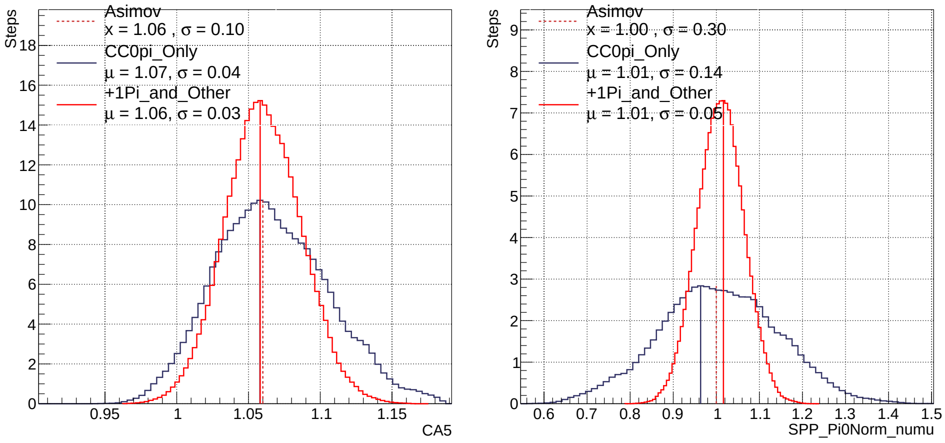

(A) C_A^5 (B) SPP π^0 norm ν_μ

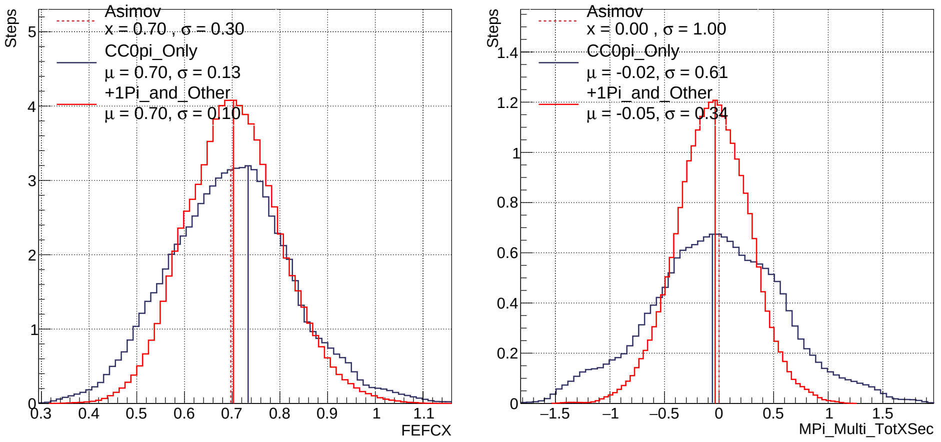

(C) π FSI Cex low E (D) Mπ Multi TotXSec

FIGURE 7.24: Posterior distributions from the SFGD+ND280 fit for selected parameters, showing the impact of adding π-tagged samples.

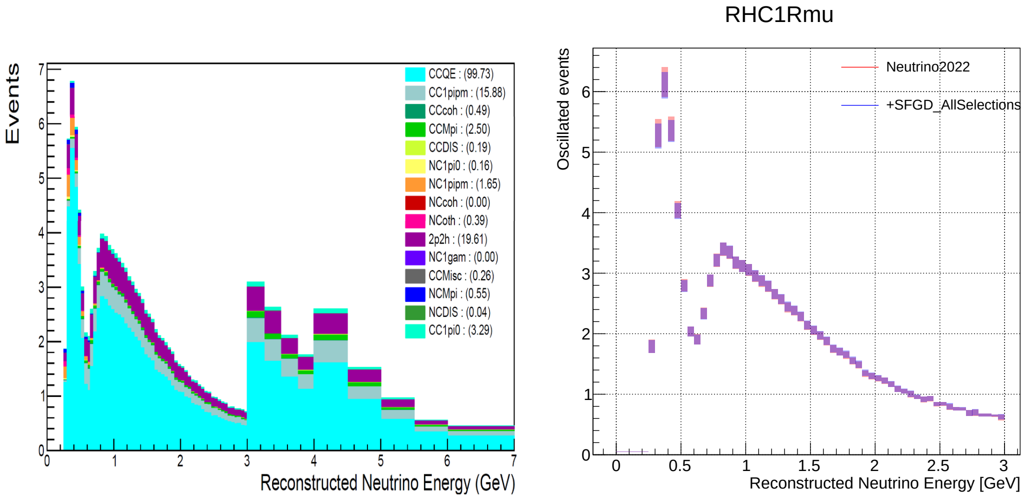

(A) Reaction breakdown for RHC 1Rμ

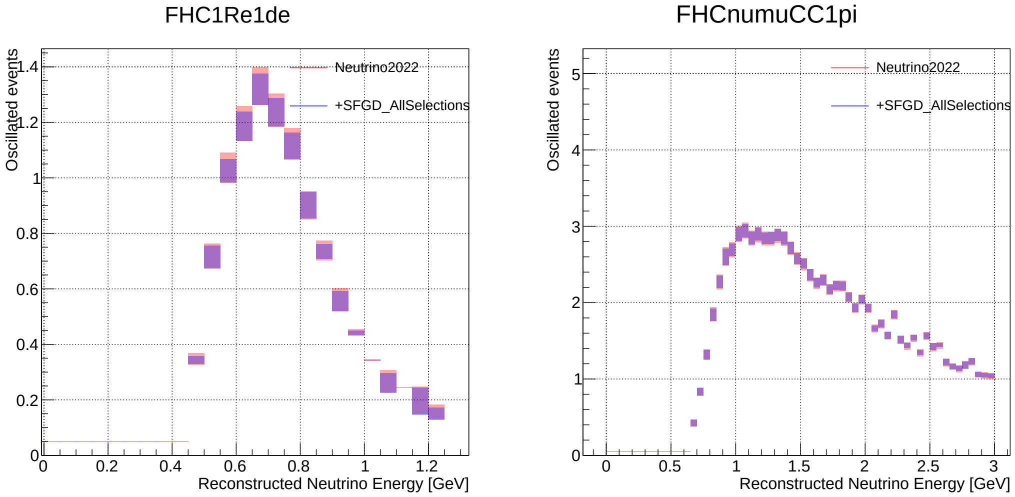

FIGURE 7.25: Selected FD event spectra showing the impact of adding SFGD π-tagged samples.

8

Summary and Outlook

> From the heights of these pyramids, forty centuries look down on us.
>
> **Napoléon Bonaparte**

In 2022, the Tokai to Kamioka (T2K) experiment presented new oscillation results at the Neutrino 2022 conference. The new analysis introduced several important improvements. New flux predictions were introduced, based on recent T2K replica target data analysis published by NA61/SHINE [86], which included, for example, measurements of kaons emerging from the target. Thanks to NA61/SHINE, the flux systematic error at higher neutrino energies was reduced, which is important as intrinsic ν_e, being the background to ν_e appearance, are mostly produced in kaon decays. The neutrino interaction model also went through several changes, most notably the CCQE-related part, which is the most significant channel for T2K OA. The changes in CCQE modelling included, among others, improvements to spectral function and Pauli blocking. Furthermore, new systematic parameters related to nucleon FSI and 2p2h pn to nn pair ratio were added. The number of parameters describing the cross-section model almost doubled in the analysis. Because of all the changes, previously used ND280 samples, based on π multiplicity, were not sufficient anymore. New ND280 samples were introduced, using photon and proton tagging. Photon samples allow for reducing the error related to π^0 production, which is a significant source of uncertainty at FD. Proton-tagged samples help to constrain the error on physical phenomena related to low Q^2 reactions, FSI, or nucleon pair ratio in 2p2h interactions. To accommodate for new samples, the ND detector systematics had to be expanded, including new ECal systematic errors and updated tuning of proton SI. Lastly, new FHC ν_μCC1π sample was introduced to FD analysis, increasing the available ν_μ event statistic by 30% and serving as an important cross-check of the model at higher neutrino energies.

To validate the analysis method, multiple studies were performed, for example: Asimov fits, cross-validating with the frequentist framework (BANFF), estimating the impact of expanded parametrisation of ND detector systematics, Principal Component Analysis (PCA) of the flux covariance matrix, posterior predictive p-value estimation, or fits with an alternative likelihood definition. Those tests demonstrated that the analysis method is robust and not biased.

Thanks to the use of diverse samples and available data statistics, ND280 is able to significantly reduce errors on flux and cross-section parameters. Using ND280 samples allowed to reduce the uncertainty on the number of expected events at FD by a factor of five–six, for example, the error for FHC 1Rμ sample decreased from 16.7% to 3.4%.

New T2K oscillation results prefer nearly maximal CP violation with the value of δ_{CP} close to $-\pi/2$ and exclude CP conserving values of 0 and π within 90% credible intervals.

This fact has significant consequences as, if true, it can explain why there is more matter than antimatter in the observed Universe. Moreover, T2K has a weak preference for normal mass hierarchy and the upper octant of θ_{23}, which is most precisely measured by T2K. Despite all the improvements, the new results are consistent with previous T2K results [80], showing the robustness of the analysis.

The analysis is the work of several people, with the Author being the main Bayesian Markov chain Monte Carlo ND280 analyser, whose work was essential to obtain new results. The Author was involved in all the tasks mentioned above, except flux improvements and FD sample development. In addition, the Author introduced many enhancements to the OA framework used by T2K, like speed-up or increased flexibility improvements. Thanks to his significant contributions, the Author was selected to present new T2K results at the ICHEP 2022 conference [4].

Another long-baseline neutrino experiment currently taking data is NOνA, located in the USA, which has a much longer baseline than T2K (∼810 km). The comparison of T2K, NOνA and SK atmospheric results for δ_{CP} and $\sin^2\theta_{23}$ are shown in Fig. 8.1. There is no significant tension between the results, as in many regions the contours overlap. To better understand and produce more precise results, there are ongoing joint analyses, one for T2K and NOνA data [3] and another for T2K and SK atmospheric samples [121]. T2K, NOνA and SK experiments will also continue collecting data for several years.

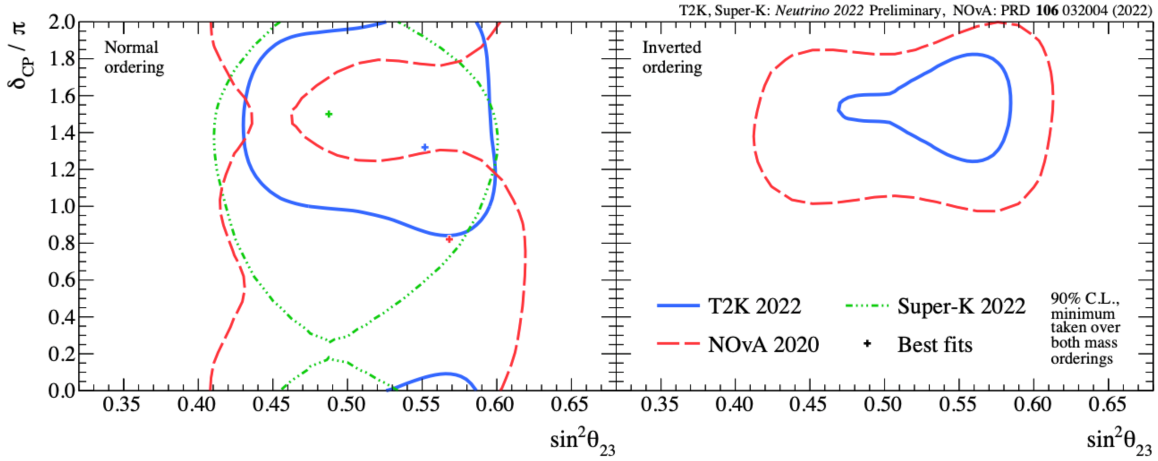

FIGURE 8.1: Comparison of the results for δ_{CP} and $\sin^2\theta_{23}$ from T2K, NOνA and SK, presented separately for both mass hierarchies.

While waiting for new data, we can try to use the collected data in a new way. The Author was involved in performing a sensitivity study with proton kinematics, which demonstrated that using proton information can greatly help to constrain errors on the nuclear effects modelling. However, it outlined that the current cross-section model is not sufficient to properly describe nucleon kinematics. This analysis provided guidelines on what effects need to be added in the future to neutrino interaction generators.

Currently, T2K is undergoing several improvements to its facilities. Thanks to J-PARC accelerator enhancement, the beam power will increase from ∼515 kW to ∼750 kW, while the horn current will increase from 250 kA to 320 kA, allowing for better focusing and a 10% increase in flux. In 2020, the SK detector was doped with gadolinium salts, which allow for efficient neutron tagging [71] by observation of photons from Gd nuclei deexcitation after neutron capture. Although the main reason for adding gadolinium was the search for diffuse supernova neutrino background [122], the neutron capture is also useful for T2K, as it helps to distinguish between ν and $\bar{\nu}$ interactions in RHC mode. For this reason, constraining the uncertainties of nuclear effects and FSI will become crucial. Neutron tagging for T2K is in preparation and is going to be used in the next analysis. Therefore, the work presented in the Thesis will help to use the new feature at the FD.

The remaining part of the facility overhaul is the upgrade of the ND280 detector with a new sub-detector complex. Part of the upgraded ND280 will be a novel SFGD detector consisting of 1 cm^3 scintillation cubes, with a much lower threshold for detecting protons. SFGD will be sandwiched between two High Angle TPCs providing significantly better angular acceptance. The Author performed the first sensitivity studies using simulated event samples from the upgraded ND280. They demonstrated that the upgraded detector can reduce errors for many systematic parameters even by half. However, because the new interaction target mostly consists of carbon, SFGD samples don't constrain ^{16} O-related parameters important for FD. Hence, to fully utilise the upgraded ND280, it is necessary to work a on better understanding of the ^{12}C and ^{16}O parameters correlations in the near future.

The successor to the T2K experiment, called Hyper-Kamiokande (HK) [123], is already under construction and is expected to start taking data in 2027. With orders of magnitude higher expected data statistics, mostly thanks to 8 times larger FD mass, it should be able to resolve the CP violation mystery with $\sim 5\sigma$ for a large fraction of possible δ_{CP} values. HK results will be dominated by systematic errors rather than statistical ones as in the case of T2K. Therefore, the Intermediate Water Cherenkov Detector [120] is going to be built in order to help constrain ^{16}O-related uncertainties. ND280 will still serve as ND for the HK experiment, and the tools and models are likely going to be inherited by HK, including the work within this Thesis dedicated to reducing systematic errors.

A

Additional Studies

> New weapons require new tactics. Never put new wine into old bottles.
>
> **Heinz Guderian**

A.1 Proton-Tagged Samples in RHC Mode

In the main part of the Thesis, the impact of proton-tagged samples in FHC was discussed in detail. Here, we briefly present the properties and benefits of proton-tagged samples in RHC mode, as they might be included in future T2K analysis. We shall remind that there is no photon tagging for RHC yet, although there is ongoing work to introduce it.

Proton Tagging in $\bar{\nu}_\mu$ samples in RHC

In the CCQE interaction of an antineutrino, there is no outgoing proton: $\bar{\nu}_l + p \to l^+ + n$. Proton can only be ejected as a result of FSI or in more energetic processes like RES. Due to that fact, we expect a much lower number of reconstructed protons compared to FHC samples.

Fig. A.1 presents the number of reconstructed isoFGD or TPC-matched protons in the CC0π RHC samples. One outstanding feature is that in RHC there is a comparable number of isoFGD protons and TPC-matched protons, which is a consequence of lower energies. Contrary to FHC samples, events with more than one reconstructed proton are almost non-existent. This is an expected outcome worth emphasizing, as samples are obviously different from their FHC counterparts.

Fig. A.2 shows the kinematic properties of μ^+ candidate for RHC CC0π FGD1 sample and after splitting it based on the proton tagging. It can be observed that CC0π-0p is very similar to CC0π, whereas CC0π-Np is a significantly different sample, as expected dominated by RES, the main source of protons in RHC mode. Furthermore, μ^+ momenta are much higher for CC0π-Np sample. However, problems with events statistics can be observed for CC0π-Np samples.

Predicted event rates are summarized in Tab. A.1: we expect $\sim$ 600 events for CC0π-Np, which is a very low number when compared to most of currently used samples, with the RHC FGD2 CC1π sample having the lowest event rate of 660 events. Therefore, once T2K collects more data in RHC mode, using proton-tagged samples in RHC will become much more feasible.

For a better understanding of the properties of the proton-tagged samples in RHC mode, Tab. A.2 outlines the reaction breakdown. We find that over 20% of events in CC0π-Np come from CCQE, which could be the effect of FSI or particle misidentification. Tab A.3 is

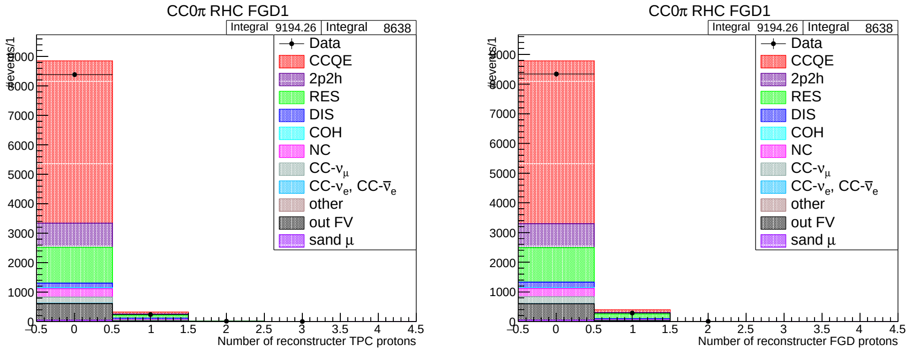

(A) TPC-matched FGD1 (B) isoFGD1

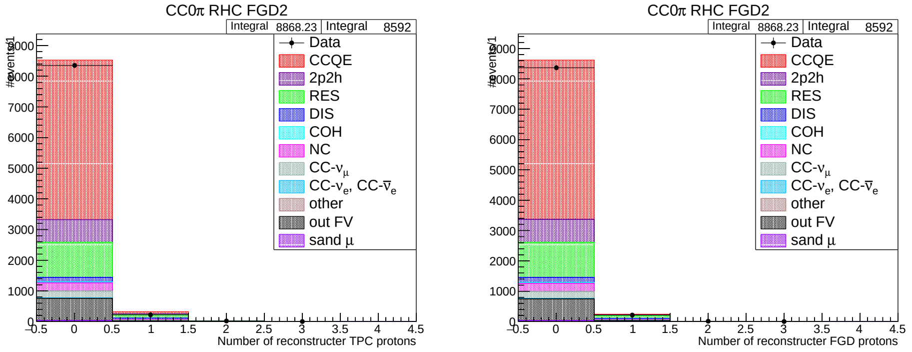

(C) TPC-matched FGD2 (D) isoFGD2

FIGURE A.1: Number of reconstructed protons in CC0π RHC samples. Most events have no reconstructed protons.

	RHC		
	CC0π	CC0π-0p	CC0π-Np
FGD1	8676	7992	684
FGD2	8608	8047	561

TABLE A.1: Data event rates in CC0π RHC samples before and after proton tagging cut.

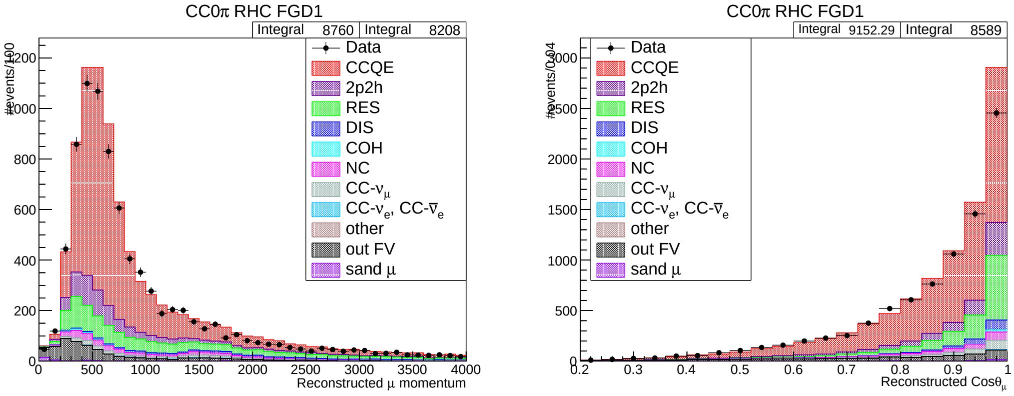

(A) CC0π (B) CC0π

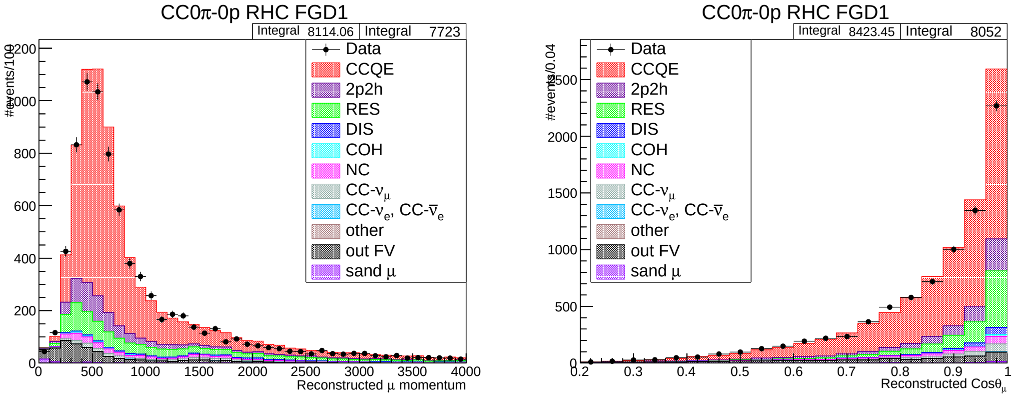

(C) CC0π-0p (D) CC0π-0p

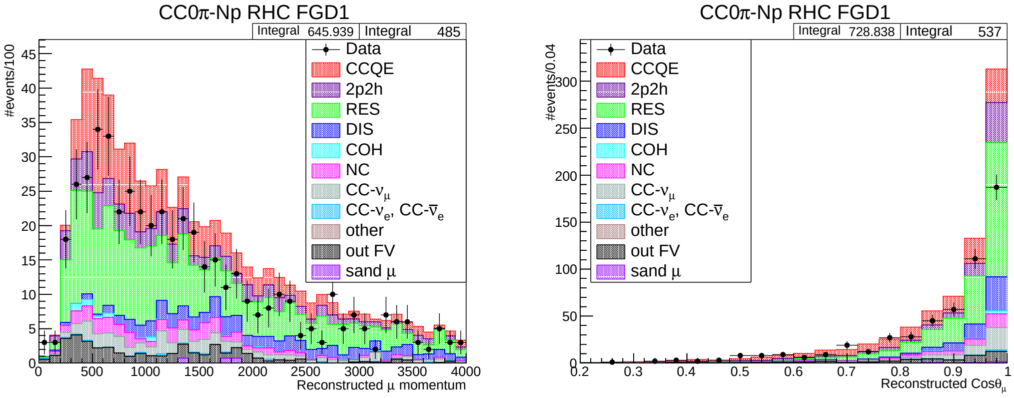

(E) CC0π-Np (F) CC0π-Np

FIGURE A.2: Muon momentum and $\cos\theta_\mu$ distributions for FGD1 CC0π RHC samples before and after proton tagging cut.

summarizing PID performance for protons in RHC. PID for TPC-matched protons works equally well as in FHC. However, isoFGD PID performs worse, with high contamination of π^-, which is the consequence of FGD reconstruction not distinguishing the sign of particle charge. Moreover, there are usually no Michel electrons coming from $\pi^- \to \mu^-$ decays, which could help to separate protons from pions. Overall PID for proton is performing well (83% for FGD1 and 70% for FGD2), but not as good as for FHC, due to a higher fraction of isoFGD protons to TPC-matched protons on top of the aforementioned problem with pions. However, for true CCQE events, proton PID is around 97%, indicating that most of the reconstructed protons in CCQE events originate from FSI. According to Tab. A.2, a large fraction of reconstructed protons in RHC samples comes from RES or other processes such as DIS[1].

	RHC		
	CC0π	CC0π-0p	CC0π-Np
CCQE	61%	64%	22%
2p2h	9%	9%	11%
RES	14%	12%	38%
Other	16%	15%	29%

TABLE A.2: Reaction breakdown for CC0π RHC samples before and after proton tagging cut.

	FGD1		FGD2	
	isoFGD (%)	TPC-matched (%)	isoFGD (%)	TPC-matched (%)
proton	69.32	97.85	30.12	98.14
π^+	1.34	0.61	4.66	0.47
π^-	24.43	0.03	22.36	0.11
μ^-	0.82	0.15	4.66	0.31
μ^+	0.38	0.55	1.24	0.40
Other	3.79	0.81	36.96	0.57

TABLE A.3: True identity of proton candidate for CC0π RHC samples.

Fig. A.3 shows the reconstructed momentum of the proton candidate. In general, the distributions are similar to those of FHC samples; however, the data/MC agreement is worse, but also the statistical fluctuations due to small statistics are larger.

Fig. A.4 shows the true Q^2 distributions. Similarly to FHC samples, we observe that proton-tagged samples have different distributions of this variable. As a consequence, the samples would help to constrain many cross-section parameters (like Pauli blocking).

Proton Tagging in ν_μ samples in RHC

CCQE interaction of the neutrino component of RHC produces a proton (before FSI), so we expect behaviour more similar to that of FHC samples. On the other hand, the RHC ν_μ contamination component[2] tends, on average, to have higher energy than ν_μ in FHC; therefore, the properties of the samples will be different.

Fig. A.5 shows the number of reconstructed isoFGD or TPC-matched protons in CC0π RHC BKG samples. First of all, we can observe that there are plenty of reconstructed protons; however, due to higher neutrino energies, we can expect differences in distributions with respect to FHC.

---

[1] See Tab. 3.2 on page 42 for a comparison with FHC.

[2] Also called RHC BKG.

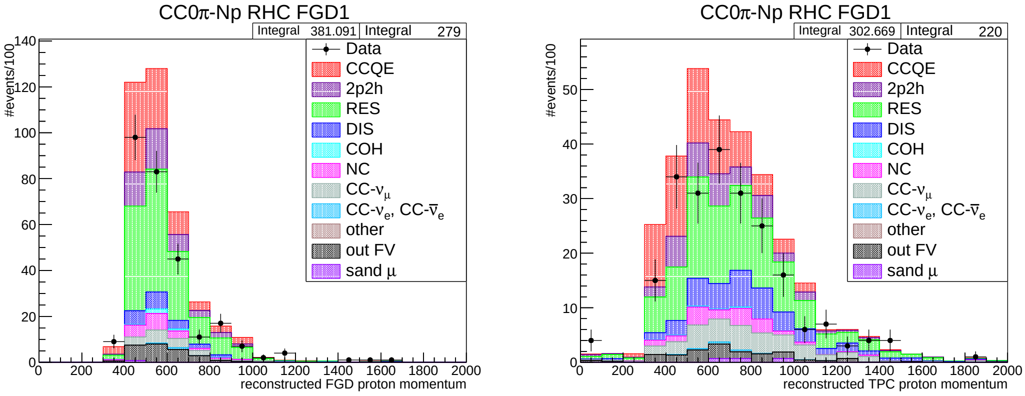

(A) isoFGD1 (B) TPC-matched FGD1

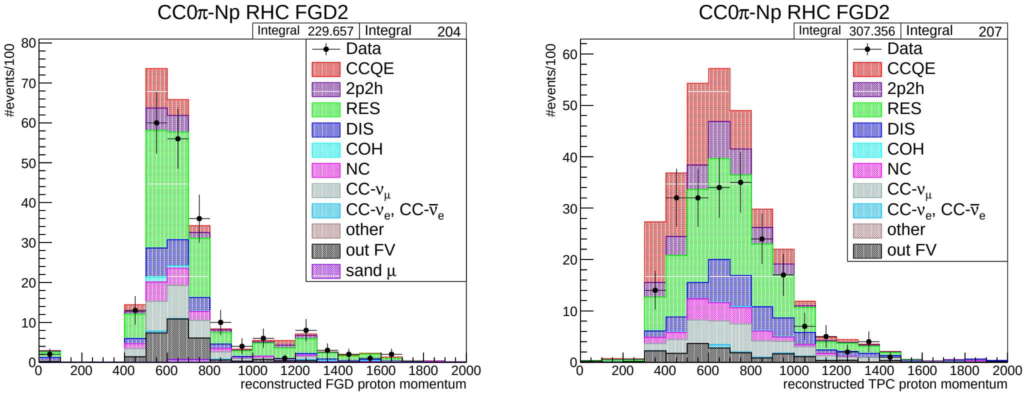

(C) isoFGD2 (D) TPC-matched FGD2

FIGURE A.3: Momentum distributions of proton candidates in CC0π-Np RHC samples.

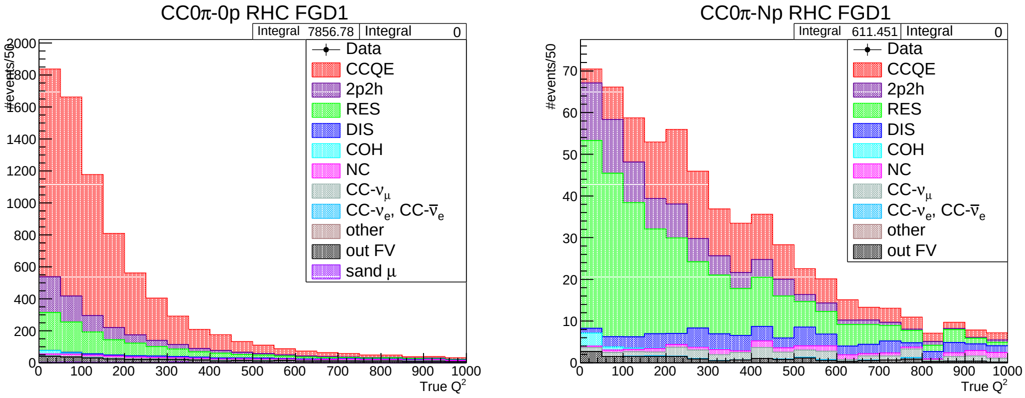

(A) CC0π-0p (B) CC0π-Np

FIGURE A.4: True Q^2 distributions for FGD1 proton-tagged samples in RHC.

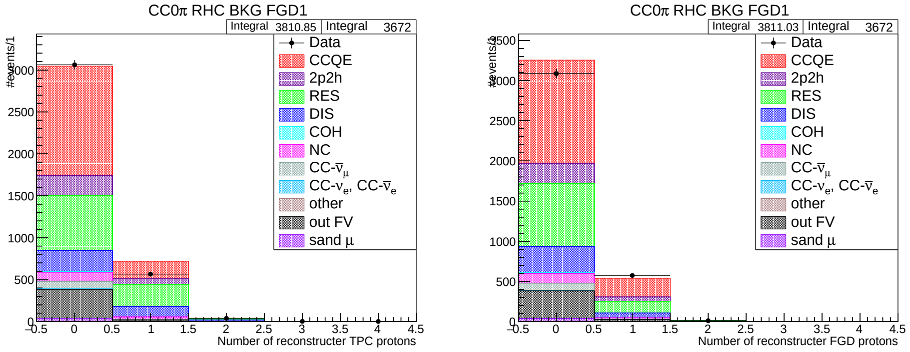

(A) TPC-matched FGD1 (B) isoFGD1

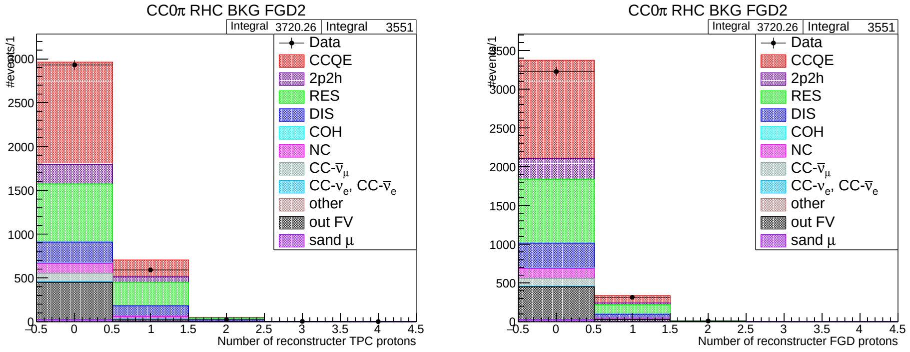

(C) TPC-matched FGD2 (D) isoFGD2

FIGURE A.5: Number of reconstructed protons in CC0π RHC BKG samples. Most events have no reconstructed protons.

Fig. A.6 presents the muon kinematic variables for ν_μ CC0π and samples based on proton tagging cut. We observe much higher μ^- momentum than in FHC or for μ^+ in RHC $\bar{\nu}_\mu$ samples. Tab A.4 summarizes the expected event rates. Comparing this table with an analogous table 6.1 for FHC samples, we can conclude that the overall fractions of CC0π-0p and CC0π-Np are comparable between FHC and RHC BKG samples, although the relative number of CC0π-Np is larger[3] in RHC BKG samples because of higher neutrino energies.

	RHC BKG		
	CC0π	CC0π-0p	CC0π-Np
FGD1	3714	2477	1237
FGD2	3537	2544	993

TABLE A.4: Data event rates in CC0π RHC BKG samples before and after proton tagging cut.

Tab. A.5 outlines the reaction breakdown for RHC BKG proton-tagged samples. The fractions of interaction modes are similar to FHC samples, although due to higher neutrino energies, some effects are less impressive. We can see that the CC0π-0p sample has slightly higher purity for CCQE than CC0π, though the difference is much smaller than in FHC samples. CC0π-Np has a higher fraction of all other interactions.

Fig. A.7 presents the distributions of proton candidate momentum, which are similar to FHC samples, while the true Q^2 distributions are shown in Fig. A.8. Similarly to FHC samples, the proton-tagged samples have different Q^2 distributions, with CC0π-0p having on average lower values than CC0π-Np.

---

[3] 43% vs. 49% (39% vs. 32%) for FHC and RHC BKG samples in FGD1 (FGD2), respectively.

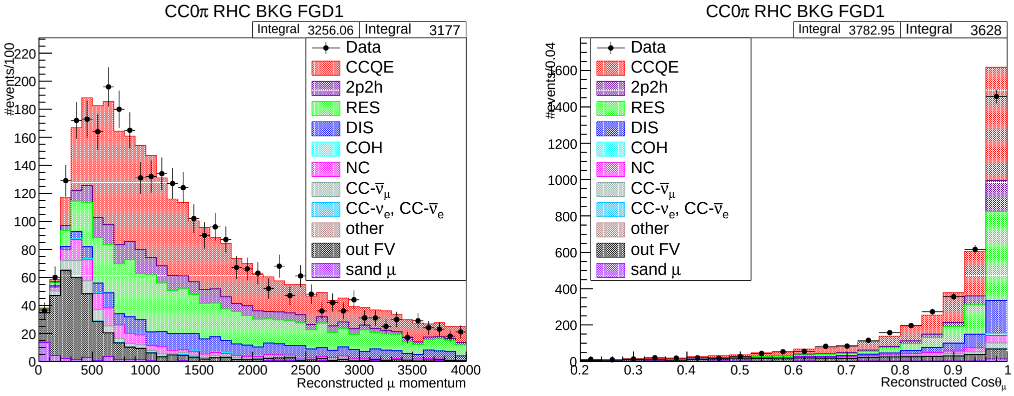

(A) CC0π (B) CC0π

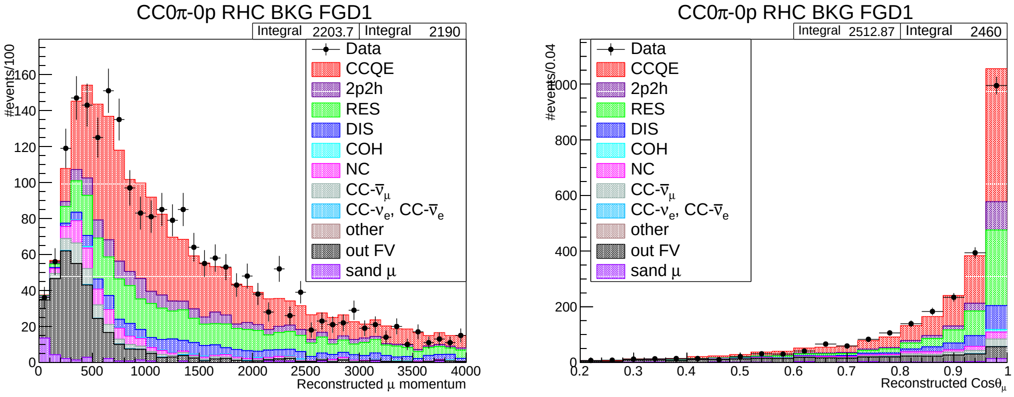

(C) CC0π-0p (D) CC0π-0p

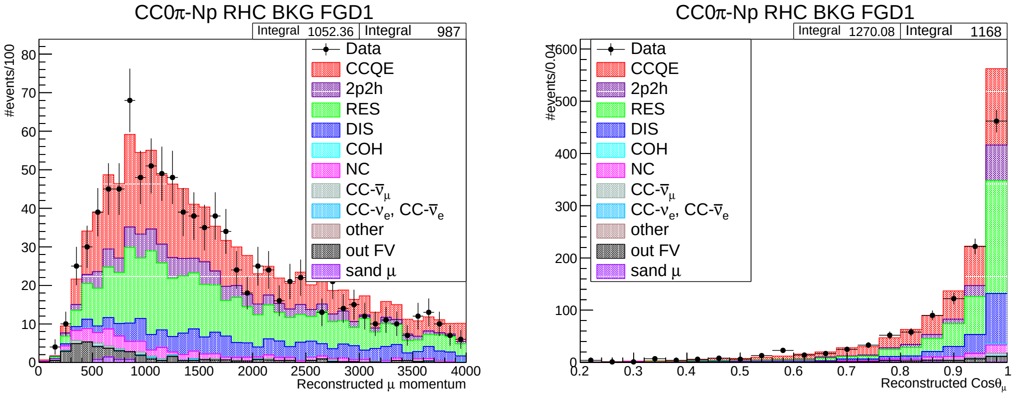

(E) CC0π-Np (F) CC0π-Np

FIGURE A.6: Muon momentum and $\cos\theta_\mu$ distributions for FGD1 CC0π RHC BKG samples before and after proton tagging cut.

	RHC BKG		
	CC0π	CC0π-0p	CC0π-Np
CCQE	40%	42%	35%
2p2h	8%	7%	10%
RES	25%	21%	25%
Other	27%	30%	30%

TABLE A.5: Reaction breakdown for CC0π RHC BKG samples before and after proton tagging cut.

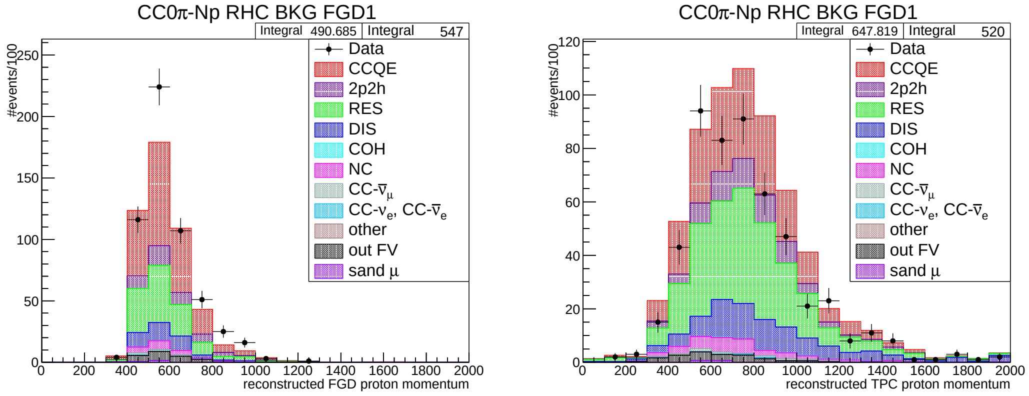

(A) TPC-matched FGD1 (B) isoFGD1

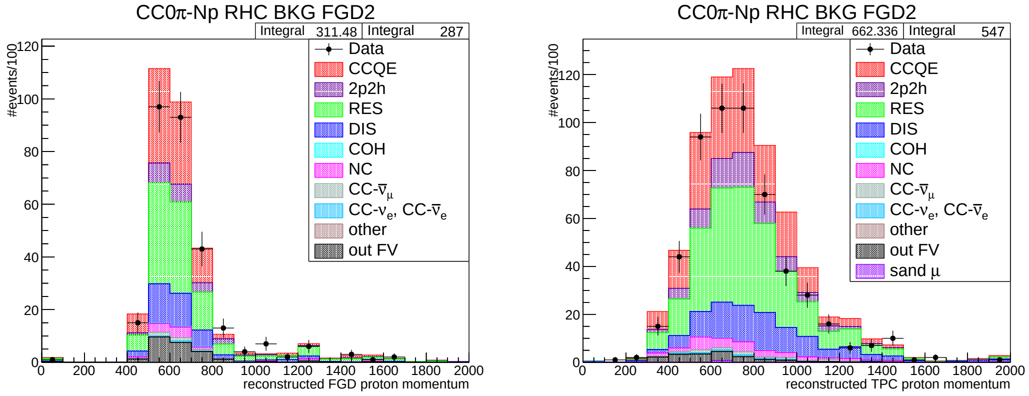

(C) TPC-matched FGD2 (D) isoFGD2

FIGURE A.7: Momentum distributions of proton candidates in CC0π-Np RHC BKG samples.

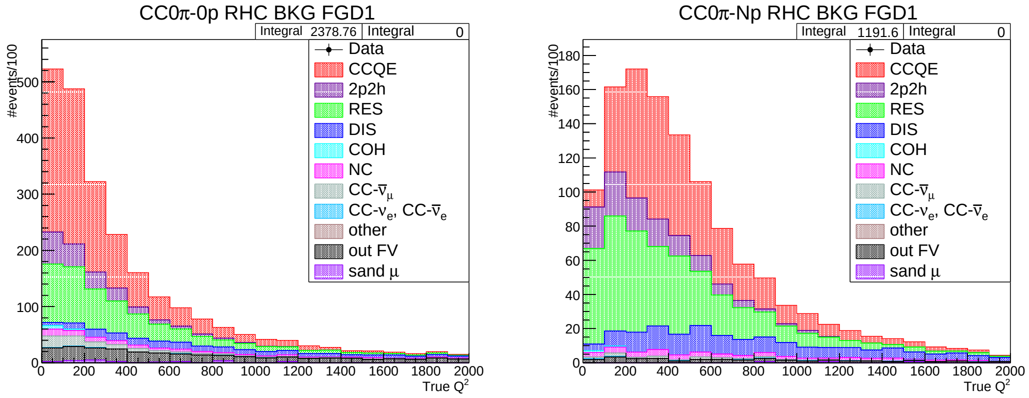

(A) CC0π-0p (B) CC0π-Np

FIGURE A.8: True Q^2 distributions for FGD1 proton-tagged samples in RHC BKG.

Tab. A.6 summarizes the PID performance for protons coming from ν_μ interactions in RHC mode. The performance of TPC PID is very similar as for both FHC and $\bar{\nu}_\mu$ RHC samples, whereas the performance of isoFGD PID is much better than for $\bar{\nu}_\mu$ RHC samples and similar to that obtained in FHC selection. The main reason is a much smaller number of π^- produced in ν_μ interactions with regard to $\bar{\nu}_\mu$ interactions, and π^+ can be tagged and rejected using a signal from Michel electron. The overall accuracy of proton PID is 95% for FGD1 and 89% for FGD2.

	FGD1		FGD2	
	isoFGD (%)	TPC-matched (%)	isoFGD (%)	TPC-matched (%)
proton	90.52	97.91	67.86	98.01
π^+	5.39	1.21	16.96	1.23
π^-	1.67	0.02	3.87	0.03
μ^-	0.07	0.00	0.92	0.00
μ^+	0.24	0.17	1.37	0.20
Other	2.10	0.69	9.02	0.52

TABLE A.6: True identity of proton candidate for CC0π RHC BKG samples.

Conclusions

In general, the inclusion of proton-tagged samples in RHC appears to be a valid point to investigate; however, the events rates, particularly in RHC $\bar{\nu}_\mu$ CC0π-Np, would be quite low for the number of POT currently accumulated by T2K. Once this obstacle is gone, the new samples could strengthen sensitivity to many effects, as FHC proton-tagged samples demonstrated, but also explore new effects like indirectly probing neutrons interacting via FSI. It is worth to remind of the upgrade to the T2K beamline (see Section 2.7) which will result in T2K being able to collect data faster.

A.2 Multi-π and Multi-π-Photon-Proton Selections

This Section is devoted to the estimation of the impact of new ND280 samples, especially proton-tagged samples.

Fig. A.9 presents an overlay of selected posterior distributions from two Asimov fits, one using multi-π samples and the other using multi-π-photon-proton samples. We see that the addition of proton information increases sensitivity to SF parameters, for example, the normalisation of SRC. Furthermore, we notice a smaller error for `2p2h norm`, which mostly comes from the better separation of 2p2h and CCQE interactions thanks to the proton-tagged samples. Error reduction for `2p2h shape` dial is the consequence of different $q_0/|\vec{q}_3|$ distributions in both proton-tagged samples. The increase in sensitivity for nucleon FSI is most significant as the error is decreased by 1/3. This outcome is expected, as this dial was introduced because of proton-tagged samples. `SPP` π^0 parameter error decreased thanks to the inclusion of photon information. The case of `Res` E_b ^{12}`C` is particularly interesting, because reduced uncertainty for this dial is the result of both photon and proton tagging.

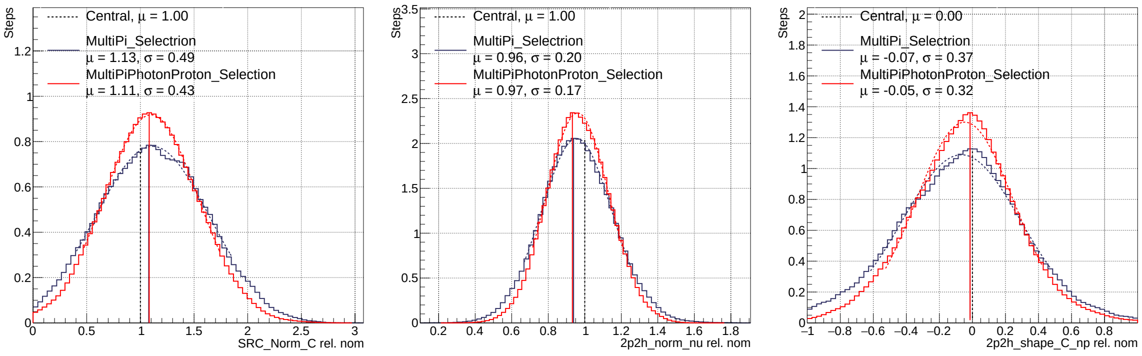

(A) SRC norm ^{12}C

(B) 2p2h norm ν

(C) 2p2h shape ^{12}C np

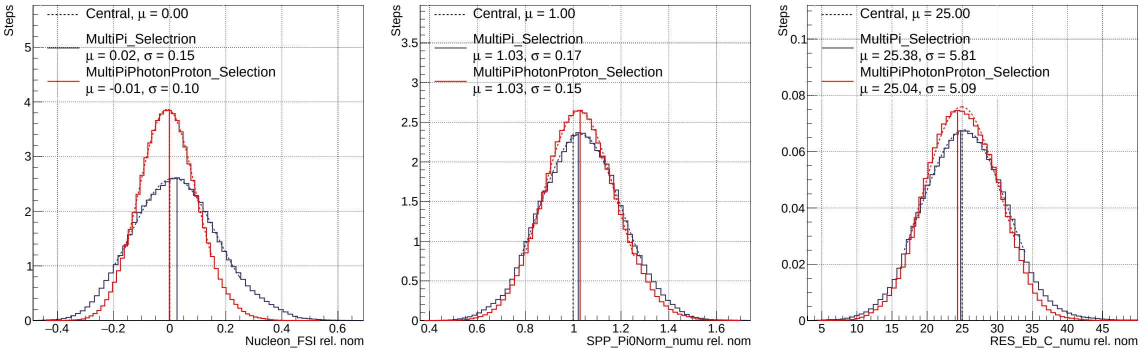

(D) Nucleon FSI

(E) SPP π^0 norm ν_μ

(F) RES E_b ^{12}C ν_μ

FIGURE A.9: Marginalised posterior distributions for selected parameters from Asimov fits using multi-π and multi-π-photon-proton selections.

Lastly, predicted FD spectra are presented in Fig. A.10. Improvements can be observed for some samples and kinematics bins. It is also worth reminding that FD does not currently use nucleon information. However, there is ongoing work to include neutron-tagged samples at FD and for those, the constraining of nucleon-related effects will become more important.

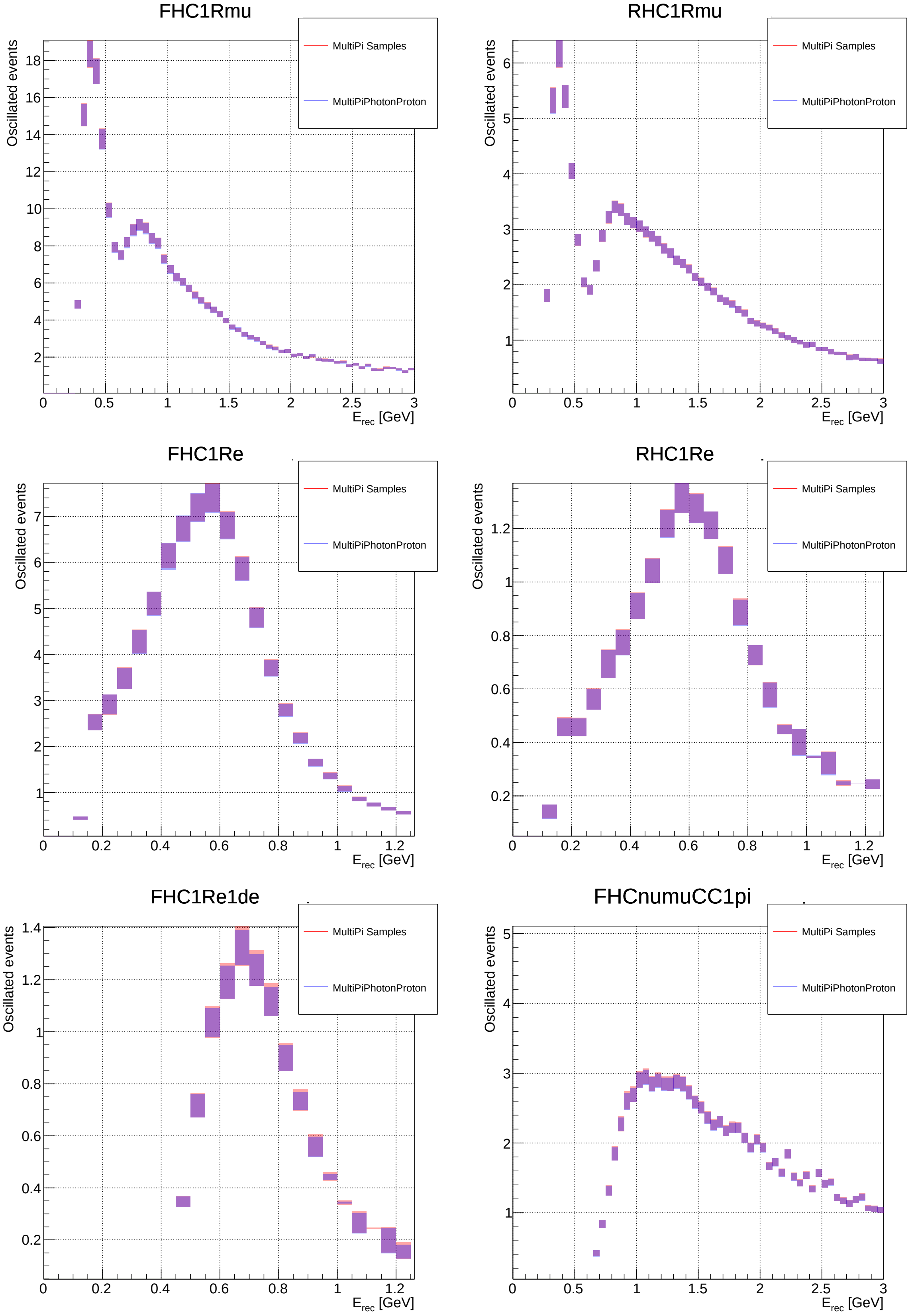

FIGURE A.10: FD posterior predictive distributions obtained using ND280 constraints from two different Asimov fits: one using the multi-π selection and the other using the multi-π-photon-proton selection. The uncertainties come only from ND-constrained parameters.

A.3 ND280 Detector Uncertainty - Efficiency of isoFGD Tracks Reconstruction

FGD hybrid tracking efficiency describes how likely it is to reconstruct a track contained within FGD (isoFGD track) in the presence of a longer track passing to a TPC (TPC-matched track, usually the muon candidate). In such a case, it can happen that the global reconstruction algorithm may wrongly assign the hits left by the isoFGD track to the TPC-matched track, which will result in not reconstructing the isoFGD track. Such a study was performed in 2014 using an older reconstruction algorithm, and the efficiencies were only calculated for FHC (identical efficiencies were assumed for RHC runs). Since this efficiency and the related systematic error are important for short proton tracks, the Author has revisited them before implementing proton-tagged samples.

To estimate the error, data or MC events with a muon candidate and without reconstructed isoFGD tracks are selected. Proton, π^+ or π^- are then separately simulated using GEANT4 Particle Gun, starting from the same vertices as the muon candidates in selected data/MC events: 100 isotropically distributed Particle Gun tracks per each event. The hits created by Particle Gun tracks in the detector are inserted into the corresponding data or MC event (for each Particle Gun event separately), creating so-called hybrid events, and the reconstruction procedure is run again. Finally, the efficiency for each particle is obtained as the ratio of the number of events with reconstructed isoFGD track to the number of events with true isoFGD track, separately for data and MC.

Fig. A.11 shows the proton reconstruction efficiency as a function of Particle Gun proton momentum, $\cos\theta$ relative to the detector axis, and $\cos\theta$ relative to the muon candidate track marked as $\cos(\theta\ \mathrm{HMNT, Stub})$, for two binning schemes. The values obtained for coarse binning are used in the T2K framework for systematic errors propagation. One interesting feature is that the efficiency drops at $\cos(\theta\ \mathrm{HMNT, Stub}) \sim 1$, which is due to the Particle Gun proton travelling very close to the muon candidate when the FGD hits produced by the proton are often associated to the muon track. This effect is well reproduced by the detector Monte Carlo and the overall data/MC agreement is very good.

Fig. A.12 depicts the fractional error as a function of muon momentum for FGD1 CC0π samples in FHC and RHC, using the efficiencies calculated for pions previously and in this study. The validations were performed for ND280 samples before the inclusion of proton- and photon-tagged samples to make the comparison with older analysis easier. In the left plot, made for FHC, we can see that the updated values result in an overall smaller error, which is the consequence of improved reconstruction. The right plot shows the analogous errors for RHC. Since the previous study assumed the same efficiencies for RHC as for FHC, we show also the error for old and new FHC efficiencies on RHC for comparison, marked by the blue and red lines. The green line shows the impact of using RHC hybrid events (prepared by the Author) instead of FHC (as in the old analysis) for error calculation, and we can see that error decreased significantly. Furthermore, in the previous study, the same efficiency was assumed for π^- as for π^+; thus, the purple line shows the impact of using efficiencies obtained by the Author for π^- Particle Gun tracks instead of π^+. The last change has a negligible effect; nevertheless, the confirmation of this fact was necessary, as it was not checked in the old study.

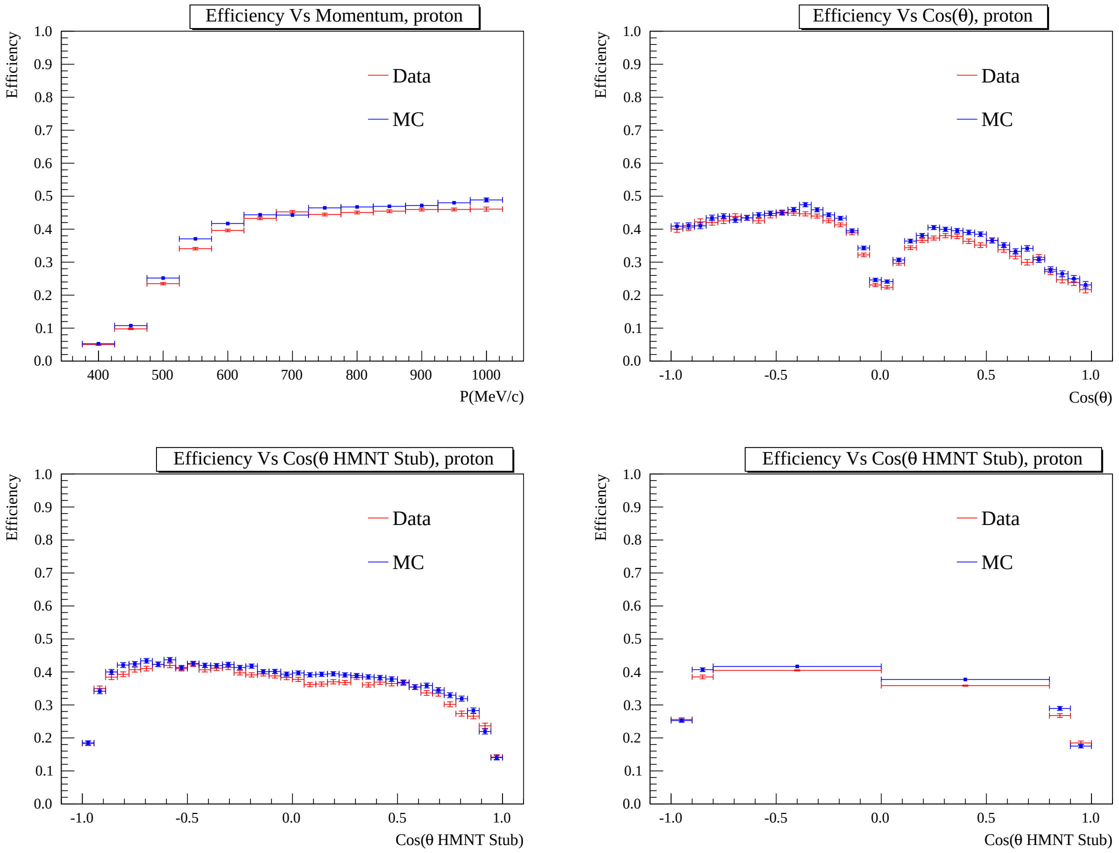

FIGURE A.11: Proton reconstruction efficiency for data and MC as a function of proton momentum, $\cos\theta$ relative to the detector axis and $\cos\theta$ relative to the muon candidate direction (for two binning schemes). All plots are produced for FHC data and MC.

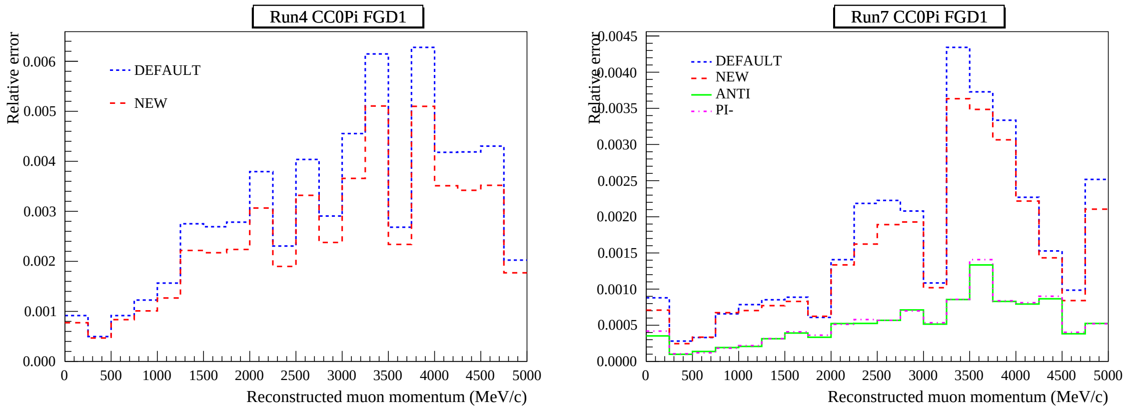

(A) FHC

(B) RHC

FIGURE A.12: Fractional systematic error for FGD hybrid tracking efficiency using 2014 and updated efficiency tables.

A.4 Fit Binning Matrix

As it was discussed in Section 4.2, the original ND280 covariance matrix has ∼5000 bins (called fit binning), exactly the same number as for the $-2\log\mathcal{L}_{\mathrm{Stat}}$ calculation (see Eq. 5.11). Each diagonal element of the fit binning covariance matrix corresponds to one kinematic bin for a particular sample used in the analysis.

There are several reasons why the fit binning matrix is not used in the official ND280 analysis. Firstly, the frequentist framework (BANFF) or, in general, the Minuit fitter struggles with such a high number of parameters, while MCMC can cope with it. However, it requires additional diagnosis of MCMC (see Section 5.4).

Furthermore, such an increase in the number of systematic parameters makes fit slower[4], but most importantly, it requires massive amounts of memory as we have to store the value of each parameter for each step. For comparison, a chain with 4 million MCMC steps using a fit binning matrix requires 50 GB memory, while a standard chain with 4 million steps around 4 GB. Therefore, we use the process of bin merging to reduce the number of bins to ∼500. Such a smaller matrix will be called the standard covariance matrix throughout this Section. The presented study aims to evaluate whether the process of bin merging biases the results.

Results of the ND280-only data fits with the standard covariance matrix and the fit binning matrix are compared in Fig. A.13. It is clearly visible that both fits give almost identical results.

Fig. A.14 shows a comparison of the posterior distributions for the CCQE E_b parameters from both fits. The results are also consistent, but we can see that the fitter has more freedom to explore the phase space when using the fit binning matrix.

Fig. A.15 shows the predicted FD spectra after propagating the ND constraints from the two fits. The uncertainties on the plots come only from ND-constrained parameters (FD detector systematic errors are not included). The FD posterior predictive distributions are almost identical, confirming that the bin merging process used in the standard ND280 detector covariance matrix doesn't impact the results.

---

[4] A single MCMC step takes around 20% more time.

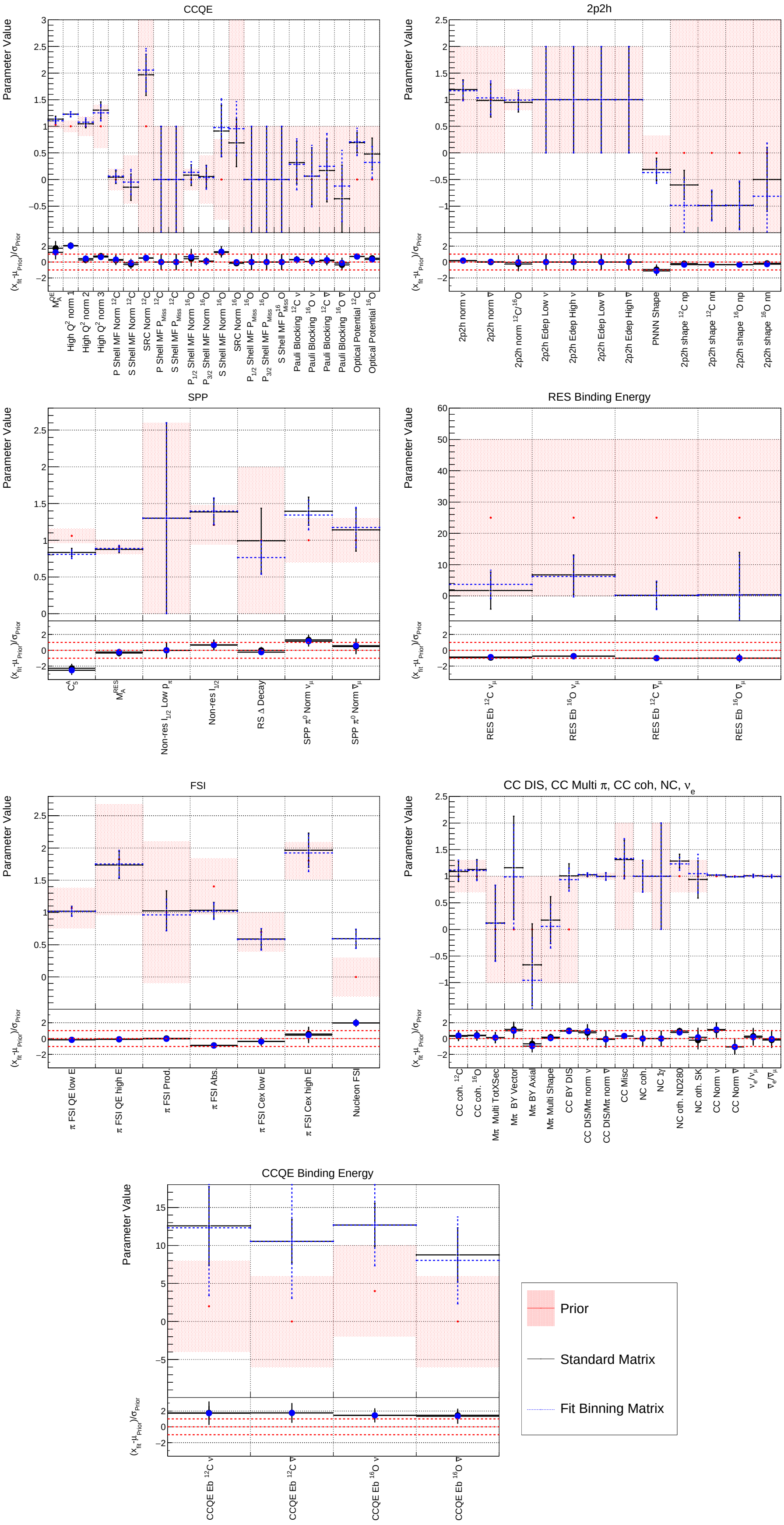

FIGURE A.13: Overlay of cross-section parameters from the fits using different ND280 covariance matrices.

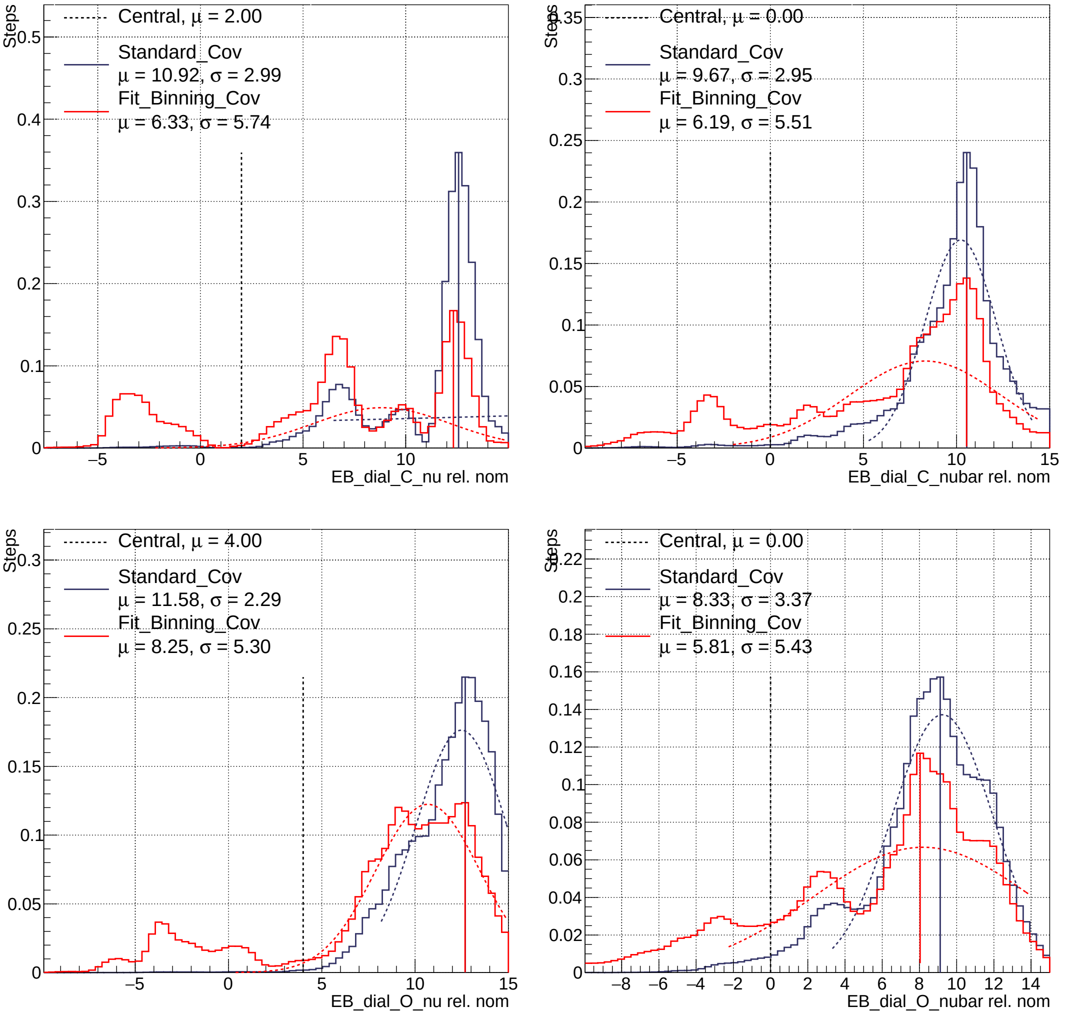

FIGURE A.14: Overlay of posterior distributions for the CCQE E_b dials from the fits with different ND280 covariance matrices.

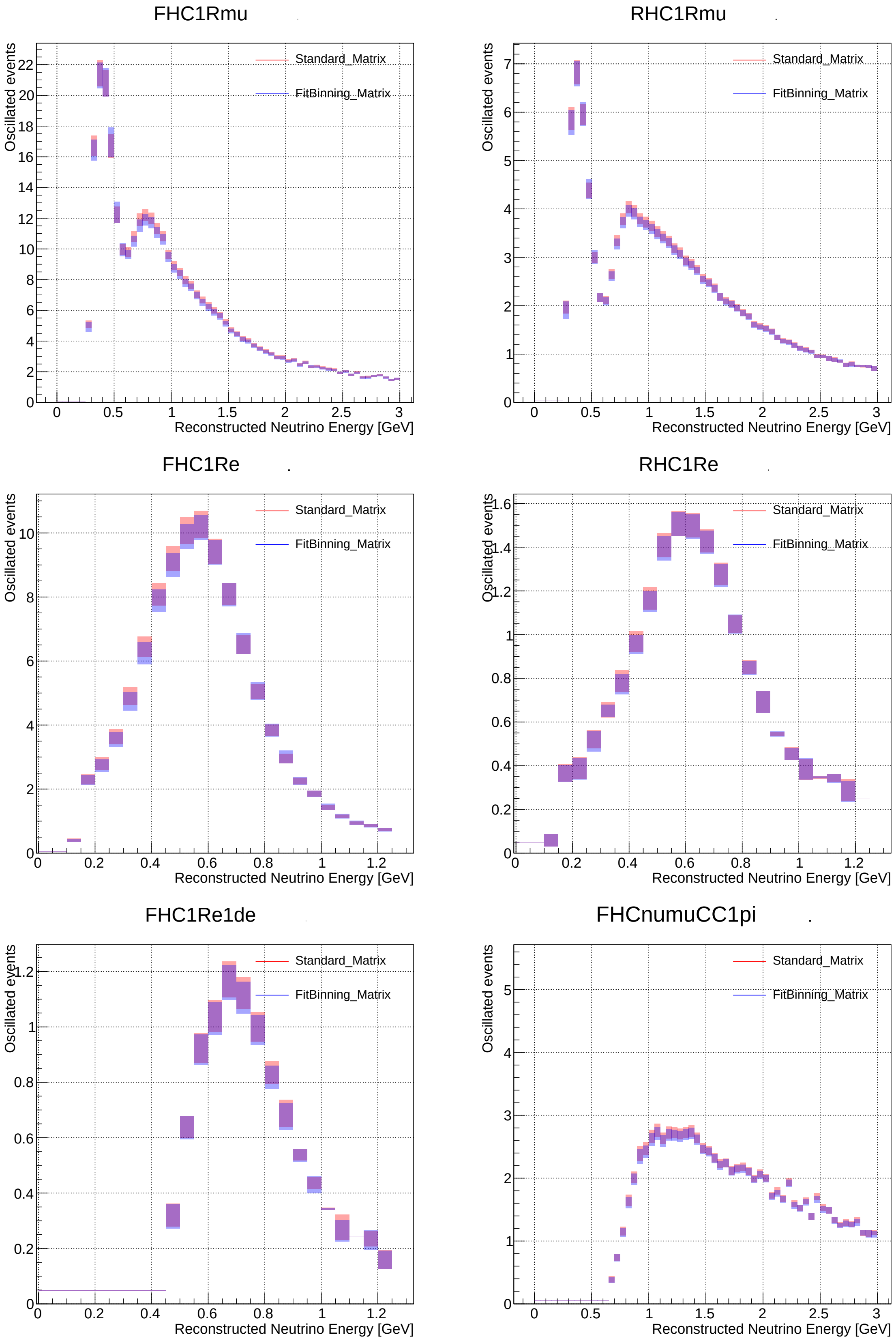

FIGURE A.15: FD posterior predictive distributions obtained using ND280 constraints from the fit with the standard covariance matrix and with the fit binning matrix.

A.5 Fake Data Studies

In the official ND280 fit, a particular set of neutrino interaction models is used. There are many models available in the neutrino generators; however, generating MC with all possible models would require huge computer resources, which are not available. However, what can be done is to reweight MC to a different cross-section model and treat it as data (fake data). Then, the fit of the official MC to the fake data is performed (Fake Data Study, FDS). This allows to estimate the impact of using a different cross-section model but also whether the current systematic parameters give enough freedom to account for such changes in predictions.

In the official T2K analysis, the SF model is used, while in the past (before 2020), T2K used the Local Fermi Gas (LFG) model [124]. As the first FDS, we will discuss changing SF to LFG. In Fig. A.16 we can see that the nominal MC overestimates the fake data, so we can expect some parameters to be strongly shifted after the fit. When looking at the exemplary posterior predictive distribution, we see very good agreement with fake data, which means the cross-section model offers enough freedom to the fitter to accommodate for the model change.

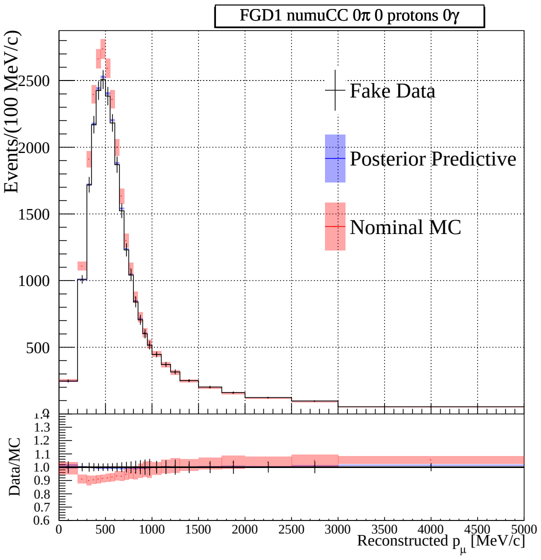

FIGURE A.16: Nominal MC and Posterior Predictive distribution for SF to LFG fake data fit.

In Fig. A.17 we compare the parameter values from Asimov fit and FDS. We observe that Pauli blocking dials are pulled to higher values, resulting in the suppression of low Q^2, which is expected as nominal MC overestimates fake data.

In Section 4.4 it was mentioned that we use three `high` Q^2 `norm` parameters rather than 3-component or Z-expansion models [35]. Both models cannot be used in the fit, as they are described by a few parameters that are highly dependent on each other. This means that a one-dimensional spline response will not work properly, as varying two parameters simultaneously will not give the same response as varying them separately. In such a case, one would need multi-dimensional splines, which are currently not implemented. However, it is possible to use the alternative models in fake data studies, as we need to reweight MC only once there.

Firstly, let's consider the 3-component FDS results presented in Fig. A.18. Values of `high` Q^2 `norm` parameters are strongly pulled from their priors, as expected, because those parameters are supposed to mimic the effect of the 3-component model. Fig. A.19 shows an exemplary posterior predictive distribution and fake data predictions, both of which are in

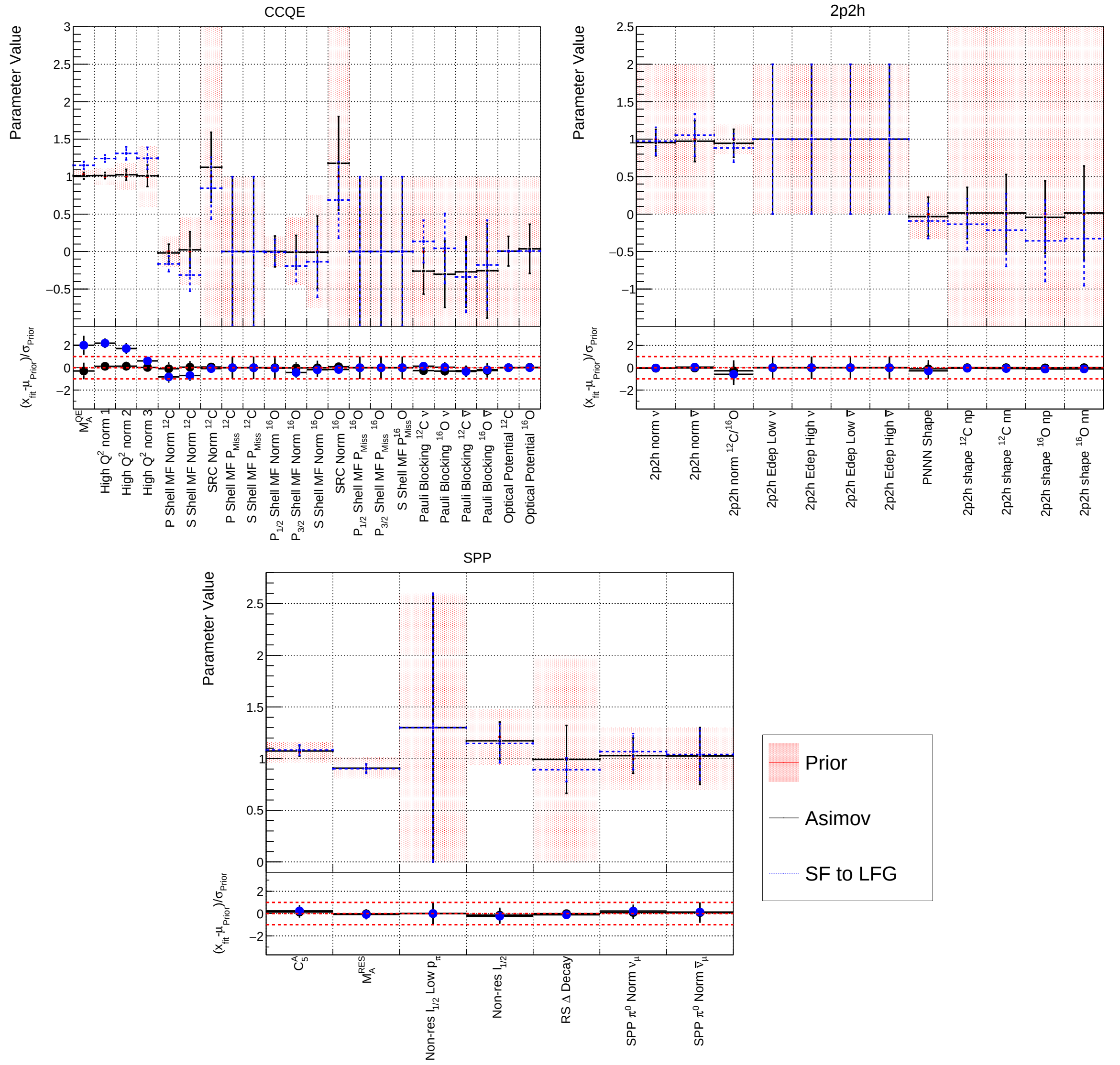

FIGURE A.17: Comparison of postfit parameter values from Asimov fit and SF to LFG FDS.

very good agreement, demonstrating that the fit has converged, and thus we can conclude that our model provides enough freedom.

As for Z-expansion FDS, the results are shown in Fig. A.20. Since Z-expansion has a much smaller impact compared with 3-component, the parameters are in most cases very close to their prior values. This conclusion is reinforced by studying the posterior predictive distribution and fake data predictions in Fig. A.21.

In total, 14 FDS were performed. Those mentioned here are the most interesting, considering the presented results. Other fake data studies include reweighting to CRPA Constrained Random Phase Approximation (CRPA) [125, 126], Martini 1π model [127] or changing the resonant model by modifying density matrix elements in the Feynman-Kislinger-Ravndal (FKR) model [47].

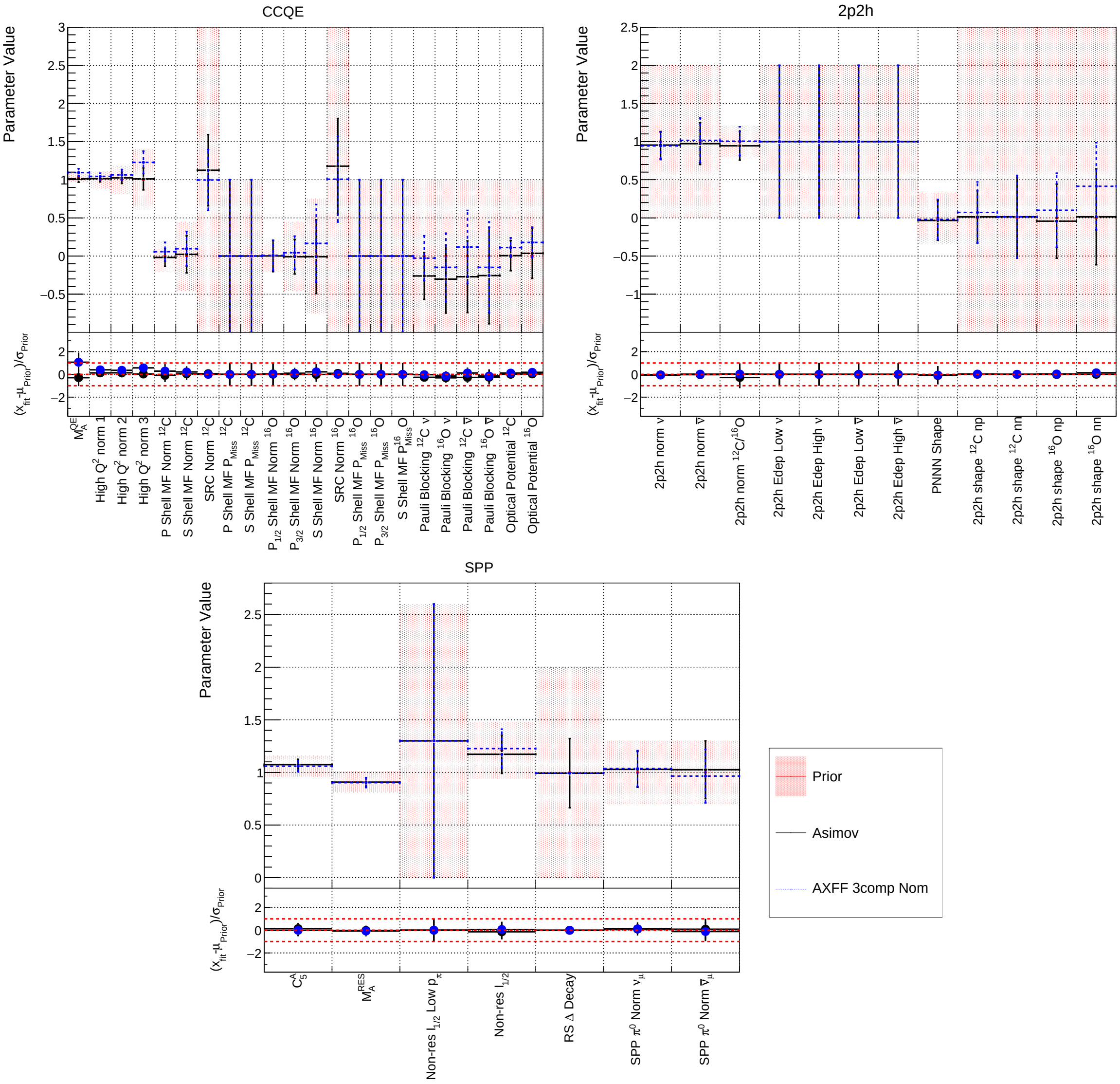

FIGURE A.18: Comparison of postfit parameter values from Asimov fit and 3-component FDS.

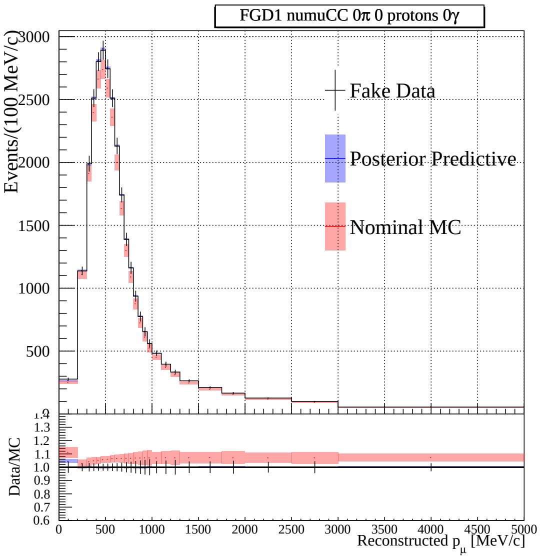

FIGURE A.19: Nominal MC and Posterior Predictive distribution from 3-component fake data fit.

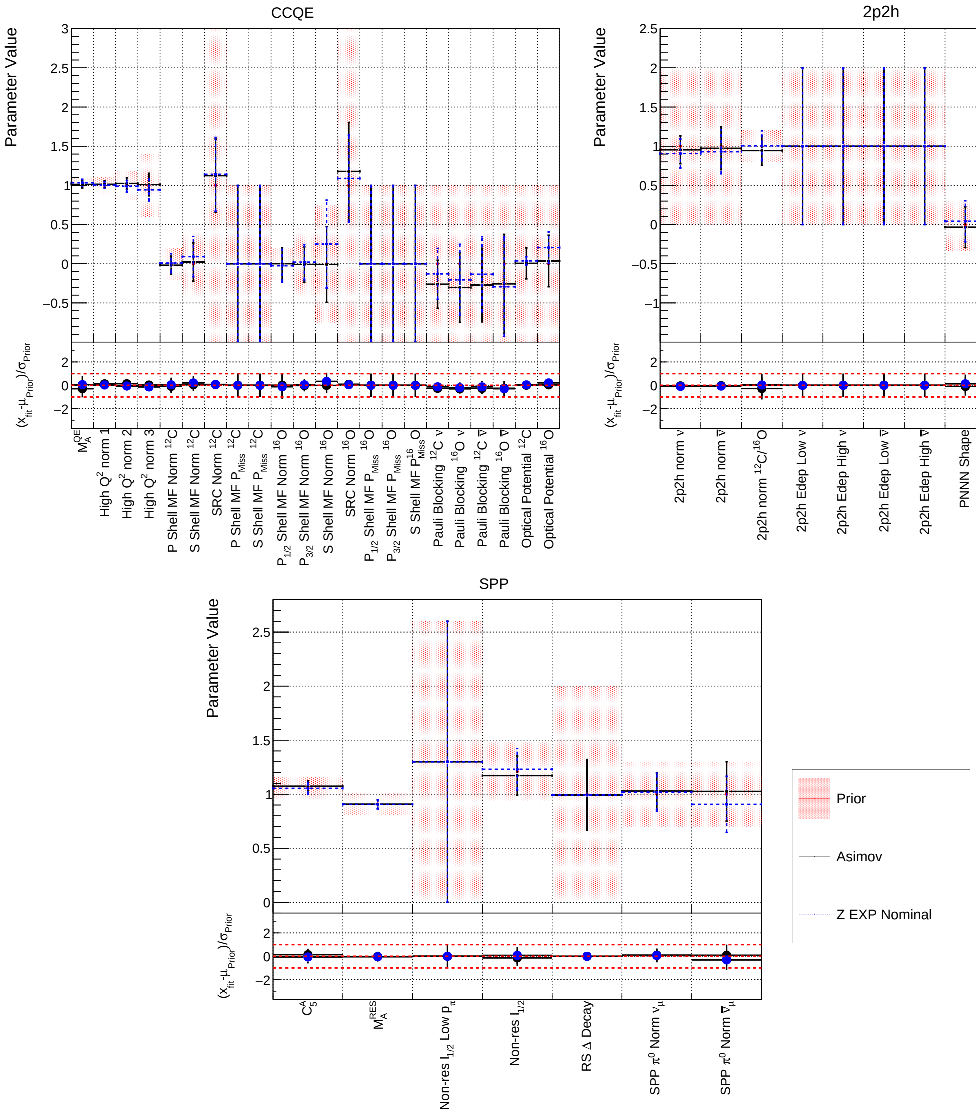

FIGURE A.20: Comparison of postfit parameter values from Asimov fit and Z-expansion FDS.

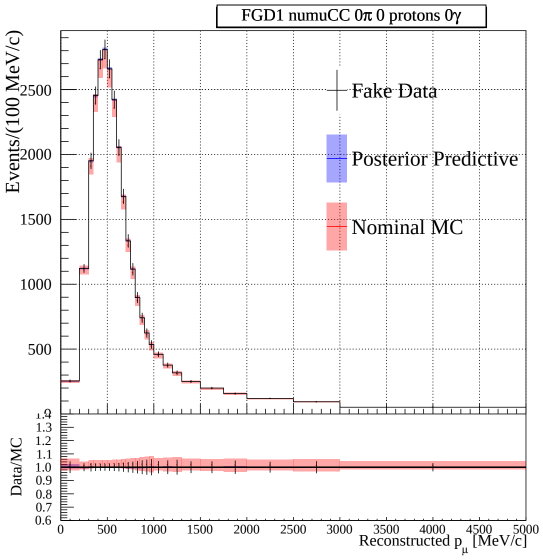

FIGURE A.21: Nominal MC and Posterior Predictive distribution from Z-expansion fake data fit.

A.6 Validating Against the BANFF Framework

In this Section, we show the selected results of the cross-validation of the BANFF and MaCh3 frameworks. For the sake of brevity, we only present examples of validation plots, while in actual analysis such plots were prepared and analysed for each parameter and each sample.

Fig. A.22 presents the LLH scans for both fitters, showing perfect agreement. A similar agreement was found for other parameters, which are not shown here. As was mentioned before, both fitters use the same event samples and have the same set of systematic parameters[5].

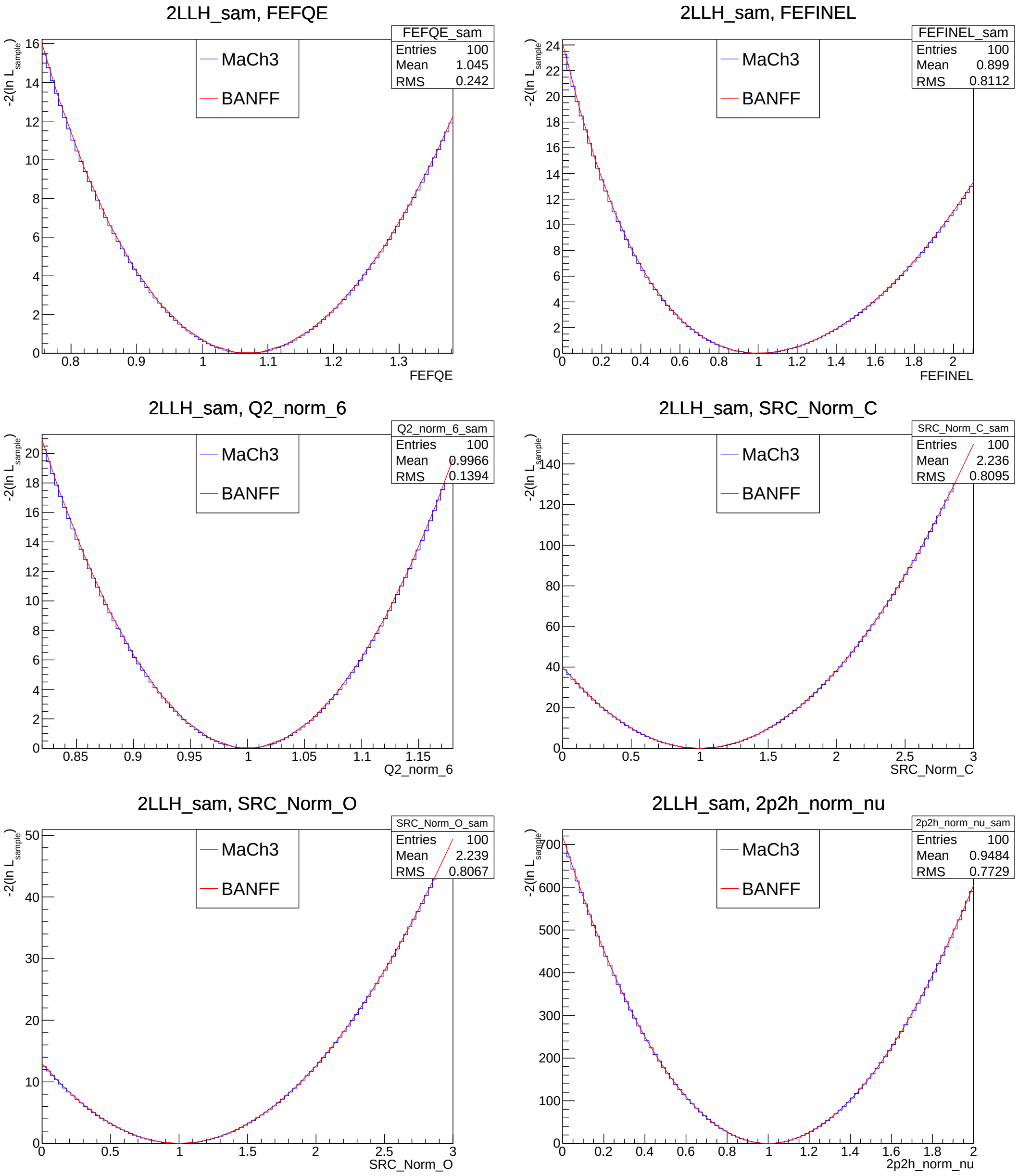

FIGURE A.22: Comparison of selected LLH scans for BANFF and MaCh3.

Results of ND280-only data fit for both fitters are shown in Fig. A.23 and A.24. Since BANFF has two different implementations of E_b, results for both are presented in blue and

---

[5] Implementation of CCQE E_b is different, though.

purple colours. Very good agreement is observed, which is even more compelling considering that MaCh3 shows HPD, while BANFF results present the best-fit point with the error calculated using Hessian. On the top-left plot, one can see that the Pauli blocking and optical potential parameters are different. BANFF, contrary to MaCh3, assumes each parameter distribution is Gaussian; however, BANFF's best fit is overlapping with one of the peaks in non-Gaussian MaCh3 posterior distribution. Furthermore, as shown in Appendix A.10, Pauli blocking and optical potential parameters are strongly correlated with CCQE E_b parameters, which are implemented differently in both fitters. In summary, those differences are expected due to framework differences and are well understood. When it comes to `2p2h shape` ^{12}`C np`, the difference is related to the spline mirroring being used at BANFF due to shortcomings of MINUIT[6]. If we make a mirror reflection of the BANFF point with respect to -1, the results are identical to MaCh3, hence the conclusion that both fitters agree.

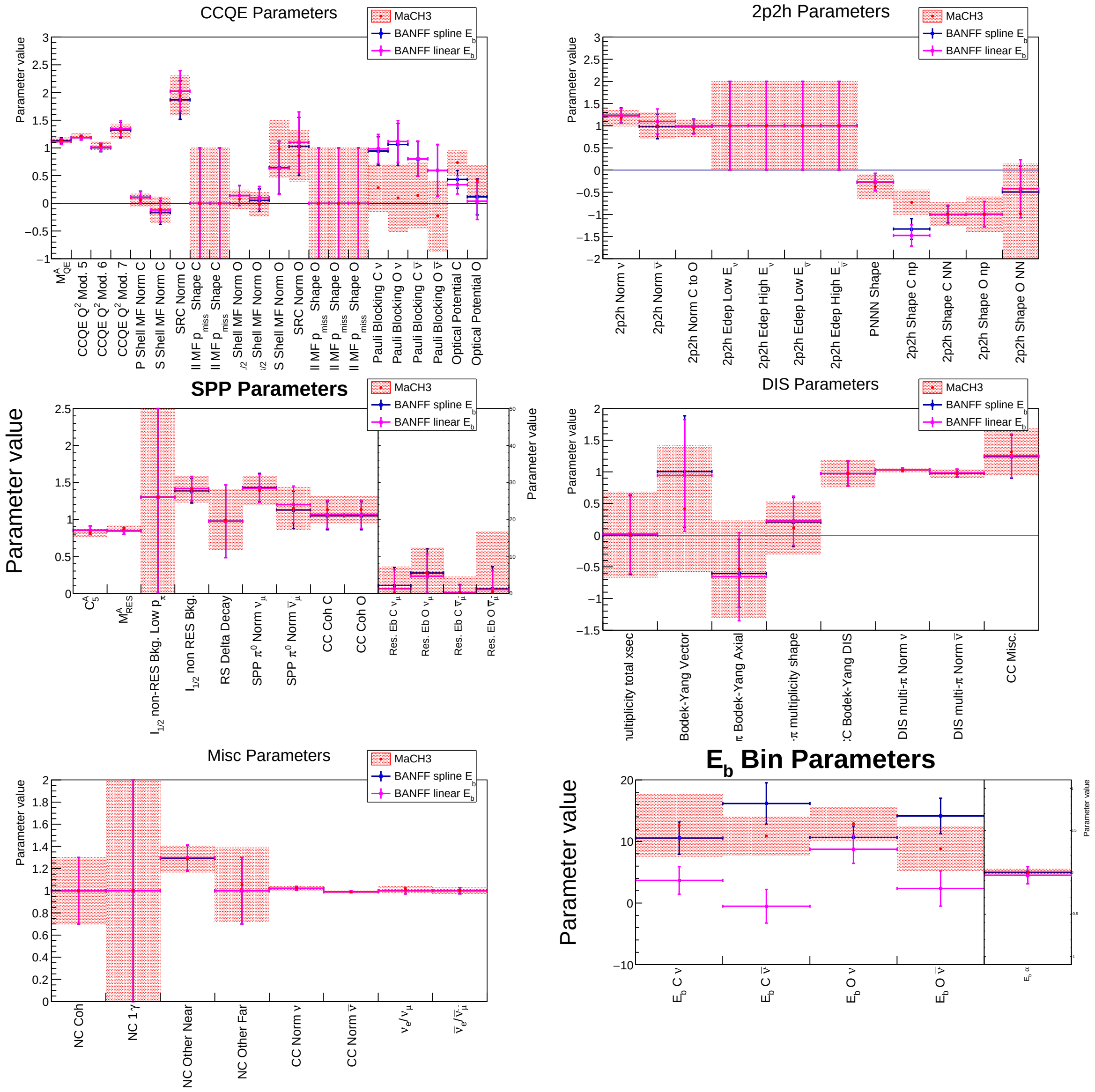

FIGURE A.23: Overlay of postfit cross-section parameters for BANFF and MaCh3.

---

[6] At boundary function is not differentiable, impacting Hessian matrix calculations.

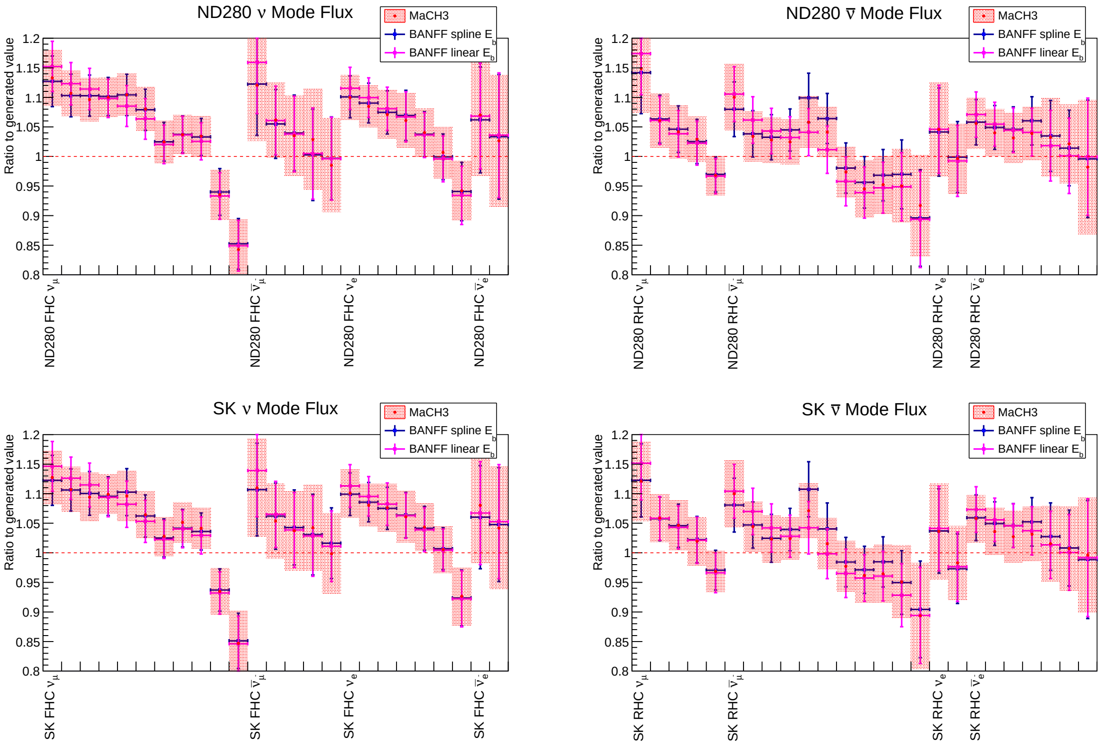

FIGURE A.24: Overlay of postfit flux parameters for BANFF and MaCh3.

Finally, we compare the ND spectra in Fig. A.25 for FGD1 proton-tagged samples. For MaCh3 those are posterior predictive distributions, while for BANFF the spectra were reweighted to the best-fit parameters values. Even though the methods differ, the results are consistent.

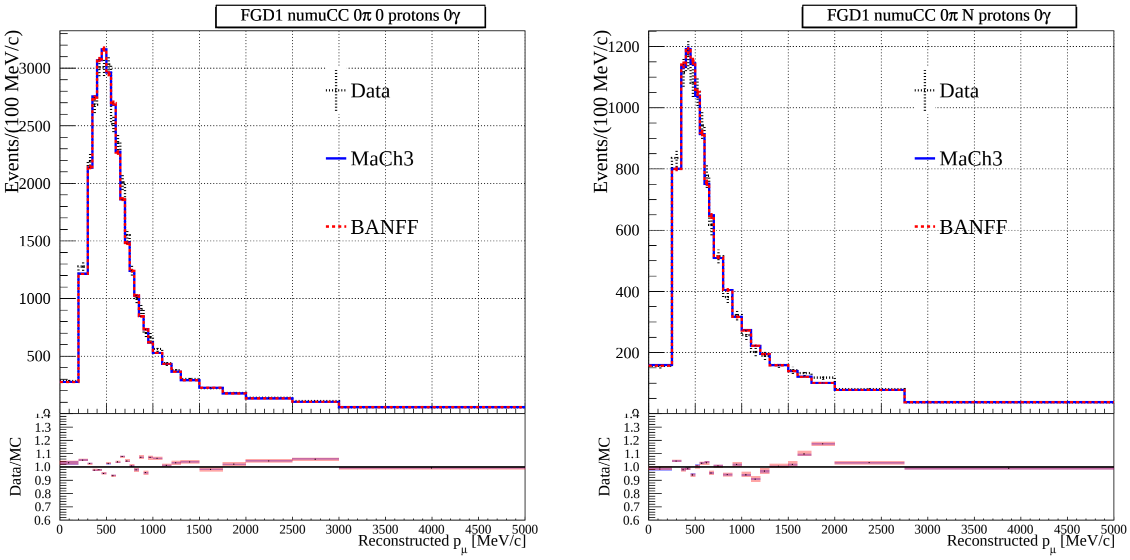

(A) FGD1 FHC CC0π-0p-0γ

(B) FGD1 FHC CC0π-Np-0γ

FIGURE A.25: Overlay of data, BANFF spectra at best-fit values and MaCh3 posterior predictive distributions for proton-tagged samples in FGD1.

A.7 Alternative Likelihood - IceCube

In the official ND280 analysis, the Poisson likelihood with the Barlow-Beeston correction was used (Eq. 5.11 on page 72); however, there is an alternative likelihood definition described by the IceCube collaboration in equation 3.16 in [128], which takes the form:

$$-2log\mathcal{L} = -2\sum_i \left(a_i \log(b_i) + \log[\Gamma(N_i^{\text{data}} + a)] - (N_i^{\text{data}} + a)\log(b_i + 1) - \log[\Gamma(a_i)]\right), \tag{A.1}$$

where the auxiliary variables $a_i = N^{\text{gen}}_{\text{MC},i} b_i + 1$ and $b_i = N^{\text{gen}}_{\text{MC},i} / \sum w_i^2$.

An example of an LLH scan using IceCube likelihood is shown in Fig. A.26. What may look odd is the fact that it is not equal to 0 at prior values, as in the case of Poisson+Barlow-Beeston likelihood. As it will be shown later, this poses no threat to fitter convergence, as the offset is constant and cancels out when we calculate $\Delta\chi^2$.

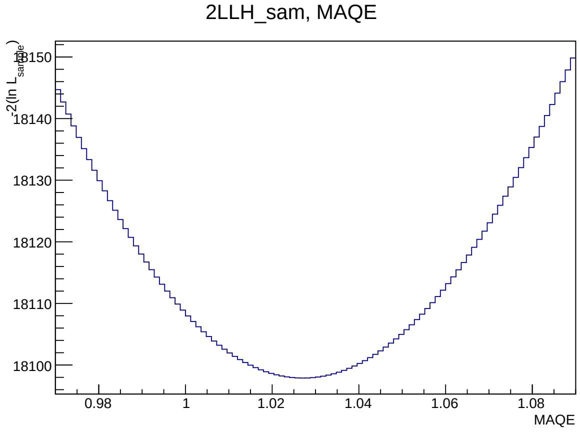

FIGURE A.26: Example of IceCube LLH scan.

Barlow-Beeston formalism neglects the variance of a sum of the square of the weight (w_i^2) [128], hence it is only valid if the weight distribution for each process is narrow. As a consequence, it was necessary to keep values of w_i^2 at their priors when calculating the Barlow-Beeston correction in the official ND280 analysis. According to the authors of IceCube LLH, their likelihood includes the variance of a sum of the square of the weight; thus, when using IceCube LLH, it was possible to update w_i^2 values during the fit[7]. In this Section, we compare fit results obtained with Poisson LLH, Poisson LLH with Barlow-Beeston correction, and IceCube LLH. In IceCube LLH, w_i^2 were updated during each iteration of the fit, whereas for Poisson LLH with Barlow-Beeston correction, w_i^2 were fixed at prior values. For Poisson LLH, there is no term depending on w_i^2.

The results of the ND280-only data fit are shown in Fig. A.27. As can be seen, the choice of likelihood does not impact the results. The reason might be that T2K ensures to have significantly more generated MC than data, resulting in a small MC statistical error.

As the final proof, Fig. A.28 shows the predicted FD spectra after the ND constraints coming from the aforementioned fits. Since the differences at ND were minimal, they are also negligible at FD.

In conclusion, the choice of LLH and fixing w_i^2 for the Barlow-Beeston correction calculation doesn't bias the results. IceCube LLH is statistically more correct, though. However, it was not used in the official ND280 analysis due to technical reasons, as the second fitter (BANFF) did not have IceCube LLH implemented.

---

[7] According to the authors, IceCube LLH performs much better for a low amount of data, although this isn't tested here.

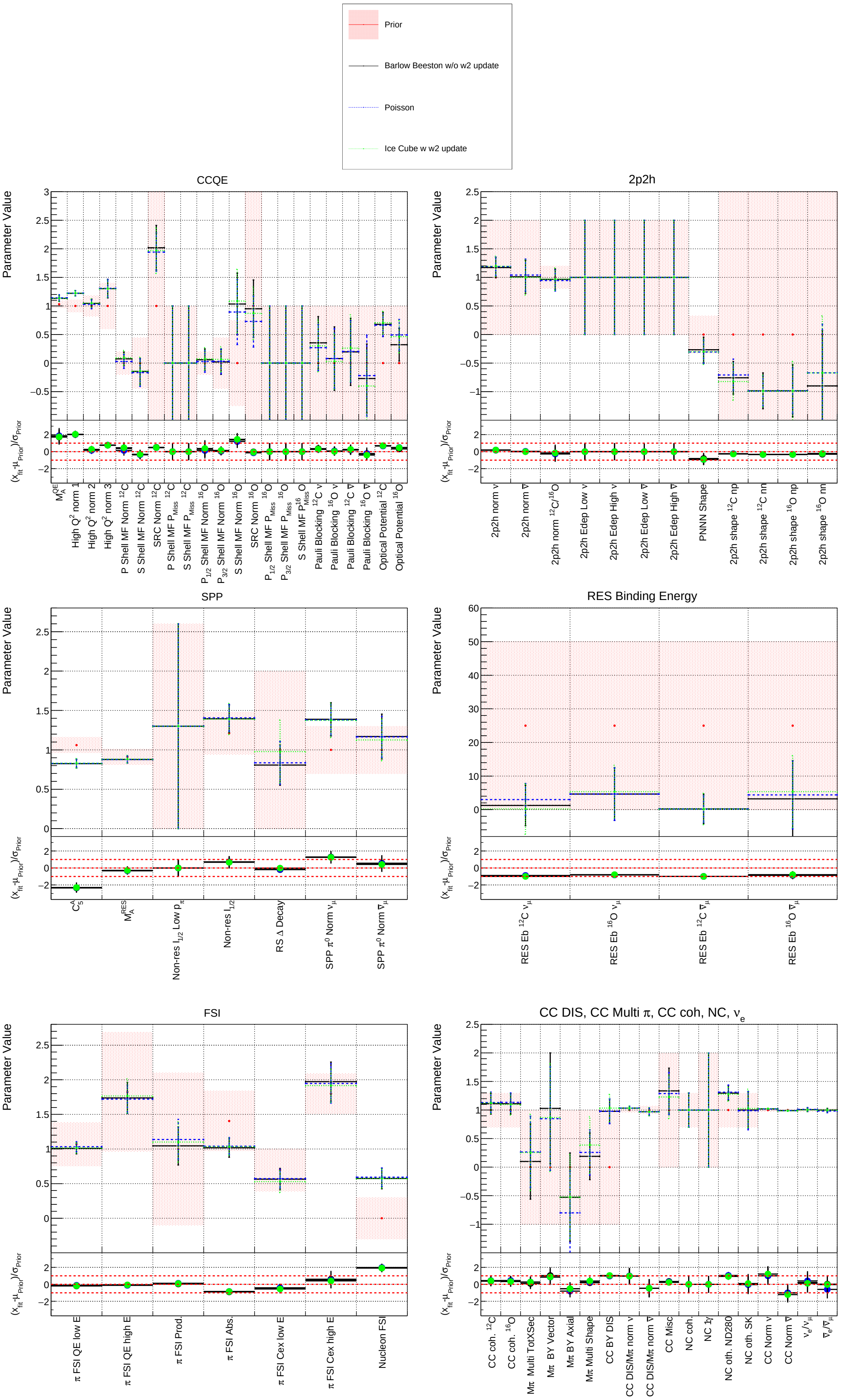

FIGURE A.27: Cross-section parameters overlayed for fits with different LLH definitions.

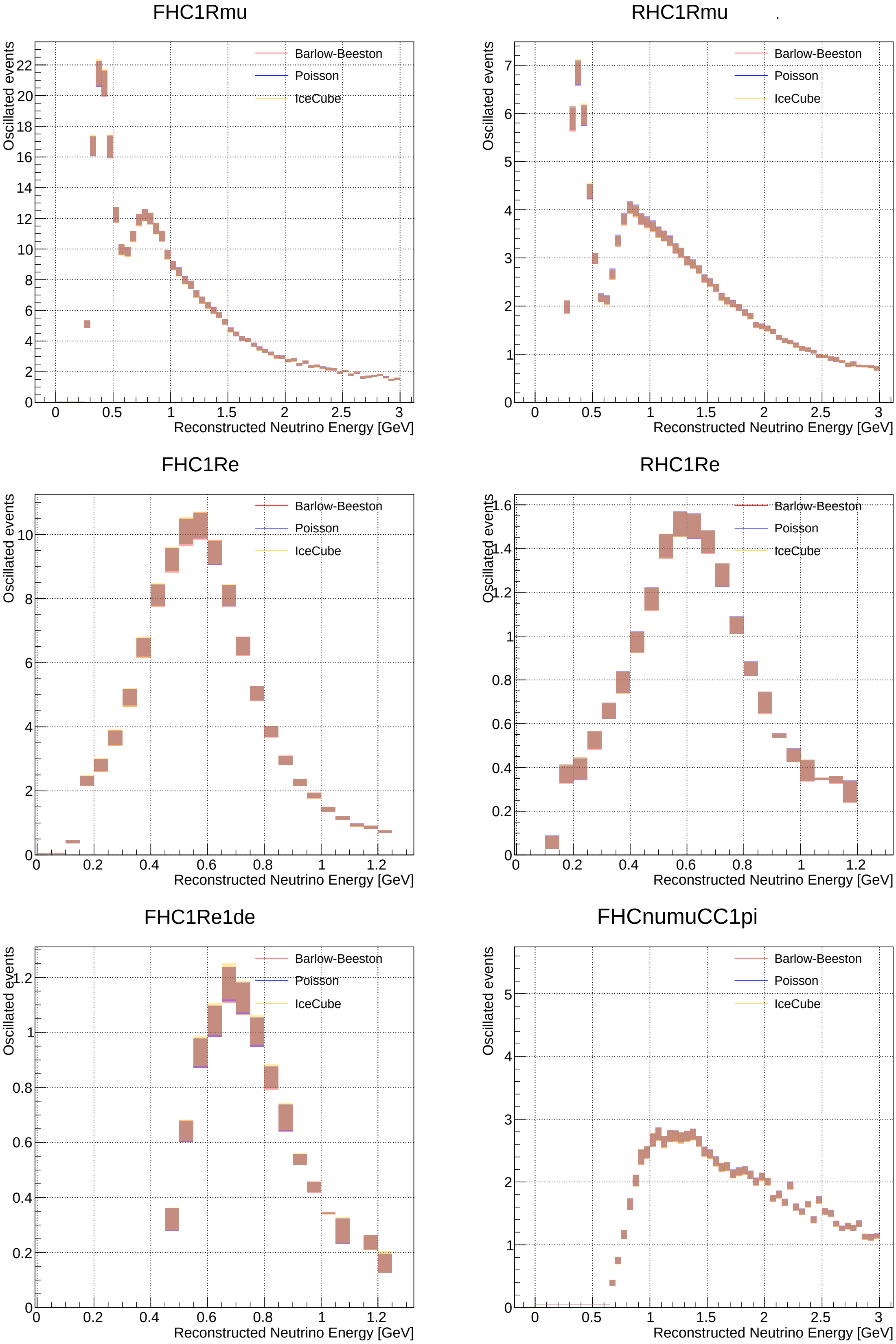

FIGURE A.28: FD posterior predictive distributions obtained using ND280 constraints from the fits with different LLH definitions. The uncertainties come only from ND-constrained parameters.

A.8 Posterior Predictive p-Value

Since this analysis was performed using Bayesian reasoning, in this Section the Bayesian p-value, also known as the posterior predictive p-value, is discussed. The approach outlined here is based on [129–131].

Firstly, an ensemble of parameter values explored by the MCMC, once the stationary state has been reached, is used. We draw parameter values from a random MCMC step after *burn-in*[8] stage and build the ND280 predictions for each sample (by reweighting the nominal MC to drawn parameters values). Then, we statistically fluctuate the drawn prediction by applying Poissonian smearing to each bin. Afterwards, for each sample, we calculate $-2\log\mathcal{L}_{\text{Stat}}$ between the drawn prediction and its statistical fluctuation: $-$*2LLH(Draw Fluc, Draw)*, and similarly between the drawn prediction and the data distribution: $-$*2LLH(Data, Draw)*. We repeat this process a few thousand times. An example of $-$*2LLH(Data, Draw)* vs. $-$*2LLH(Draw Fluc, Draw)* is shown in Fig. A.29. In this example, we only consider the p-value for one ND280 sample (FGD1 FHC CC-Other-0γ), but depending on chosen ensemble, a global p-value for all samples can be calculated as well.

One can think of $-$*2LLH(Data, Draw)* as a term describing the systematic variance as each draw has different values of systematic parameters. An increase in the number of dials would result in a greater spread of this distribution. $-$*2LLH(Draw Fluc, Draw)* informs about the vulnerability to statistical fluctuations.

To calculate the p-value, we count the draws with the $-$*2LLH(Data, Draw)* smaller than $-$*2LLH(Draw Fluc, Draw)* (below the red line on the picture). In such a case, we can say the draw is likely given the data distribution. The p-value is the ratio of number of draws below the $y = x$ line to all considered draws.

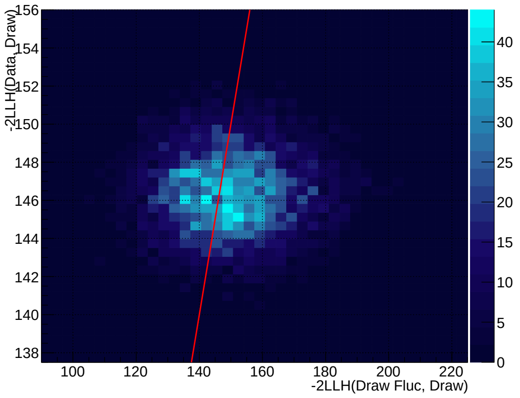

FIGURE A.29: Example of $-$*2LLH(Data, Draw)* vs. $-$*2LLH(Draw Fluc, Draw)* for FGD1 FHC CC-Other-0γ sample. Bayesian Posterior Predictive p-value is calculated as the ratio of points below the $y = x$ line to all considered draws and in this example is p-value $= 0.6$.

We identify two methods for calculating the p-value, statistically fluctuating two different distributions. The first method uses the prediction from the draw $-$*2LLH(Draw Fluc, Draw)*, and the other uses the averaged prediction for all draws and its statistical fluctuation $-$*2LLH(Pred Fluc, Draw)*. On average, we expect the p-value from the second method to be better.

Bayesian posterior predictive p-value is meant to estimate how likely we are to observe the data described by our postfit model if we were to take the same amount of data again. Therefore, it is a much more “demanding” p-value test than the frequentist p-value, which uses the larger prior parameter phase space. Furthermore, since we are propagating the

---

[8] See Section 5.4 on page 76.

ND280 fit result to a much lower statistics environment at SK, a poor p-value at ND280 does not imply a poor p-value at SK, due to the much larger impact of the statistical uncertainty at SK compared to ND280.

Tab. A.7 shows individual p-values for each ND280 sample, and many of those are low. Interestingly, the FGD1 FHC CC-Photon sample has a p-value of 0, whereas the FGD1 FHC CC-Other-0γ sample has a p-value of $\sim$0.6, which is very good. In previous analysis [80], before the introduction of the photon tagging, CC-Other was the sample with $p\text{-value} = 0$. One interpretation is that removing events with a photon from CC-Other improved the p-value and this might hint at our limited knowledge regarding π^0 production. However, it is also important to recognise the relevance of the change in the event count of the CC-Other sample in the two analyses; in the current analysis, the sample has shrunk by 80% (from 8000 events to 1700 events), which introduced much larger statistical uncertainty compared to the systematic uncertainty. Furthermore, we can see that the p-values for respective FGD1 and FGD2 samples are not consistent, suggesting differences in how well the interactions in the two are modelled. Finally, we can observe that, as expected, the fluctuation of averaged prediction results in a higher or equal p-value than the fluctuation of the draw. This is expected, as the aim is to estimate the vulnerability to statistical fluctuations, and the averaged prediction resembles data more than a single draw.

Sample	p-value	
	Fluctuation of Draw	Fluctuation of Prediction
FGD1 FHC CC0π-0p-0γ	0.008	0.015
FGD1 FHC CC0π-Np-0γ	0.022	0.032
FGD1 FHC CC1π-0γ	0.005	0.006
FGD1 FHC CC-Other-0γ	0.577	0.615
FGD1 FHC CC-Photon	0.000	0.000
FGD2 FHC CC0π-0p-0γ	0.015	0.029
FGD2 FHC CC0π-Np-0γ	0.379	0.435
FGD2 FHC CC1π-0γ	0.100	0.116
FGD2 FHC CC-Other-0γ	0.427	0.465
FGD2 FHC CC-Photon	0.033	0.048
FGD1 RHC CC0π	0.001	0.001
FGD1 RHC CC1π	0.013	0.018
FGD1 RHC CC-Other	0.022	0.025
FGD2 RHC CC0π	0.001	0.001
FGD2 RHC CC1π	0.106	0.118
FGD2 RHC CC-Other	0.034	0.045
FGD1 RHC BKG CC0π	0.022	0.028
FGD1 RHC BKG CC1π	0.010	0.013
FGD1 RHC BKG CC-Other	0.042	0.044
FGD2 RHC BKG CC0π	0.021	0.028
FGD2 RHC BKG CC1π	0.005	0.007
FGD2 RHC BKG CC-Other	0.132	0.151
Global	0.000	0.000

TABLE A.7: Posterior predictive p-values for each ND280 sample.

The global p-value is 0.00 using both described methods, as shown in Fig. A.30. While it is very discouraging, an identical p-value was obtained in the previous analysis [80]. However, this doesn't discredit T2K analysis. Firstly, we will discuss why such results do not compromise the analyses and then what can be done to improve the p-value in the future.

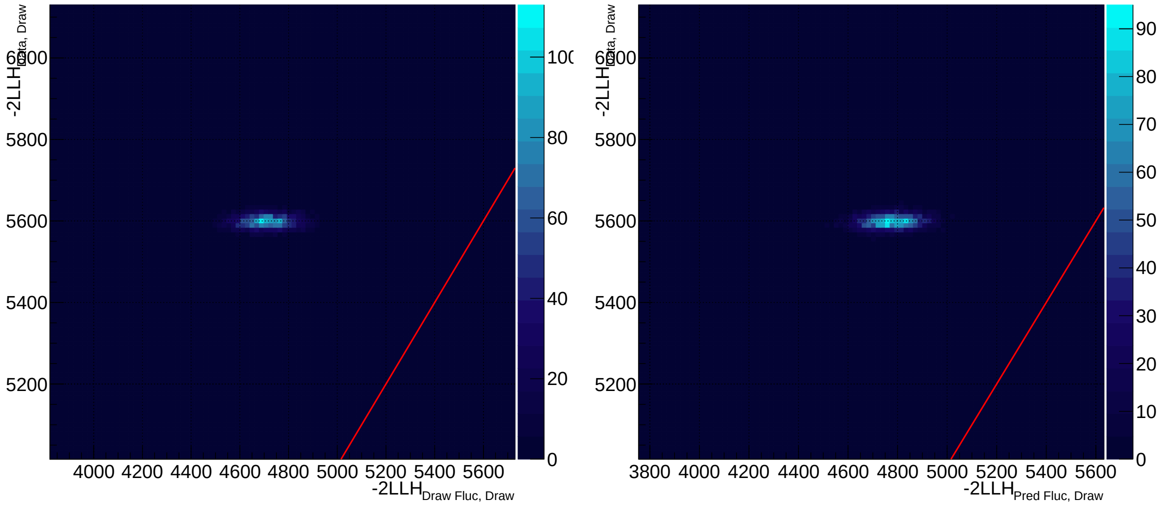

(A) Fluctuation of draw

(B) Fluctuation of prediction

FIGURE A.30: Distribution of *−2LLH(Data, Draw)* vs. *−2LLH(Draw Fluc, Draw)* using the two methods described in the text for all ND280 samples.

Since the main results of T2K analysis are the oscillation parameters and the ND280-only fit is only an intermediate step, we should study more carefully the p-value for FD analysis. Fig. A.31 presents the distribution of *−2LLH(Data, Draw)* vs *−2LLH(Draw Fluc, Draw)* obtained in the same manner, but for all six FD samples from ND+FD joint-fit. In this case, the global p-value is very good and equal to 0.86. Since FD has significantly fewer events, it is no surprise that by collecting more data we would obtain better results, as this is the interpretation of the posterior predictive p-value.

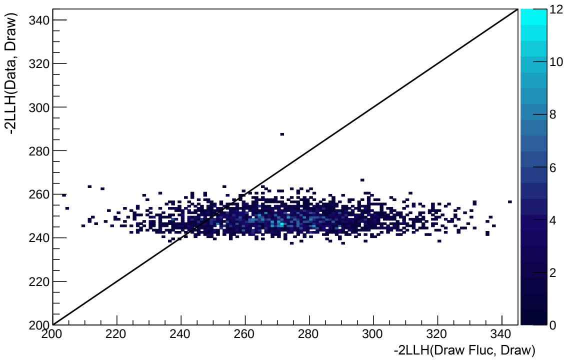

FIGURE A.31: Distribution of *−2LLH(Data, Draw)* vs *−2LLH(Draw Fluc, Draw)* for all FD samples.

Additional tests were performed to validate and better understand the interpretation of this p-value. In the first test, we sampled from the official ND280-only fit, while only a limited number of POT was used for creating the predictions. This is done to mimic FD-like p-value: as the systematic error is constrained in the same way, the spread of *-2LLH(Draw Fluc, Draw)* is bigger with fewer data, because we become more vulnerable to statistical fluctuations. In Fig. A.32 one can clearly observe that reducing the available data sets allows to obtain better p-value at ND. The results may seem obvious; however, since ND and FD use different frameworks for calculating p-value it was important to perform those checks as they haven't been done before.

An additional test was performed to finally confirm, that good FD p-value is driven by the statistical fluctuations. *−2LLH(Data, Draw)* RMS divided by *−2LLH(Draw Fluc, Draw)* RMS is

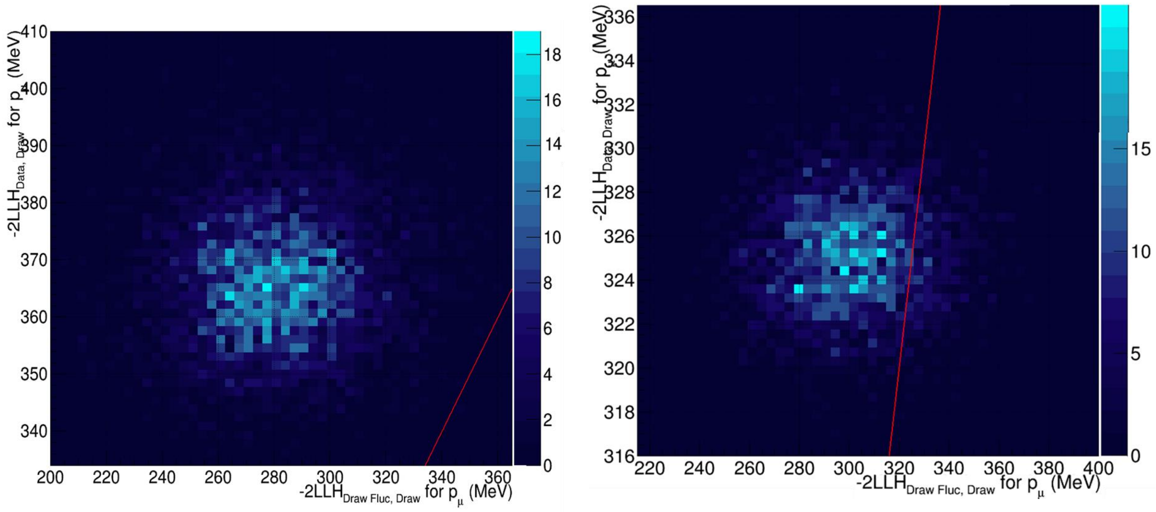

(A) 97.38×10^{19} POT, p-value $= 0.0003$ (B) 8.05×10^{19} POT, p-value $= 0.17$

FIGURE A.32: Distribution of $-2LLH(Data,\ Draw)$ vs $-2LLH(Draw\ Fluc,\ Draw)$ obtained by sampling from fit with the full data set and calculating the test statistics using only part of collected data.

shown in Tab. A.8. As can be seen, FD and ND with a restricted number of POT have a small relative spread of $-2LLH(Data,\ Draw)$ compared to $-2LLH(Draw\ Fluc,\ Draw)$, while the situation changes significantly for ND with the full statistics. Such a case might be interpreted as ND280 having too much data given its systematic model, suggesting a shortcoming in the T2K uncertainty model. The cross-section model is certainly not perfect, as was mentioned several times in the Thesis (for example, in Section 7.1.1). However, what needs changes most is the treatment of ND detector systematics.

ND280		
8.05×10^{19} POT	202.12×10^{19} POT	FD
11%	60%	20%

TABLE A.8: $-2LLH(Data,\ Draw)$ RMS divided by $-2LLH(Draw\ Fluc,\ Draw)$ RMS for p-value in three different configurations.

In the official analysis, the ND280 covariance matrix after bin merging is used (see Appendix A.4). This can lead to a lower p-value as, naively thinking, the fit binning matrix should result in a much higher variance of *-2LLH(Draw Fluc, Draw)*. T2K collaboration is working on introducing splines for detector systematic parameters in the same way that cross-section dials are handled. This way, pion SI, for example, would be treated similarly to cross-section dials.

Still, it was possible to calculate the p-value using the fit binning matrix. Tab. A.9 summarizes the p-value for each sample using both ND280 covariance matrices. It is clear that, when using fit binning, the p-value is better for the majority of samples. Unfortunately, the global p-value is still 0.

To better understand why the analysis with the fit binning ND280 covariance matrix gives better p-values, we checked the distributions of $-2LLH(Data,\ Draw)$ presented in Fig. A.33. When using the fit binning matrix, the spread is greater: 8.5 in comparison with 4.9 for the standard covariance matrix. The fit binning matrix has more parameters, which translates to greater variation; hence the p-value is better. Furthermore, when the fit binning is used, $-2\log\mathcal{L}_{Stat} = 366$ compared to 387 for the standard covariance matrix, indicating a marginally better fit.

Sample	p-value Fluctuation of Prediction	
	Standard Binning	Fit Binning
FGD1 FHC CC0π-0p-0γ	0.015	0.040
FGD1 FHC CC0π-Np-0γ	0.032	0.014
FGD1 FHC CC1π-0γ	0.006	0.020
FGD1 FHC CC-Other-0γ	0.615	0.624
FGD1 FHC CC-Photon	0.000	0.000
FGD2 FHC CC0π-0p-0γ	0.029	0.056
FGD2 FHC CC0π-Np-0γ	0.435	0.638
FGD2 FHC CC1π-0γ	0.116	0.156
FGD2 FHC CC-Other-0γ	0.465	0.510
FGD2 FHC CC-Photon	0.048	0.061
FGD1 RHC CC0π	0.001	0.007
FGD1 RHC CC1π	0.018	0.018
FGD1 RHC CC-Other	0.025	0.058
FGD2 RHC CC0π	0.001	0.024
FGD2 RHC CC1π	0.118	0.159
FGD2 RHC CC-Other	0.045	0.084
FGD1 RHC BKG CC0π	0.028	0.044
FGD1 RHC BKG CC1π	0.013	0.016
FGD1 RHC BKG CC-Other	0.044	0.048
FGD2 RHC BKG CC0π	0.028	0.046
FGD2 RHC BKG CC1π	0.007	0.008
FGD2 RHC BKG CC-Other	0.151	0.202
Global	0.000	0.000

TABLE A.9: Posterior predictive p-values for each sample using MaCh3 fits with different ND280 covariance matrices.

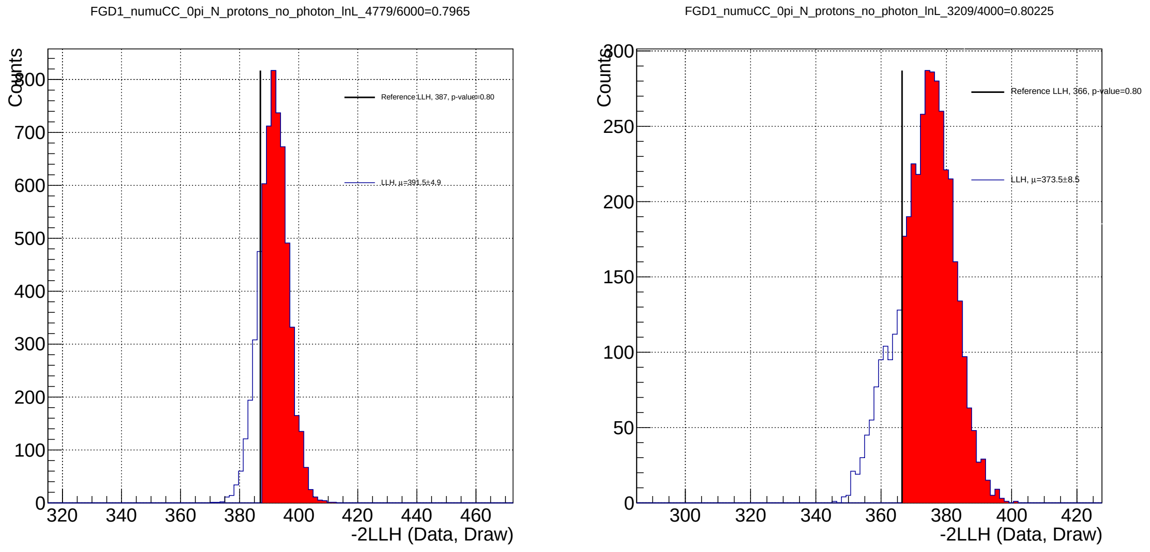

(A) Standard Matrix, $\sigma_{(\text{-2LLH})} = 4.9$

(B) Fit Binning Matrix, $\sigma_{(\text{-2LLH})} = 8.5$

FIGURE A.33: -2LLH for data and randomly selected draws using the standard ND280 covariance matrix (left), and the fir binning covariance matrix (right). Reference LLH (black line) indicates the value for posterior predictive. Both plots show the results for FGD1 FHC CC0π-Np-0γ sample.

A.9 Impact of ND Detector Uncertainty on FD Prediction Error

ND280 detector systematic errors are not propagated directly to FD; however, that doesn't mean that they have no impact on FD spectra uncertainties. This study aims to evaluate how big this effect is. Firstly, we extract the HPD of the ND280 detector parameters from the official ND280 fit. Then we run another ND280-only fit with the ND detector parameters fixed at their HPD values. This way, the ND detector parameters are set at values resembling the best-fit point but without any error.

Fig. A.34 summarises this study. We can observe smaller FD uncertainties when the ND detector parameters have no error. Since the ND detector parameters are strongly correlated with the cross-section and flux parameters, ND detector systematic error widens their distributions. The main conclusion of this study is that the uncertainty of FD predictions is not dominated by ND detector systematic error, which was tested here for the first time in T2K analysis history.

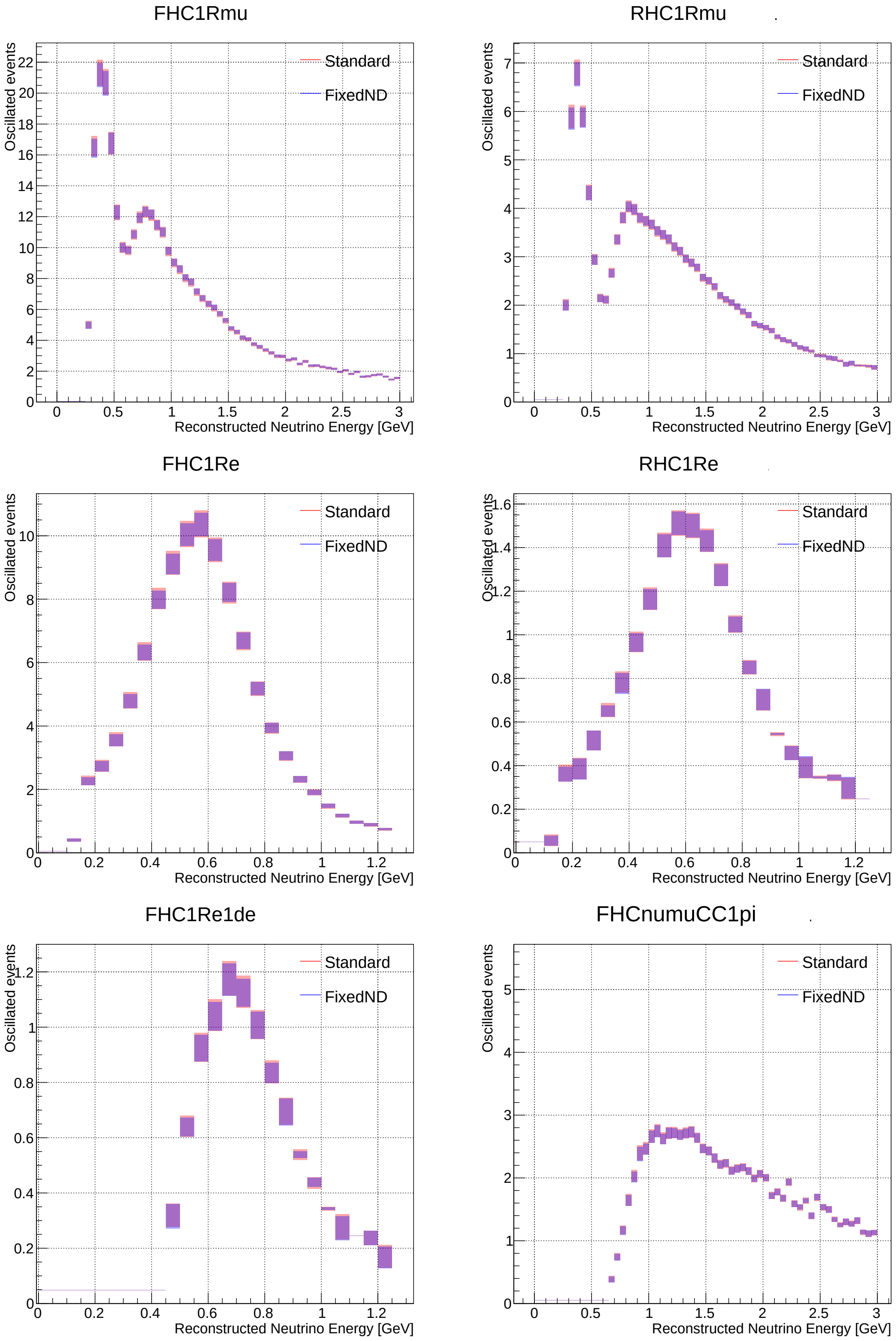

FIGURE A.34: FD posterior predictive distributions using constraints from official ND280-only fit and the fit with ND detector parameters fixed at their HPD values. The uncertainties come only from ND-constrained parameters.

A.10 Fixed CCQE E_b Parameters Study

In Section 6.2 the official ND280 data fit results were presented, where some parameters showed non-Gaussian posterior distributions. The implementation of the CCQE E_b parameters differs from that of the other cross-section parameters. Rather than reweighting events based on spline response, the CCQE E_b parameters migrate events from one bin to the other. Such event migration may be problematic because we use the Barlow-Beeston likelihood without updating w_i^2, so when an event migrates to another bin, the w_i^2 values remain unchanged. Therefore, an ND280-only data fit was performed with the CCQE E_b and α parameter (defined in Eq. 4.1 on page 57) fixed at their prior values.

Fig. A.35 shows the posterior distributions for parameters most influenced by this change. We can see that the fit prefers higher values of Pauli blocking parameters, which results in much stronger suppression at low Q^2. Also, the posterior distribution takes a different shape when the CCQE E_b and α parameters are fixed, especially for ^{16}O-related dials. Overall, we see shifts in the Pauli blocking and the optical potential posterior distributions. This confirms that Pauli blocking, optical potential and CCQE E_b are all highly correlated and we cannot fully distinguish the effects related to them at the ND280.

Predicted FD spectra were generated and no significant bias is observed, as presented in Fig. A.36. Thus, we conclude that results are not biased by the migration systematic when not updating w_i^2 in -2LLH calculation.

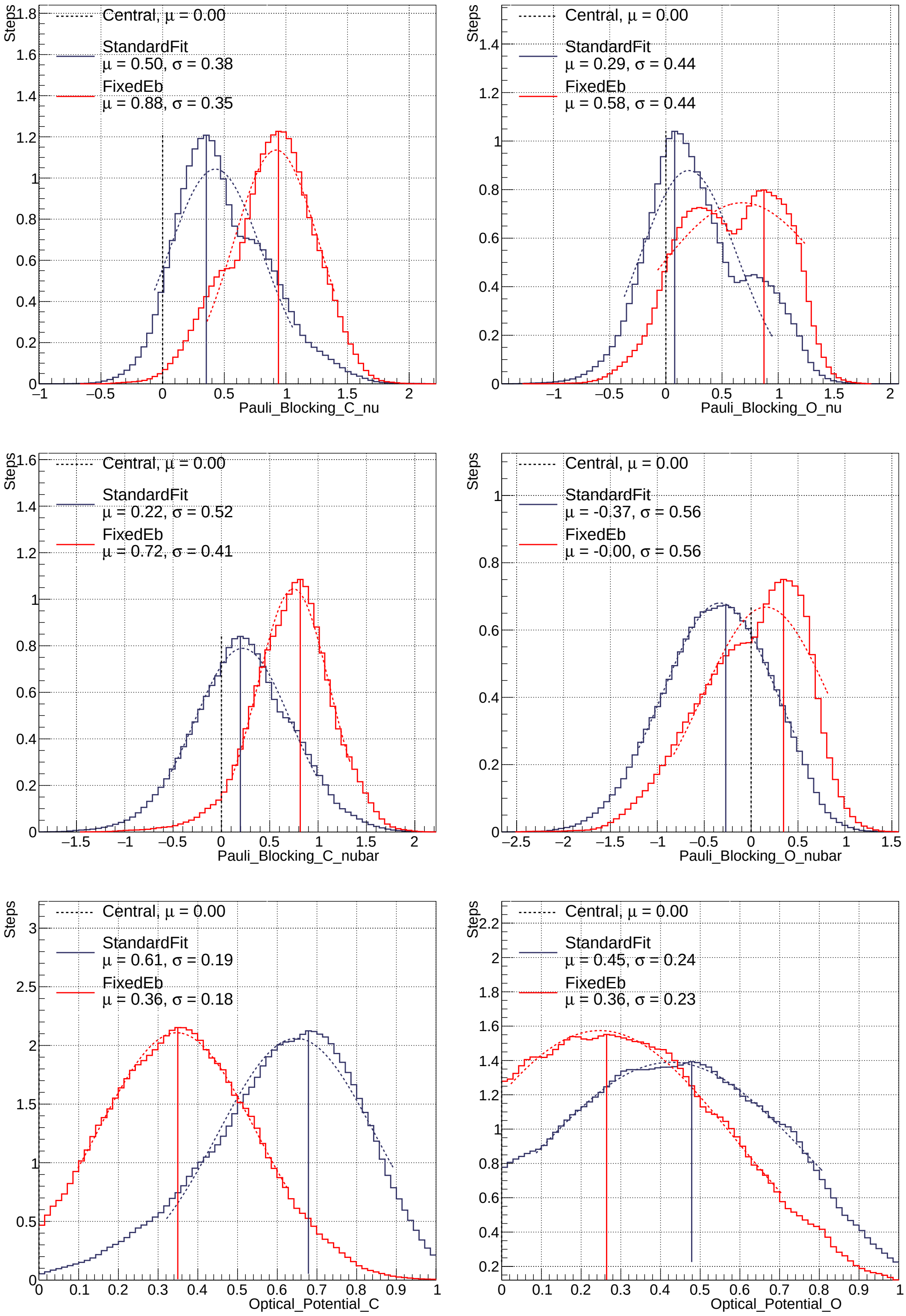

FIGURE A.35: Posterior distributions of selected parameters showing the impact of fixing CCQE E_b and α dials.

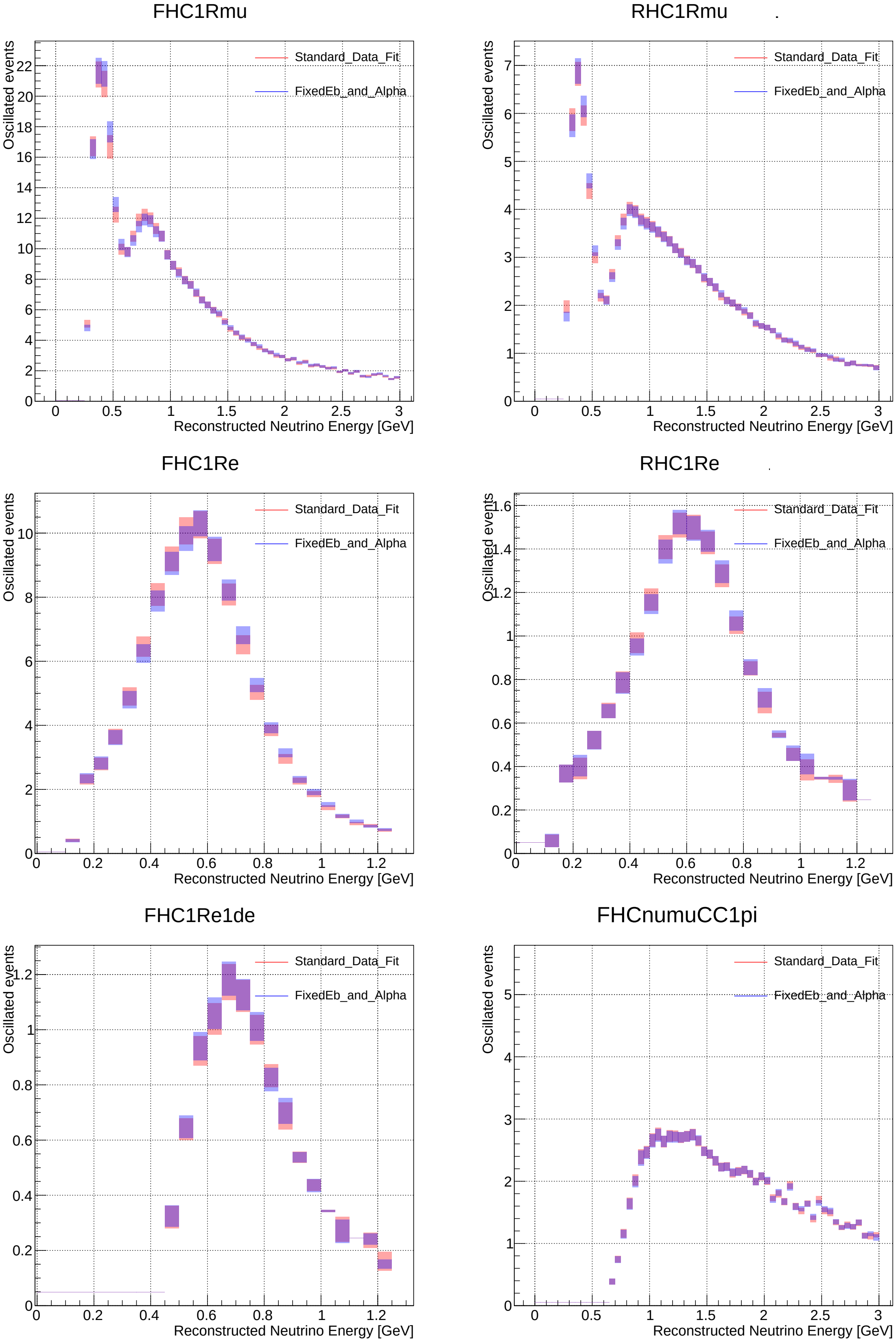

FIGURE A.36: FD posterior predictive distributions obtained using ND280 constraints from two ND280-only data fits with different settings of CCQE E_b and α dials. The uncertainties come only from ND-constrained parameters.

A.11 Principal Component Analysis of Flux Covariance Matrix

Principal Component Analysis (PCA) is a method used for reducing dimensionality, which should lower the number of operations necessary for MCMC to reach stationary state. However, in this study, we use PCA on the flux matrix to better understand why flux parameters responsible for low energy are shifted above value 1, while those responsible for high energy are pulled below value 1. To perform PCA, we need to find Eigenvalues and Eigenvectors for the flux covariance matrix, then sort them from highest to lowest, and finally remove Eigenvectors with the corresponding smallest Eigenvalues. Intuitively, the smaller the Eigenvalue, the smaller contribution to the system variance.

The left plot in Fig. A.37 shows the Eigenvalues of the flux matrix. The red histogram represents the Eigenvalues sorted from highest to lowest; the green histogram is the cumulative sum of absolute values; and the blue histogram shows the values from the red one divided by the total sum. We see that by setting the threshold to 10^{-5} marked as the vertical red line, we only remove 10^{-5} variation, while being able to cut some parameters (11 in this case).

The right plot in Fig. A.37 shows the Eigenvectors of the flux matrix, where the horizontal axis corresponds to the normal base and the vertical one to the decomposed or Eigen base. In PCA, the parameters in the decomposed base are used, but only the parameters in the normal base have physical interpretation, in this case, the normalisation of a particular region of E_ν. In consequence, we use the matrix in Fig. A.37 to transform from one base to another. In the same Figure, the green line shows which Eigenvectors are removed after the cut on Eigenvalues. After removing Eigenvectors, based on the threshold in the decomposed base, the numbers of matrix rows and columns are no longer equal.

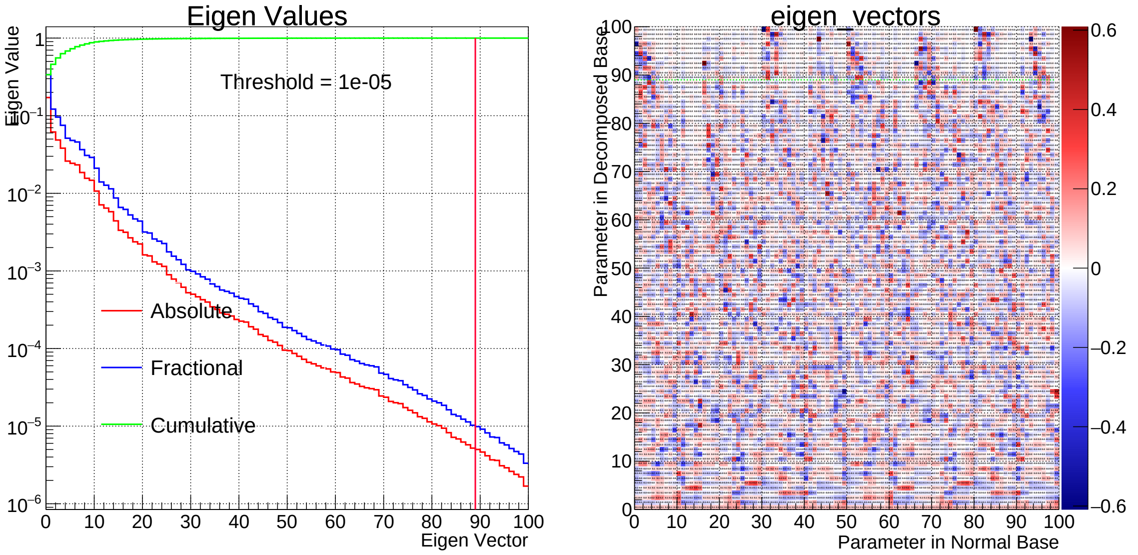

FIGURE A.37: Sorted Eigenvalues of the flux covariance matrix (left) and corresponding Eigenvectors (right).

It is worth mentioning that the parameters in the Eigen base are only used for proposing a step. After the step is proposed, the parameters are transformed from Eigen to normal base. This is necessary, as we can reweight events only using parameters in the normal base. Furthermore, we can diagnose posterior distributions in the normal base to interpret results.

Fig. A.38 presents the posterior distributions for selected cross-section parameters. The results are presented for the official ND280 analysis without PCA and two ND280-only data fits using PCA with different thresholds, resulting in a reduction of the flux dials number from 100 to 89 and 75. The three fits are in very good agreement with negligible differences.

The agreement for cross-section parameters not presented here is similar to the presented ones.

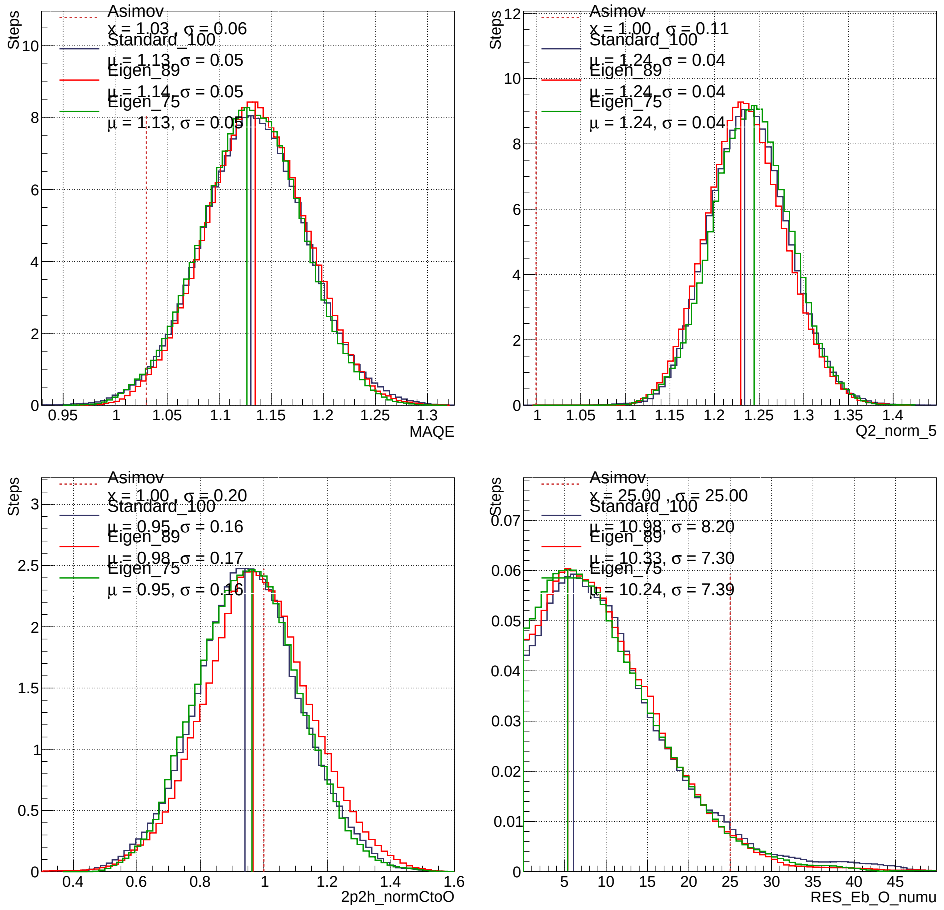

FIGURE A.38: Posterior distributions for selected cross-section parameters from the ND280-only data fits with different PCA thresholds and the official ND280 fit (without PCA).

Fig. A.39 shows the overlay of flux parameters, and similarly, as for cross-section dials, we observe a good agreement. Interestingly, the biggest discrepancy is seen for flux parameters corresponding to low or high neutrino energy, for which the constraints are weak. This might indicate that those parameters are driven by correlations, so when using PCA the results start to diverge.

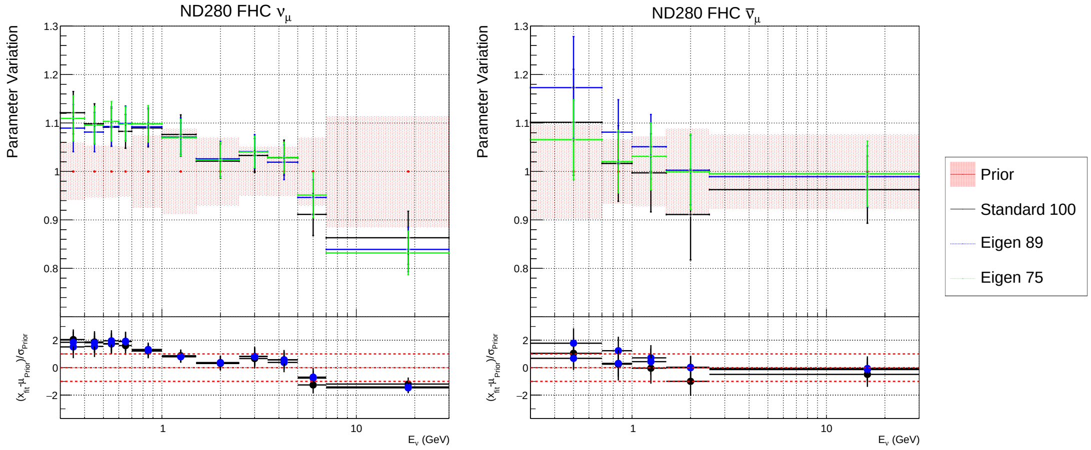

FIGURE A.39: Overlay of selected flux parameters from the ND280-only data fits with different PCA thresholds and the official ND280 fit (without PCA).

Lastly, we compare predicted FD spectra after propagating the aforementioned fits in Fig. A.40. As can be seen, using PCA doesn't bias the predictions.

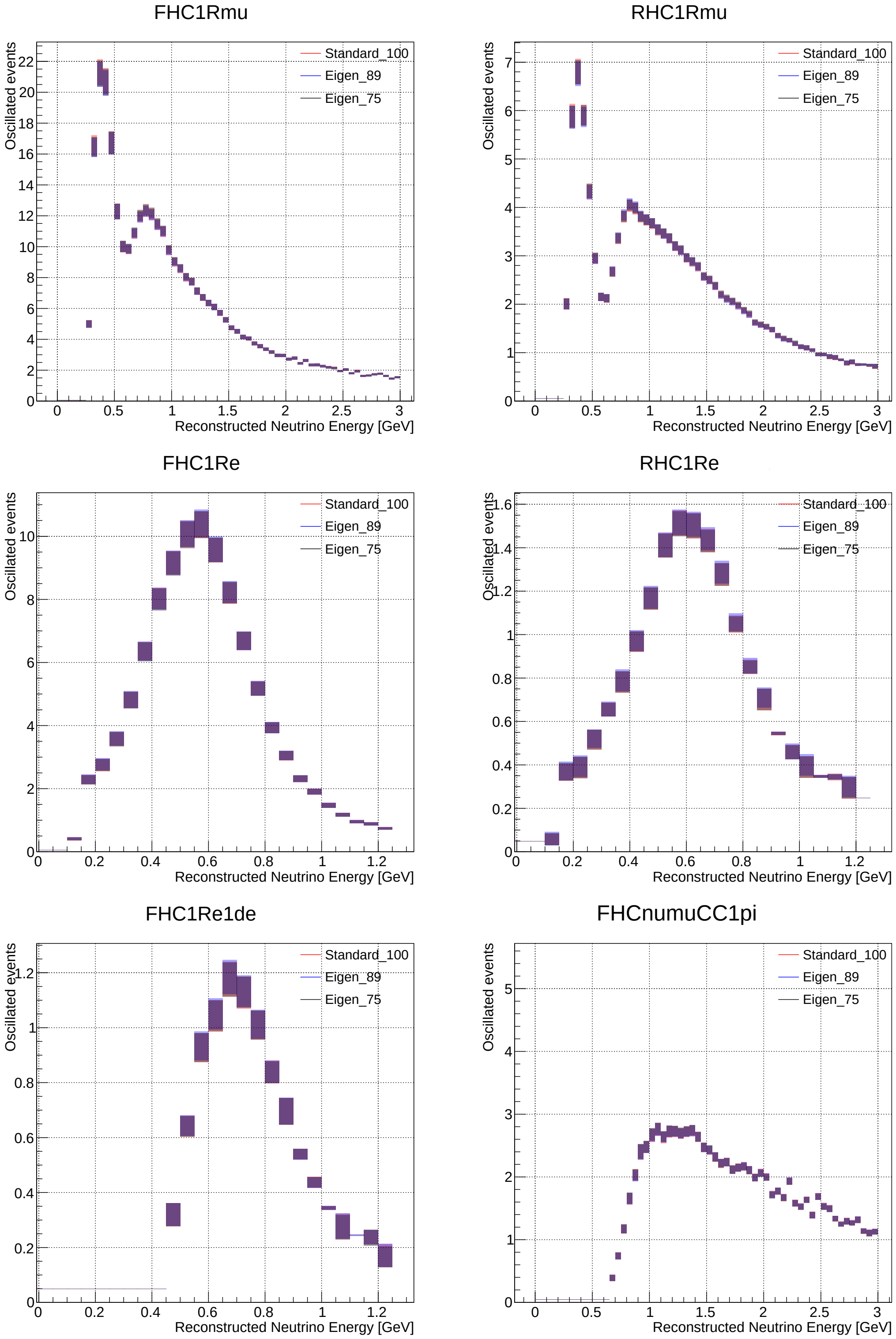

FIGURE A.40: FD posterior predictive distributions obtained using ND280-only data fits with different PCA thresholds and the official ND280 fit (without PCA). The uncertainties come only from ND-constrained parameters.

A.12 Postfit Parameters from ND+FD Joint-Fit

In the main part of the Thesis, ND280-only fit was very carefully validated, and the impact of the cross-section and flux parameters has been estimated. For the final oscillation results, MaCh3 framework performs simultaneous ND+FD joint-fit. Since FD has low event rates that are affected by oscillations, we don't expect the flux and cross-section parameters to differ in ND280-only and ND+FD joint-fit. Nevertheless, it is an important check that should be performed.

Fig. A.41 shows the overlays of cross-section parameters from both fits. The results are nearly identical; however, there are differences for p_{miss} `shape` or `2p2h Edep` dials. It is worth reminding that those parameters were fixed in ND280-only fit but free in ND+FD fit. In the ND280-only analysis, the parameters for which ND280 has no sensitivity or the constraints are very poor are fixed, mostly because the other fitting framework (BANFF) tends to experience stability issues. Since those parameters are not fixed in ND+FD fit, they might be shifted from prior values by ND data.

Another parameter worth mentioning is `Non-Res` $\mathtt{I}_{1/2}$ `Low` $\mathtt{p}_{\pi}$, as it affects only FD samples. Hence, it is expected that this dial has a different postfit value in ND+FD fit with respect to ND280-only fit.

Fig. A.42 presents the overlays of SK flux parameters. Similarly, as for cross-section parameters, ND280-only and ND+FD fit results are almost identical. It is worth reminding that ND280 constrains SK flux parameters only via their correlations with ND flux parameters. Hence, adding SK samples doesn't affect the posterior distribution of SK flux parameters.

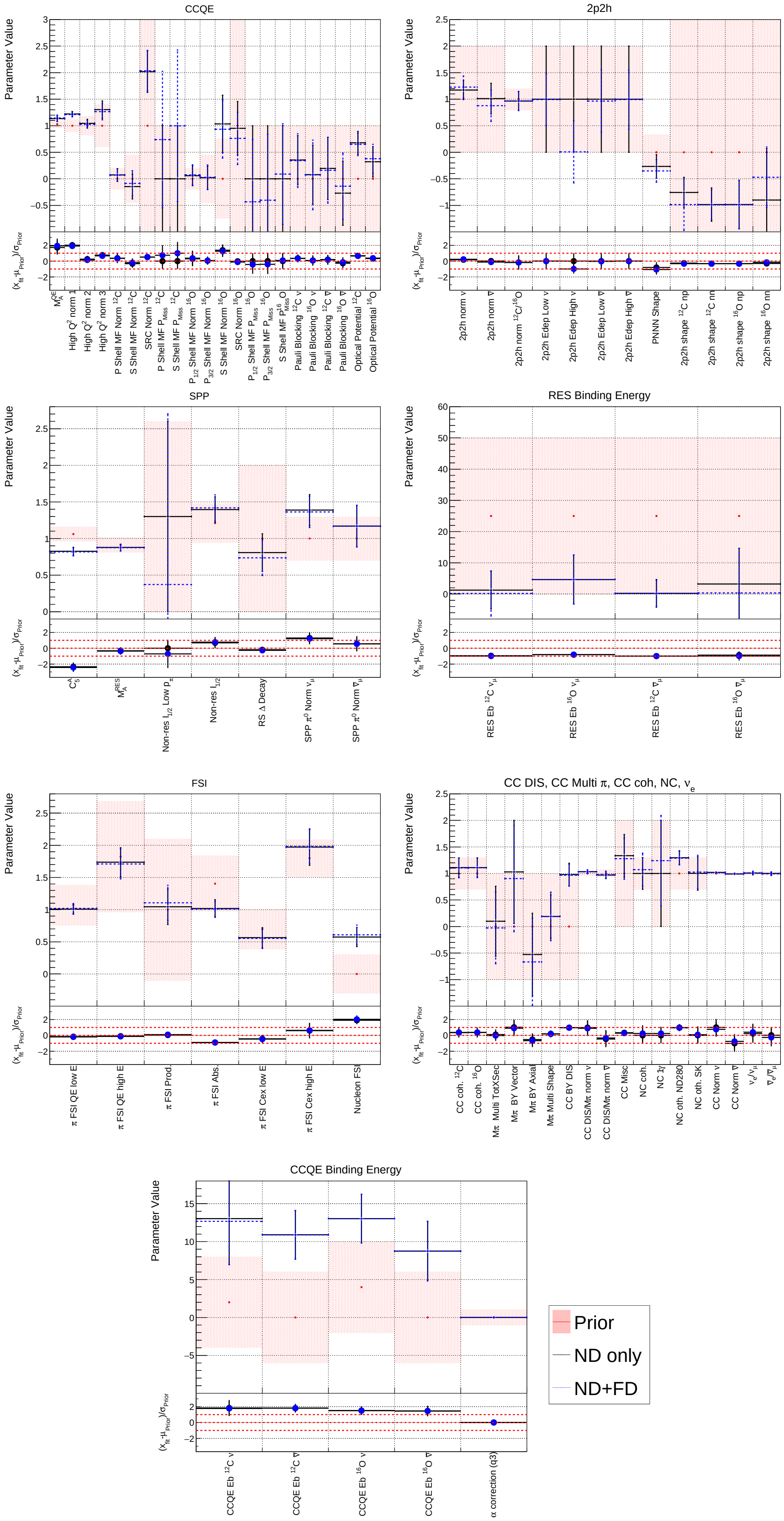

FIGURE A.41: Overlay of cross-section parameters from ND280-only and ND+FD fit.

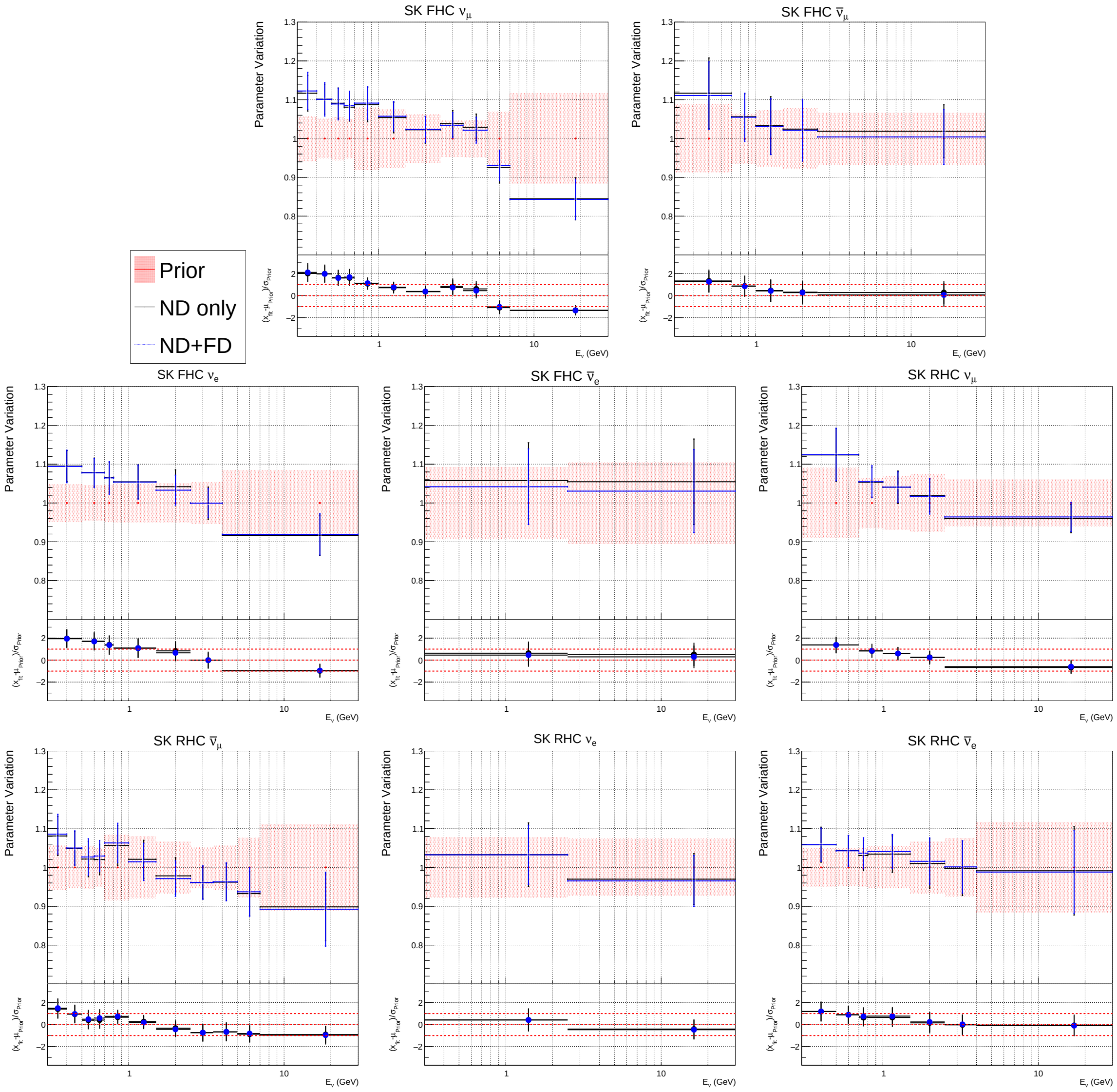

FIGURE A.42: Overlay of SK flux parameters from ND280-only and ND+FD fit.

B

Additional Informations

> But it is a well-known maxim of war that whoever tries to hold on to everything at once, finishes up by holding nothing at all.
>
> **Erich von Manstein**

B.1 Full Oscillation Formula in Vacuum

The oscillation probability for $\nu_\mu \to \nu_e$ in vacuum has following form:

$$\begin{aligned}
P(\nu_\mu \to \nu_e) = {} & 4c_{13}^2\, s_{13}^2\, s_{23}^2 \sin^2 \Delta_{31} \\
& + 8c_{13}^2\, s_{12}\, s_{13}\, s_{23}\, (c_{12}\, c_{23} \cos\delta_{CP} - s_{12}\, s_{13}\, s_{23}) \cos\Delta_{32} \sin\Delta_{31} \sin\Delta_{21} \\
& - 8c_{13}^2\, c_{12}\, c_{23}\, s_{12}\, s_{13}\, s_{23} \sin\delta_{CP} \sin\Delta_{32} \sin\Delta_{32} \sin\Delta_{21} \\
& + 4s_{12}\, c_{13}\, (c_{12}\, c_{23} + s_{12}\, s_{23}\, s_{13} - 2c_{12}\, c_{23}\, s_{12}\, s_{23}\, s_{13} \cos\delta_{CP}) \sin^2 \Delta_{21}
\end{aligned} \tag{B.1}$$

where $s_{ij} = \sin\theta_{ij}$, $c_{ij} = \cos\theta_{ij}$ and $\Delta_{ij} = \frac{\Delta m_{ij} L}{4E}$. The first term is sensitive to θ_{13}, the second one is CP conserving, the third one is CP violating and the fourth is usually called the solar term.

B.2 Binning of the ND280 Event Samples

In total there are 4952 bins. The edges of the bins for all samples are listed below.

- **FHC CC0π-0p-0γ** (650 bins)
  p_μ (MeV/c): 0, 200, 300, 350, 400, 450, 500, 550, 600, 650, 700, 750, 800, 850, 900, 950, 1000, 1100, 1200, 1300, 1500, 1750, 2000, 2500, 3000, 5000, 30000.
  $\cos\theta_\mu$: -1, 0.5, 0.6, 0.68, 0.72, 0.76, 0.82, 0.84, 0.86, 0.88, 0.9, 0.91, 0.92, 0.93, 0.94, 0.95, 0.955, 0.96, 0.965, 0.97, 0.975, 0.98, 0.985, 0.99, 0.995, 1.

- **FHC CC0π-Np-0γ** (352 bins)
  p_μ (MeV/c): 0, 250, 350, 400, 450, 500, 550, 600, 650, 700, 800, 900, 1000, 1100, 1200, 1300, 1500, 1600, 1750, 2000, 2750, 5000, 30000.
  $\cos\theta_\mu$: -1, 0.55, 0.65, 0.75, 0.8, 0.85, 0.88, 0.9, 0.92, 0.93, 0.94, 0.95, 0.96, 0.97, 0.98, 0.988, 1.

- **FHC CC1π-0γ** (272 bins)
  p_μ (MeV/c): 0, 300, 350, 400, 500, 600, 650, 700, 750, 800, 900, 1000, 1100, 1200, 1500, 2000, 5000, 30000.
  $\cos\theta_\mu$: -1, 0.6, 0.68, 0.74, 0.79, 0.85, 0.9, 0.91, 0.92, 0.93, 0.94, 0.95, 0.96, 0.97, 0.98, 0.99, 1.

- **FHC CC-Other-0γ** (154 bins)
  p_μ (MeV/c): 0, 350, 500, 600, 650, 700, 800, 900, 1000, 1150, 1250, 1500, 2000, 5000, 30000.
  $\cos\theta_\mu$: -1, 0.6, 0.7, 0.8, 0.85, 0.88, 0.9, 0.92, 0.94, 0.96, 0.98, 1.

- **FHC CC-Photon** (400 bins)
  p_μ (MeV/c): 0, 300, 400, 500, 600, 650, 700, 750, 800, 900, 1000, 1100, 1250, 1500, 1600, 1750, 2000, 2500, 3000, 5000, 30000.
  $\cos\theta_\mu$: -1, 0.6, 0.7, 0.76, 0.8, 0.84, 0.86, 0.88, 0.89, 0.9, 0.91, 0.92, 0.93, 0.94, 0.95, 0.96, 0.97, 0.98, 0.99, 0.995, 1.

- **RHC CC0π** (306 bins)
  p_μ (MeV/c): 0, 300, 400, 500, 550, 600, 650, 700, 750, 800, 900, 1000, 1100, 1200, 1500, 2000, 4000, 30000.
  $\cos\theta_\mu$: -1, 0.6, 0.7, 0.8, 0.85, 0.9, 0.92, 0.93, 0.94, 0.95, 0.96, 0.965, 0.97, 0.975, 0.98, 0.985, 0.99, 0.995, 1.

- **RHC CC1π** (48 bins)
  p_μ (MeV/c): 0, 500, 700, 900, 1300, 2500, 30000.
  $\cos\theta_\mu$: -1, 0.7, 0.8, 0.9, 0.94, 0.96, 0.98, 0.99, 1.

- **RHC CC-Other** (80 bins)
  p_μ (MeV/c): 0, 600, 800, 1000, 1250, 1500, 2000, 4000, 30000.
  $\cos\theta_\mu$: -1, 0.7, 0.8, 0.85, 0.9, 0.93, 0.95, 0.97, 0.98, 0.99, 1.

- **RHC BKG CC0π** (120 bins)
  p_μ (MeV/c): 0, 300, 500, 700, 800, 900, 1250, 1500, 2000, 4000, 30000.
  $\cos\theta_\mu$: -1, 0.7, 0.8, 0.85, 0.88, 0.9, 0.92, 0.94, 0.96, 0.97, 0.98, 0.99, 1.

- **RHC BKG CC1π** (40 bins)
  p_μ (MeV/c): 0, 600, 800, 1500, 30000.
  $\cos\theta_\mu$: -1, 0.7, 0.8, 0.86, 0.9, 0.94, 0.96, 0.97, 0.98, 0.99, 1.

- **RHC BKG CC-Other** (54 bins)
  p_μ (MeV/c): 0, 600, 1000, 1250, 2000, 4000, 30000.
  $\cos\theta_\mu$: -1, 0.7, 0.8, 0.86, 0.9, 0.93, 0.95, 0.97, 0.99, 1.

B.3 Binning of the ND280 Detector Covariance Matrix

Binning presented here is after the bin merging procedure as outlined in Section 4.2, in total there are 552 bins.

- **FHC CC0π-0p-0γ**
  p_μ (MeV/c): 0, 200, 300, 800, 850, 2000, 5000, 30000.
  $\cos\theta_\mu$: -1, 0.5, 0.6, 0.72, 0.82, 0.86, 0.9, 0.95, 0.96, 1.
- **FHC CC0π-Np-0γ**
  p_μ (MeV/c): 0, 250, 1200, 1300, 2750, 5000, 30000.
  $\cos\theta_\mu$: -1, 0.55, 0.65, 0.8, 0.85, 0.97, 0.98, 0.988, 1.
- **FHC CC1π-0γ**
  p_μ (MeV/c): 0, 300, 1000, 2000, 5000, 30000.
  $\cos\theta_\mu$: -1, 0.6, 0.68, 0.79, 0.92, 0.96, 0.98, 0.99, 1.
- **FHC CC-Other-0γ**
  p_μ (MeV/c): 0, 350, 1250, 2000, 5000, 30000.
  $\cos\theta_\mu$: -1, 0.6, 0.8, 0.92, 0.94, 0.98, 1.
- **FHC CC-Photon**
  p_μ (MeV/c): 0, 300, 500, 1500, 3000, 5000, 30000.
  $\cos\theta_\mu$: -1, 0.7, 0.76, 0.8, 0.84, 0.88, 0.89, 0.96, 1.
- **RHC CC0π**
  p_μ (MeV/c): 0, 300, 2000, 4000, 30000.
  $\cos\theta_\mu$: -1, 0.6, 0.8, 0.9, 0.96, 1.
- **RHC CC1π**
  p_μ (MeV/c): 0, 500, 30000.
  $\cos\theta_\mu$: -1, 0.7, 1.
- **RHC CC-Other**
  p_μ (MeV/c): 0, 600, 800, 30000.
  $\cos\theta_\mu$: -1, 0.7, 0.95, 0.97, 1.
- **RHC BKG CC0π**
  p_μ (MeV/c): 0, 300, 1500, 30000.
  $\cos\theta_\mu$: -1, 0.7, 1.
- **RHC BKG CC1π**
  p_μ (MeV/c): 0, 600, 800, 30000.
  $\cos\theta_\mu$: -1, 0.7, 1.
- **RHC BKG CC-Other**
  p_μ (MeV/c): 0, 600, 30000.
  $\cos\theta_\mu$: -1, 0.7, 1.

B.4 Binning of the Flux Covariance Matrix

Identical binning is used for ND280 and FD flux parameters. There are 50 bins for each detector resulting in 100 bins in total.

- FHC ν_μ; RHC $\bar{\nu}_\mu$:
  E_ν^{true} (GeV): 0, 0.4, 0.5, 0.6, 0.7, 1, 1.5, 2.5, 3.5, 5, 7, 30.
- FHC $\bar{\nu}_\mu$; RHC ν_μ:
  E_ν^{true} (GeV): 0, 0.7, 1, 1.5, 2.5, 30.
- FHC ν_e; RHC $\bar{\nu}_e$:
  E_ν^{true} (GeV): 0, 0.5, 0.7, 0.8, 1.5, 2.5, 4, 30.
- FHC $\bar{\nu}_e$; RHC ν_e:
  E_ν^{true} (GeV): 0, 2.5, 30.

B.5 Detector Systematic Uncertainties for FHC Samples

Systematic error source	**Total error in [%]**									
	CC0π-0p-0γ		CC0π-Np-0γ		CC1π^+-0γ		CC-Photon		CC-Other-0γ	
	FGD1	FGD2	FGD1	FGD2	FGD1	FGD2	FGD1	FGD2	FGD1	FGD2
Observable-like systematics										
Magnetic field distortions	0.0033	0.0074	0.0025	0.0087	0.0040	0.0153	0.0073	0.0291	0.0237	0.0244
TPC momentum resolution	0.0051	0.0036	0.0080	0.0082	0.0103	0.0104	0.0260	0.0369	0.0434	0.0650
TPC momentum scale	0.0147	0.0170	0.0109	0.0161	0.0171	0.0181	0.0191	0.0350	0.0371	0.0360
TPC PID	0.3145	0.4494	0.6191	0.7884	0.8771	1.1762	0.4758	0.4268	1.2715	1.4023
FGD PID	0.0890	0.0360	0.1801	0.0979	0.0279	0.0426	-	-	0.0276	0.0329
Efficiency-like systematics										
Charge ID efficiency	0.0814	0.2002	0.2440	0.3681	0.1141	0.3246	0.0333	0.1683	0.0673	0.1591
TPC cluster efficiency	0.0095	0.0096	0.0162	0.0165	0.0154	0.0169	0.0300	0.0300	0.0318	0.0331
TPC tracking efficiency	0.3036	0.7394	0.7527	1.3844	0.6682	1.3976	0.4873	0.8888	0.6551	1.6224
TPC-FGD matching efficiency	0.0767	0.1592	0.1898	0.3297	0.1463	0.2302	0.0922	0.1410	0.1376	0.1813
FGD hybrid tracking efficiency	0.2600	0.0512	0.8183	0.1560	0.2658	0.0308	0.2678	0.0488	0.2973	0.0660
Michel electron efficiency	0.0489	0.0759	0.0768	0.1671	0.2846	0.5191	0.0618	0.0646	0.1007	0.1506
ECal tracking efficiency	0.3414	0.3784	0.5168	0.6917	1.0693	1.5114	0.9993	0.8862	2.6425	4.3522
TPC-ECal matching efficiency	0.6082	0.3178	1.0097	1.0251	0.7418	0.6726	0.9861	1.0375	1.2677	1.2513
ECal PID `EmHip`	0.0790	0.0648	0.0597	0.0561	0.1036	0.0653	0.4188	0.3280	0.0869	0.0851
ECal photon pile-up	0.0689	0.0490	0.0423	0.0424	0.0808	0.0439	1.1732	1.1095	0.0461	0.0414
Normalisation systematics										
OOFV background	0.5425	0.7194	0.1389	0.1978	0.8043	0.6665	0.6977	0.7637	0.1680	0.1688
Pile-up	0.1782	0.1722	0.1789	0.1742	0.1834	0.1746	0.1912	0.1799	0.1841	0.1786
FGD mass	0.5651	0.3850	0.5757	0.3959	0.5558	0.3849	0.5447	0.3743	0.5775	0.3984
Pion secondary interactions	0.3605	0.3833	1.3837	1.3321	1.3141	1.4718	1.6202	1.2123	3.4770	3.1754
Proton secondary interactions	1.0580	1.2580	2.6137	3.0793	0.5876	0.7522	0.6395	0.7262	0.8371	1.0406
Sand muon background	0.0571	0.0280	0.0117	0.0113	0.0714	0.0170	0.0190	0.0146	0.0224	0.0059
All										
Total uncertainty	1.6808	1.9692	3.6612	4.2466	2.5623	3.0641	2.7519	2.8189	4.7243	5.6945

TABLE B.1: Total relative errors (in %) for each source of detector systematics, in each sample. The FGD PID systematic is not applied to the CC-Photon samples since these do not rely on the charged pion tag which uses FGD PID.

B.6 Individual Detector Systematic Errors for Proton-Tagged Samples

Here we summarise the fractional error for each ND280 detector systematic uncertainty as a function of p_μ. A few conclusions can be drawn: for the dominant systematic sources, such as proton SI or pion SI, the uncertainties increase on average with higher p_μ. This is a consequence of the fact that with an increase of neutrino energy, it is more likely to produce more energetic protons/pions or a higher multiplicity of them. On the other hand, for very low p_μ the error is significantly larger, which most likely comes from the fact that the chance of μ-misidentification is higher in such a case.

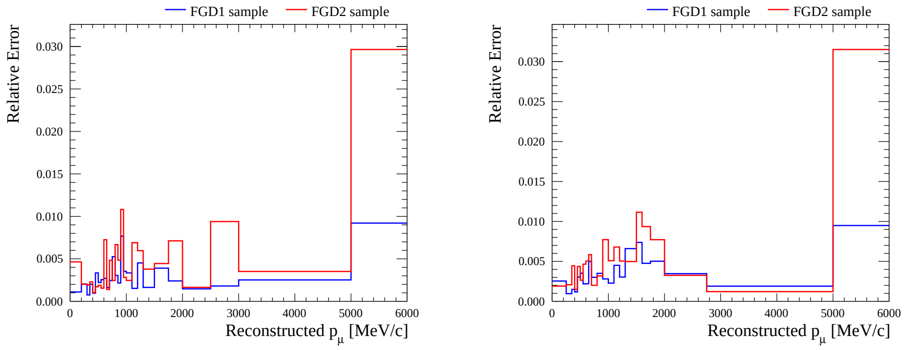

(A) CC0π-0p-0γ

(B) CC0π-Np-0γ

FIGURE B.1: Magnetic field distortions.

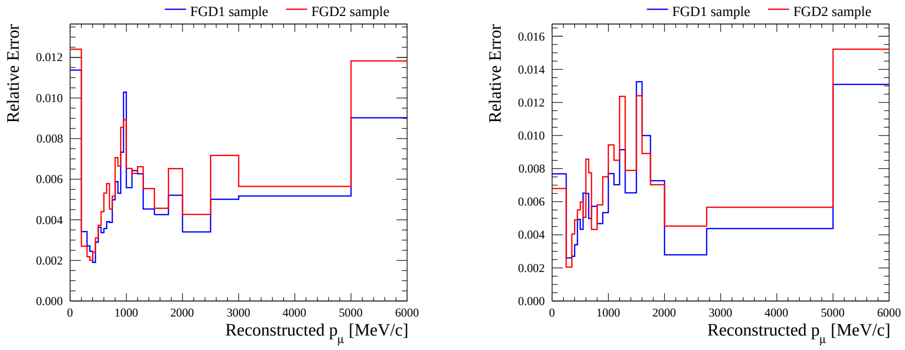

(A) CC0π-0p-0γ

(B) CC0π-Np-0γ

FIGURE B.2: TPC momentum resolution.

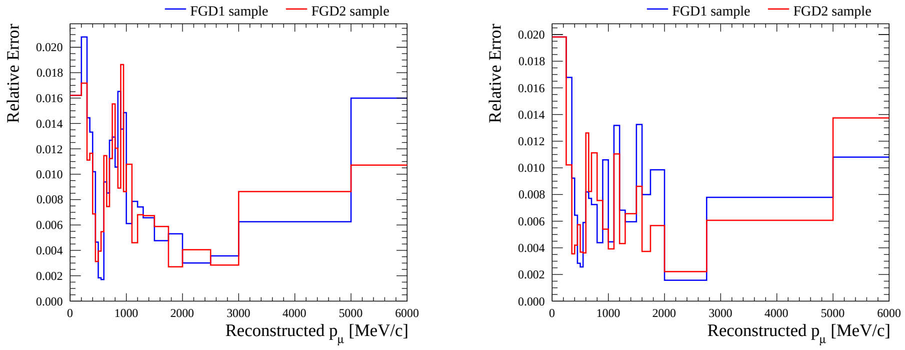

(A) CC0π-0p-0γ

(B) CC0π-Np-0γ

FIGURE B.3: TPC momentum scale.

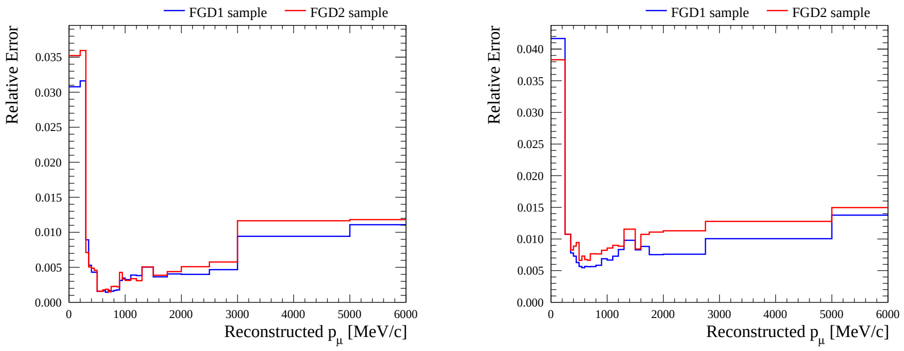

(A) CC0π-0p-0γ (B) CC0π-Np-0γ

FIGURE B.4: TPC PID.

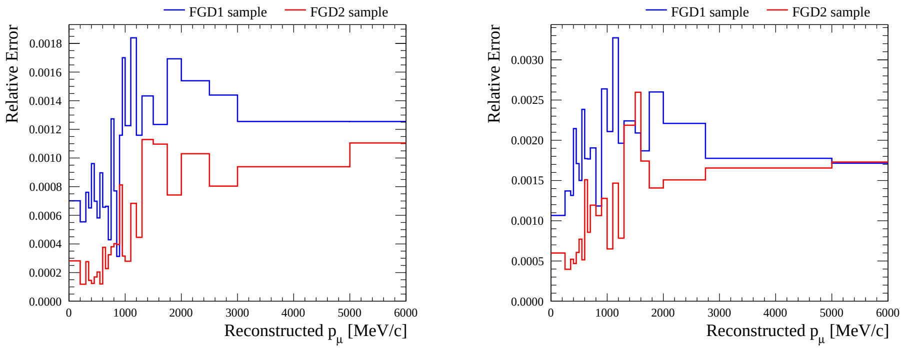

(A) CC0π-0p-0γ (B) CC0π-Np-0γ

FIGURE B.5: FGD PID.

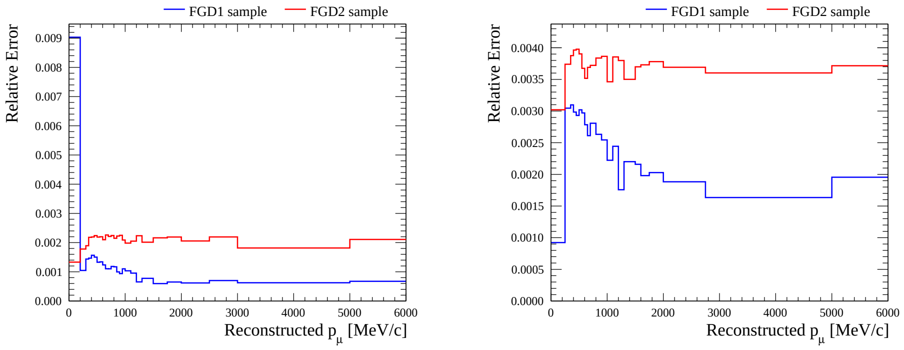

(A) CC0π-0p-0γ (B) CC0π-Np-0γ

FIGURE B.6: Charge ID efficiency.

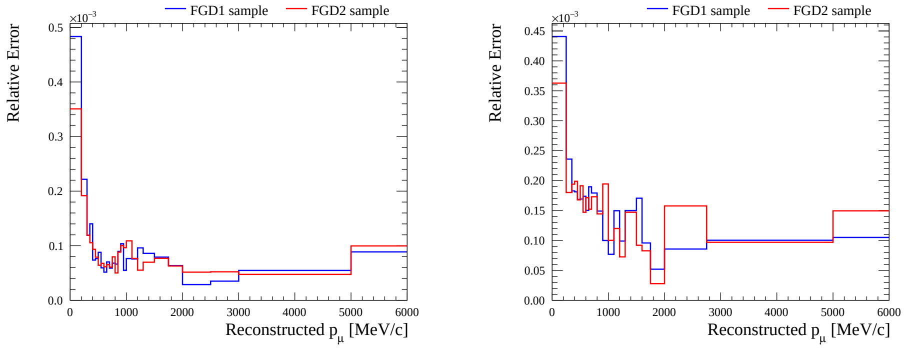

(A) CC0π-0p-0γ (B) CC0π-Np-0γ

FIGURE B.7: TPC cluster efficiency.

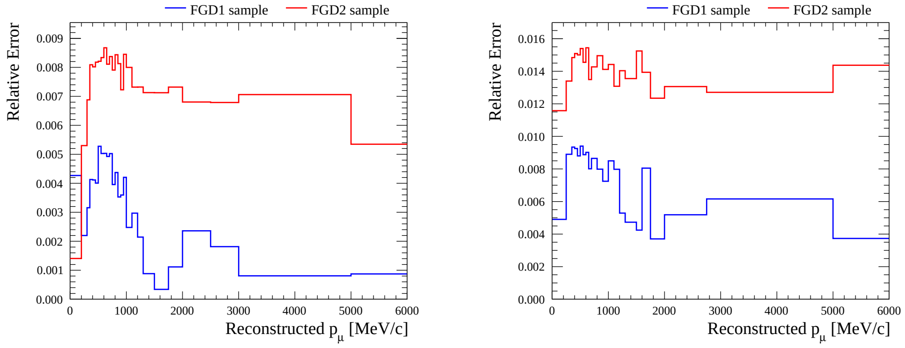

(A) CC0π-0p-0γ (B) CC0π-Np-0γ

FIGURE B.8: TPC tracking efficiency.

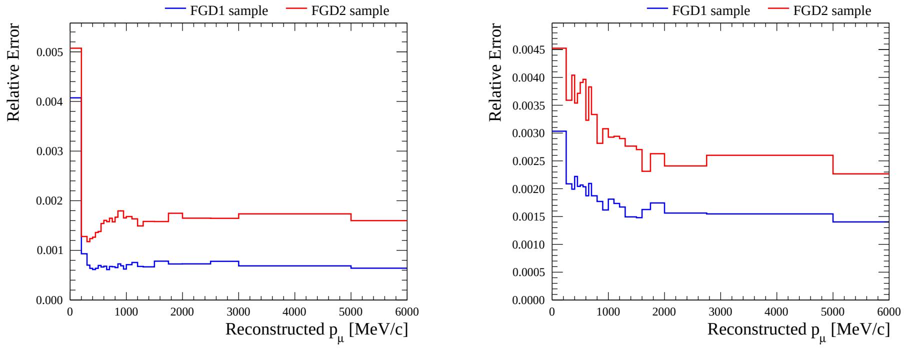

(A) CC0π-0p-0γ (B) CC0π-Np-0γ

FIGURE B.9: TPC-FGD matching efficiency.

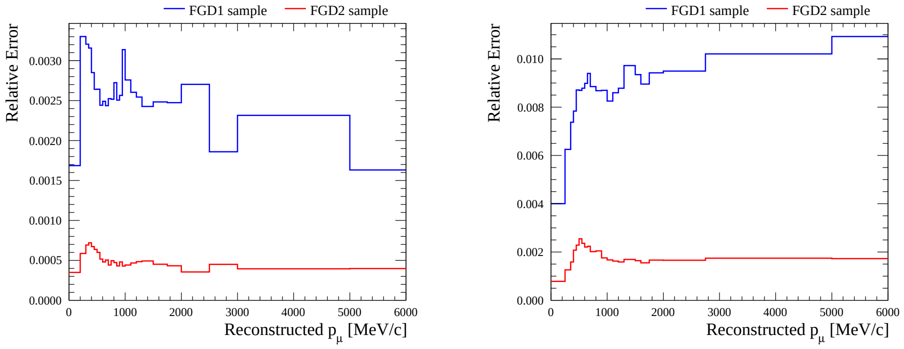

(A) CC0π-0p-0γ (B) CC0π-Np-0γ

FIGURE B.10: FGD hybrid tracking efficiency.

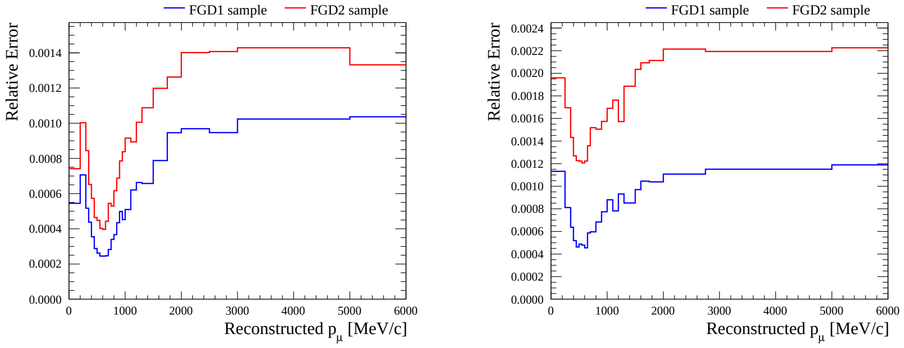

(A) CC0π-0p-0γ (B) CC0π-Np-0γ

FIGURE B.11: Michel electron efficiency.

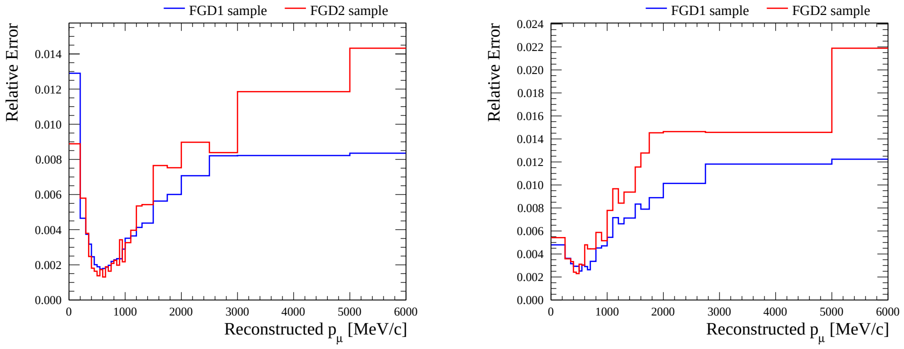

(A) CC0π-0p-0γ (B) CC0π-Np-0γ

FIGURE B.12: ECal tracking efficiency.

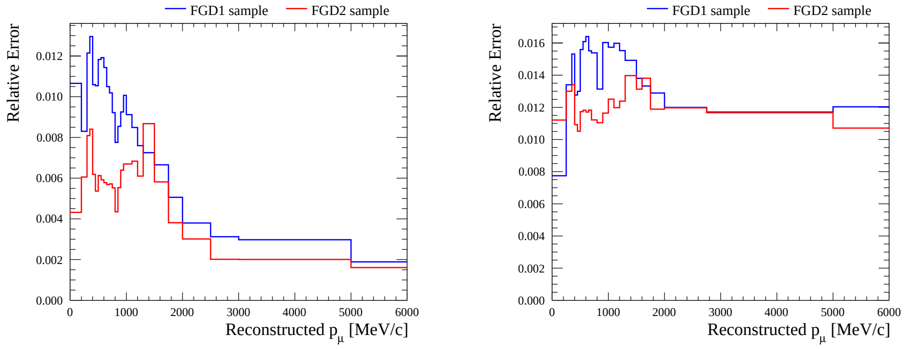

(A) CC0π-0p-0γ (B) CC0π-Np-0γ

FIGURE B.13: TPC-ECal matching efficiency.

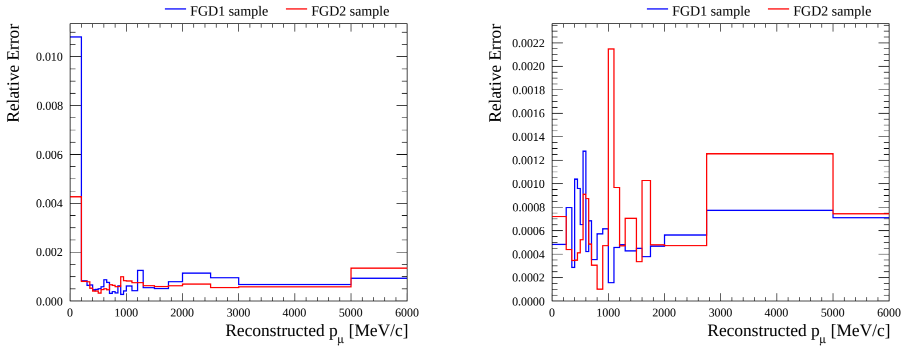

(A) CC0π-0p-0γ (B) CC0π-Np-0γ

FIGURE B.14: ECal PID `EmHip`.

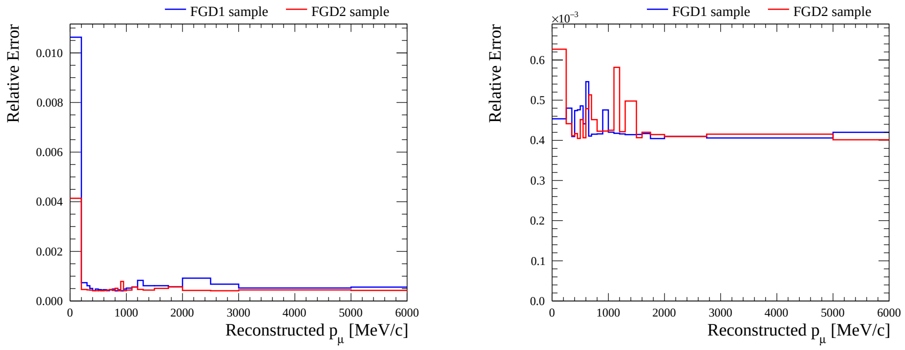

(A) CC0π-0p-0γ (B) CC0π-Np-0γ

FIGURE B.15: ECal photon pile-up.

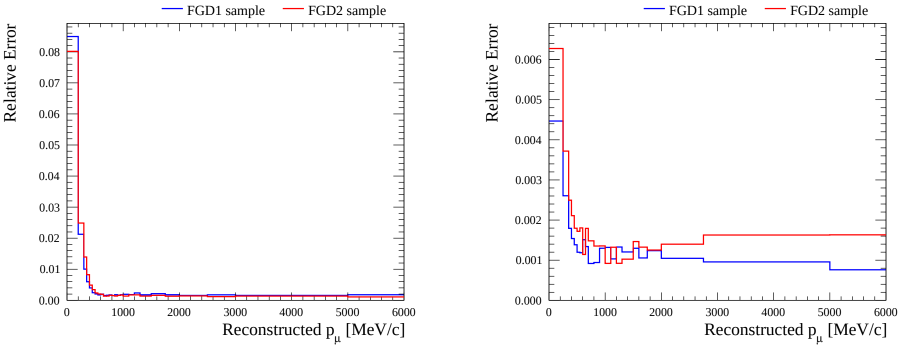

(A) CC0π-0p-0γ (B) CC0π-Np-0γ

FIGURE B.16: OOFV background.

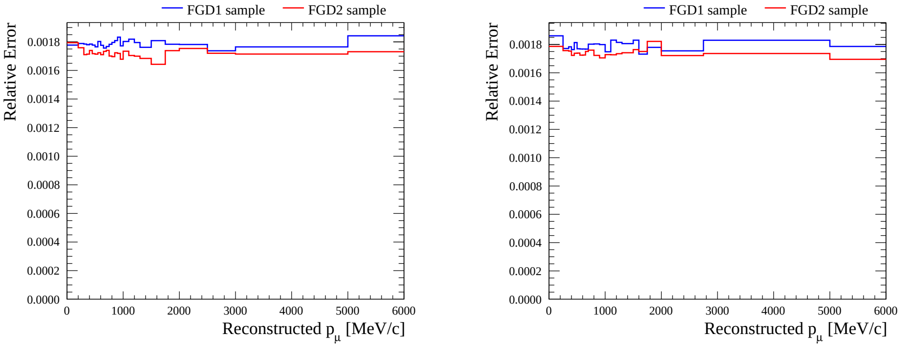

(A) CC0π-0p-0γ (B) CC0π-Np-0γ

FIGURE B.17: Pile-up.

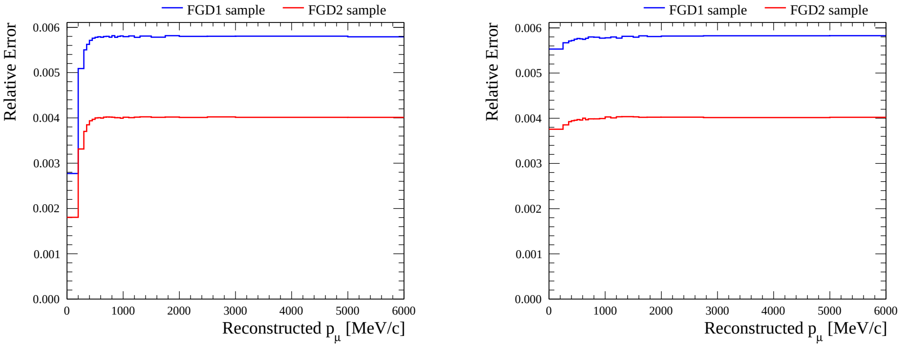

(A) CC0π-0p-0γ (B) CC0π-Np-0γ

FIGURE B.18: FGD mass.

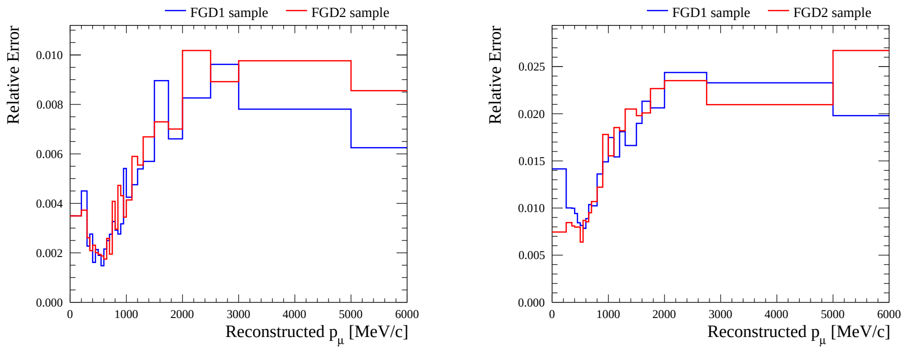

(A) CC0π-0p-0γ (B) CC0π-Np-0γ

FIGURE B.19: Pion secondary interactions.

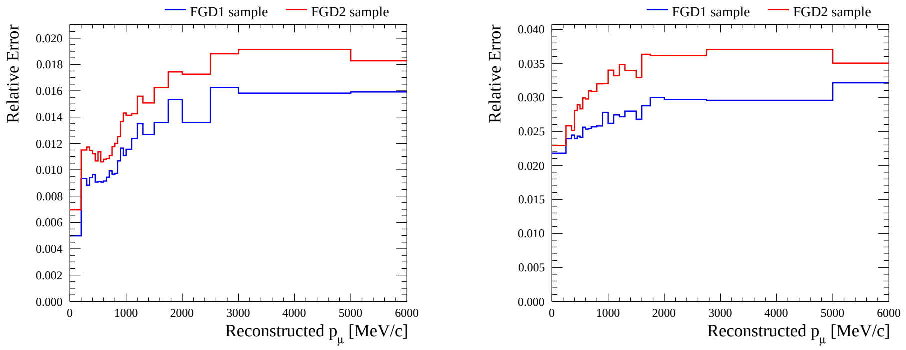

(A) CC0π-0p-0γ (B) CC0π-Np-0γ

FIGURE B.20: Proton secondary interactions.

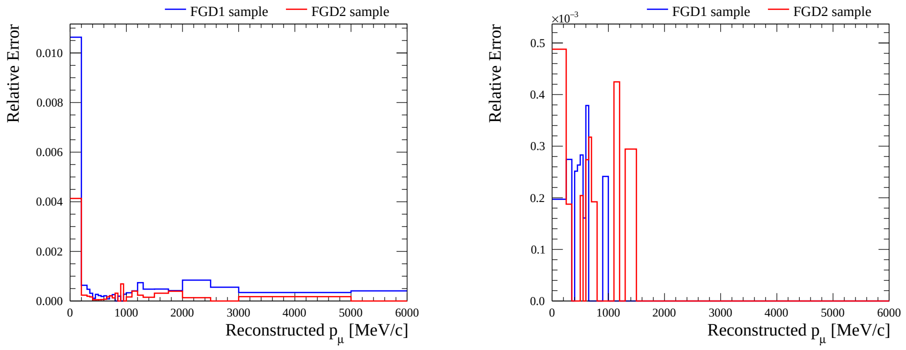

(A) CC0π-0p-0γ (B) CC0π-Np-0γ

FIGURE B.21: Sand muon background.

B.7 Fractional Error Broken by Systematic Type

Sample	$\delta N/N(\%)$							
	Flux		Xsec		ND280		Total	
	pri.	post.	pri.	post.	pri.	post.	pri.	post.
FGD1 FHC CC0π-0p-0γ	5.0	2.7	11.8	2.8	1.8	1.2	12.8	0.6
FGD1 FHC CC0π-Np-0γ	5.5	2.8	11.7	3.2	3.5	2.2	12.9	0.9
FGD1 FHC CC1π-0γ	5.2	2.7	9.1	2.7	3.0	1.4	10.6	1.0
FGD1 FHC CC-Other-0γ	5.4	2.8	8.0	2.8	5.2	2.3	11.0	1.6
FGD1 FHC CC-Photon	5.5	2.8	8.5	2.8	2.8	1.8	10.5	0.8
FGD2 FHC CC0π-0p-0γ	5.1	2.7	11.2	2.8	2.1	1.1	11.5	0.6
FGD2 FHC CC0π-Np-0γ	5.5	2.8	11.3	3.3	3.9	2.4	12.2	1.0
FGD2 FHC CC1π-0γ	5.2	2.7	9.0	2.7	3.6	1.6	10.5	1.0
FGD2 FHC CC-Other-0γ	5.6	2.8	8.0	2.8	6.3	2.7	11.5	1.9
FGD2 FHC CC-Photon	5.4	2.8	8.3	2.8	2.5	1.6	10.4	0.8
FGD1 RHC CC0π	4.9	3.2	11.3	3.2	1.9	1.2	12.2	0.9
FGD1 RHC CC1π	4.6	3.1	10.3	3.0	4.2	2.6	11.4	1.9
FGD1 RHC CC-Other	4.5	2.9	9.3	3.0	3.5	2.0	10.5	1.5
FGD2 RHC CC0π	4.8	3.2	10.4	3.0	2.1	1.2	13.8	0.9
FGD2 RHC CC1π	4.6	3.0	9.9	3.2	3.9	2.3	10.9	1.9
FGD2 RHC CC-Other	4.6	2.9	9.7	3.1	2.9	1.8	11.3	1.4
FGD1 RHC BKG CC0π	5.8	2.8	10.1	2.8	2.2	1.1	10.6	1.1
FGD1 RHC BKG CC1π	5.6	2.8	8.0	2.5	3.3	1.6	11.2	1.3
FGD1 RHC BKG CC-Other	5.9	2.9	8.6	2.7	2.6	1.4	10.1	1.4
FGD2 RHC BKG CC0π	5.8	2.8	9.5	2.8	2.2	1.1	10.4	1.1
FGD2 RHC BKG CC1π	5.6	2.8	8.2	2.5	3.2	1.6	10.7	1.3
FGD2 RHC BKG CC-Other	5.9	2.9	8.6	2.7	2.5	1.4	10.6	1.4
Total	4.5	2.7	8.0	2.6	2.1	1.2	9.1	0.3

TABLE B.2: Event rate uncertainties for the prior (pri.) and posterior (post.) predictions broken down by ND280 sample and systematic group.

B.8 Nominal MC Predictions for Each ND280 Sample

Here we present nominal MC predictions only as a function of p_μ with reaction breakdown. All plots exclude the high momentum bin going up to 30 GeV/c.

Additionally, this Section presents p_μ and $\cos\theta_\mu$ two-dimensional distributions with Q^2 lines visually marking the value of true Q^2. Those plots are produced with the restricted binning range as well, focusing on the most important region of the phase space.

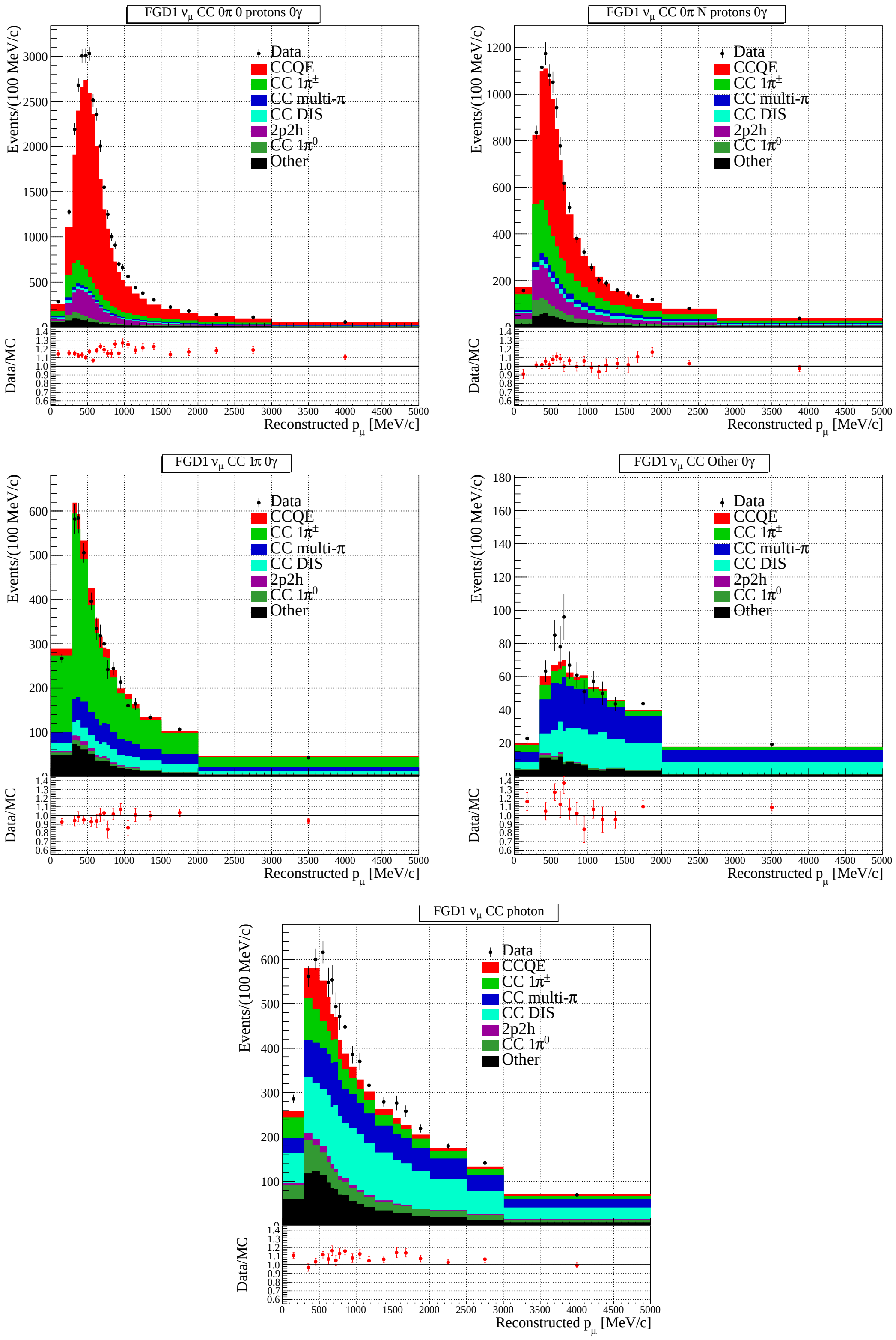

FIGURE B.22: Nominal MC predictions for FGD1 FHC samples.

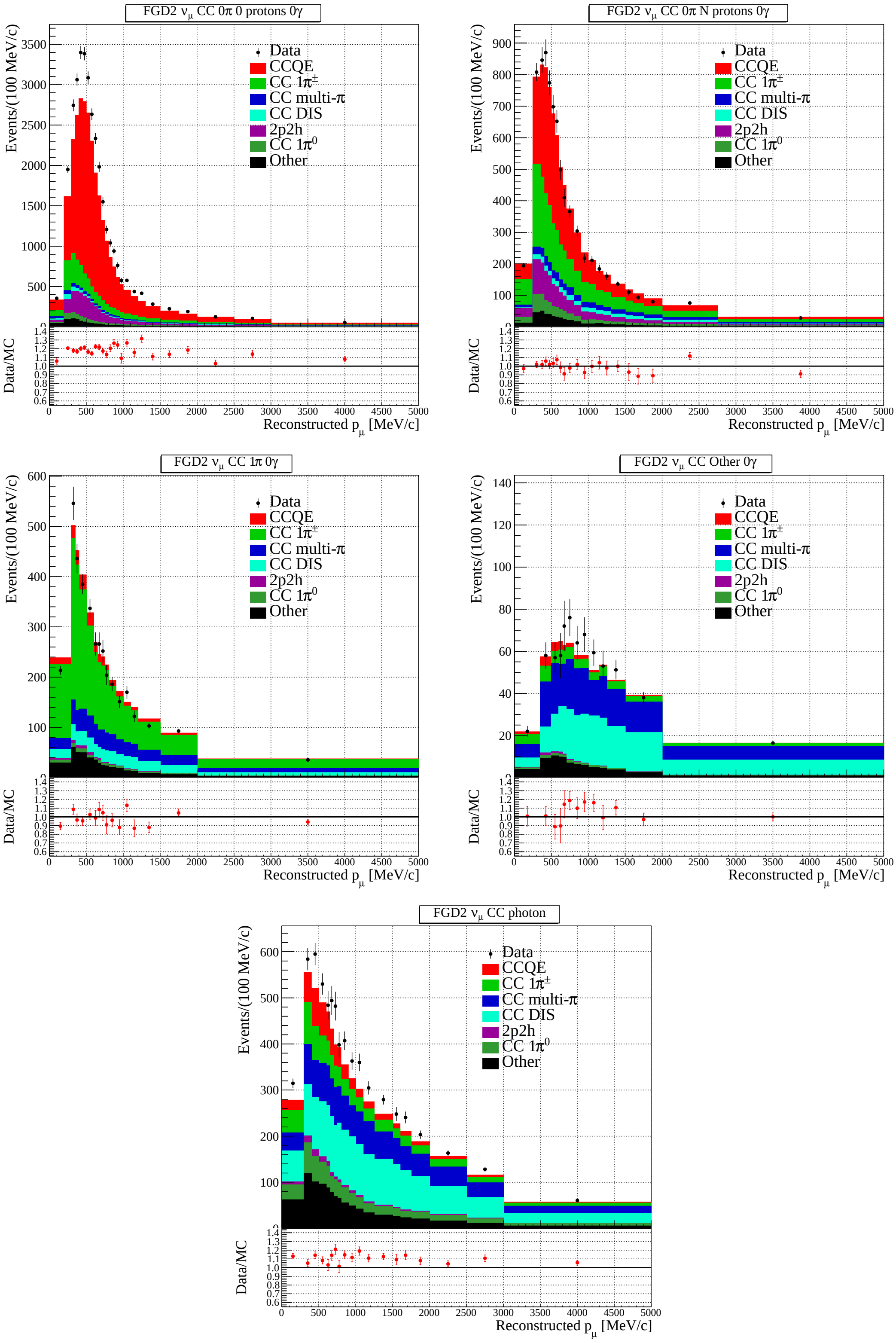

FIGURE B.23: Nominal MC predictions for FGD2 FHC samples.

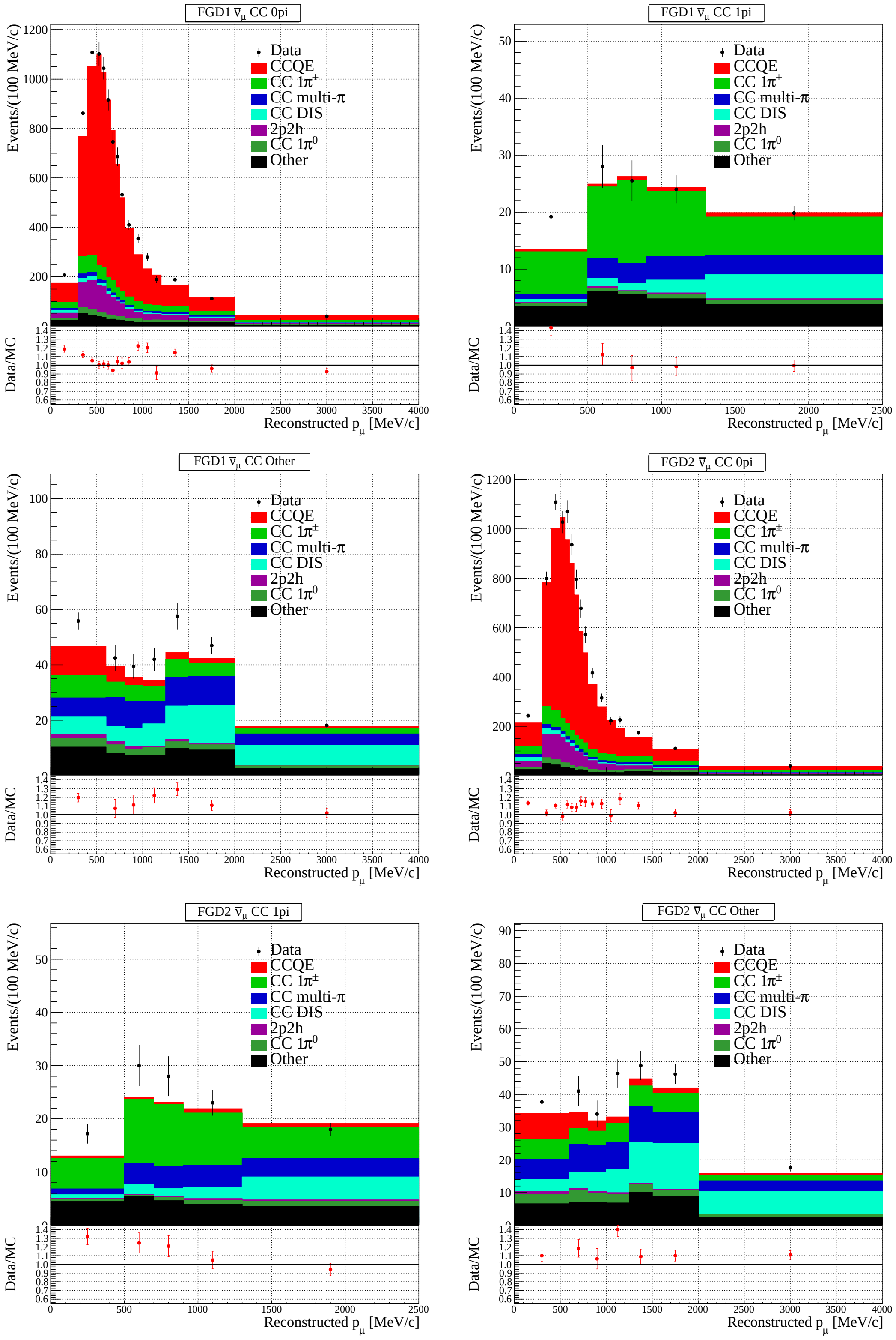

FIGURE B.24: Nominal MC predictions for RHC samples.

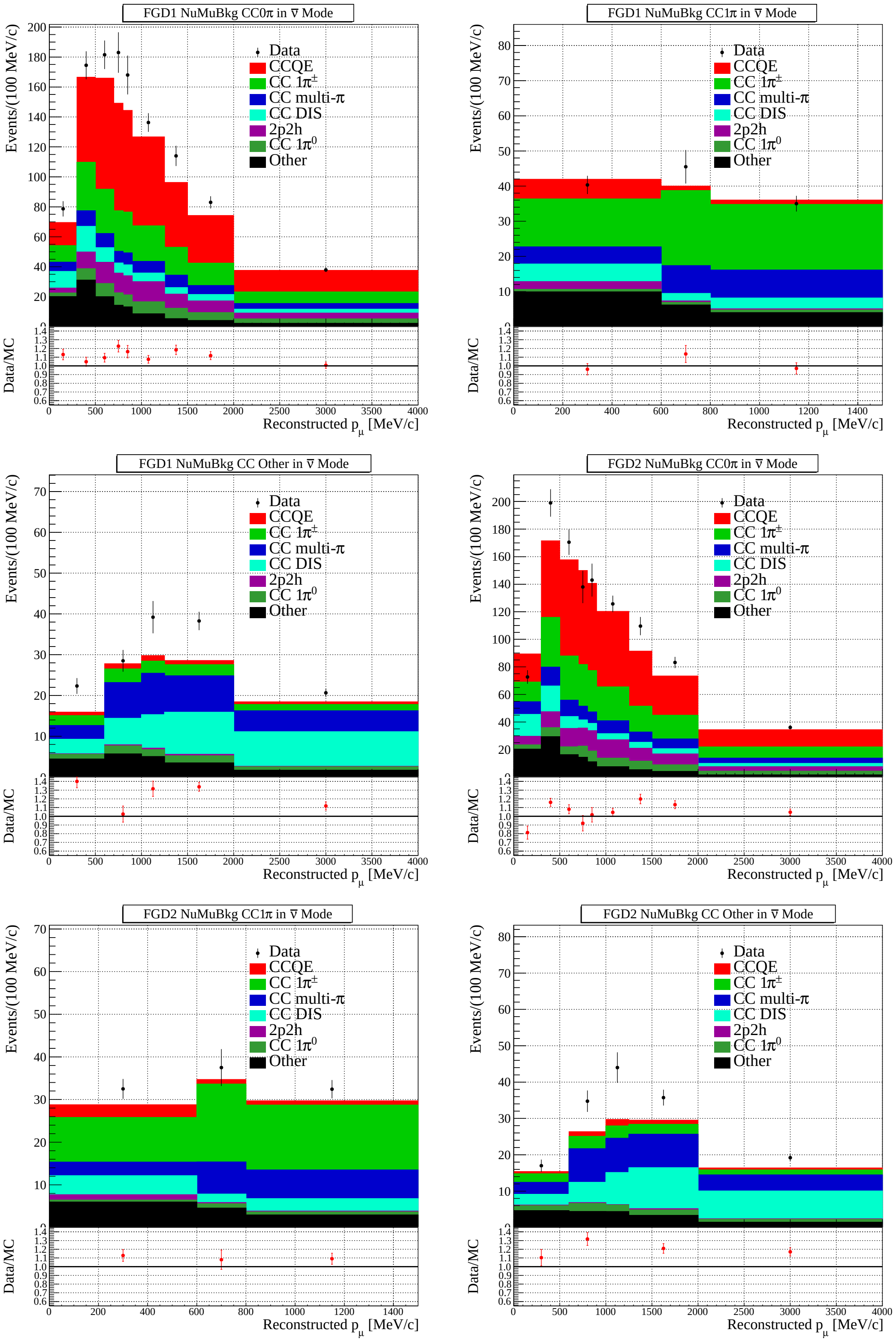

FIGURE B.25: Nominal MC predictions for RHC BKG samples.

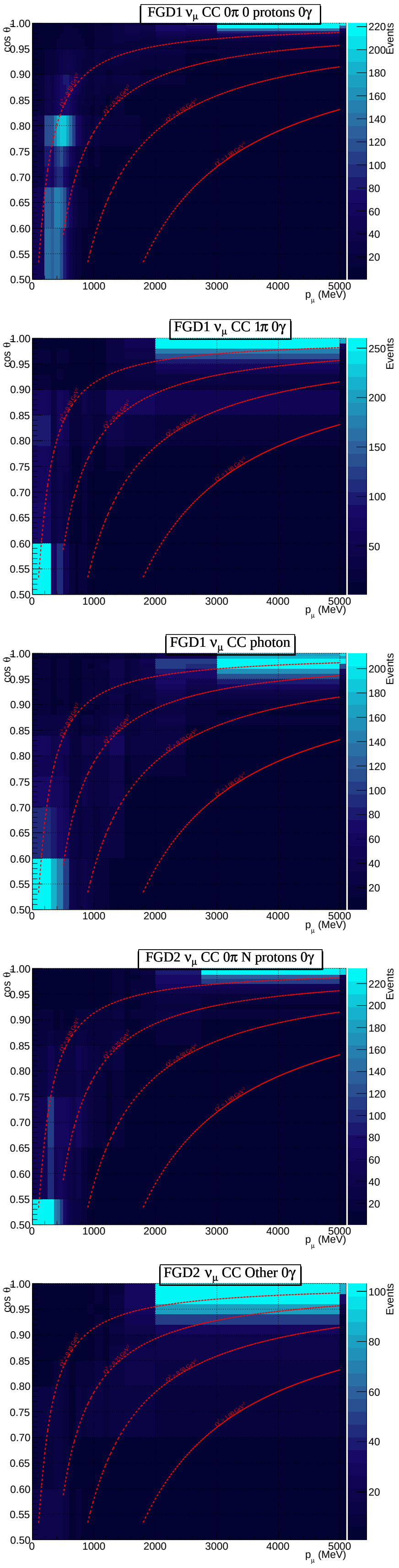

FIGURE B.26: 2D nominal event rates for FHC samples with lines showing true values of Q^2. All plots are zoomed.

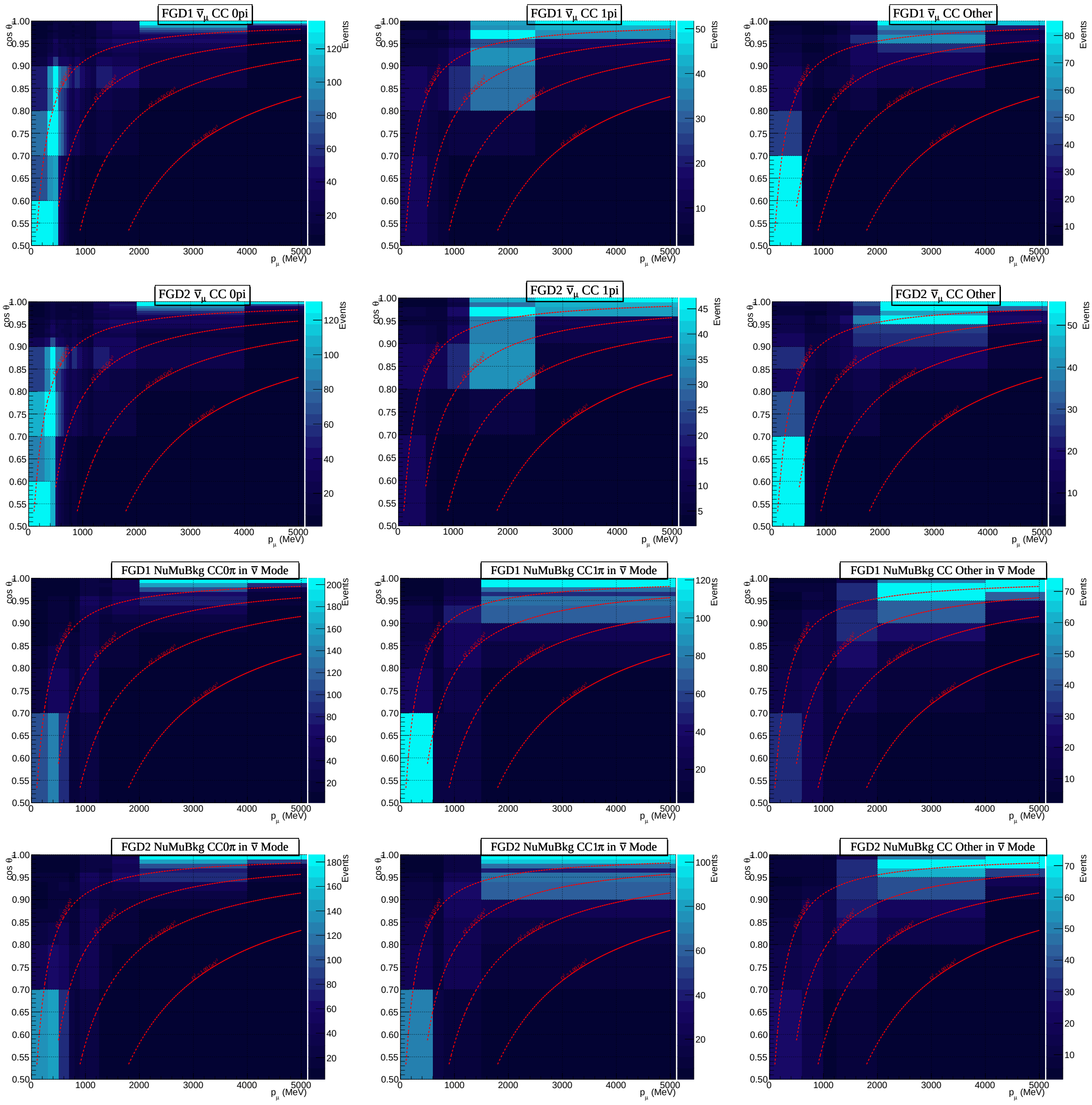

FIGURE B.27: 2D nominal event rates for RHC samples with lines showing true values of Q^2. All plots are zoomed.

B.9 Posterior Predictive Distributions for Each ND280 Sample

Here we present prior and posterior predictive distributions only as a function of p_μ with reaction breakdown. We can observe the impact of ND280 and the reduction of systematic errors.

The second set of plots displays posterior predictive distributions with reaction breakdown.

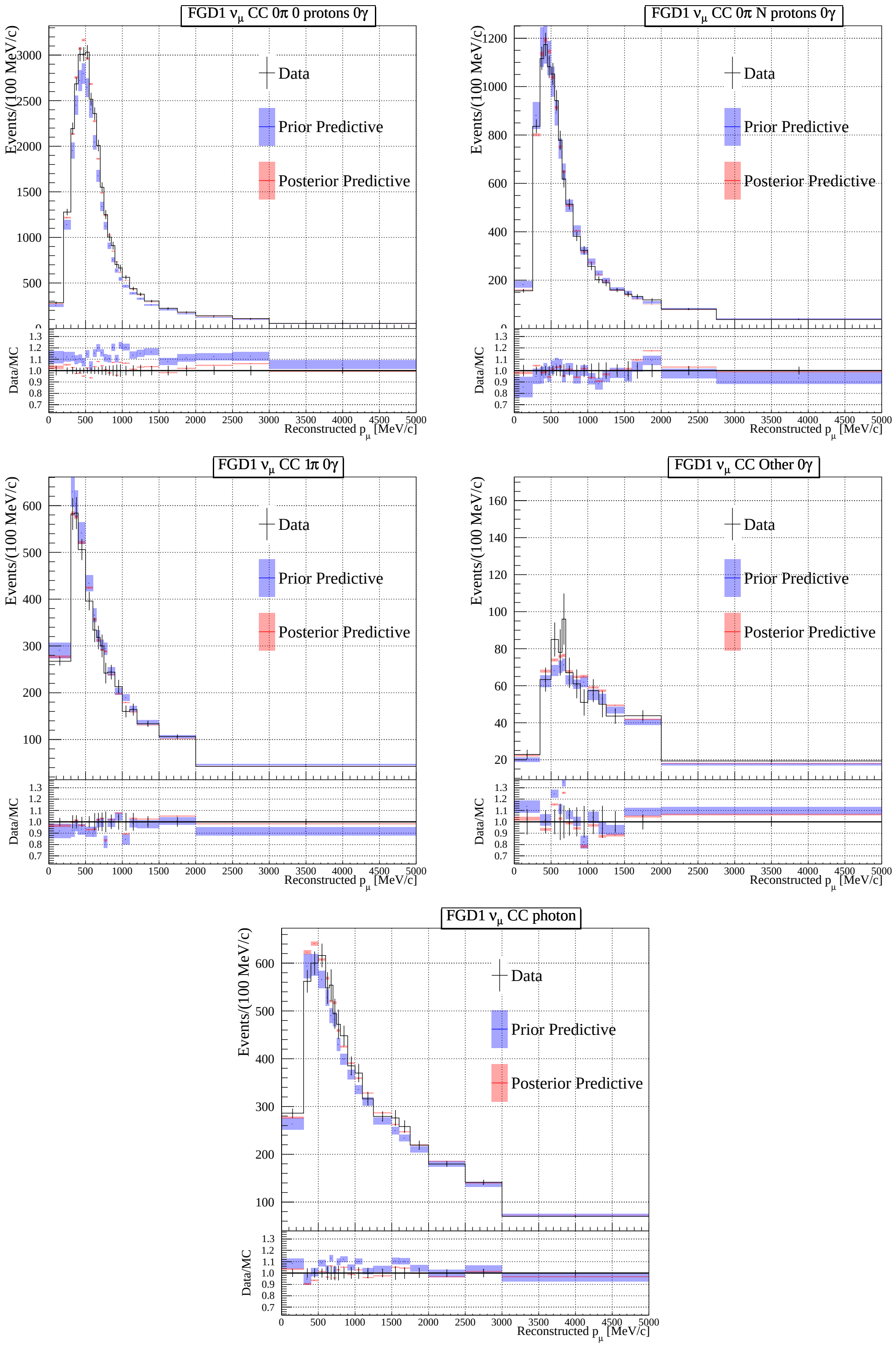

FIGURE B.28: Overlay of prior and posterior predictive distributions for FHC FGD1 samples.

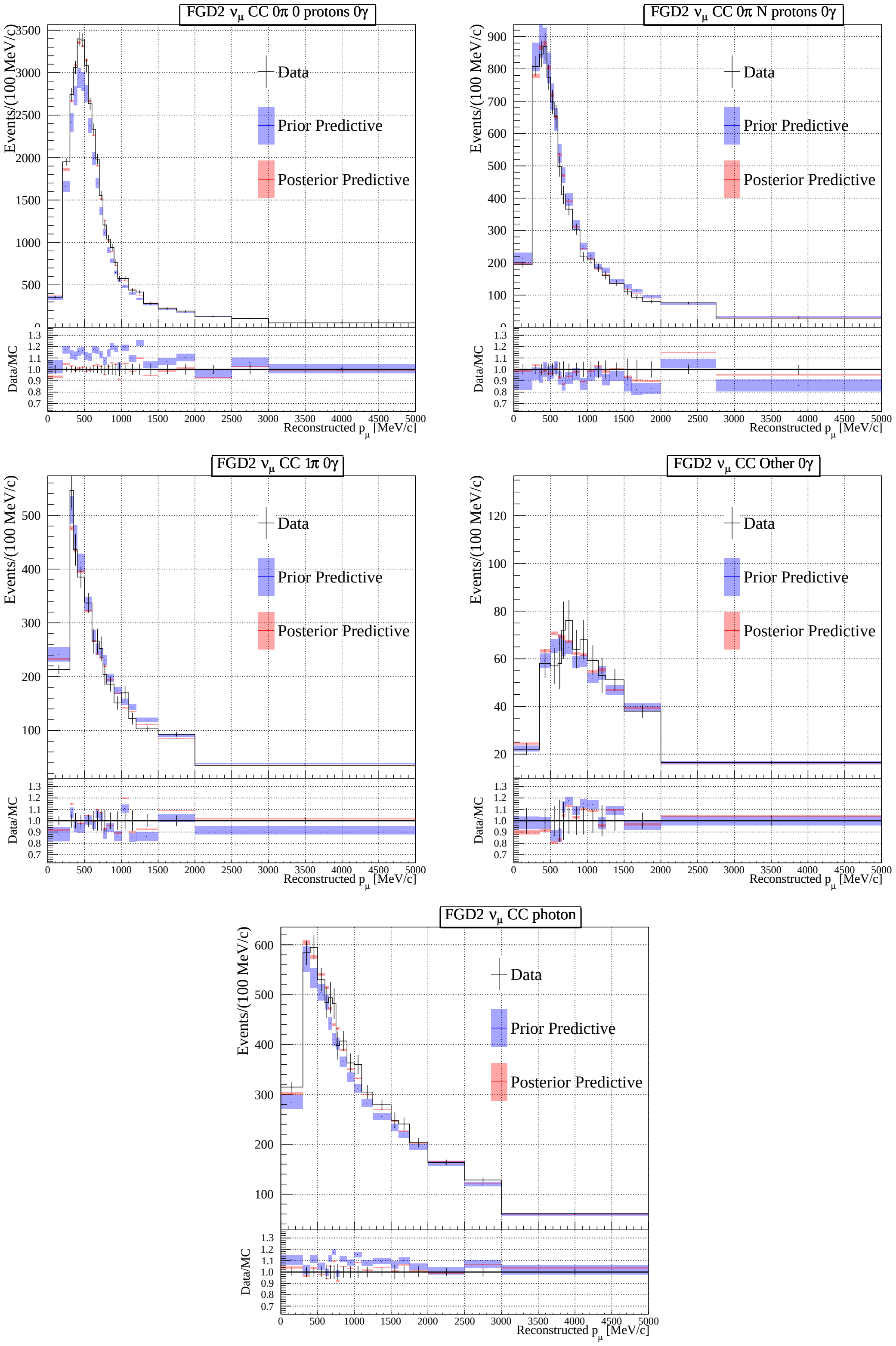

FIGURE B.29: Overlay of prior and posterior predictive distributions for FHC FGD2 samples.

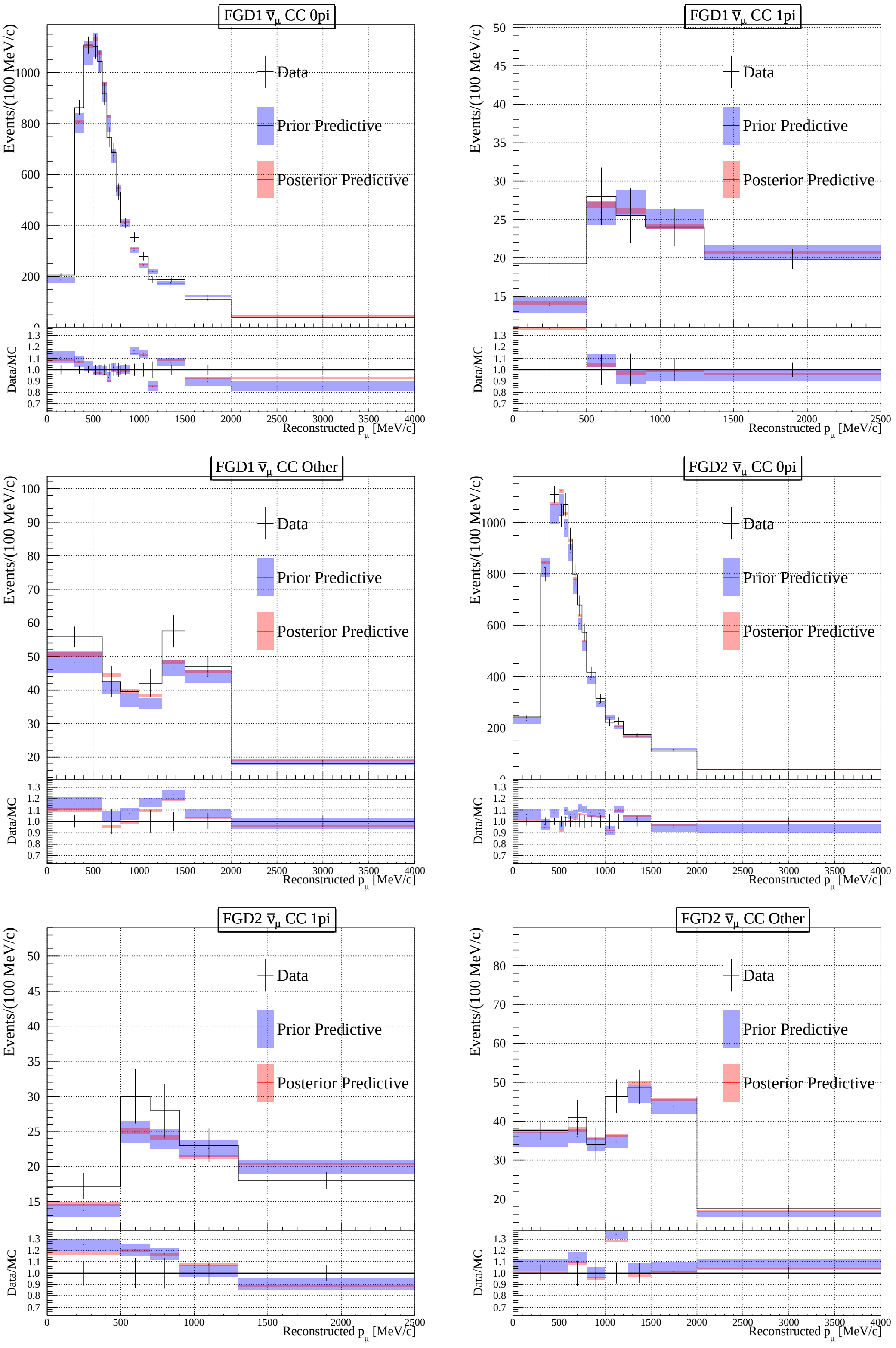

FIGURE B.30: Overlay of prior and posterior predictive distributions for RHC samples.

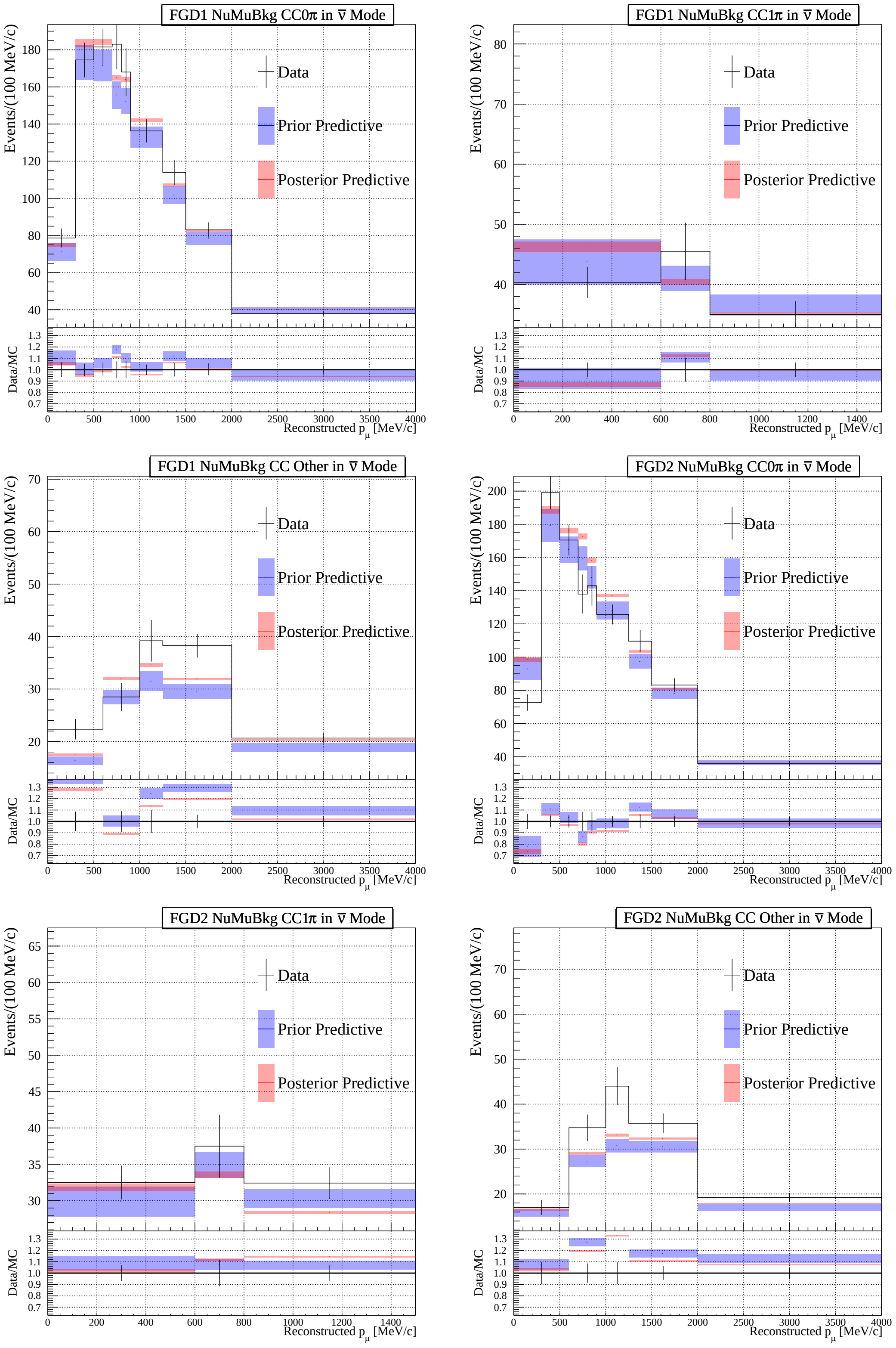

FIGURE B.31: Overlay of prior and posterior predictive distributions for RHC BKG samples.

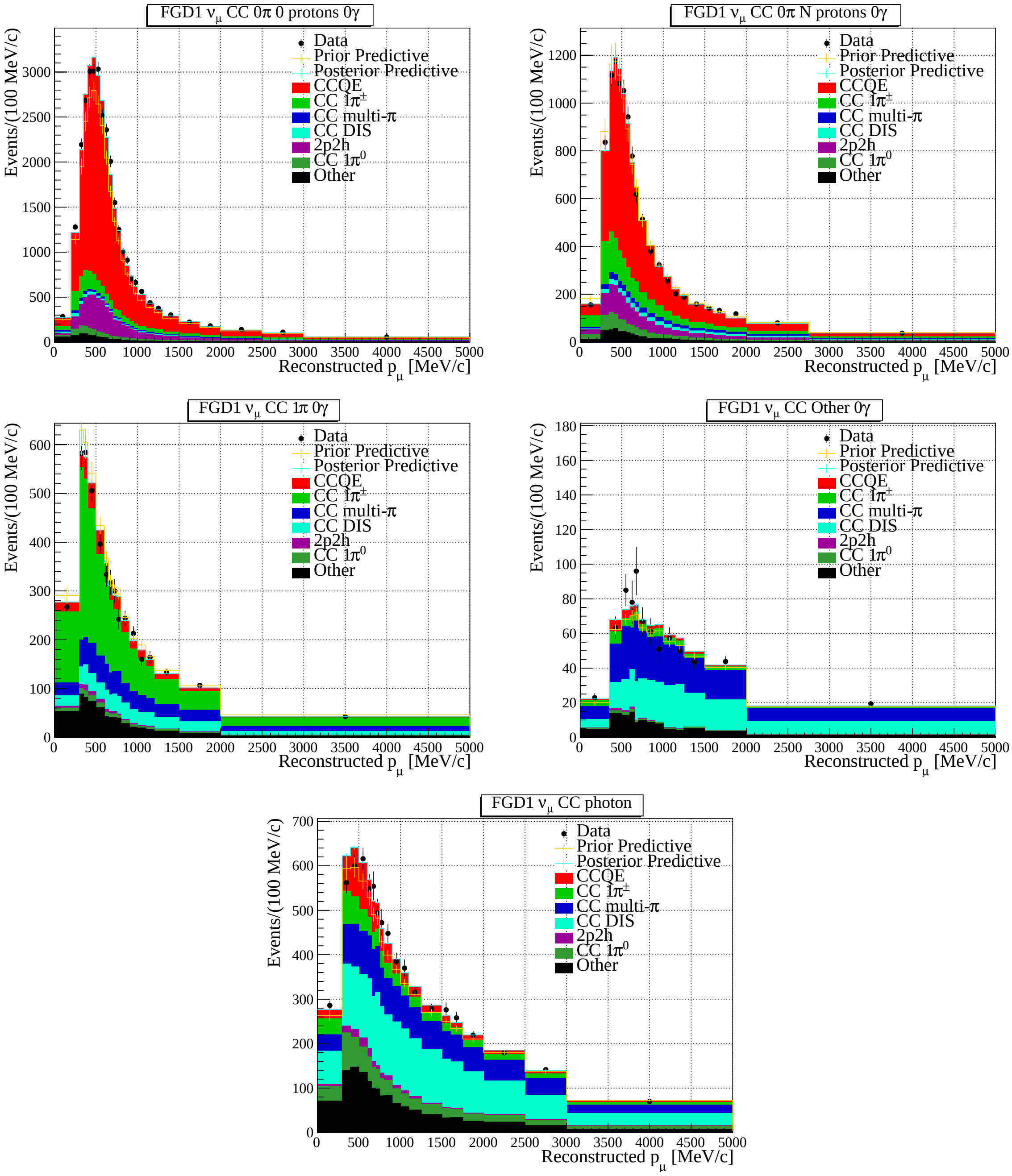

FIGURE B.32: Posterior predictive distributions with reaction breakdown for FHC FGD1 samples.

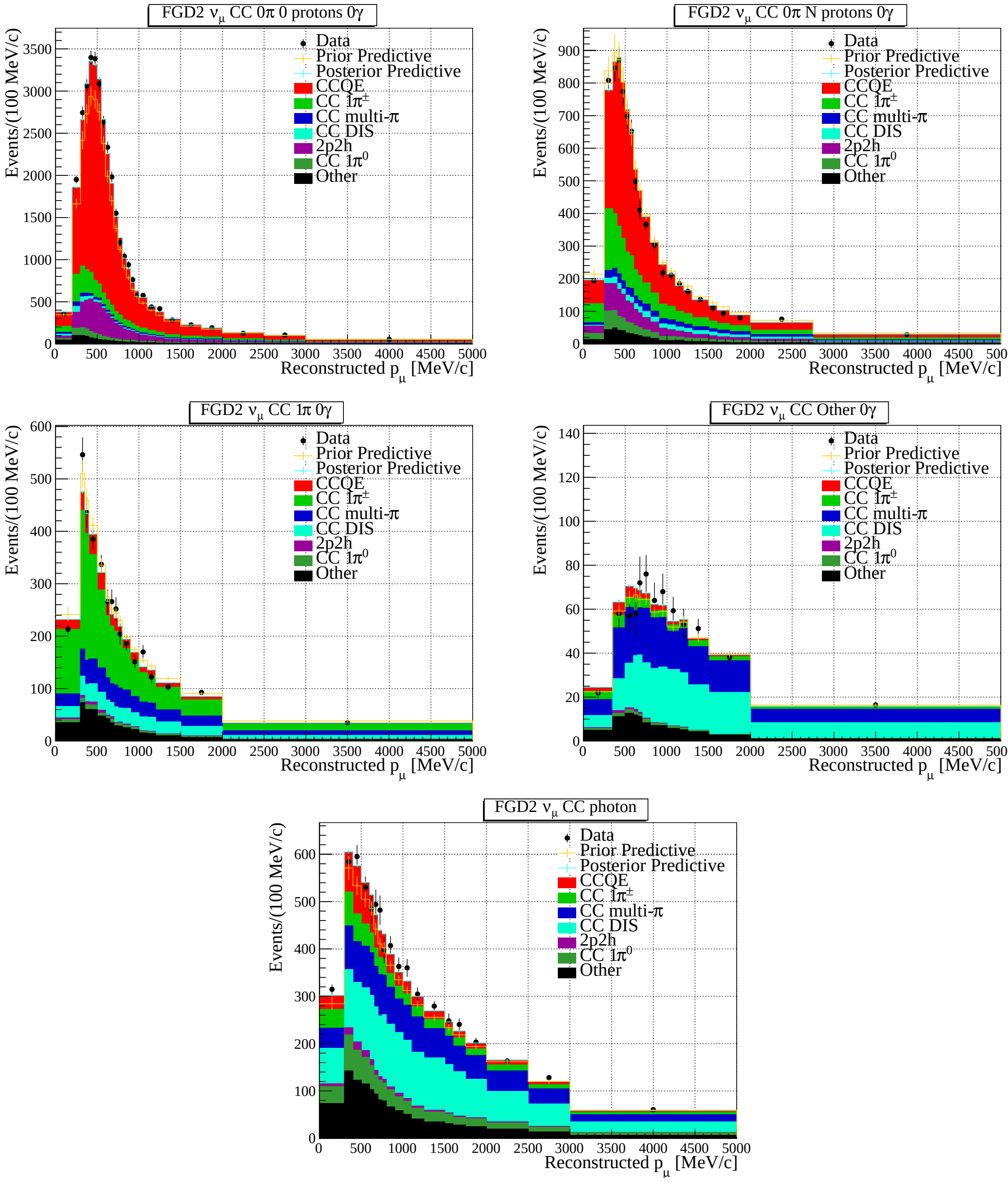

FIGURE B.33: Posterior predictive distributions with reaction breakdown for FHC FGD2 samples.

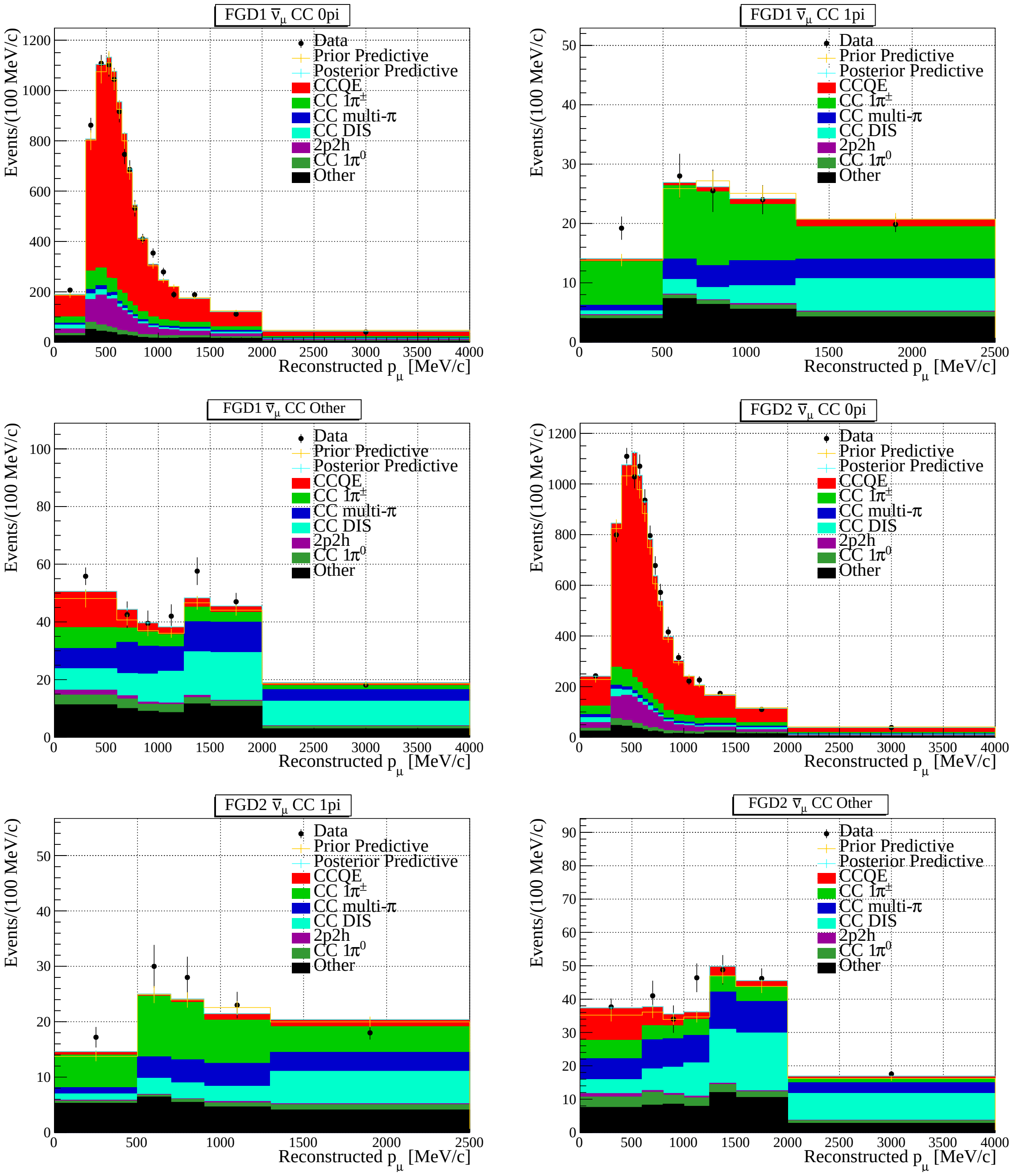

FIGURE B.34: Posterior predictive distributions with reaction breakdown for RHC samples.

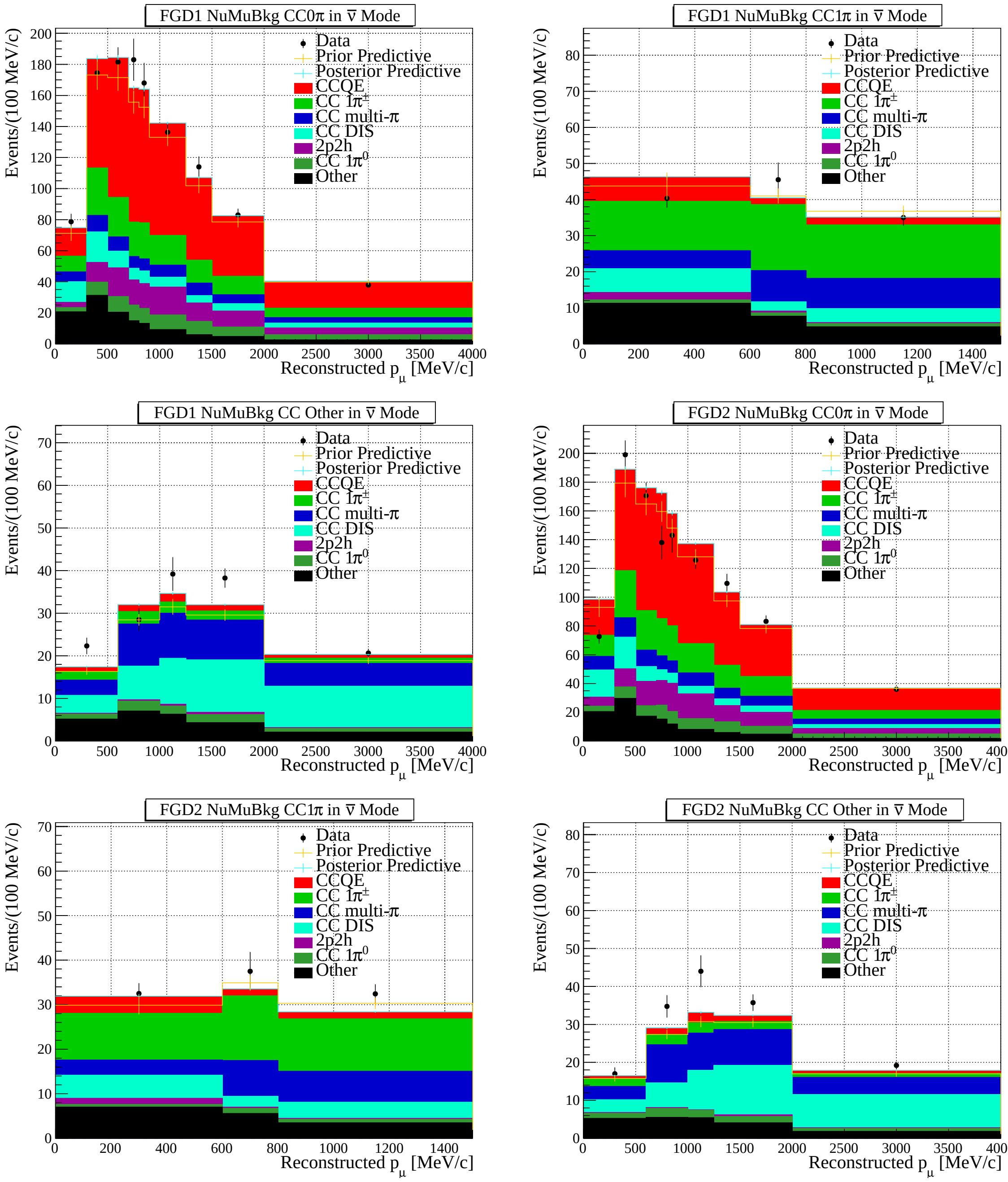

FIGURE B.35: Posterior predictive distributions with reaction breakdown for RHC BKG samples.

B.10 Posterior Distribution for Each Parameter

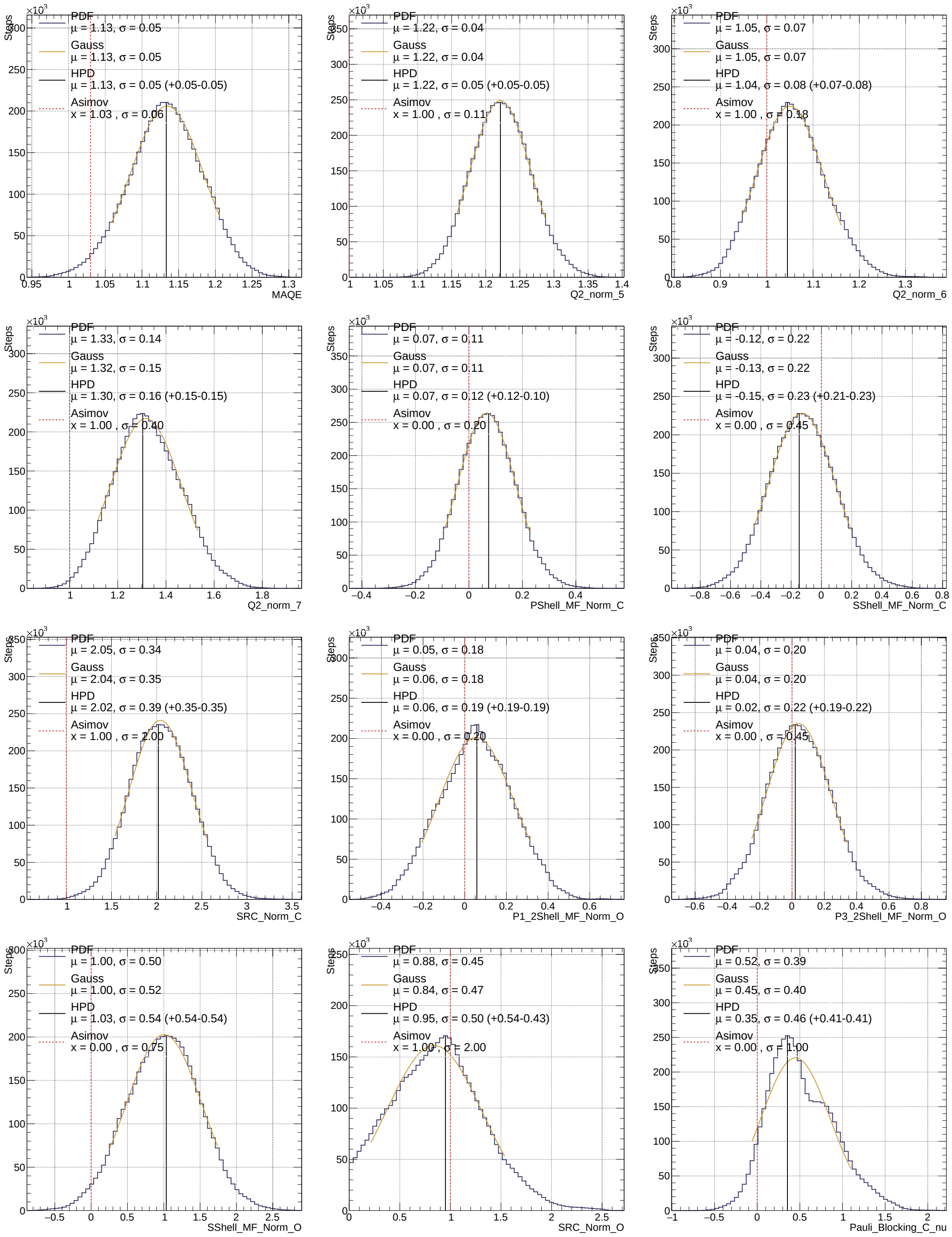

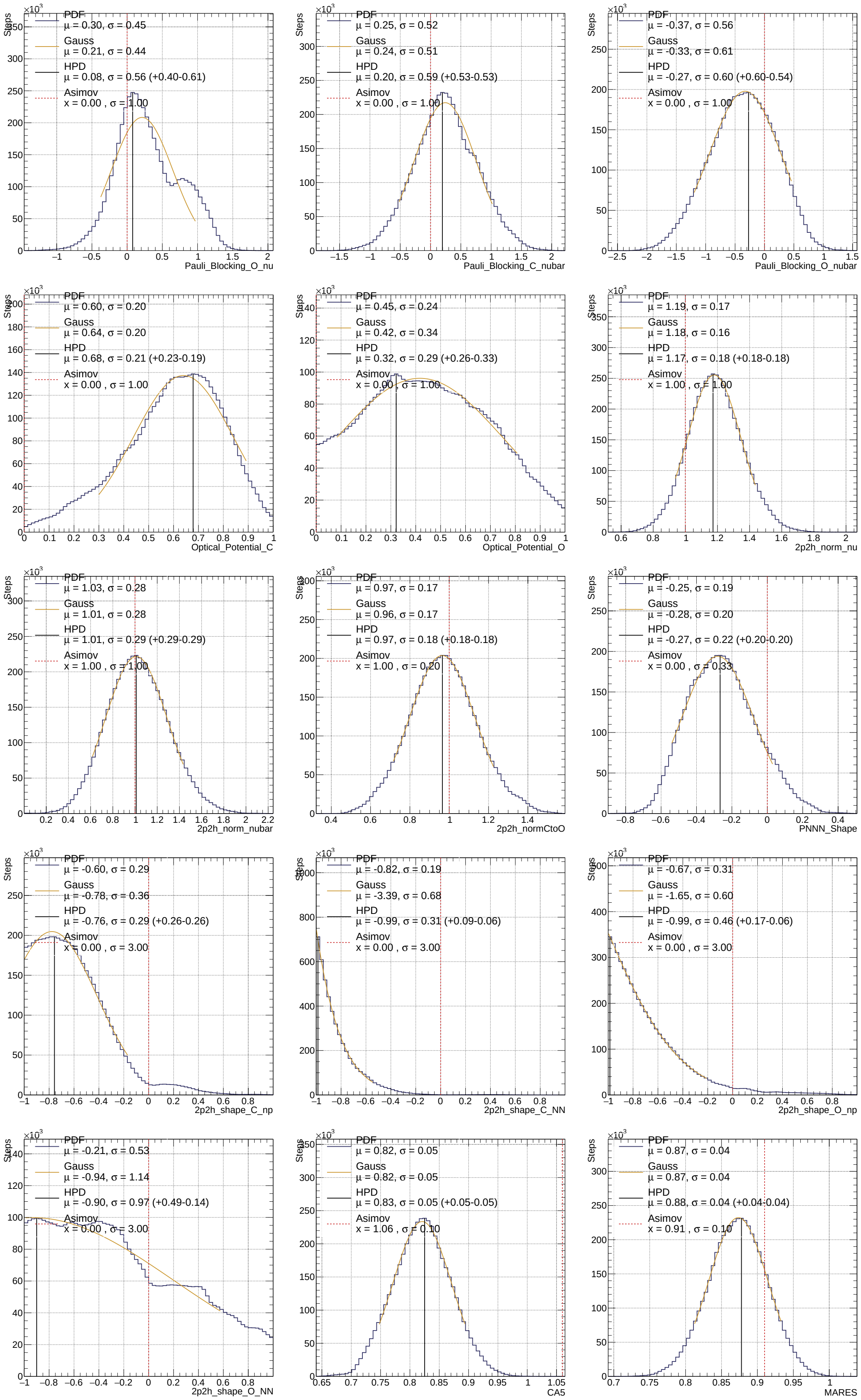
Steps
×10^3
PDF
μ = 0.30, σ = 0.45
Gauss
μ = 0.21, σ = 0.44
HPD
μ = 0.08, σ = 0.56 (+0.40-0.61)
Asimov
x = 0.00 , σ = 1.00
0 50 100 150 200 250 300 350
−1 −0.5 0 0.5 1 1.5 2
Pauli_Blocking_O_nu
Steps
×10^3
PDF
μ = 0.25, σ = 0.52
Gauss
μ = 0.24, σ = 0.51
HPD
μ = 0.20, σ = 0.59 (+0.53-0.53)
Asimov
x = 0.00 , σ = 1.00
0 50 100 150 200 250 300
−1.5 −1 −0.5 0 0.5 1 1.5 2
Pauli_Blocking_C_nubar
Steps
×10^3
PDF
μ = -0.37, σ = 0.56
Gauss
μ = -0.33, σ = 0.61
HPD
μ = -0.27, σ = 0.60 (+0.60-0.54)
Asimov
x = 0.00 , σ = 1.00
0 50 100 150 200 250
−2.5 −2 −1.5 −1 −0.5 0 0.5 1 1.5
Pauli_Blocking_O_nubar
Steps
×10^3
PDF
μ = 0.60, σ = 0.20
Gauss
μ = 0.64, σ = 0.20
HPD
μ = 0.68, σ = 0.21 (+0.23-0.19)
Asimov
x = 0.00 , σ = 1.00
0 20 40 60 80 100 120 140 160 180 200
0 0.1 0.2 0.3 0.4 0.5 0.6 0.7 0.8 0.9 1
Optical_Potential_C
Steps
×10^3
PDF
μ = 0.45, σ = 0.24
Gauss
μ = 0.42, σ = 0.34
HPD
μ = 0.32, σ = 0.29 (+0.26-0.33)
Asimov
x = 0.00 , σ = 1.00
0 20 40 60 80 100 120 140
0 0.1 0.2 0.3 0.4 0.5 0.6 0.7 0.8 0.9 1
Optical_Potential_O
Steps
×10^3
PDF
μ = 1.19, σ = 0.17
Gauss
μ = 1.18, σ = 0.16
HPD
μ = 1.17, σ = 0.18 (+0.18-0.18)
Asimov
x = 1.00 , σ = 1.00
0 50 100 150 200 250 300 350
0.6 0.8 1 1.2 1.4 1.6 1.8 2
2p2h_norm_nu
Steps
×10^3
PDF
μ = 1.03, σ = 0.28
Gauss
μ = 1.01, σ = 0.28
HPD
μ = 1.01, σ = 0.29 (+0.29-0.29)
Asimov
x = 1.00 , σ = 1.00
0 50 100 150 200 250 300
0.2 0.4 0.6 0.8 1 1.2 1.4 1.6 1.8 2 2.2
2p2h_norm_nubar
Steps
×10^3
PDF
μ = 0.97, σ = 0.17
Gauss
μ = 0.96, σ = 0.17
HPD
μ = 0.97, σ = 0.18 (+0.18-0.18)
Asimov
x = 1.00 , σ = 0.20
0 50 100 150 200 250 300
0.4 0.6 0.8 1 1.2 1.4
2p2h_normCtoO
Steps
×10^3
PDF
μ = -0.25, σ = 0.19
Gauss
μ = -0.28, σ = 0.20
HPD
μ = -0.27, σ = 0.22 (+0.20-0.20)
Asimov
x = 0.00 , σ = 0.33
0 50 100 150 200 250
−0.8 −0.6 −0.4 −0.2 0 0.2 0.4
PNNN_Shape
Steps
×10^3
PDF
μ = -0.60, σ = 0.29
Gauss
μ = -0.78, σ = 0.36
HPD
μ = -0.76, σ = 0.29 (+0.26-0.26)
Asimov
x = 0.00 , σ = 3.00
0 50 100 150 200 250
−1 −0.8 −0.6 −0.4 −0.2 0 0.2 0.4 0.6 0.8
2p2h_shape_C_np
Steps
×10^3
PDF
μ = -0.82, σ = 0.19
Gauss
μ = -3.39, σ = 0.68
HPD
μ = -0.99, σ = 0.31 (+0.09-0.06)
Asimov
x = 0.00 , σ = 3.00
0 200 400 600 800 1000
−1 −0.8 −0.6 −0.4 −0.2 0 0.2 0.4 0.6 0.8
2p2h_shape_C_NN
Steps
×10^3
PDF
μ = -0.67, σ = 0.31
Gauss
μ = -1.65, σ = 0.60
HPD
μ = -0.99, σ = 0.46 (+0.17-0.06)
Asimov
x = 0.00 , σ = 3.00
0 100 200 300 400 500
−1 −0.8 −0.6 −0.4 −0.2 0 0.2 0.4 0.6 0.8
2p2h_shape_O_np
Steps
×10^3
PDF
μ = -0.21, σ = 0.53
Gauss
μ = -0.94, σ = 1.14
HPD
μ = -0.90, σ = 0.97 (+0.49-0.14)
Asimov
x = 0.00 , σ = 3.00
0 20 40 60 80 100 120 140
−1 −0.8 −0.6 −0.4 −0.2 0 0.2 0.4 0.6 0.8
2p2h_shape_O_NN
Steps
×10^3
PDF
μ = 0.82, σ = 0.05
Gauss
μ = 0.82, σ = 0.05
HPD
μ = 0.83, σ = 0.05 (+0.05-0.05)
Asimov
x = 1.06 , σ = 0.10
0 50 100 150 200 250 300 350
0.65 0.7 0.75 0.8 0.85 0.9 0.95 1 1.05
CA5
Steps
×10^3
PDF
μ = 0.87, σ = 0.04
Gauss
μ = 0.87, σ = 0.04
HPD
μ = 0.88, σ = 0.04 (+0.04-0.04)
Asimov
x = 0.91 , σ = 0.10
0 50 100 150 200 250 300
0.7 0.75 0.8 0.85 0.9 0.95 1
MARES

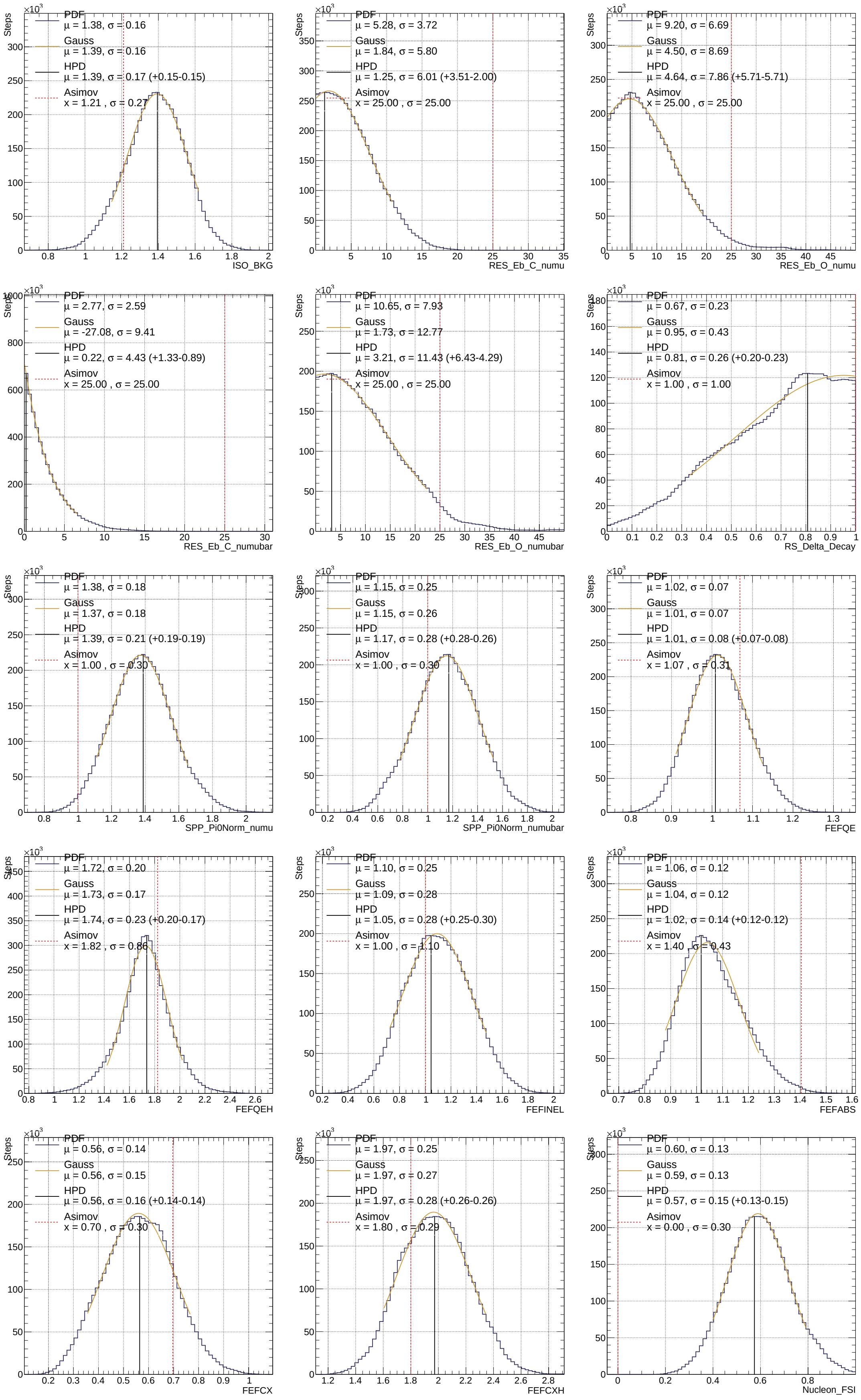
PDF μ = 1.38, σ = 0.16
Gauss μ = 1.39, σ = 0.16
HPD μ = 1.39, σ = 0.17 (+0.15-0.15)
Asimov x = 1.21 , σ = 0.27
ISO_BKG
PDF μ = 5.28, σ = 3.72
Gauss μ = 1.84, σ = 5.80
HPD μ = 1.25, σ = 6.01 (+3.51-2.00)
Asimov x = 25.00 , σ = 25.00
RES_Eb_C_numu
PDF μ = 9.20, σ = 6.69
Gauss μ = 4.50, σ = 8.69
HPD μ = 4.64, σ = 7.86 (+5.71-5.71)
Asimov x = 25.00 , σ = 25.00
RES_Eb_O_numu
PDF μ = 2.77, σ = 2.59
Gauss μ = -27.08, σ = 9.41
HPD μ = 0.22, σ = 4.43 (+1.33-0.89)
Asimov x = 25.00 , σ = 25.00
RES_Eb_C_numubar
PDF μ = 10.65, σ = 7.93
Gauss μ = 1.73, σ = 12.77
HPD μ = 3.21, σ = 11.43 (+6.43-4.29)
Asimov x = 25.00 , σ = 25.00
RES_Eb_O_numubar
PDF μ = 0.67, σ = 0.23
Gauss μ = 0.95, σ = 0.43
HPD μ = 0.81, σ = 0.26 (+0.20-0.23)
Asimov x = 1.00 , σ = 1.00
RS_Delta_Decay
PDF μ = 1.38, σ = 0.18
Gauss μ = 1.37, σ = 0.18
HPD μ = 1.39, σ = 0.21 (+0.19-0.19)
Asimov x = 1.00 , σ = 0.30
SPP_Pi0Norm_numu
PDF μ = 1.15, σ = 0.25
Gauss μ = 1.15, σ = 0.26
HPD μ = 1.17, σ = 0.28 (+0.28-0.26)
Asimov x = 1.00 , σ = 0.30
SPP_Pi0Norm_numubar
PDF μ = 1.02, σ = 0.07
Gauss μ = 1.01, σ = 0.07
HPD μ = 1.01, σ = 0.08 (+0.07-0.08)
Asimov x = 1.07 , σ = 0.31
FEFQE
PDF μ = 1.72, σ = 0.20
Gauss μ = 1.73, σ = 0.17
HPD μ = 1.74, σ = 0.23 (+0.20-0.17)
Asimov x = 1.82 , σ = 0.86
FEFQEH
PDF μ = 1.10, σ = 0.25
Gauss μ = 1.09, σ = 0.28
HPD μ = 1.05, σ = 0.28 (+0.25-0.30)
Asimov x = 1.00 , σ = 1.10
FEFINEL
PDF μ = 1.06, σ = 0.12
Gauss μ = 1.04, σ = 0.12
HPD μ = 1.02, σ = 0.14 (+0.12-0.12)
Asimov x = 1.40 , σ = 0.43
FEFABS
PDF μ = 0.56, σ = 0.14
Gauss μ = 0.56, σ = 0.15
HPD μ = 0.56, σ = 0.16 (+0.14-0.14)
Asimov x = 0.70 , σ = 0.30
FEFCX
PDF μ = 1.97, σ = 0.25
Gauss μ = 1.97, σ = 0.27
HPD μ = 1.97, σ = 0.28 (+0.26-0.26)
Asimov x = 1.80 , σ = 0.29
FEFCXH
PDF μ = 0.60, σ = 0.13
Gauss μ = 0.59, σ = 0.13
HPD μ = 0.57, σ = 0.15 (+0.13-0.15)
Asimov x = 0.00 , σ = 0.30
Nucleon_FSI
Steps
×10³

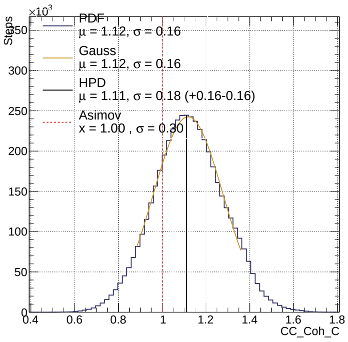
×10³
Steps
PDF
μ = 1.12, σ = 0.16
Gauss
μ = 1.12, σ = 0.16
HPD
μ = 1.11, σ = 0.18 (+0.16-0.16)
Asimov
x = 1.00 , σ = 0.30
CC_Coh_C

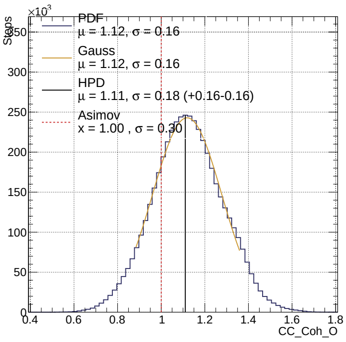
×10³
Steps
PDF
μ = 1.12, σ = 0.16
Gauss
μ = 1.12, σ = 0.16
HPD
μ = 1.11, σ = 0.18 (+0.16-0.16)
Asimov
x = 1.00 , σ = 0.30
CC_Coh_O

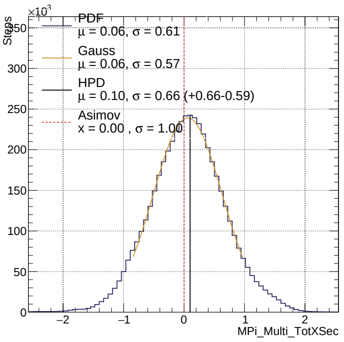
×10³
Steps
PDF
μ = 0.06, σ = 0.61
Gauss
μ = 0.06, σ = 0.57
HPD
μ = 0.10, σ = 0.66 (+0.66-0.59)
Asimov
x = 0.00 , σ = 1.00
MPi_Multi_TotXSec

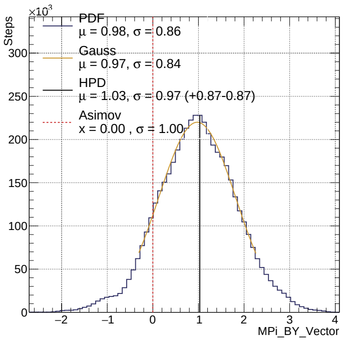
×10³
Steps
PDF
μ = 0.98, σ = 0.86
Gauss
μ = 0.97, σ = 0.84
HPD
μ = 1.03, σ = 0.97 (+0.87-0.87)
Asimov
x = 0.00 , σ = 1.00
MPi_BY_Vector

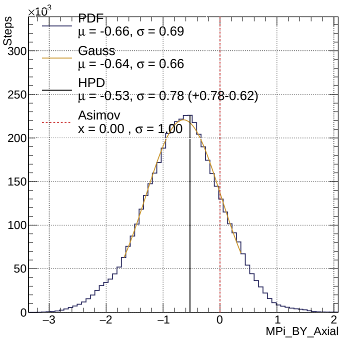
×10³
Steps
PDF
μ = -0.66, σ = 0.69
Gauss
μ = -0.64, σ = 0.66
HPD
μ = -0.53, σ = 0.78 (+0.78-0.62)
Asimov
x = 0.00 , σ = 1.00
MPi_BY_Axial

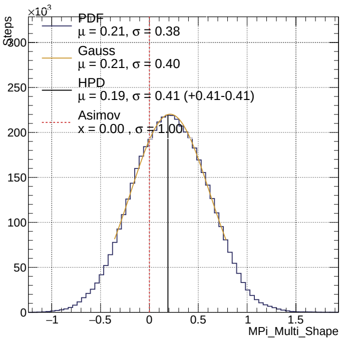
×10³
Steps
PDF
μ = 0.21, σ = 0.38
Gauss
μ = 0.21, σ = 0.40
HPD
μ = 0.19, σ = 0.41 (+0.41-0.41)
Asimov
x = 0.00 , σ = 1.00
MPi_Multi_Shape

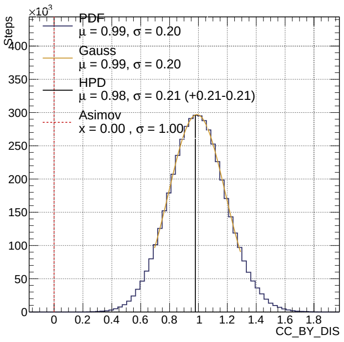
×10³
Steps
PDF
μ = 0.99, σ = 0.20
Gauss
μ = 0.99, σ = 0.20
HPD
μ = 0.98, σ = 0.21 (+0.21-0.21)
Asimov
x = 0.00 , σ = 1.00
CC_BY_DIS

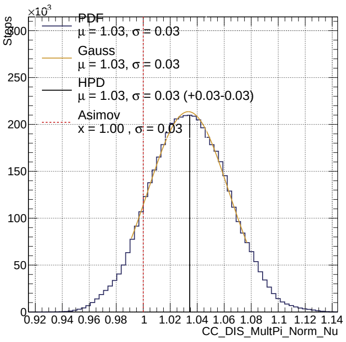
×10³
Steps
PDF
μ = 1.03, σ = 0.03
Gauss
μ = 1.03, σ = 0.03
HPD
μ = 1.03, σ = 0.03 (+0.03-0.03)
Asimov
x = 1.00 , σ = 0.03
CC_DIS_MultPi_Norm_Nu

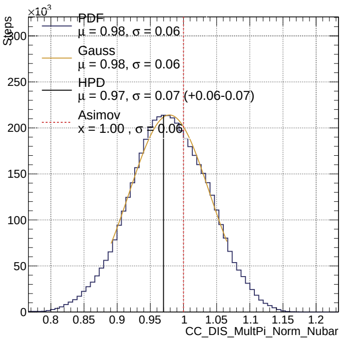
×10³
Steps
PDF
μ = 0.98, σ = 0.06
Gauss
μ = 0.98, σ = 0.06
HPD
μ = 0.97, σ = 0.07 (+0.06-0.07)
Asimov
x = 1.00 , σ = 0.06
CC_DIS_MultPi_Norm_Nubar

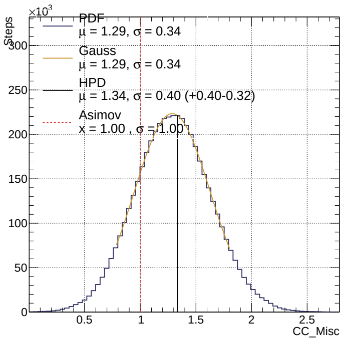
×10³
Steps
PDF
μ = 1.29, σ = 0.34
Gauss
μ = 1.29, σ = 0.34
HPD
μ = 1.34, σ = 0.40 (+0.40-0.32)
Asimov
x = 1.00 , σ = 1.00
CC_Misc

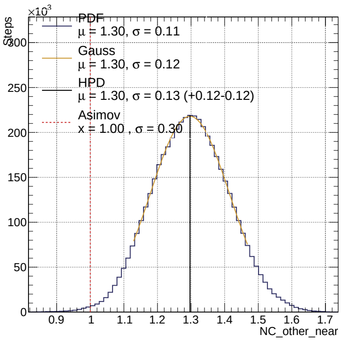
×10³
Steps
PDF
μ = 1.30, σ = 0.11
Gauss
μ = 1.30, σ = 0.12
HPD
μ = 1.30, σ = 0.13 (+0.12-0.12)
Asimov
x = 1.00 , σ = 0.30
NC_other_near

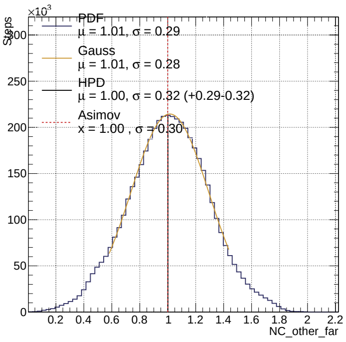
×10³
Steps
PDF
μ = 1.01, σ = 0.29
Gauss
μ = 1.01, σ = 0.28
HPD
μ = 1.00, σ = 0.32 (+0.29-0.32)
Asimov
x = 1.00 , σ = 0.30
NC_other_far

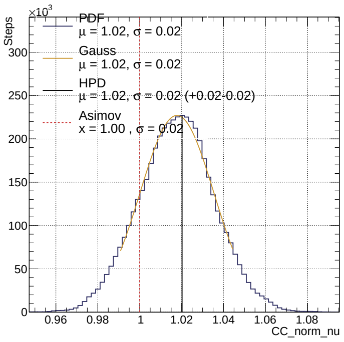
×10³
Steps
PDF
μ = 1.02, σ = 0.02
Gauss
μ = 1.02, σ = 0.02
HPD
μ = 1.02, σ = 0.02 (+0.02-0.02)
Asimov
x = 1.00 , σ = 0.02
CC_norm_nu

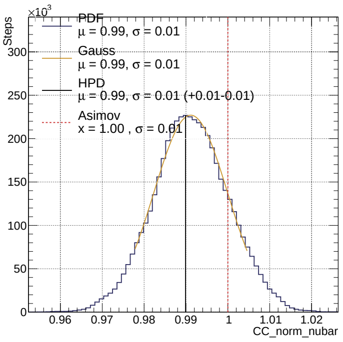
×10³
Steps
PDF
μ = 0.99, σ = 0.01
Gauss
μ = 0.99, σ = 0.01
HPD
μ = 0.99, σ = 0.01 (+0.01-0.01)
Asimov
x = 1.00 , σ = 0.01
CC_norm_nubar

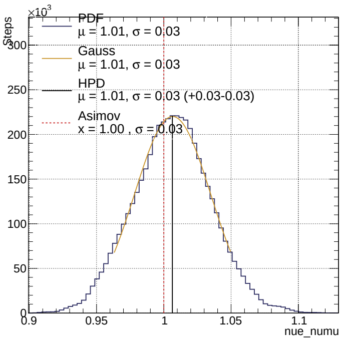
×10³
Steps
PDF
μ = 1.01, σ = 0.03
Gauss
μ = 1.01, σ = 0.03
HPD
μ = 1.01, σ = 0.03 (+0.03-0.03)
Asimov
x = 1.00 , σ = 0.03
nue_numu

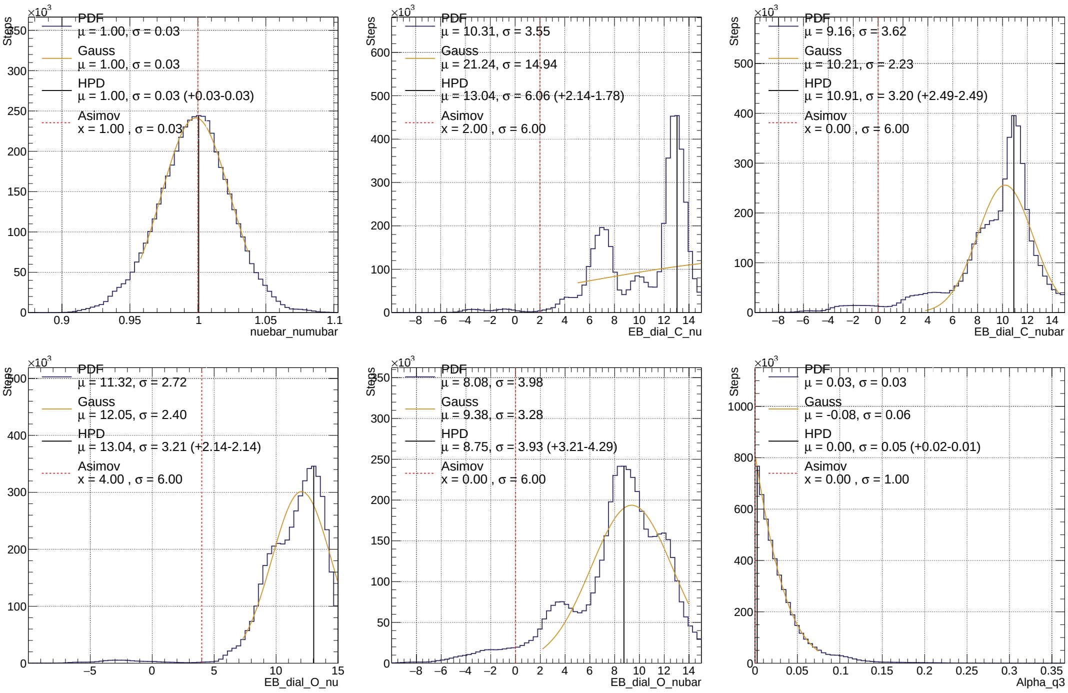
Steps
×10³
PDF
μ = 1.00, σ = 0.03
Gauss
μ = 1.00, σ = 0.03
HPD
μ = 1.00, σ = 0.03 (+0.03-0.03)
Asimov
x = 1.00 , σ = 0.03
nuebar_numubar
PDF
μ = 10.31, σ = 3.55
Gauss
μ = 21.24, σ = 14.94
HPD
μ = 13.04, σ = 6.06 (+2.14-1.78)
Asimov
x = 2.00 , σ = 6.00
EB_dial_C_nu
PDF
μ = 9.16, σ = 3.62
Gauss
μ = 10.21, σ = 2.23
HPD
μ = 10.91, σ = 3.20 (+2.49-2.49)
Asimov
x = 0.00 , σ = 6.00
EB_dial_C_nubar
PDF
μ = 11.32, σ = 2.72
Gauss
μ = 12.05, σ = 2.40
HPD
μ = 13.04, σ = 3.21 (+2.14-2.14)
Asimov
x = 4.00 , σ = 6.00
EB_dial_O_nu
PDF
μ = 8.08, σ = 3.98
Gauss
μ = 9.38, σ = 3.28
HPD
μ = 8.75, σ = 3.93 (+3.21-4.29)
Asimov
x = 0.00 , σ = 6.00
EB_dial_O_nubar
PDF
μ = 0.03, σ = 0.03
Gauss
μ = -0.08, σ = 0.06
HPD
μ = 0.00, σ = 0.05 (+0.02-0.01)
Asimov
x = 0.00 , σ = 1.00
Alpha_q3

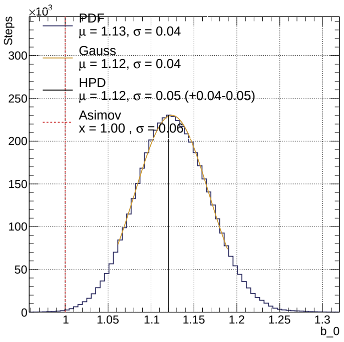
×10^3
Steps
PDF
μ = 1.13, σ = 0.04
Gauss
μ = 1.12, σ = 0.04
HPD
μ = 1.12, σ = 0.05 (+0.04-0.05)
Asimov
x = 1.00 , σ = 0.06
0
50
100
150
200
250
300
1
1.05
1.1
1.15
1.2
1.25
1.3
b_0

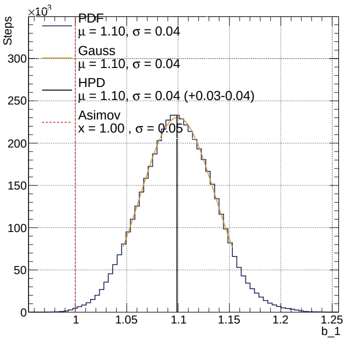
×10^3
Steps
PDF
μ = 1.10, σ = 0.04
Gauss
μ = 1.10, σ = 0.04
HPD
μ = 1.10, σ = 0.04 (+0.03-0.04)
Asimov
x = 1.00 , σ = 0.05
0
50
100
150
200
250
300
1
1.05
1.1
1.15
1.2
1.25
b_1

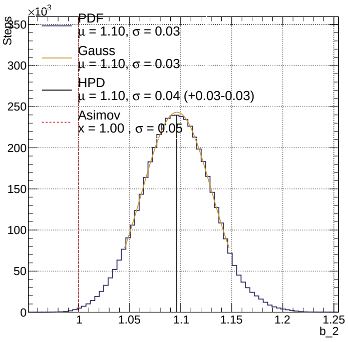
×10^3
Steps
PDF
μ = 1.10, σ = 0.03
Gauss
μ = 1.10, σ = 0.03
HPD
μ = 1.10, σ = 0.04 (+0.03-0.03)
Asimov
x = 1.00 , σ = 0.05
0
50
100
150
200
250
300
350
1
1.05
1.1
1.15
1.2
1.25
b_2

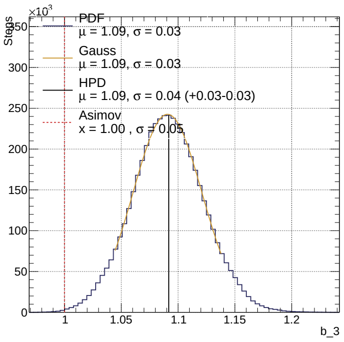
×10^3
Steps
PDF
μ = 1.09, σ = 0.03
Gauss
μ = 1.09, σ = 0.03
HPD
μ = 1.09, σ = 0.04 (+0.03-0.03)
Asimov
x = 1.00 , σ = 0.05
0
50
100
150
200
250
300
350
1
1.05
1.1
1.15
1.2
b_3

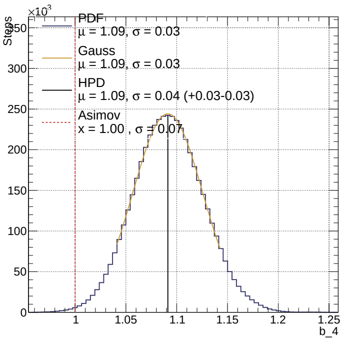
×10^3
Steps
PDF
μ = 1.09, σ = 0.03
Gauss
μ = 1.09, σ = 0.03
HPD
μ = 1.09, σ = 0.04 (+0.03-0.03)
Asimov
x = 1.00 , σ = 0.07
0
50
100
150
200
250
300
350
1
1.05
1.1
1.15
1.2
1.25
b_4

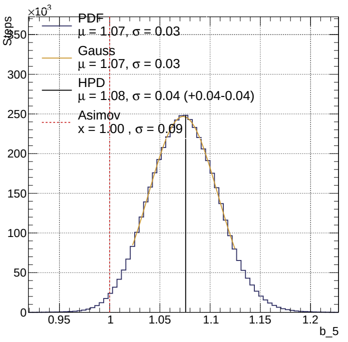
×10^3
Steps
PDF
μ = 1.07, σ = 0.03
Gauss
μ = 1.07, σ = 0.03
HPD
μ = 1.08, σ = 0.04 (+0.04-0.04)
Asimov
x = 1.00 , σ = 0.09
0
50
100
150
200
250
300
350
0.95
1
1.05
1.1
1.15
1.2
b_5

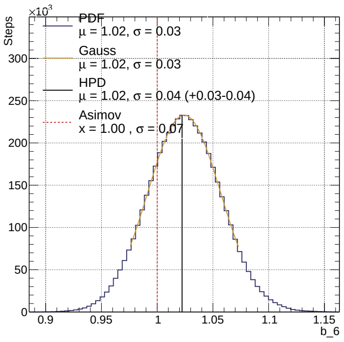
×10^3
Steps
PDF
μ = 1.02, σ = 0.03
Gauss
μ = 1.02, σ = 0.03
HPD
μ = 1.02, σ = 0.04 (+0.03-0.04)
Asimov
x = 1.00 , σ = 0.07
0
50
100
150
200
250
300
0.9
0.95
1
1.05
1.1
1.15
b_6

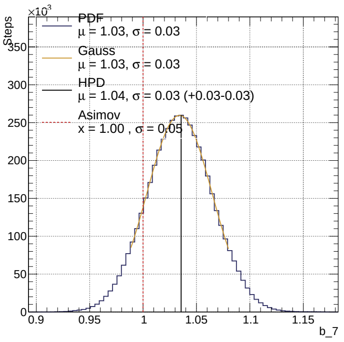
×10^3
Steps
PDF
μ = 1.03, σ = 0.03
Gauss
μ = 1.03, σ = 0.03
HPD
μ = 1.04, σ = 0.03 (+0.03-0.03)
Asimov
x = 1.00 , σ = 0.05
0
50
100
150
200
250
300
350
0.9
0.95
1
1.05
1.1
1.15
b_7

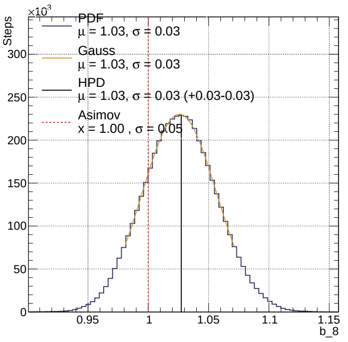
×10^3
Steps
PDF
μ = 1.03, σ = 0.03
Gauss
μ = 1.03, σ = 0.03
HPD
μ = 1.03, σ = 0.03 (+0.03-0.03)
Asimov
x = 1.00 , σ = 0.05
0
50
100
150
200
250
300
0.95
1
1.05
1.1
1.15
b_8

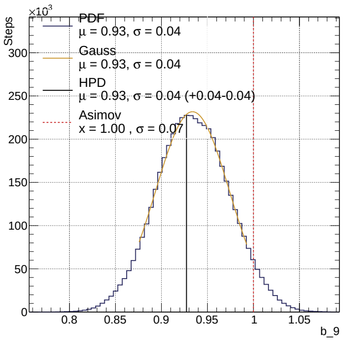
×10^3
Steps
PDF
μ = 0.93, σ = 0.04
Gauss
μ = 0.93, σ = 0.04
HPD
μ = 0.93, σ = 0.04 (+0.04-0.04)
Asimov
x = 1.00 , σ = 0.07
0
50
100
150
200
250
300
0.8
0.85
0.9
0.95
1
1.05
b_9

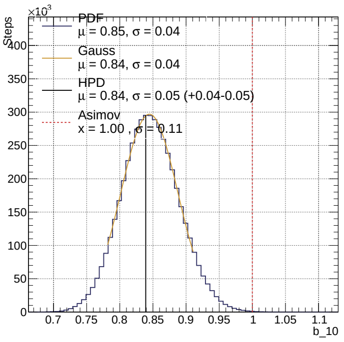
×10^3
Steps
PDF
μ = 0.85, σ = 0.04
Gauss
μ = 0.84, σ = 0.04
HPD
μ = 0.84, σ = 0.05 (+0.04-0.05)
Asimov
x = 1.00 , σ = 0.11
0
50
100
150
200
250
300
350
400
0.7
0.75
0.8
0.85
0.9
0.95
1
1.05
1.1
b_10

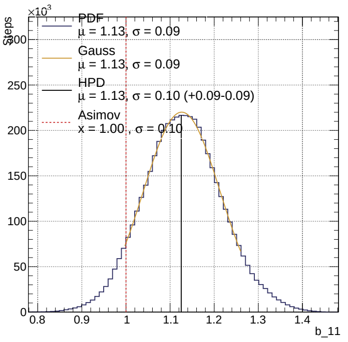
×10^3
Steps
PDF
μ = 1.13, σ = 0.09
Gauss
μ = 1.13, σ = 0.09
HPD
μ = 1.13, σ = 0.10 (+0.09-0.09)
Asimov
x = 1.00 , σ = 0.10
0
50
100
150
200
250
300
0.8
0.9
1
1.1
1.2
1.3
1.4
b_11

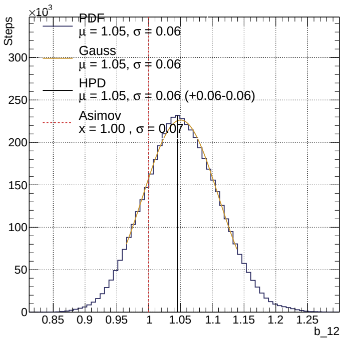
×10^3
Steps
PDF
μ = 1.05, σ = 0.06
Gauss
μ = 1.05, σ = 0.06
HPD
μ = 1.05, σ = 0.06 (+0.06-0.06)
Asimov
x = 1.00 , σ = 0.07
0
50
100
150
200
250
300
0.85
0.9
0.95
1
1.05
1.1
1.15
1.2
1.25
b_12

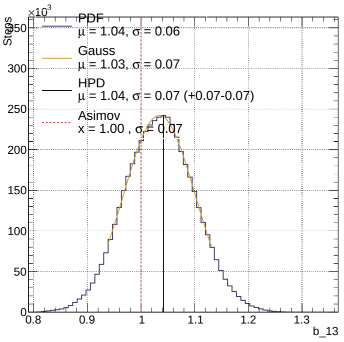
×10^3
Steps
PDF
μ = 1.04, σ = 0.06
Gauss
μ = 1.03, σ = 0.07
HPD
μ = 1.04, σ = 0.07 (+0.07-0.07)
Asimov
x = 1.00 , σ = 0.07
0
50
100
150
200
250
300
350
0.8
0.9
1
1.1
1.2
1.3
b_13

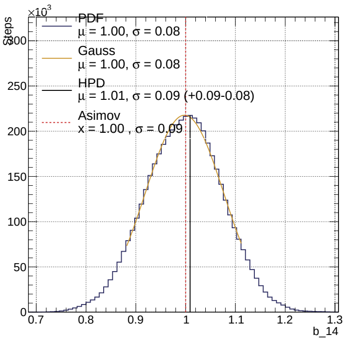
×10^3
Steps
PDF
μ = 1.00, σ = 0.08
Gauss
μ = 1.00, σ = 0.08
HPD
μ = 1.01, σ = 0.09 (+0.09-0.08)
Asimov
x = 1.00 , σ = 0.09
0
50
100
150
200
250
300
0.7
0.8
0.9
1
1.1
1.2
1.3
b_14

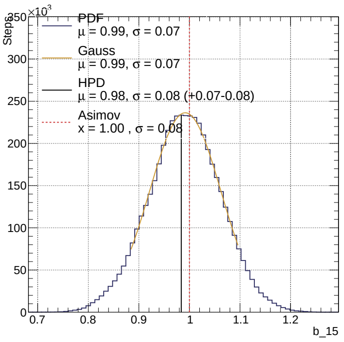
×10^3
Steps
PDF
μ = 0.99, σ = 0.07
Gauss
μ = 0.99, σ = 0.07
HPD
μ = 0.98, σ = 0.08 (+0.07-0.08)
Asimov
x = 1.00 , σ = 0.08
0
50
100
150
200
250
300
350
0.7
0.8
0.9
1
1.1
1.2
b_15

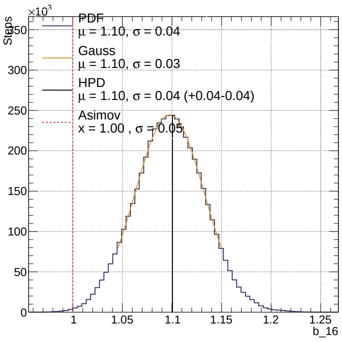
×10^3
Steps
PDF
μ = 1.10, σ = 0.04
Gauss
μ = 1.10, σ = 0.03
HPD
μ = 1.10, σ = 0.04 (+0.04-0.04)
Asimov
x = 1.00 , σ = 0.05
0
50
100
150
200
250
300
350
1
1.05
1.1
1.15
1.2
1.25
b_16

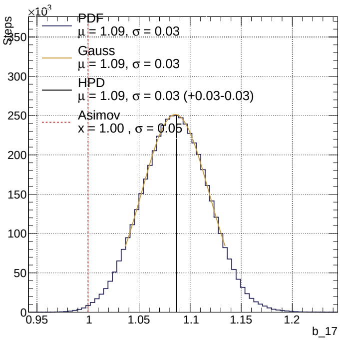
×10^3
Steps
PDF
μ = 1.09, σ = 0.03
Gauss
μ = 1.09, σ = 0.03
HPD
μ = 1.09, σ = 0.03 (+0.03-0.03)
Asimov
x = 1.00 , σ = 0.05
0
50
100
150
200
250
300
350
0.95
1
1.05
1.1
1.15
1.2
b_17

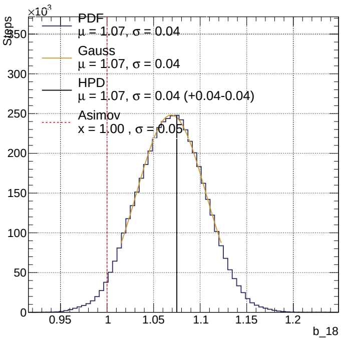
×10^3
Steps
PDF
μ = 1.07, σ = 0.04
Gauss
μ = 1.07, σ = 0.04
HPD
μ = 1.07, σ = 0.04 (+0.04-0.04)
Asimov
x = 1.00 , σ = 0.05
0
50
100
150
200
250
300
350
0.95
1
1.05
1.1
1.15
1.2
b_18

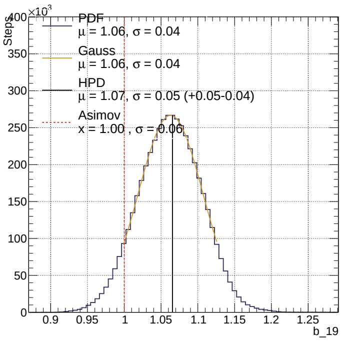
×10^3
Steps
PDF
μ = 1.06, σ = 0.04
Gauss
μ = 1.06, σ = 0.04
HPD
μ = 1.07, σ = 0.05 (+0.05-0.04)
Asimov
x = 1.00 , σ = 0.06
0
50
100
150
200
250
300
350
400
0.9
0.95
1
1.05
1.1
1.15
1.2
1.25
b_19

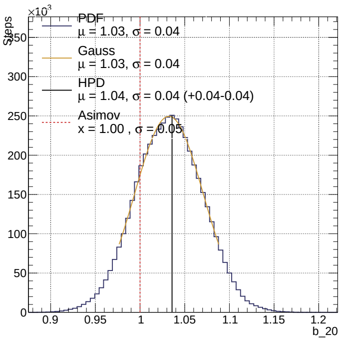
×10^3
Steps
PDF
μ = 1.03, σ = 0.04
Gauss
μ = 1.03, σ = 0.04
HPD
μ = 1.04, σ = 0.04 (+0.04-0.04)
Asimov
x = 1.00 , σ = 0.05
0
50
100
150
200
250
300
350
0.9
0.95
1
1.05
1.1
1.15
1.2
b_20

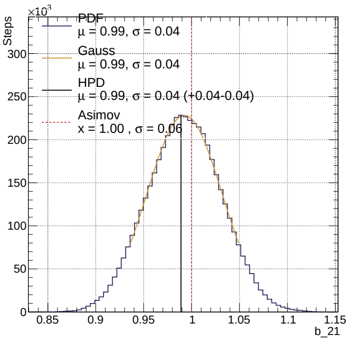
×10^3
Steps
PDF
μ = 0.99, σ = 0.04
Gauss
μ = 0.99, σ = 0.04
HPD
μ = 0.99, σ = 0.04 (+0.04-0.04)
Asimov
x = 1.00 , σ = 0.06
0
50
100
150
200
250
300
0.85
0.9
0.95
1
1.05
1.1
1.15
b_21

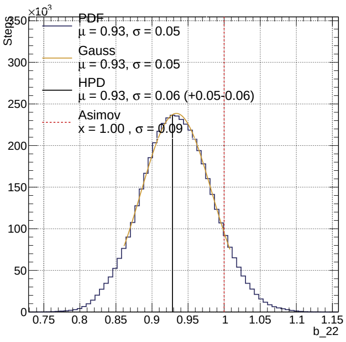
×10^3
Steps
PDF
μ = 0.93, σ = 0.05
Gauss
μ = 0.93, σ = 0.05
HPD
μ = 0.93, σ = 0.06 (+0.05-0.06)
Asimov
x = 1.00 , σ = 0.09
0
50
100
150
200
250
300
350
0.75
0.8
0.85
0.9
0.95
1
1.05
1.1
1.15
b_22

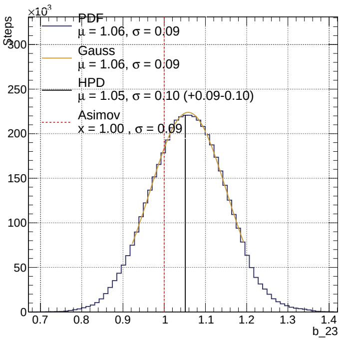
×10^3
Steps
PDF
μ = 1.06, σ = 0.09
Gauss
μ = 1.06, σ = 0.09
HPD
μ = 1.05, σ = 0.10 (+0.09-0.10)
Asimov
x = 1.00 , σ = 0.09
0
50
100
150
200
250
300
0.7
0.8
0.9
1
1.1
1.2
1.3
1.4
b_23

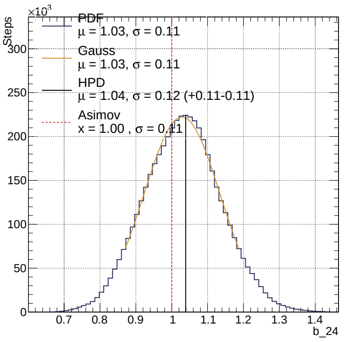
×10^3
Steps
PDF
μ = 1.03, σ = 0.11
Gauss
μ = 1.03, σ = 0.11
HPD
μ = 1.04, σ = 0.12 (+0.11-0.11)
Asimov
x = 1.00 , σ = 0.11
0
50
100
150
200
250
300
0.7
0.8
0.9
1
1.1
1.2
1.3
1.4
b_24

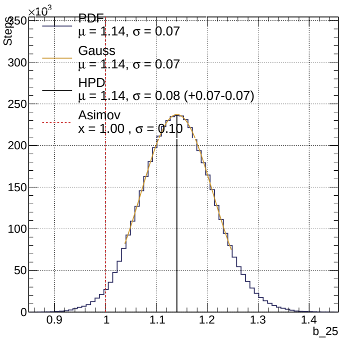
×10^3
Steps
PDF
μ = 1.14, σ = 0.07
Gauss
μ = 1.14, σ = 0.07
HPD
μ = 1.14, σ = 0.08 (+0.07-0.07)
Asimov
x = 1.00 , σ = 0.10
0
50
100
150
200
250
300
350
0.9
1
1.1
1.2
1.3
1.4
b_25

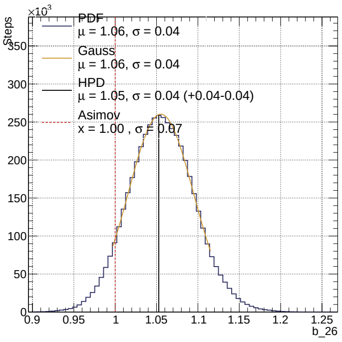
×10^3
Steps
PDF
μ = 1.06, σ = 0.04
Gauss
μ = 1.06, σ = 0.04
HPD
μ = 1.05, σ = 0.04 (+0.04-0.04)
Asimov
x = 1.00 , σ = 0.07
0
50
100
150
200
250
300
350
0.9
0.95
1
1.05
1.1
1.15
1.2
1.25
b_26

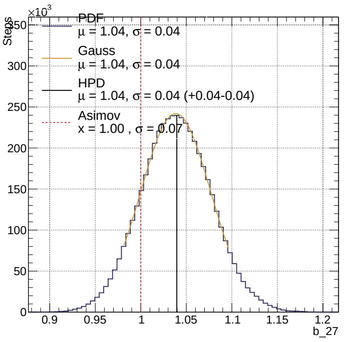
×10^3
Steps
PDF
μ = 1.04, σ = 0.04
Gauss
μ = 1.04, σ = 0.04
HPD
μ = 1.04, σ = 0.04 (+0.04-0.04)
Asimov
x = 1.00 , σ = 0.07
0
50
100
150
200
250
300
350
0.9
0.95
1
1.05
1.1
1.15
1.2
b_27

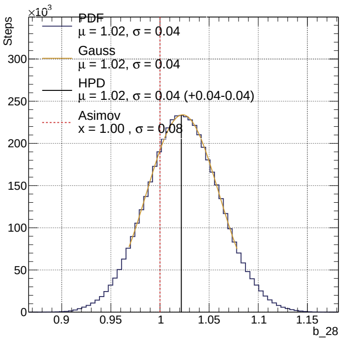
×10^3
Steps
PDF
μ = 1.02, σ = 0.04
Gauss
μ = 1.02, σ = 0.04
HPD
μ = 1.02, σ = 0.04 (+0.04-0.04)
Asimov
x = 1.00 , σ = 0.08
0
50
100
150
200
250
300
0.9
0.95
1
1.05
1.1
1.15
b_28

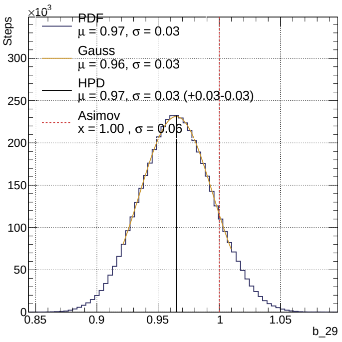
×10^3
Steps
PDF
μ = 0.97, σ = 0.03
Gauss
μ = 0.96, σ = 0.03
HPD
μ = 0.97, σ = 0.03 (+0.03-0.03)
Asimov
x = 1.00 , σ = 0.06
0
50
100
150
200
250
300
0.85
0.9
0.95
1
1.05
b_29

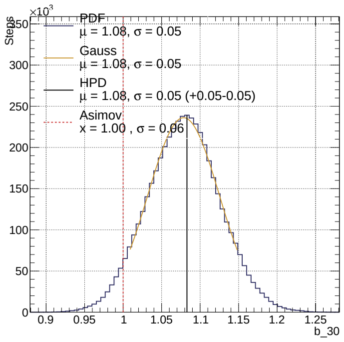
×10^3
Steps
PDF
μ = 1.08, σ = 0.05
Gauss
μ = 1.08, σ = 0.05
HPD
μ = 1.08, σ = 0.05 (+0.05-0.05)
Asimov
x = 1.00 , σ = 0.06
0
50
100
150
200
250
300
350
0.9
0.95
1
1.05
1.1
1.15
1.2
1.25
b_30

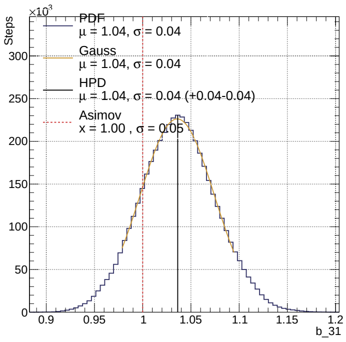
×10^3
Steps
PDF
μ = 1.04, σ = 0.04
Gauss
μ = 1.04, σ = 0.04
HPD
μ = 1.04, σ = 0.04 (+0.04-0.04)
Asimov
x = 1.00 , σ = 0.05
0
50
100
150
200
250
300
0.9
0.95
1
1.05
1.1
1.15
1.2
b_31

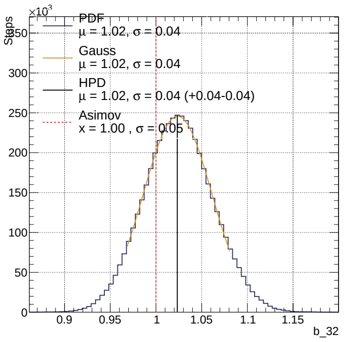
×10^3
Steps
PDF
μ = 1.02, σ = 0.04
Gauss
μ = 1.02, σ = 0.04
HPD
μ = 1.02, σ = 0.04 (+0.04-0.04)
Asimov
x = 1.00 , σ = 0.05
0
50
100
150
200
250
300
350
0.9
0.95
1
1.05
1.1
1.15
b_32

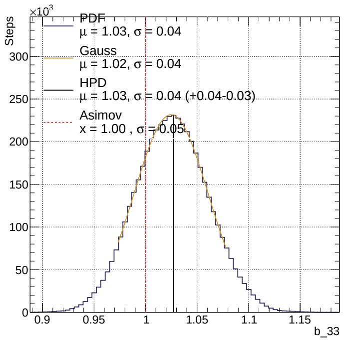
×10^3
Steps
PDF
μ = 1.03, σ = 0.04
Gauss
μ = 1.02, σ = 0.04
HPD
μ = 1.03, σ = 0.04 (+0.04-0.03)
Asimov
x = 1.00 , σ = 0.05
0
50
100
150
200
250
300
0.9
0.95
1
1.05
1.1
1.15
b_33

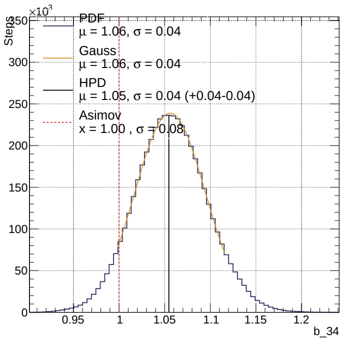
×10^3
Steps
PDF
μ = 1.06, σ = 0.04
Gauss
μ = 1.06, σ = 0.04
HPD
μ = 1.05, σ = 0.04 (+0.04-0.04)
Asimov
x = 1.00 , σ = 0.08
0
50
100
150
200
250
300
350
0.95
1
1.05
1.1
1.15
1.2
b_34

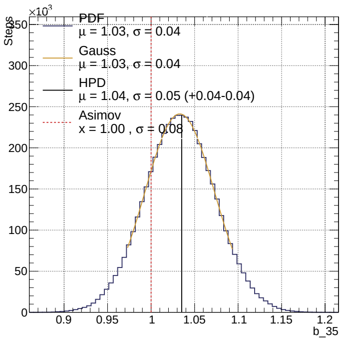
×10^3
Steps
PDF
μ = 1.03, σ = 0.04
Gauss
μ = 1.03, σ = 0.04
HPD
μ = 1.04, σ = 0.05 (+0.04-0.04)
Asimov
x = 1.00 , σ = 0.08
0
50
100
150
200
250
300
350
0.9
0.95
1
1.05
1.1
1.15
1.2
b_35

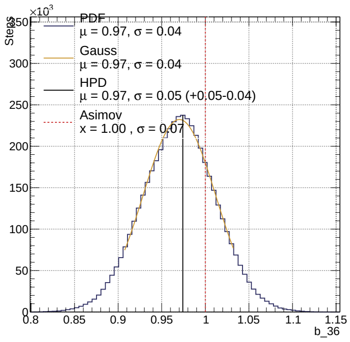
×10^3
Steps
PDF
μ = 0.97, σ = 0.04
Gauss
μ = 0.97, σ = 0.04
HPD
μ = 0.97, σ = 0.05 (+0.05-0.04)
Asimov
x = 1.00 , σ = 0.07
0
50
100
150
200
250
300
350
0.8
0.85
0.9
0.95
1
1.05
1.1
1.15
b_36

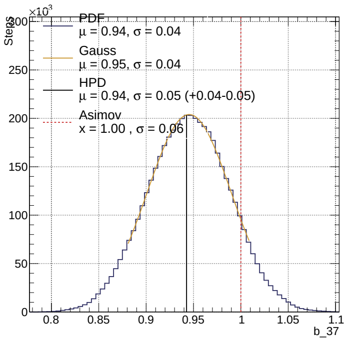
×10^3
Steps
PDF
μ = 0.94, σ = 0.04
Gauss
μ = 0.95, σ = 0.04
HPD
μ = 0.94, σ = 0.05 (+0.04-0.05)
Asimov
x = 1.00 , σ = 0.06
0
50
100
150
200
250
300
0.8
0.85
0.9
0.95
1
1.05
1.1
b_37

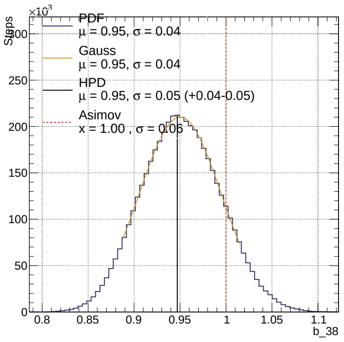
×10^3
Steps
PDF
μ = 0.95, σ = 0.04
Gauss
μ = 0.95, σ = 0.04
HPD
μ = 0.95, σ = 0.05 (+0.04-0.05)
Asimov
x = 1.00 , σ = 0.06
0
50
100
150
200
250
300
0.8
0.85
0.9
0.95
1
1.05
1.1
b_38

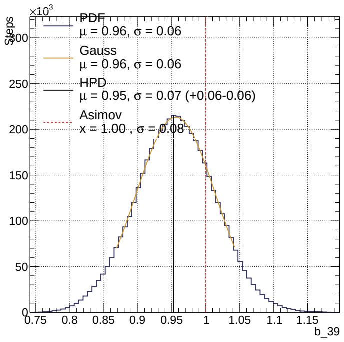
×10^3
Steps
PDF
μ = 0.96, σ = 0.06
Gauss
μ = 0.96, σ = 0.06
HPD
μ = 0.95, σ = 0.07 (+0.06-0.06)
Asimov
x = 1.00 , σ = 0.08
0
50
100
150
200
250
300
0.75
0.8
0.85
0.9
0.95
1
1.05
1.1
1.15
b_39

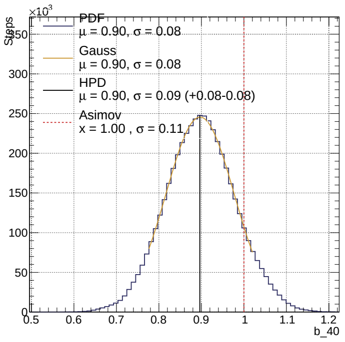
×10^3
Steps
PDF
μ = 0.90, σ = 0.08
Gauss
μ = 0.90, σ = 0.08
HPD
μ = 0.90, σ = 0.09 (+0.08-0.08)
Asimov
x = 1.00 , σ = 0.11
0
50
100
150
200
250
300
350
0.5
0.6
0.7
0.8
0.9
1
1.1
1.2
b_40

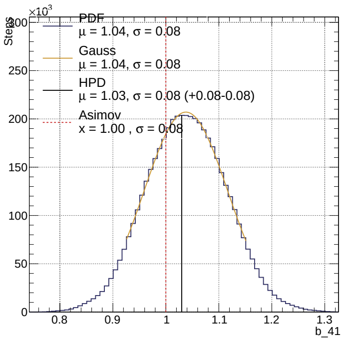
×10^3
Steps
PDF
μ = 1.04, σ = 0.08
Gauss
μ = 1.04, σ = 0.08
HPD
μ = 1.03, σ = 0.08 (+0.08-0.08)
Asimov
x = 1.00 , σ = 0.08
0
50
100
150
200
250
300
0.8
0.9
1
1.1
1.2
1.3
b_41

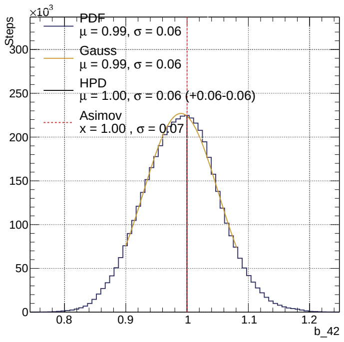
×10^3
Steps
PDF
μ = 0.99, σ = 0.06
Gauss
μ = 0.99, σ = 0.06
HPD
μ = 1.00, σ = 0.06 (+0.06-0.06)
Asimov
x = 1.00 , σ = 0.07
0
50
100
150
200
250
300
0.8
0.9
1
1.1
1.2
b_42

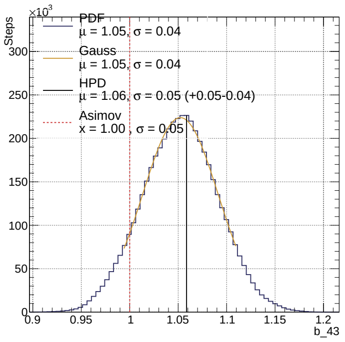
×10^3
Steps
PDF
μ = 1.05, σ = 0.04
Gauss
μ = 1.05, σ = 0.04
HPD
μ = 1.06, σ = 0.05 (+0.05-0.04)
Asimov
x = 1.00 , σ = 0.05
0
50
100
150
200
250
300
0.9
0.95
1
1.05
1.1
1.15
1.2
b_43

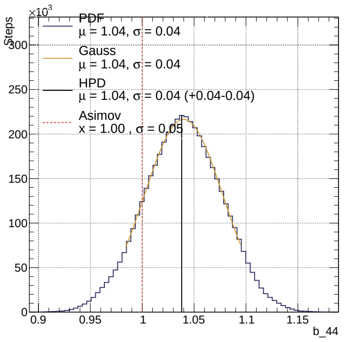
×10^3
Steps
PDF
μ = 1.04, σ = 0.04
Gauss
μ = 1.04, σ = 0.04
HPD
μ = 1.04, σ = 0.04 (+0.04-0.04)
Asimov
x = 1.00 , σ = 0.05
0
50
100
150
200
250
300
0.9
0.95
1
1.05
1.1
1.15
b_44

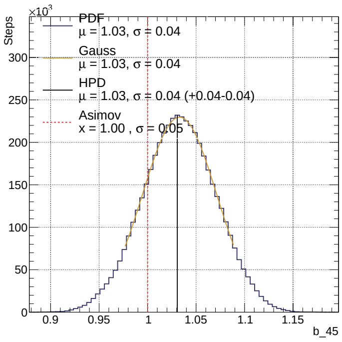
Steps
×10^3
PDF
μ = 1.03, σ = 0.04
Gauss
μ = 1.03, σ = 0.04
HPD
μ = 1.03, σ = 0.04 (+0.04-0.04)
Asimov
x = 1.00 , σ = 0.05
0 50 100 150 200 250 300
0.9 0.95 1 1.05 1.1 1.15
b_45

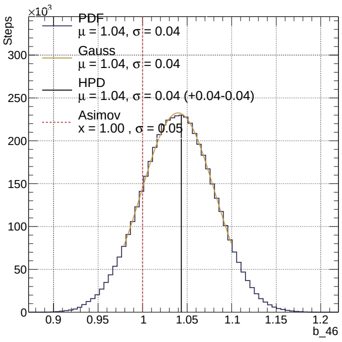
Steps
×10^3
PDF
μ = 1.04, σ = 0.04
Gauss
μ = 1.04, σ = 0.04
HPD
μ = 1.04, σ = 0.04 (+0.04-0.04)
Asimov
x = 1.00 , σ = 0.05
0 50 100 150 200 250 300
0.9 0.95 1 1.05 1.1 1.15 1.2
b_46

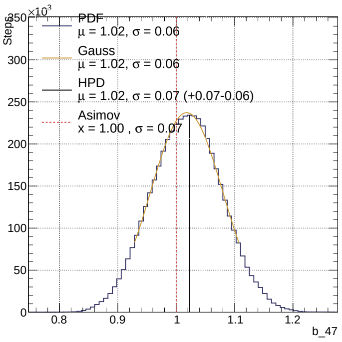
Steps
×10^3
PDF
μ = 1.02, σ = 0.06
Gauss
μ = 1.02, σ = 0.06
HPD
μ = 1.02, σ = 0.07 (+0.07-0.06)
Asimov
x = 1.00 , σ = 0.07
0 50 100 150 200 250 300 350
0.8 0.9 1 1.1 1.2
b_47

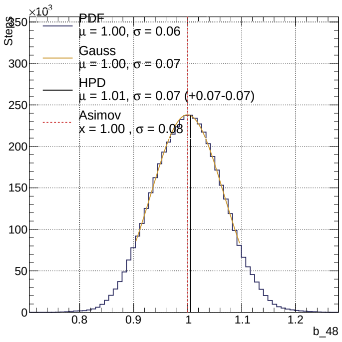
Steps
×10^3
PDF
μ = 1.00, σ = 0.06
Gauss
μ = 1.00, σ = 0.07
HPD
μ = 1.01, σ = 0.07 (+0.07-0.07)
Asimov
x = 1.00 , σ = 0.08
0 50 100 150 200 250 300 350
0.8 0.9 1 1.1 1.2
b_48

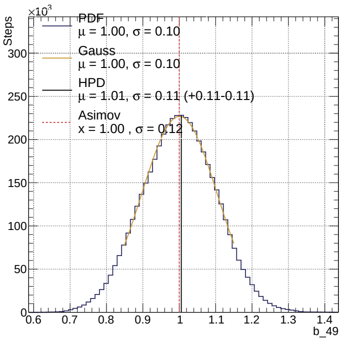
Steps
×10^3
PDF
μ = 1.00, σ = 0.10
Gauss
μ = 1.00, σ = 0.10
HPD
μ = 1.01, σ = 0.11 (+0.11-0.11)
Asimov
x = 1.00 , σ = 0.12
0 50 100 150 200 250 300
0.6 0.7 0.8 0.9 1 1.1 1.2 1.3 1.4
b_49

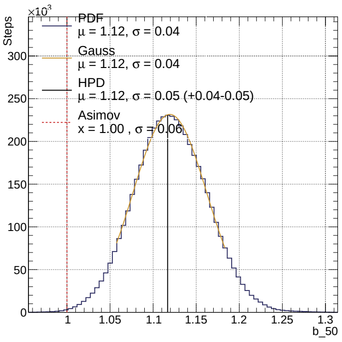
Steps
×10^3
PDF
μ = 1.12, σ = 0.04
Gauss
μ = 1.12, σ = 0.04
HPD
μ = 1.12, σ = 0.05 (+0.04-0.05)
Asimov
x = 1.00 , σ = 0.06
0 50 100 150 200 250 300
1 1.05 1.1 1.15 1.2 1.25 1.3
b_50

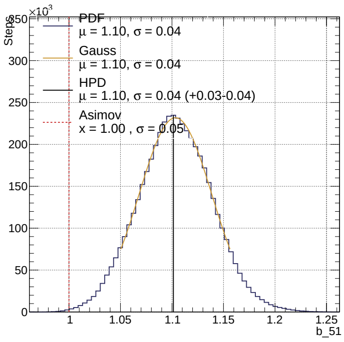
Steps
×10^3
PDF
μ = 1.10, σ = 0.04
Gauss
μ = 1.10, σ = 0.04
HPD
μ = 1.10, σ = 0.04 (+0.03-0.04)
Asimov
x = 1.00 , σ = 0.05
0 50 100 150 200 250 300 350
1 1.05 1.1 1.15 1.2 1.25
b_51

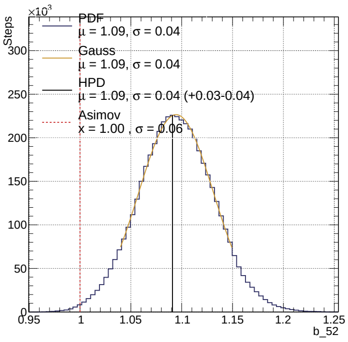
Steps
×10^3
PDF
μ = 1.09, σ = 0.04
Gauss
μ = 1.09, σ = 0.04
HPD
μ = 1.09, σ = 0.04 (+0.03-0.04)
Asimov
x = 1.00 , σ = 0.06
0 50 100 150 200 250 300
0.95 1 1.05 1.1 1.15 1.2 1.25
b_52

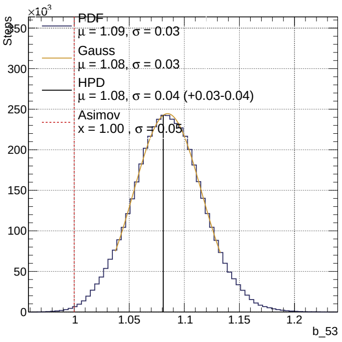
Steps
×10^3
PDF
μ = 1.09, σ = 0.03
Gauss
μ = 1.08, σ = 0.03
HPD
μ = 1.08, σ = 0.04 (+0.03-0.04)
Asimov
x = 1.00 , σ = 0.05
0 50 100 150 200 250 300 350
1 1.05 1.1 1.15 1.2
b_53

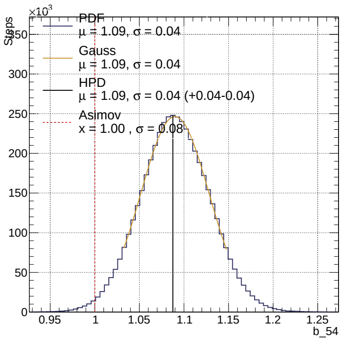
Steps
×10^3
PDF
μ = 1.09, σ = 0.04
Gauss
μ = 1.09, σ = 0.04
HPD
μ = 1.09, σ = 0.04 (+0.04-0.04)
Asimov
x = 1.00 , σ = 0.08
0 50 100 150 200 250 300 350
0.95 1 1.05 1.1 1.15 1.2 1.25
b_54

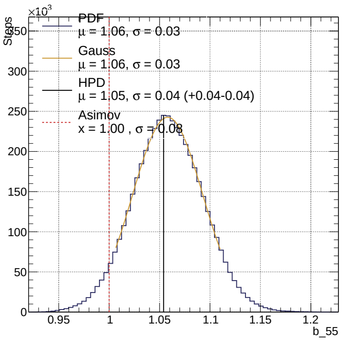
Steps
×10^3
PDF
μ = 1.06, σ = 0.03
Gauss
μ = 1.06, σ = 0.03
HPD
μ = 1.05, σ = 0.04 (+0.04-0.04)
Asimov
x = 1.00 , σ = 0.08
0 50 100 150 200 250 300 350
0.95 1 1.05 1.1 1.15 1.2
b_55

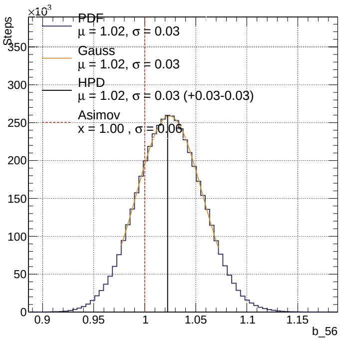
Steps
×10^3
PDF
μ = 1.02, σ = 0.03
Gauss
μ = 1.02, σ = 0.03
HPD
μ = 1.02, σ = 0.03 (+0.03-0.03)
Asimov
x = 1.00 , σ = 0.06
0 50 100 150 200 250 300 350
0.9 0.95 1 1.05 1.1 1.15
b_56

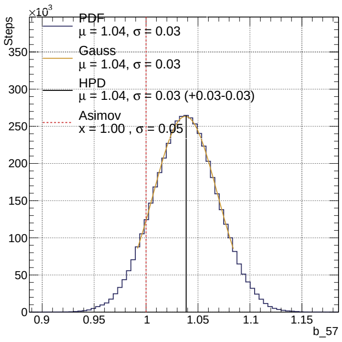
Steps
×10^3
PDF
μ = 1.04, σ = 0.03
Gauss
μ = 1.04, σ = 0.03
HPD
μ = 1.04, σ = 0.03 (+0.03-0.03)
Asimov
x = 1.00 , σ = 0.05
0 50 100 150 200 250 300 350
0.9 0.95 1 1.05 1.1 1.15
b_57

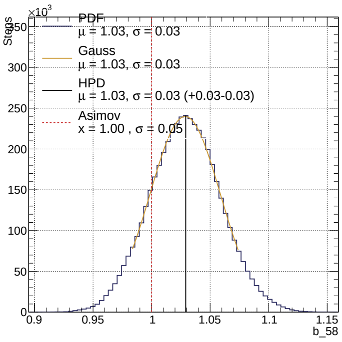
Steps
×10^3
PDF
μ = 1.03, σ = 0.03
Gauss
μ = 1.03, σ = 0.03
HPD
μ = 1.03, σ = 0.03 (+0.03-0.03)
Asimov
x = 1.00 , σ = 0.05
0 50 100 150 200 250 300 350
0.9 0.95 1 1.05 1.1 1.15
b_58

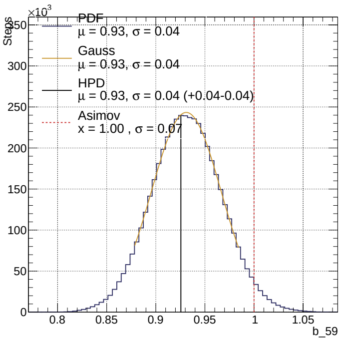
Steps
×10^3
PDF
μ = 0.93, σ = 0.04
Gauss
μ = 0.93, σ = 0.04
HPD
μ = 0.93, σ = 0.04 (+0.04-0.04)
Asimov
x = 1.00 , σ = 0.07
0 50 100 150 200 250 300 350
0.8 0.85 0.9 0.95 1 1.05
b_59

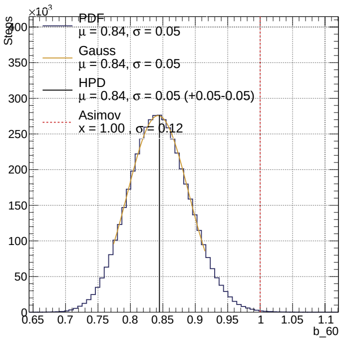
×10^3
Steps
PDF
μ = 0.84, σ = 0.05
Gauss
μ = 0.84, σ = 0.05
HPD
μ = 0.84, σ = 0.05 (+0.05-0.05)
Asimov
x = 1.00 , σ = 0.12
400 350 300 250 200 150 100 50 0
0.65 0.7 0.75 0.8 0.85 0.9 0.95 1 1.05 1.1
b_60

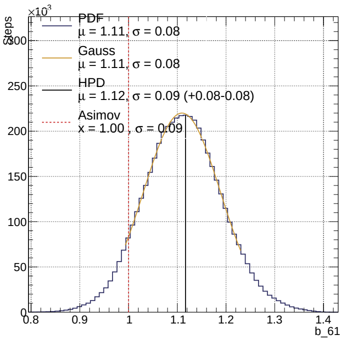
×10^3
Steps
PDF
μ = 1.11, σ = 0.08
Gauss
μ = 1.11, σ = 0.08
HPD
μ = 1.12, σ = 0.09 (+0.08-0.08)
Asimov
x = 1.00 , σ = 0.09
300 250 200 150 100 50 0
0.8 0.9 1 1.1 1.2 1.3 1.4
b_61

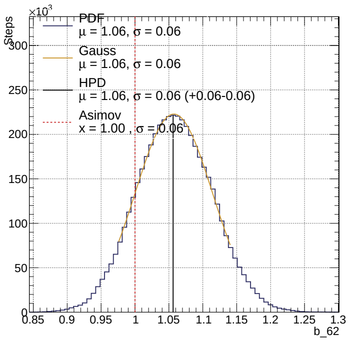
×10^3
Steps
PDF
μ = 1.06, σ = 0.06
Gauss
μ = 1.06, σ = 0.06
HPD
μ = 1.06, σ = 0.06 (+0.06-0.06)
Asimov
x = 1.00 , σ = 0.06
300 250 200 150 100 50 0
0.85 0.9 0.95 1 1.05 1.1 1.15 1.2 1.25 1.3
b_62

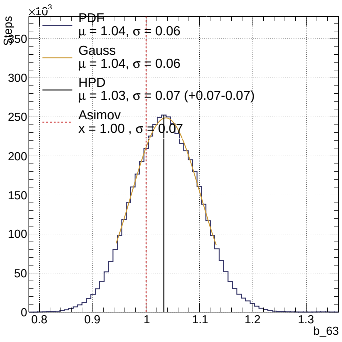
×10^3
Steps
PDF
μ = 1.04, σ = 0.06
Gauss
μ = 1.04, σ = 0.06
HPD
μ = 1.03, σ = 0.07 (+0.07-0.07)
Asimov
x = 1.00 , σ = 0.07
350 300 250 200 150 100 50 0
0.8 0.9 1 1.1 1.2 1.3
b_63

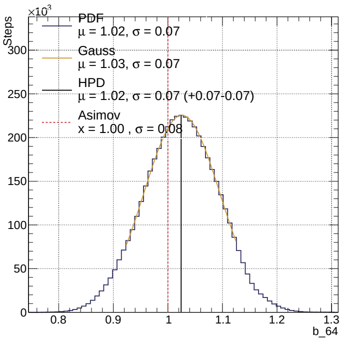
×10^3
Steps
PDF
μ = 1.02, σ = 0.07
Gauss
μ = 1.03, σ = 0.07
HPD
μ = 1.02, σ = 0.07 (+0.07-0.07)
Asimov
x = 1.00 , σ = 0.08
300 250 200 150 100 50 0
0.8 0.9 1 1.1 1.2 1.3
b_64

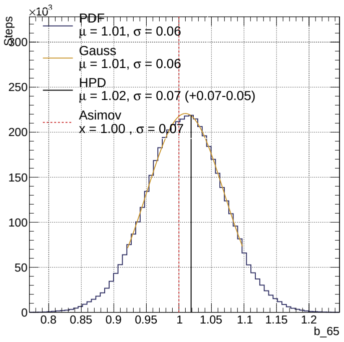
×10^3
Steps
PDF
μ = 1.01, σ = 0.06
Gauss
μ = 1.01, σ = 0.06
HPD
μ = 1.02, σ = 0.07 (+0.07-0.05)
Asimov
x = 1.00 , σ = 0.07
300 250 200 150 100 50 0
0.8 0.85 0.9 0.95 1 1.05 1.1 1.15 1.2
b_65

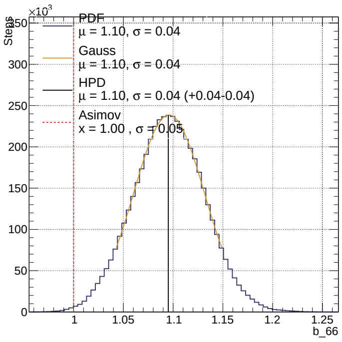
×10^3
Steps
PDF
μ = 1.10, σ = 0.04
Gauss
μ = 1.10, σ = 0.04
HPD
μ = 1.10, σ = 0.04 (+0.04-0.04)
Asimov
x = 1.00 , σ = 0.05
350 300 250 200 150 100 50 0
1 1.05 1.1 1.15 1.2 1.25
b_66

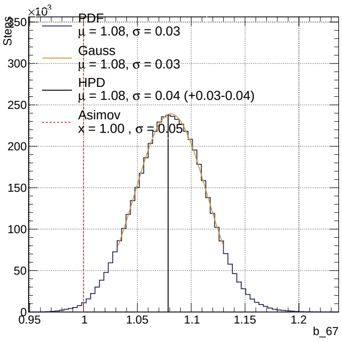
×10^3
Steps
PDF
μ = 1.08, σ = 0.03
Gauss
μ = 1.08, σ = 0.03
HPD
μ = 1.08, σ = 0.04 (+0.03-0.04)
Asimov
x = 1.00 , σ = 0.05
350 300 250 200 150 100 50 0
0.95 1 1.05 1.1 1.15 1.2
b_67

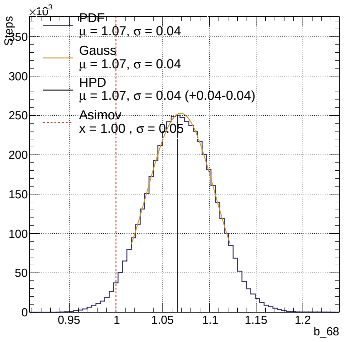
×10^3
Steps
PDF
μ = 1.07, σ = 0.04
Gauss
μ = 1.07, σ = 0.04
HPD
μ = 1.07, σ = 0.04 (+0.04-0.04)
Asimov
x = 1.00 , σ = 0.05
350 300 250 200 150 100 50 0
0.95 1 1.05 1.1 1.15 1.2
b_68

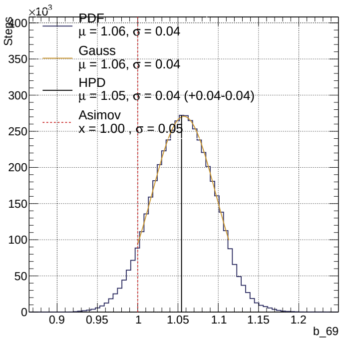
×10^3
Steps
PDF
μ = 1.06, σ = 0.04
Gauss
μ = 1.06, σ = 0.04
HPD
μ = 1.05, σ = 0.04 (+0.04-0.04)
Asimov
x = 1.00 , σ = 0.05
400 350 300 250 200 150 100 50 0
0.9 0.95 1 1.05 1.1 1.15 1.2
b_69

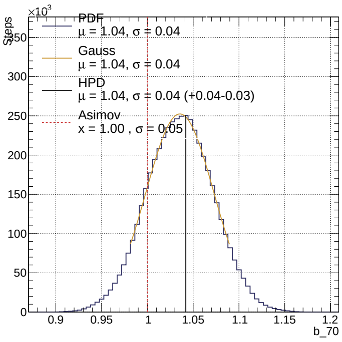
×10^3
Steps
PDF
μ = 1.04, σ = 0.04
Gauss
μ = 1.04, σ = 0.04
HPD
μ = 1.04, σ = 0.04 (+0.04-0.03)
Asimov
x = 1.00 , σ = 0.05
350 300 250 200 150 100 50 0
0.9 0.95 1 1.05 1.1 1.15 1.2
b_70

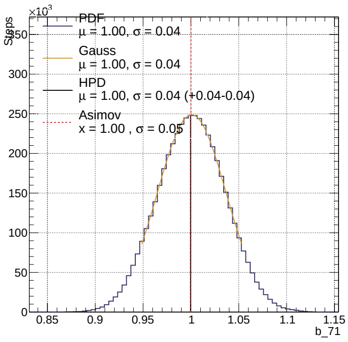
×10^3
Steps
PDF
μ = 1.00, σ = 0.04
Gauss
μ = 1.00, σ = 0.04
HPD
μ = 1.00, σ = 0.04 (+0.04-0.04)
Asimov
x = 1.00 , σ = 0.05
350 300 250 200 150 100 50 0
0.85 0.9 0.95 1 1.05 1.1 1.15
b_71

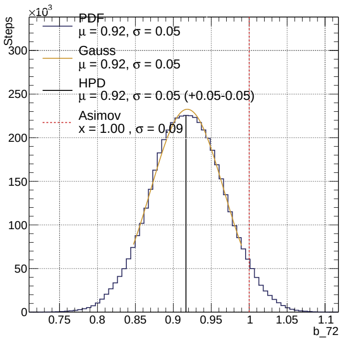
×10^3
Steps
PDF
μ = 0.92, σ = 0.05
Gauss
μ = 0.92, σ = 0.05
HPD
μ = 0.92, σ = 0.05 (+0.05-0.05)
Asimov
x = 1.00 , σ = 0.09
300 250 200 150 100 50 0
0.75 0.8 0.85 0.9 0.95 1 1.05 1.1
b_72

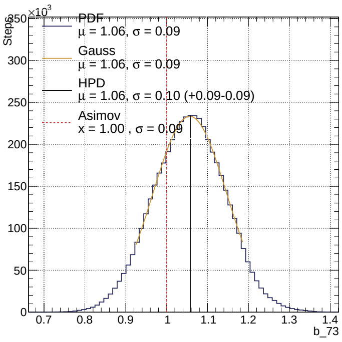
×10^3
Steps
PDF
μ = 1.06, σ = 0.09
Gauss
μ = 1.06, σ = 0.09
HPD
μ = 1.06, σ = 0.10 (+0.09-0.09)
Asimov
x = 1.00 , σ = 0.09
350 300 250 200 150 100 50 0
0.7 0.8 0.9 1 1.1 1.2 1.3 1.4
b_73

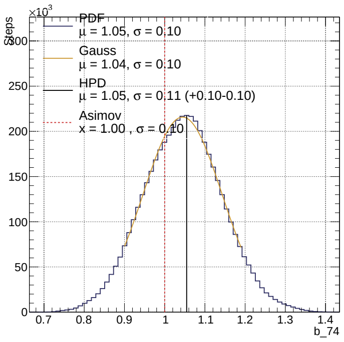
×10^3
Steps
PDF
μ = 1.05, σ = 0.10
Gauss
μ = 1.04, σ = 0.10
HPD
μ = 1.05, σ = 0.11 (+0.10-0.10)
Asimov
x = 1.00 , σ = 0.10
300 250 200 150 100 50 0
0.7 0.8 0.9 1 1.1 1.2 1.3 1.4
b_74

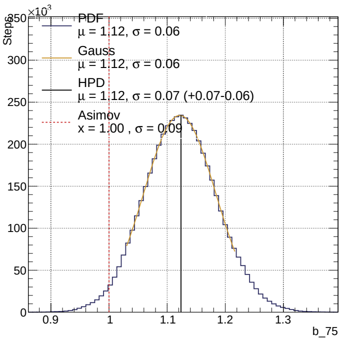
Steps
×10^3
0 50 100 150 200 250 300 350
PDF
μ = 1.12, σ = 0.06
Gauss
μ = 1.12, σ = 0.06
HPD
μ = 1.12, σ = 0.07 (+0.07-0.06)
Asimov
x = 1.00 , σ = 0.09
0.9 1 1.1 1.2 1.3
b_75

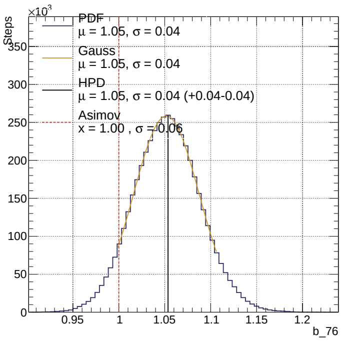
Steps
×10^3
0 50 100 150 200 250 300 350
PDF
μ = 1.05, σ = 0.04
Gauss
μ = 1.05, σ = 0.04
HPD
μ = 1.05, σ = 0.04 (+0.04-0.04)
Asimov
x = 1.00 , σ = 0.06
0.95 1 1.05 1.1 1.15 1.2
b_76

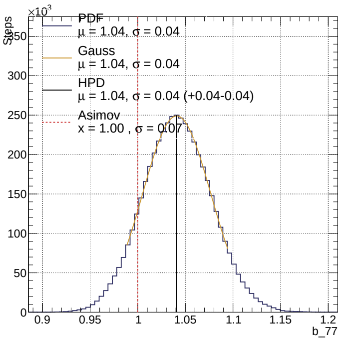
Steps
×10^3
0 50 100 150 200 250 300 350
PDF
μ = 1.04, σ = 0.04
Gauss
μ = 1.04, σ = 0.04
HPD
μ = 1.04, σ = 0.04 (+0.04-0.04)
Asimov
x = 1.00 , σ = 0.07
0.9 0.95 1 1.05 1.1 1.15 1.2
b_77

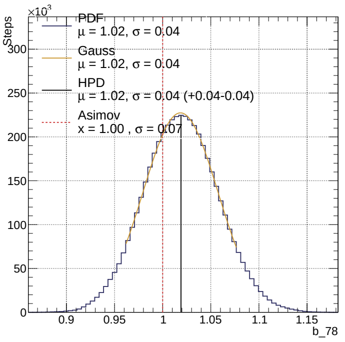
Steps
×10^3
0 50 100 150 200 250 300
PDF
μ = 1.02, σ = 0.04
Gauss
μ = 1.02, σ = 0.04
HPD
μ = 1.02, σ = 0.04 (+0.04-0.04)
Asimov
x = 1.00 , σ = 0.07
0.9 0.95 1 1.05 1.1 1.15
b_78

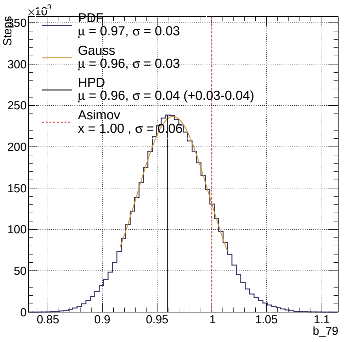
Steps
×10^3
0 50 100 150 200 250 300 350
PDF
μ = 0.97, σ = 0.03
Gauss
μ = 0.96, σ = 0.03
HPD
μ = 0.96, σ = 0.04 (+0.03-0.04)
Asimov
x = 1.00 , σ = 0.06
0.85 0.9 0.95 1 1.05 1.1
b_79

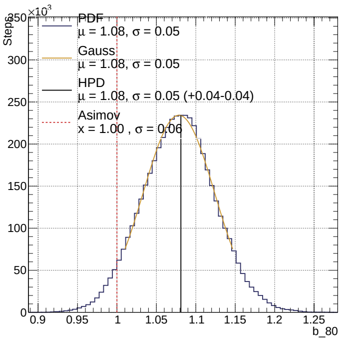
Steps
×10^3
0 50 100 150 200 250 300 350
PDF
μ = 1.08, σ = 0.05
Gauss
μ = 1.08, σ = 0.05
HPD
μ = 1.08, σ = 0.05 (+0.04-0.04)
Asimov
x = 1.00 , σ = 0.06
0.9 0.95 1 1.05 1.1 1.15 1.2 1.25
b_80

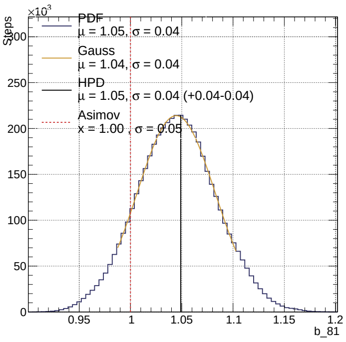
Steps
×10^3
0 50 100 150 200 250 300
PDF
μ = 1.05, σ = 0.04
Gauss
μ = 1.04, σ = 0.04
HPD
μ = 1.05, σ = 0.04 (+0.04-0.04)
Asimov
x = 1.00 , σ = 0.05
0.95 1 1.05 1.1 1.15 1.2
b_81

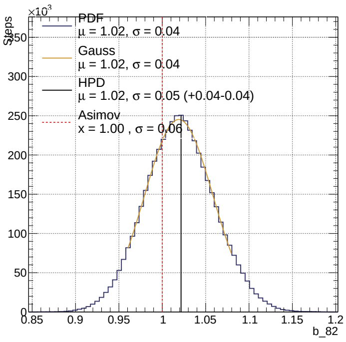
Steps
×10^3
0 50 100 150 200 250 300 350
PDF
μ = 1.02, σ = 0.04
Gauss
μ = 1.02, σ = 0.04
HPD
μ = 1.02, σ = 0.05 (+0.04-0.04)
Asimov
x = 1.00 , σ = 0.06
0.85 0.9 0.95 1 1.05 1.1 1.15 1.2
b_82

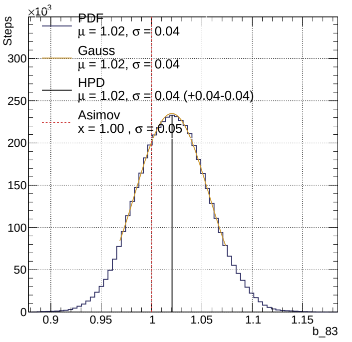
Steps
×10^3
0 50 100 150 200 250 300
PDF
μ = 1.02, σ = 0.04
Gauss
μ = 1.02, σ = 0.04
HPD
μ = 1.02, σ = 0.04 (+0.04-0.04)
Asimov
x = 1.00 , σ = 0.05
0.9 0.95 1 1.05 1.1 1.15
b_83

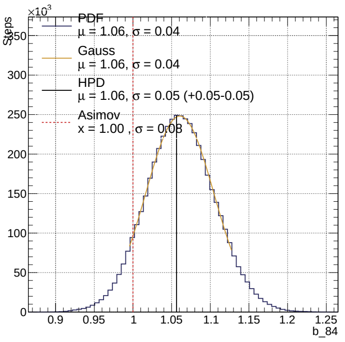
Steps
×10^3
0 50 100 150 200 250 300 350
PDF
μ = 1.06, σ = 0.04
Gauss
μ = 1.06, σ = 0.04
HPD
μ = 1.06, σ = 0.05 (+0.05-0.05)
Asimov
x = 1.00 , σ = 0.08
0.9 0.95 1 1.05 1.1 1.15 1.2 1.25
b_84

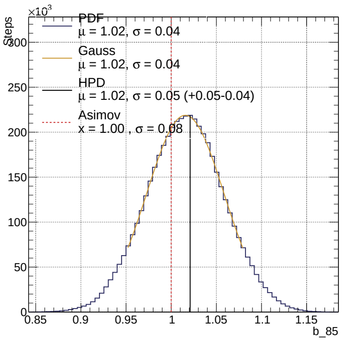
Steps
×10^3
0 50 100 150 200 250 300
PDF
μ = 1.02, σ = 0.04
Gauss
μ = 1.02, σ = 0.04
HPD
μ = 1.02, σ = 0.05 (+0.05-0.04)
Asimov
x = 1.00 , σ = 0.08
0.85 0.9 0.95 1 1.05 1.1 1.15
b_85

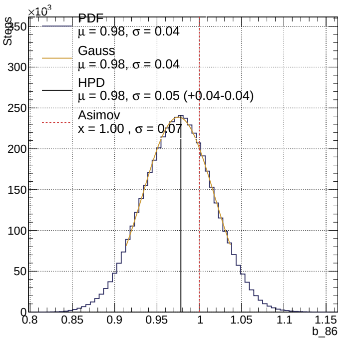
Steps
×10^3
0 50 100 150 200 250 300 350
PDF
μ = 0.98, σ = 0.04
Gauss
μ = 0.98, σ = 0.04
HPD
μ = 0.98, σ = 0.05 (+0.04-0.04)
Asimov
x = 1.00 , σ = 0.07
0.8 0.85 0.9 0.95 1 1.05 1.1 1.15
b_86

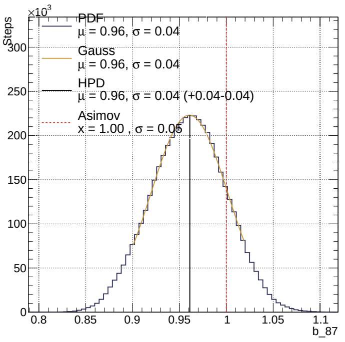
Steps
×10^3
0 50 100 150 200 250 300
PDF
μ = 0.96, σ = 0.04
Gauss
μ = 0.96, σ = 0.04
HPD
μ = 0.96, σ = 0.04 (+0.04-0.04)
Asimov
x = 1.00 , σ = 0.05
0.8 0.85 0.9 0.95 1 1.05 1.1
b_87

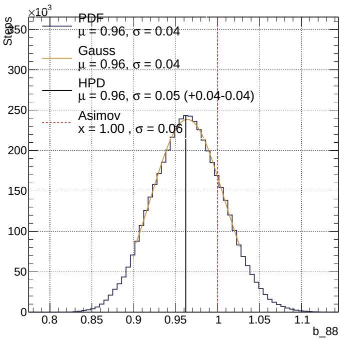
Steps
×10^3
0 50 100 150 200 250 300 350
PDF
μ = 0.96, σ = 0.04
Gauss
μ = 0.96, σ = 0.04
HPD
μ = 0.96, σ = 0.05 (+0.04-0.04)
Asimov
x = 1.00 , σ = 0.06
0.8 0.85 0.9 0.95 1 1.05 1.1
b_88

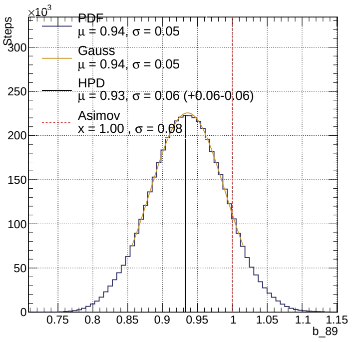
Steps
×10^3
0 50 100 150 200 250 300
PDF
μ = 0.94, σ = 0.05
Gauss
μ = 0.94, σ = 0.05
HPD
μ = 0.93, σ = 0.06 (+0.06-0.06)
Asimov
x = 1.00 , σ = 0.08
0.75 0.8 0.85 0.9 0.95 1 1.05 1.1 1.15
b_89

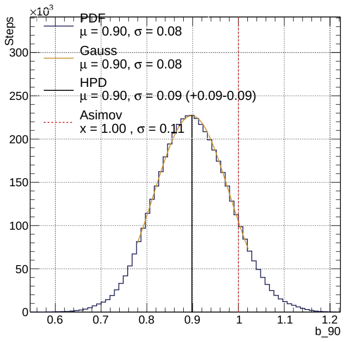
Steps
×10³
PDF
μ = 0.90, σ = 0.08
Gauss
μ = 0.90, σ = 0.08
HPD
μ = 0.90, σ = 0.09 (+0.09-0.09)
Asimov
x = 1.00 , σ = 0.11
0
50
100
150
200
250
300
0.6
0.7
0.8
0.9
1
1.1
1.2
b_90

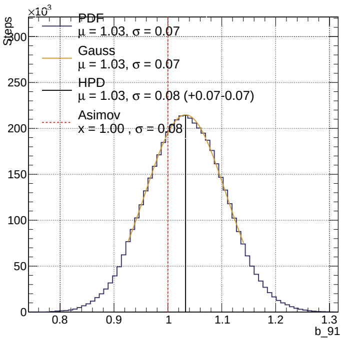
Steps
×10³
PDF
μ = 1.03, σ = 0.07
Gauss
μ = 1.03, σ = 0.07
HPD
μ = 1.03, σ = 0.08 (+0.07-0.07)
Asimov
x = 1.00 , σ = 0.08
0
50
100
150
200
250
300
0.8
0.9
1
1.1
1.2
1.3
b_91

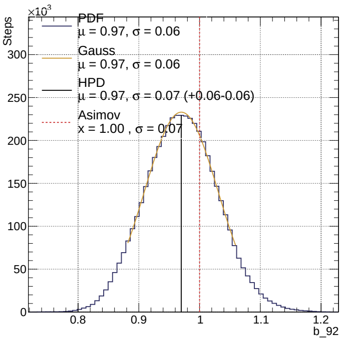
Steps
×10³
PDF
μ = 0.97, σ = 0.06
Gauss
μ = 0.97, σ = 0.06
HPD
μ = 0.97, σ = 0.07 (+0.06-0.06)
Asimov
x = 1.00 , σ = 0.07
0
50
100
150
200
250
300
0.8
0.9
1
1.1
1.2
b_92

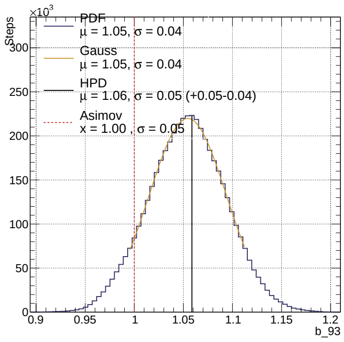
Steps
×10³
PDF
μ = 1.05, σ = 0.04
Gauss
μ = 1.05, σ = 0.04
HPD
μ = 1.06, σ = 0.05 (+0.05-0.04)
Asimov
x = 1.00 , σ = 0.05
0
50
100
150
200
250
300
0.9
0.95
1
1.05
1.1
1.15
1.2
b_93

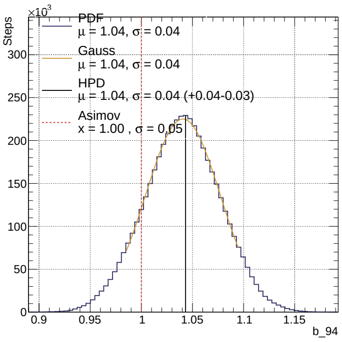
Steps
×10³
PDF
μ = 1.04, σ = 0.04
Gauss
μ = 1.04, σ = 0.04
HPD
μ = 1.04, σ = 0.04 (+0.04-0.03)
Asimov
x = 1.00 , σ = 0.05
0
50
100
150
200
250
300
0.9
0.95
1
1.05
1.1
1.15
b_94

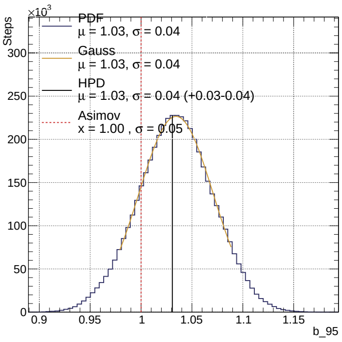
Steps
×10³
PDF
μ = 1.03, σ = 0.04
Gauss
μ = 1.03, σ = 0.04
HPD
μ = 1.03, σ = 0.04 (+0.03-0.04)
Asimov
x = 1.00 , σ = 0.05
0
50
100
150
200
250
300
0.9
0.95
1
1.05
1.1
1.15
b_95

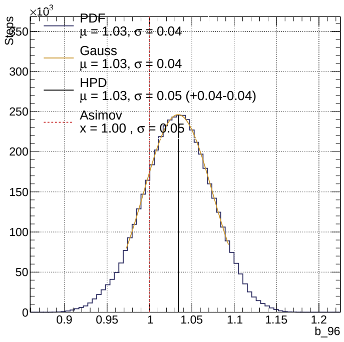
Steps
×10³
PDF
μ = 1.03, σ = 0.04
Gauss
μ = 1.03, σ = 0.04
HPD
μ = 1.03, σ = 0.05 (+0.04-0.04)
Asimov
x = 1.00 , σ = 0.05
0
50
100
150
200
250
300
350
0.9
0.95
1
1.05
1.1
1.15
1.2
b_96

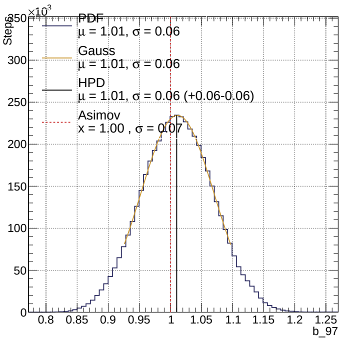
Steps
×10³
PDF
μ = 1.01, σ = 0.06
Gauss
μ = 1.01, σ = 0.06
HPD
μ = 1.01, σ = 0.06 (+0.06-0.06)
Asimov
x = 1.00 , σ = 0.07
0
50
100
150
200
250
300
350
0.8
0.85
0.9
0.95
1
1.05
1.1
1.15
1.2
1.25
b_97

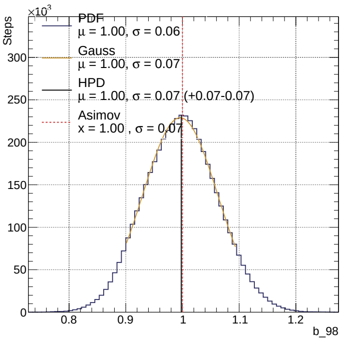
Steps
×10³
PDF
μ = 1.00, σ = 0.06
Gauss
μ = 1.00, σ = 0.07
HPD
μ = 1.00, σ = 0.07 (+0.07-0.07)
Asimov
x = 1.00 , σ = 0.07
0
50
100
150
200
250
300
0.8
0.9
1
1.1
1.2
b_98

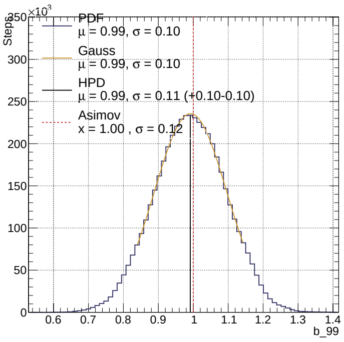
Steps
×10³
PDF
μ = 0.99, σ = 0.10
Gauss
μ = 0.99, σ = 0.10
HPD
μ = 0.99, σ = 0.11 (+0.10-0.10)
Asimov
x = 1.00 , σ = 0.12
0
50
100
150
200
250
300
350
0.6
0.7
0.8
0.9
1
1.1
1.2
1.3
1.4
b_99

B.11 Postfit Values for Detector Parameters

This Section presents the postfit distributions of ND280 detector systematic parameters from the ND280-only analysis, for each event sample. Fig. B.48 shows the plots for FHC samples, while Fig. B.49 for RHC samples. The bin numbering corresponds to the ND280 detector covariance matrix after the bin merging procedure. Oscillatory-like behaviour can be observed, which is the consequence of groups of bins corresponding to regions with increasing p_μ values for a fixed $\cos\theta_\mu$ bin. When reaching the upper edge of p_μ range, the results for the next region of $\cos\theta_\mu$ are plotted, with p_μ starting from 0 MeV/c again. Furthermore, the highest prior errors are for p_μ close to $\sim$30 GeV/c because many particles are produced at such high energy, resulting in high error for systematics such as pion or proton SI.

Additionally, we show the detector parameters for FD in Fig. B.50, where the posterior distributions come from ND+FD joint-fit. Contrary to ND detector parameters, those are very poorly constrained. This is expected, as FD has a much lower number of events and the fit poorly constrains the detector uncertainties.

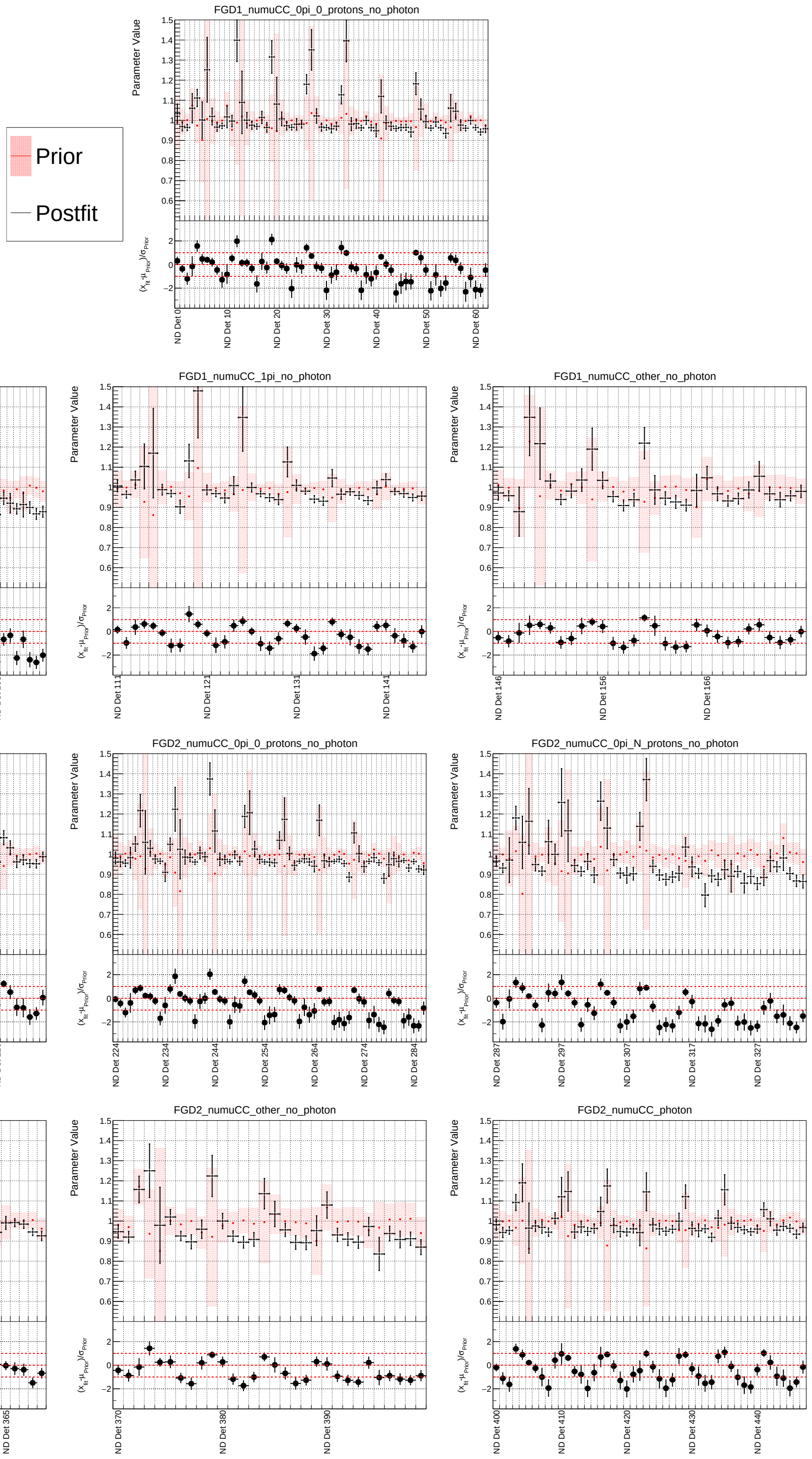

FIGURE B.48: Prefit and postfit values for ND280 detector parameters related to FHC samples.

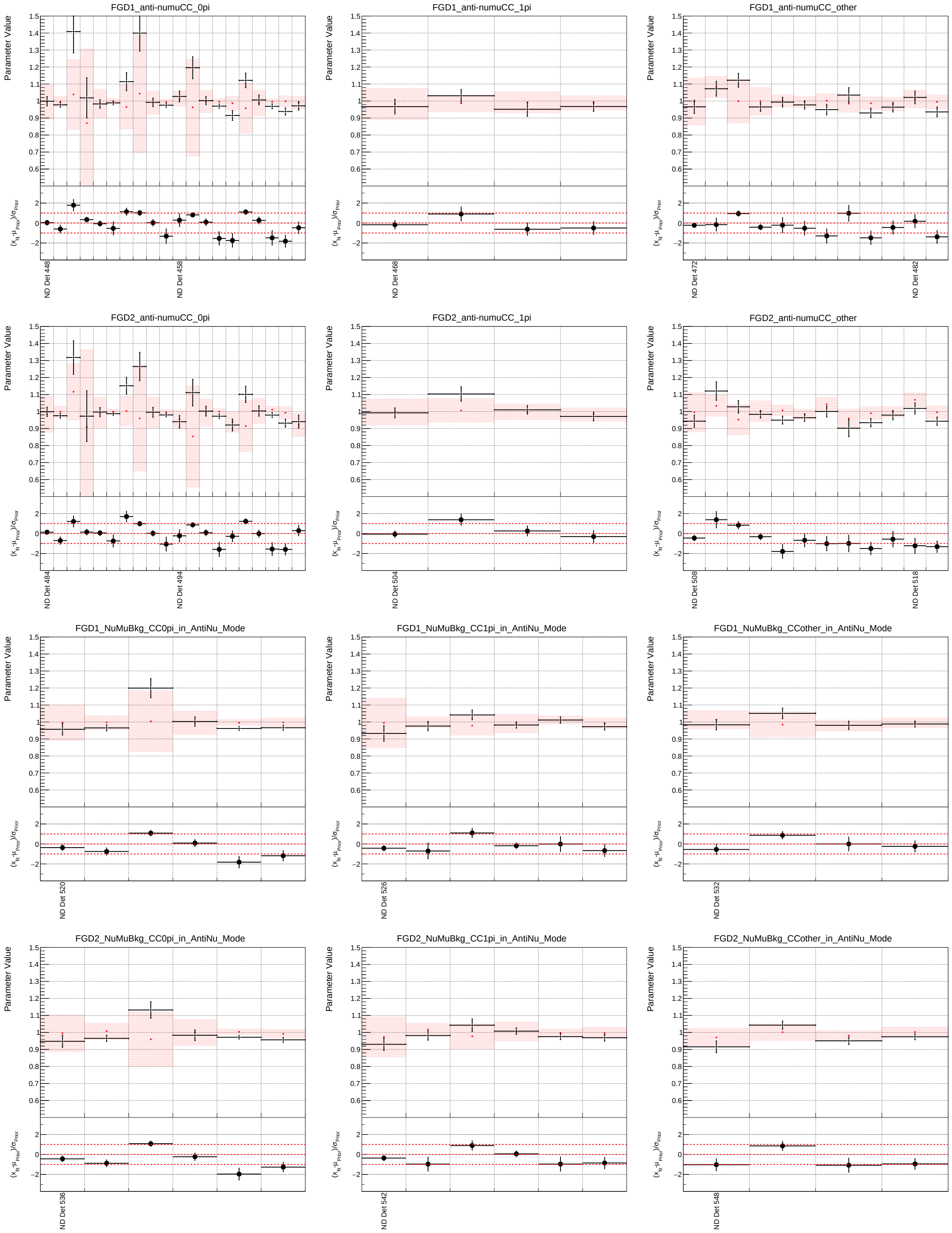

FIGURE B.49: Prefit and postfit values for ND280 detector parameters related to RHC samples.

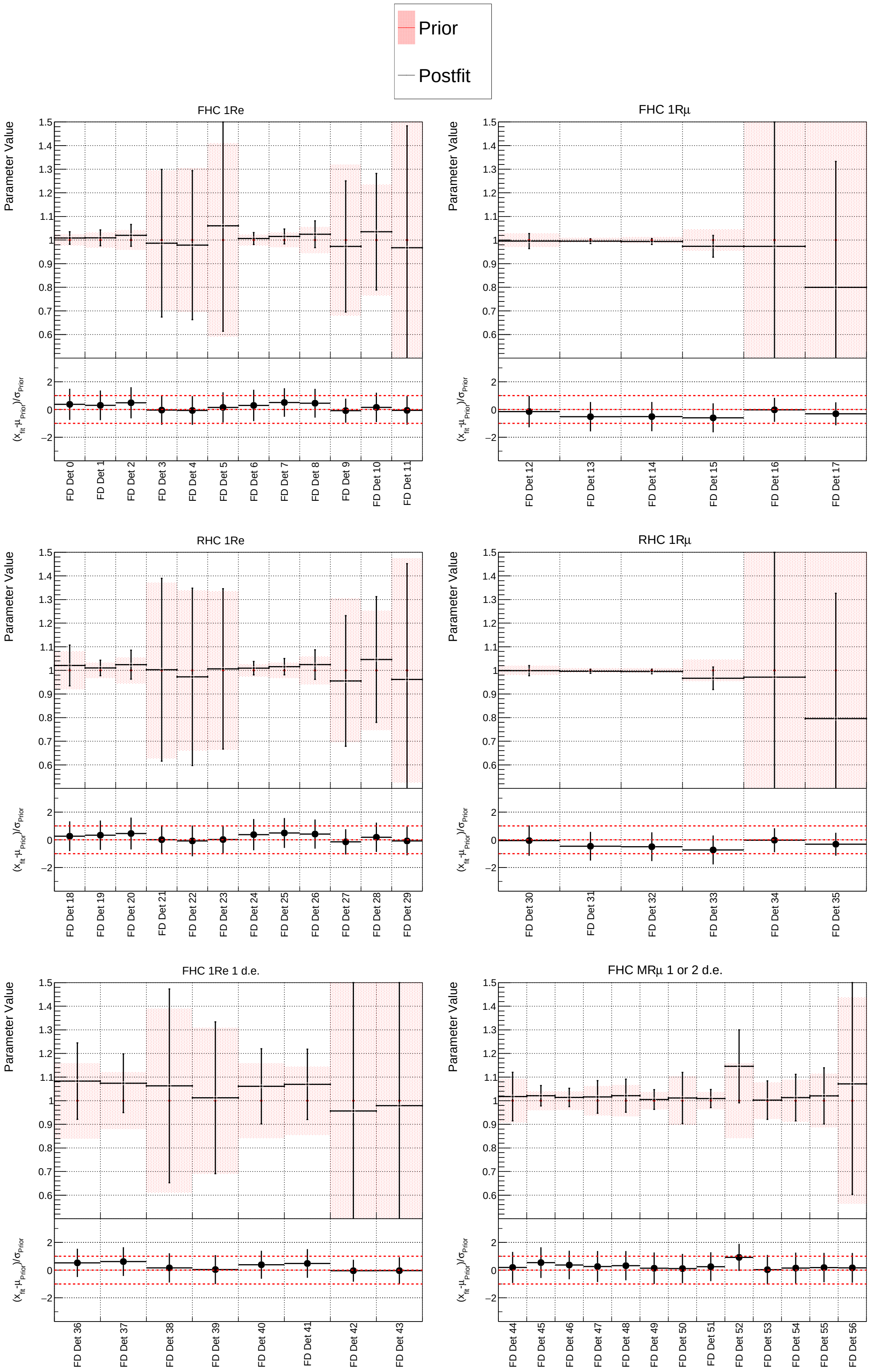

FIGURE B.50: Prefit and postfit values for FD detector parameters after ND+FD joint-fit.

Bibliography

[1] A. D. Sakharov. “Violation of CP Invariance, C asymmetry, and baryon asymmetry of the universe”. In: *Pisma Zh. Eksp. Teor. Fiz.* 5 (1967), pp. 32–35. DOI: `10.1070/PU1991v034n05ABEH002497`.

[2] D. Décamp et al. “A precise determination of the number of families with light neutrinos and of the Z boson partial widths”. In: *Phys. Lett. B* 235 (Dec. 1989), 399–411. 28 p. DOI: `10.1016/0370-2693(90)91984-J`.

[3] Ch. Bronner. *Recent results from T2K.* Neutrino 2022 Conference. URL: `https://indico.kps.or.kr/event/30/contributions/879/`.

[4] K. Skwarczynski. “Neutrino Oscillation Measurements at T2K”. In: *PoS* ICHEP2022 (2022), p. 606. DOI: `10.22323/1.414.0606`.

[5] M. Aker et al. “Direct neutrino-mass measurement with sub-electronvolt sensitivity”. In: *Nature Phys.* 18.2 (2022), pp. 160–166. DOI: `10.1038/s41567-021-01463-1`.

[6] C. Giunti and Ch. W. Kim. *Fundamentals of Neutrino Physics and Astrophysics*. Oxford University Press, 2007. DOI: `10.1093/acprof:oso/9780198508717.001.0001`.

[7] C. L. Cowan et al. “Detection of the free neutrino: A Confirmation”. In: *Science* 124 (1956), pp. 103–104. DOI: `10.1126/science.124.3212.103`.

[8] R. Davis Jr., D. S. Harmer, and K. C. Hoffman. “Search for neutrinos from the sun”. In: *Phys. Rev. Lett.* 20 (1968), pp. 1205–1209. DOI: `10.1103/PhysRevLett.20.1205`.

[9] B. Pontecorvo. “Inverse beta processes and nonconservation of lepton charge”. In: *Zh. Eksp. Teor. Fiz.* 34 (1957), p. 247.

[10] Y. Fukuda et al. “Evidence for oscillation of atmospheric neutrinos”. In: *Phys. Rev. Lett.* 81 (1998), pp. 1562–1567. DOI: `10.1103/PhysRevLett.81.1562`.

[11] L. Wolfenstein. “Neutrino oscillations in matter”. In: *Phys. Rev. D* 17 (9 May 1978), pp. 2369–2374. DOI: `10.1103/PhysRevD.17.2369`.

[12] Q. R. Ahmad et al. “Direct evidence for neutrino flavor transformation from neutral current interactions in the Sudbury Neutrino Observatory”. In: *Phys. Rev. Lett.* 89 (2002), p. 011301. DOI: `10.1103/PhysRevLett.89.011301`.

[13] University of Warwick. *Neutrino Oscillations*. URL: `https://warwick.ac.uk/fac/sci/physics/staff/academic/boyd/stuff/neutrinolectures/lec_oscillations.pdf`.

[14] A. Bellerive et al. “The Sudbury Neutrino Observatory”. In: *Nucl. Phys. B* 908 (2016), pp. 30–51. DOI: `10.1016/j.nuclphysb.2016.04.035`.

[15] M. P. Decowski. “KamLAND’s precision neutrino oscillation measurements”. In: *Nucl. Phys. B* 908 (2016), pp. 52–61. DOI: `10.1016/j.nuclphysb.2016.04.014`.

[16] JUNO Collaboration. “JUNO physics and detector”. In: *Prog. Part. Nucl. Phys.* 123 (2022), p. 103927. DOI: `10.1016/j.ppnp.2021.103927`.

[17] J. L. Hewett et al. “Fundamental Physics at the Intensity Frontier”. In: (May 2012). DOI: `10.2172/1042577`.

[18] E. Ma and G. Rajasekaran. "Softly broken A(4) symmetry for nearly degenerate neutrino masses". In: *Phys. Rev. D* 64 (2001), p. 113012. DOI: `10.1103/PhysRevD.64.113012`.

[19] C. R. Das et al. "Determination of the θ_{23} octant in long baseline neutrino experiments within and beyond the standard model". In: *Phys. Rev. D* 97.3 (2018), p. 035023. DOI: `10.1103/PhysRevD.97.035023`.

[20] I. Esteban et al. "The fate of hints: updated global analysis of three-flavor neutrino oscillations". In: *JHEP* 09 (2020), p. 178. DOI: `10.1007/JHEP09(2020)178`.

[21] J. H. Christenson et al. "Evidence for the 2π Decay of the K_2^0 Meson". In: *Phys. Rev. Lett.* 13 (4 July 1964), pp. 138–140. DOI: `10.1103/PhysRevLett.13.138`.

[22] C. Jarlskog. "Commutator of the Quark Mass Matrices in the Standard Electroweak Model and a Measure of Maximal CP Nonconservation". In: *Phys. Rev. Lett.* 55 (10 Sept. 1985), pp. 1039–1042. DOI: `10.1103/PhysRevLett.55.1039`.

[23] M. Tanabashi et al. "Review of Particle Physics". In: *Phys. Rev. D* 98 (3 Aug. 2018), p. 030001. DOI: `10.1103/PhysRevD.98.030001`.

[24] T. Suzuki and H. Senju. "A Theory of Primary Vector and Axial-Vector Interaction". In: *Progress of Theoretical Physics* 45.4 (Apr. 1971), pp. 1185–1202. ISSN: 0033-068X. DOI: `10.1143/PTP.45.1185`.

[25] M. Thomson. *Modern Particle Physics*. Cambridge University Press, 2013. DOI: `10.1017/CBO9781139525367`.

[26] E. Rutherford. "The scattering of alpha and beta particles by matter and the structure of the atom". In: *Phil. Mag. Ser. 6* 21 (1911), pp. 669–688. DOI: `10.1080/14786440508637080`.

[27] F. Zetsche et al. *Particles and Nuclei*. Springer, 2015. DOI: `10.1007/978-3-662-46321-5`.

[28] D. R. Yennie. "The Rosenbluth formula". In: (June 1963). URL: `https://www.osti.gov/biblio/4879243`.

[29] M. S. Athar and S. K. Singh. *The Physics of Neutrino Interactions*. Cambridge University Press, 2020. DOI: `10.1017/9781108489065`.

[30] D. I. Scully. "Neutrino Induced Coherent Pion Production". PhD thesis. Warwick U., 2013. URL: `https://danielscully.co.uk/thesis/thesis.pdf`.

[31] O. Tomalak. "Axial and pseudoscalar form factors from charged current quasielastic neutrino-nucleon scattering". In: *Phys. Rev. D* 103.1 (2021), p. 013006. DOI: `10.1103/PhysRevD.103.013006`.

[32] G. D. Megias et al. "New evaluation of the axial nucleon form factor from electron- and neutrino-scattering data and impact on neutrino-nucleus cross sections". In: *Phys. Rev. C* 101.2 (2020), p. 025501. DOI: `10.1103/PhysRevC.101.025501`.

[33] C. H. Llewellyn Smith. "Neutrino Reactions at Accelerator Energies". In: *Phys. Rept.* 3 (1972), pp. 261–379. DOI: `10.1016/0370-1573(72)90010-5`.

[34] C. Adamuscin et al. "Two-component model for the axial form factor of the nucleon". In: *Phys. Rev. C* 78 (2008), p. 035201. DOI: `10.1103/PhysRevC.78.035201`.

[35] B. Bhattacharya, R. J. Hill, and G. Paz. "Model independent determination of the axial mass parameter in quasielastic neutrino-nucleon scattering". In: *Phys. Rev. D* 84 (2011), p. 073006. DOI: `10.1103/PhysRevD.84.073006`.

[36] J. E. Sobczyk, J. Nieves, and F. Sánchez. "Exclusive-final-state hadron observables from neutrino-nucleus multinucleon knockout". In: *Phys. Rev. C* 102.2 (2020), p. 024601. DOI: `10.1103/PhysRevC.102.024601`.

[37] T. Golan. “Modeling nuclear effects in NuWro Monte Carlo neutrino event generator”. PhD thesis. Wroclaw U., 2014. URL: `http://wng.ift.uni.wroc.pl/files/Golan_PhD.pdf`.

[38] P. K. A. de Witt Huberts. “Proton spectral functions and momentum distributions in nuclei from high resolution (e, e-prime p) experiments”. In: *J. Phys. G* 16 (1990), pp. 507–544. DOI: `10.1088/0954-3899/16/4/004`.

[39] D. Rohe et al. “Correlated strength in nuclear spectral function”. In: *Phys. Rev. Lett.* 93 (2004), p. 182501. DOI: `10.1103/PhysRevLett.93.182501`.

[40] Y. Hayato and L. Pickering. “The NEUT neutrino interaction simulation program library”. In: *Eur. Phys. J. ST* 230.24 (2021), pp. 4469–4481. DOI: `10.1140/epjs/s11734-021-00287-7`.

[41] J. Chakrani et al. *NIWG model and uncertainties for 2021 oscillation analysis*. Tech. rep. T2K-TN-414. T2K, 2021.

[42] O. Benhar and D. Meloni. “Total neutrino and antineutrino nuclear cross sections around 1 GeV”. In: *Nuclear Physics A* 789.1 (2007), pp. 379–402. ISSN: 0375-9474. DOI: `https://doi.org/10.1016/j.nuclphysa.2007.02.015`.

[43] T. Sato, D. Uno, and T. S. H. Lee. “Dynamical model of weak pion production reactions”. In: *Phys. Rev. C* 67 (2003), p. 065201. DOI: `10.1103/PhysRevC.67.065201`.

[44] D. Rein and L. M. Sehgal. “Neutrino Excitation of Baryon Resonances and Single Pion Production”. In: *Annals Phys.* 133 (1981), pp. 79–153. DOI: `10.1016/0003-4916(81)90242-6`.

[45] K. M. Graczyk and J. T. Sobczyk. “Form Factors in the Quark Resonance Model”. In: *Phys. Rev. D* 77 (2008). [Erratum: Phys.Rev.D 79, 079903 (2009)], p. 053001. DOI: `10.1103/PhysRevD.79.079903`.

[46] C. Wilkinson et al. “Reanalysis of bubble chamber measurements of muon-neutrino induced single pion production”. In: *Phys. Rev. D* 90.11 (2014), p. 112017. DOI: `10.1103/PhysRevD.90.112017`.

[47] R. P. Feynman, M. Kislinger, and F. Ravndal. “Current matrix elements from a relativistic quark model”. In: *Phys. Rev. D* 3 (1971), pp. 2706–2732. DOI: `10.1103/PhysRevD.3.2706`.

[48] G. M. Radecky et al. “Study of Single Pion Production by Weak Charged Currents in Low-energy Neutrino *d* Interactions”. In: *Phys. Rev. D* 25 (1982). [Erratum: Phys.Rev.D 26, 3297 (1982)], pp. 1161–1173. DOI: `10.1103/PhysRevD.25.1161`.

[49] T. Kitagaki et al. “Charged Current Exclusive Pion Production in Neutrino Deuterium Interactions”. In: *Phys. Rev. D* 34 (1986), pp. 2554–2565. DOI: `10.1103/PhysRevD.34.2554`.

[50] J. M. Conrad, M. H. Shaevitz, and T. Bolton. “Precision measurements with high-energy neutrino beams”. In: *Rev. Mod. Phys.* 70 (4 Oct. 1998), pp. 1341–1392. DOI: `10.1103/RevModPhys.70.1341`.

[51] T. Katori and S. Mandalia. “PYTHIA hadronization process tuning in the GENIE neutrino interaction generator”. In: *J. Phys. G* 42.11 (2015), p. 115004. DOI: `10.1088/0954-3899/42/11/115004`.

[52] T. Yang et al. “A Hadronization Model for Few-GeV Neutrino Interactions”. In: *Eur. Phys. J. C* 63 (2009), pp. 1–10. DOI: `10.1140/epjc/s10052-009-1094-z`.

[53] Z. Koba, H. B. Nielsen, and P. Olesen. “Scaling of multiplicity distributions in high-energy hadron collisions”. In: *Nucl. Phys. B* 40 (1972), pp. 317–334. DOI: `10.1016/0550-3213(72)90551-2`.

[54] R. C. Misra. “The Koba-Nielsen-Olesen scaling function”. In: *Prog. Theor. Phys.* 51 (1974), pp. 1975–1976. DOI: 10.1143/PTP.51.1975.

[55] A. Bodek and U. K. Yang. “Higher twist, wscaling, and effective LO PDFs for lepton scattering in the few GeV region”. In: *Journal of Physics G: Nuclear and Particle Physics* 29.8 (July 2003), pp. 1899–1905. DOI: 10.1088/0954-3899/29/8/369.

[56] Ch. Bierlich et al. “A comprehensive guide to the physics and usage of PYTHIA 8.3”. In: (Mar. 2022). arXiv: 2203.11601 [hep-ph].

[57] K. Niewczas et al. “Modeling neutrino-nucleus interactions in the few-GeV region”. In: *PoS* NuFACT2018 (2019), p. 031. DOI: 10.22323/1.341.0031.

[58] A. Ershova et al. “Study of final-state interactions of protons in neutrino-nucleus scattering with INCL and NuWro cascade models”. In: (Feb. 2022). arXiv: 2202.10402 [hep-ph].

[59] M. Kabirnezhad. “Single pion production in electron-proton interactions”. In: (Mar. 2022). arXiv: 2203.15594 [hep-ph].

[60] C. Andreopoulos et al. “The GENIE Neutrino Monte Carlo Generator”. In: *Nucl. Instrum. Meth. A* 614 (2010), pp. 87–104. DOI: 10.1016/j.nima.2009.12.009.

[61] T. Golan, J. T. Sobczyk, and J. Zmuda. “NuWro: the Wroclaw Monte Carlo Generator of Neutrino Interactions”. In: *Nucl. Phys. B Proc. Suppl.* 229-232 (2012). Ed. by G. S. Tzanakos, pp. 499–499. DOI: 10.1016/j.nuclphysbps.2012.09.136.

[62] K. Abe et al. “Evidence of Electron Neutrino Appearance in a Muon Neutrino Beam”. In: *Phys. Rev. D* 88.3 (2013), p. 032002. DOI: 10.1103/PhysRevD.88.032002.

[63] G. Giacomelli et al. “Neutrino Oscillations in the Atmospheric Parameter Region: From the Early Experiments to the Present”. In: *Advances in High Energy Physics* 2013 (2013), p. 464926. URL: https://doi.org/10.1155/2013/464926.

[64] T. Sekiguchi et al. “Development and operational experience of magnetic horn system for T2K experiment”. In: *Nucl. Instrum. Meth. A* 789 (2015), pp. 57–80. DOI: 10.1016/j.nima.2015.04.008.

[65] K. Abe et al. “The T2K Neutrino Flux Prediction”. In: *Physical Review D* 87 (Nov. 2012). DOI: 10.1103/PhysRevD.87.012001.

[66] K. Abe et al. “The T2K Experiment”. In: *Nucl. Instrum. Meth. A* 659 (2011), pp. 106–135. DOI: 10.1016/j.nima.2011.06.067.

[67] G. Arnison et al. “Experimental Observation of Isolated Large Transverse Energy Electrons with Associated Missing Energy at $\sqrt{s} = 540$ GeV”. In: *Phys. Lett. B* 122 (1983), pp. 103–116. DOI: 10.1016/0370-2693(83)91177-2.

[68] P. A. Amaudruz et al. “The T2K Fine-Grained Detectors”. In: *Nucl. Instrum. Meth. A* 696 (2012), pp. 1–31. DOI: 10.1016/j.nima.2012.08.020.

[69] I. Giomataris et al. “Micromegas in a bulk”. In: *Nucl. Instrum. Meth. A* 560 (2006), pp. 405–408. DOI: 10.1016/j.nima.2005.12.222.

[70] N. Abgrall et al. “Time Projection Chambers for the T2K Near Detectors”. In: *Nucl. Instrum. Meth. A* 637 (2011), pp. 25–46. DOI: 10.1016/j.nima.2011.02.036.

[71] K. Hosokawa et al. “Development of Ultra-pure Gadolinium Sulfate for the Super-Kamiokande Gadolinium Project”. In: (Sept. 2022). arXiv: 2209.07273 [physics.ins-det].

[72] K. Abe et al. “Constraint on the matter–antimatter symmetry-violating phase in neutrino oscillations”. In: *Nature* 580.7803 (2020). [Erratum: Nature 583, E16 (2020)], pp. 339–344. DOI: 10.1038/s41586-020-2177-0.

[73] Z. Li et al. "Measurement of the tau neutrino cross section in atmospheric neutrino oscillations with Super-Kamiokande". In: *Phys. Rev. D* 98.5 (2018), p. 052006. DOI: `10.1103/PhysRevD.98.052006`.

[74] J. Lagoda. *Sand muon studies in ND280*. Tech. rep. T2K-TN-271. 2015.

[75] K. Abe et al. "Observation of Electron Neutrino Appearance in a Muon Neutrino Beam". In: *Phys. Rev. Lett.* 112 (2014), p. 061802. DOI: `10.1103/PhysRevLett.112.061802`.

[76] Y. Oyama. "J-PARC Neutrino Beamline and 1.3 MW Upgrade". In: *PoS* NuFact2019 (2020), p. 054. DOI: `10.22323/1.369.0054`. arXiv: `2004.06877 [physics.acc-ph]`.

[77] A. Blondel et al. "The SuperFGD Prototype Charged Particle Beam Tests". In: *JINST* 15.12 (2020), P12003. DOI: `10.1088/1748-0221/15/12/P12003`.

[78] L. Munteanu et al. "New method for an improved antineutrino energy reconstruction with charged-current interactions in next-generation detectors". In: *Phys. Rev. D* 101.9 (2020), p. 092003. DOI: `10.1103/PhysRevD.101.092003`.

[79] T. Doyle. "Development of New Off-Axis Near Detector Samples for the T2K Oscillation Analysis". PhD thesis. Lancaster University, 2022. URL: `https://doi.org/10.17635/lancaster/thesis/1655`.

[80] J. Lagoda. "Latest oscillation results from T2K". In: *PoS* NuFact2021 (2022), p. 054. DOI: `10.22323/1.402.0054`.

[81] J. Nieves, I. Ruiz Simo, and M. J. Vicente Vacas. "The nucleon axial mass and the MiniBooNE Quasielastic Neutrino-Nucleus Scattering problem". In: *Phys. Lett. B* 707 (2012), pp. 72–75. DOI: `10.1016/j.physletb.2011.11.061`.

[82] S. Dolan, G. D. Megias, and S. Bolognesi. "Implementation of the SuSAv2-MEC 1p1h and 2p2h models in GENIE and analysis of nuclear effects in T2K measurements". In: *Phys. Rev.* D101 (2020), p. 033003. DOI: `10.1103/PhysRevD.101.033003`.

[83] C. Wret. "Minimising systematic uncertainties in the T2K experiment using near-detector and external data". PhD thesis. Imperial College London, 2018. URL: `https://doi.org/10.25560/73862`.

[84] P. Bartet et al. *ν_μ CC event selections in the ND280 tracker using Run 2+3+4 data*. Tech. rep. T2K-TN-212. 2015.

[85] M. Lorenzo. "Measurement of muon anti-neutrino CC interactions with the ND280 detector". PhD thesis. University of Bari, 2015. URL: `https://www.t2k.org/docs/thesis/050/nubar`.

[86] N. Abgrall et al. "Measurements of $\pi^{\pm}$, $K^{\pm}$ and proton double differential yields from the surface of the T2K replica target for incoming 31 GeV/c protons with the NA61/SHINE spectrometer at the CERN SPS". In: *Eur. Phys. J. C* 79.2 (2019), p. 100. DOI: `10.1140/epjc/s10052-019-6583-0`.

[87] N. Abgrall et al. "Measurements of $\pi^{\pm}$ differential yields from the surface of the T2K replica target for incoming 31 GeV/c protons with the NA61/SHINE spectrometer at the CERN SPS". In: *Eur. Phys. J. C* 76.11 (2016), p. 617. DOI: `10.1140/epjc/s10052-016-4440-y`.

[88] L. Berns et al. *Flux Prediction and Uncertainty with NA61/SHINE 2010 Replica-Target Data*. Tech. rep. T2K-TN-401. 2022.

[89] T. Dieminger et al. *Assessing out-of-model cross-section effects with fits to simulated data*. Tech. rep. T2K-TN-441. T2K, 2022.

[90] S. Bolognesi et al. *Updated recommendation of the 2018 NIWG parameters*. Tech. rep. T2K-TN-344. 2020.

[91] M. Kabirnezhad. “Single pion production in neutrino-nucleon Interactions”. In: *Phys. Rev. D* 97.1 (2018), p. 013002. DOI: `10.1103/PhysRevD.97.013002`.

[92] A. Bodek and U. K. Yang. “Axial and Vector Structure Functions for Electron- and Neutrino- Nucleon Scattering Cross Sections at all Q^2 using Effective Leading order Parton Distribution Functions”. In: (2013). arXiv: `1011.6592`.

[93] R. Brun and F. Rademakers. “ROOT: An object oriented data analysis framework”. In: *Nucl. Instrum. Meth. A* 389 (1997). Ed. by M. Werlen and D. Perret-Gallix, pp. 81–86. DOI: `10.1016/S0168-9002(97)00048-X`.

[94] K. Niewczas and J. T. Sobczyk. “Nuclear transparency in Monte Carlo neutrino event generators”. In: *Phys. Rev. C* 100 (1 July 2019), p. 015505. DOI: `10.1103/PhysRevC.100.015505`.

[95] T. Katori. “Meson Exchange Current (MEC) Models in Neutrino Interaction Generators”. In: *AIP Conf. Proc.* 1663.1 (2015). Ed. by H. Da Motta, Jorge G. Morfin, and M. Sakuda, p. 030001. DOI: `10.1063/1.4919465`.

[96] I. R. Simo et al. “Emission of neutron–proton and proton–proton pairs in neutrino scattering”. In: *Physics Letters B* 762 (2016), pp. 124–130. ISSN: 0370-2693. DOI: `https://doi.org/10.1016/j.physletb.2016.09.021`.

[97] J. Walsh. “Constraining the T2K neutrino oscillation parameter results using data from the off-axis near detector, ND280: Implementation of a nucleon removal energy systematic uncertainty treatment in the BANFF fit”. PhD thesis. Lancaster U. (main), Lancaster U., 2022. DOI: `10.17635/lancaster/thesis/1604`.

[98] F. James. “MINUIT Fysis: Reference Manual Version 94.1”. In: (1994). URL: `https://cds.cern.ch/record/2296388`.

[99] The MaCh3 Collaboration. *MaCh3 Software*. URL: `https://zenodo.org/record/7608419#.Y-BgaC8RrpA`.

[100] A. Birnbaum. “On the Foundations of Statistical Inference”. In: *Journal of the American Statistical Association* 57.298 (1962), pp. 269–306. ISSN: 01621459. URL: `http://www.jstor.org/stable/2281640` (visited on 10/14/2022).

[101] S. S. Wilks. “The Large-Sample Distribution of the Likelihood Ratio for Testing Composite Hypotheses”. In: *The Annals of Mathematical Statistics* 9.1 (1938), pp. 60–62. DOI: `10.1214/aoms/1177732360`.

[102] R. J. Barlow and Ch. Beeston. “Fitting using finite Monte Carlo samples”. In: *Comput. Phys. Commun.* 77 (1993), pp. 219–228. DOI: `10.1016/0010-4655(93)90005-W`.

[103] J. S. Conway. “Incorporating Nuisance Parameters in Likelihoods for Multisource Spectra”. In: *PHYSTAT 2011*. 2011, pp. 115–120. DOI: `10.5170/CERN-2011-006.115`.

[104] A. A. Markov. “An Example of Statistical Investigation of the Text Eugene Onegin Concerning the Connection of Samples in Chains”. In: *Science in Context* 19.4 (2006), pp. 591–600. DOI: `10.1017/S0269889706001074`.

[105] R. Fewster. *Chapter 9: Equilibrium*. URL: `https://www.stat.auckland.ac.nz/~fewster/325/notes/ch9.pdf`.

[106] J. Wallin and D. Bolin. “Efficient adaptive MCMC through precision estimation”. In: *Journal of Computational and Graphical Statistics* 27.4 (2018), pp. 887–897. DOI: `10.1080/10618600.2018.1459303`.

[107] M. Bonamente. *Statistics and Analysis of Scientific Data*. Springer, 2013. DOI: `10.1007/978-1-4614-7984-0`.

[108] W. K. Hastings. "Monte Carlo Sampling Methods Using Markov Chains and Their Applications". In: *Biometrika* 57 (1970), pp. 97–109. DOI: `10.1093/biomet/57.1.97`.

[109] A. Sztuc. "Standard and non-standard neutrino-antineutrino oscillation analyses and event reconstruction studies using Markov chain Monte Carlo methods at T2K". PhD thesis. Imperial College London, 2020. URL: `https://spiral.imperial.ac.uk:8443/bitstream/10044/1/91769/1/Sztuc-A-2021-PhD-Thesis.pdf`.

[110] A. Gelman et al. *Bayesian Data Analysis*. Taylor & Francis Ltd, 2013. DOI: `10.1201/b16018`.

[111] T. Holvey et al. *MaCh3 2021 Run 1-10 Analysis and including Multi-Ring Sample*. Tech. rep. T2K-TN-429. T2K, 2022.

[112] H. Jeffreys. *The theory of probability*. UOP Oxford, 1998. DOI: `10.2307/3619118`.

[113] A. Nikolakopoulos et al. "Benchmarking intranuclear cascade models for neutrino scattering with relativistic optical potentials". In: *Phys. Rev. C* 105.5 (2022), p. 054603. DOI: `10.1103/PhysRevC.105.054603`.

[114] S. Dolan et al. "Sensitivity of the upgraded T2K Near Detector to constrain neutrino and antineutrino interactions with no mesons in the final state by exploiting nucleon-lepton correlations". In: *Phys. Rev. D* 105.3 (2022), p. 032010. DOI: `10.1103/PhysRevD.105.032010`.

[115] L. Pickering. "Examining nuclear effects in neutrino interactions with transverse kinematic imbalance". In: *JPS Conf. Proc.* 12 (2016), p. 010032. DOI: `10.7566/JPSCP.12.010032`.

[116] C. Jesús-Valls. "Performances of two resistive MicroMegas prototypes for the Time Projection Chambers of the T2K Near Detector upgrade". In: *JINST* 15.08 (2020), p. C08016. DOI: `10.1088/1748-0221/15/08/C08016`.

[117] D. Attié et al. "Characterization of resistive Micromegas detectors for the upgrade of the T2K Near Detector Time Projection Chambers". In: *Nucl. Instrum. Meth. A* 1025 (2022), p. 166109. DOI: `10.1016/j.nima.2021.166109`.

[118] D. Dutta et al. "A Study of the quasielastic (e,e-prime p) reaction on C-12, Fe-56 and Au-97". In: *Phys. Rev. C* 68 (2003), p. 064603. DOI: `10.1103/PhysRevC.68.064603`.

[119] K. Yasutome. "Towards the measurement of neutrino cross section on H_2O and CH target at 1 GeV region by T2K-WAGASCI experiment". In: *PoS* NuFact2021 (2022), p. 075. DOI: `10.22323/1.402.0075`.

[120] K. Abe et al. "Hyper-Kamiokande Design Report". In: (May 2018). arXiv: `1805.04163 [physics.ins-det]`.

[121] J. Xia. *T2K-Super-Kamiokande Joint Neutrino Oscillation Sensitivity*. Neutrino Oscilation Workshop 2022. URL: `https://agenda.infn.it/event/30418/contributions/170689/`.

[122] K. Abe et al. "Diffuse supernova neutrino background search at Super-Kamiokande". In: *Phys. Rev. D* 104.12 (2021), p. 122002. DOI: `10.1103/PhysRevD.104.122002`.

[123] J. Bian et al. "Hyper-Kamiokande Experiment: A Snowmass White Paper". In: *2022 Snowmass Summer Study*. Mar. 2022. arXiv: `2203.02029 [hep-ex]`.

[124] J. E. Sobczyk. "Nuclear effects in neutrino-nucleus interactions: the role of spectral functions". PhD thesis. Universitat de València, 2019. URL: `https://digital.csic.es/handle/10261/223987`.

[125] N. Jachowicz et al. “Continuum random phase approximation approach to charged current neutrino nucleus scattering”. In: *Phys. Rev. C* 65 (2002), p. 025501. DOI: 10.1103/PhysRevC.65.025501.

[126] V. Pandey et al. “Low-energy excitations and quasielastic contribution to electron-nucleus and neutrino-nucleus scattering in the continuum random-phase approximation”. In: *Phys. Rev. C* 92.2 (2015), p. 024606. DOI: 10.1103/PhysRevC.92.024606.

[127] M. Martini et al. “A Unified approach for nucleon knock-out, coherent and incoherent pion production in neutrino interactions with nuclei”. In: *Phys. Rev. C* 80 (2009), p. 065501. DOI: 10.1103/PhysRevC.80.065501.

[128] C. A. Argüelles, A. Schneider, and T. Yuan. “A binned likelihood for stochastic models”. In: *JHEP* 06 (2019), p. 030. DOI: 10.1007/JHEP06(2019)030.

[129] A. Gelman, X. L. Meng, and H. Stern. “Posterior predictive assessment of model fitness via realized discrepancies”. In: *Statistica sinica* (1996), pp. 733–760. URL: http://www.stat.columbia.edu/~gelman/research/published/A6n41.pdf.

[130] A. Gelman et al. “Diagnostic checks for discrete data regression models using posterior predictive simulations”. In: *Appl. Statist.* 49 Par 2 (2000), pp. 247–268. DOI: 10.1111/1467-9876.00190.

[131] A. Gelman. “Understanding posterior p-values”. In: *Electronic Journal of Statistics* (2013). DOI: 10.1214/13-EJS854.

Acronyms

2p2h Two Particles Two Holes - an interaction where because of correlations two nucleons are ejected from the target nucleus.

AGKY Andreopoulos-Gallagher-Kehayias-Yang - hadronization model which provides information about the multiplicities and kinematics of the produced hadrons.

BANFF Beam And ND280 Flux measurement task Force - ND280 gradient descent fitter, using frequentist approach.

BY Bodek-Yang - authors of the correction to DIS which affect cross-section at low Q^2.

CC Charged Current - an interaction mediated by $W^{\pm}$.

CCQE Charged Current Quasi Elastic - a type of neutrino interaction with a charged lepton and a nucleon in the final state.

CEX Charge Exchange - process in which $\pi^{\pm}$ turns into π^0.

COH Coherent - a process where a neutrino interacts with a nucleus as a whole.

CP Charge-Parity symmetry.

DIS Deep Inelastic Scattering - a process where the structure of hadrons is being probed.

FD Far Detector (Super-Kamiokande detector as a part of T2K experiment).

FGD Fine Grained Detector - ND280 scintillation sub-detector, part of the tracker.

FHC Forward Horn Current - neutrino beam mode.

FSI Final State Interactions - secondary interactions occurring inside target nucleus.

FV Fiducial Volume of the detector.

GPU Graphics Processing Unit.

GR Global Reconstruction, responsible for merging tracks and hits from different sub-detectors of ND280.

HMNT Highest Momentum Negative Track, muon candidate track in FHC and RHC BKG samples.

HPD Highest Posterior Density - a statistical method to extract the maximum of a distribution.

IH Inverted Hierarchy of neutrino masses.

INGRID Interactive Neutrino GRID - on-axis T2K near detector.

isoFGD a track fully contained in one of FGDs.

J-PARC Japan Proton Accelerator Research Complex - the research facility producing $\nu(\bar{\nu})$ beam for the T2K experiment, also the location of the near detectors.

KNO Koba-Nielsen-Olesen - a law stating that the cross-section for producing n charged particles is independent of energy.

LLH Log Likelihood - according to Wilks' theorem [101] -2LLH approaches asymptotically $\Delta\chi^2$.

MaCh3 Markov Chain 3 - T2K MCMC fitter, using Bayesian approach.

MCMC Markov chain Monte Carlo - a method for sampling from a probability distribution.

MEC Meson Exchange Current - a process where a meson is propagated between nucleons, and one of them also is interacting with neutrino.

MF Mean Field - part of SF where nucleon interacts only with the mean potential of the nucleus.

NC Neutral Current - an interaction mediated by Z^0.

ND Near Detector - T2K has two such detectors (on- and off-axis), however in this Thesis this abbreviation is used only for ND280.

ND280 Near Detector at 280 m - off-axis T2K near detector.

NEUT Neutrino event generator used in T2K experiment [40].

NH Normal Hierarchy of neutrino masses.

OA Oscillation Analysis.

OOFV Out-of-Fiducial-Volume.

PID Particle Identification.

POT Protons on Target - a unit to measure accumulated data.

RES Resonant - the process where Δ (or other) resonance is produced in the intermediate state. One of Δ decay products is π.

RHC Reverse Horn Current - antineutrino beam mode. When discussing event samples, it refers to $\bar{\nu}$ component of the antineutrino beam.

RHC BKG Reverse Horn Current Background - refers to ν component in RHC.

SF Spectral Function - advanced model which takes into account the shell structure of the nucleus and is tuned to electron scattering data.

SFGD Super Fine Grained Detector - part of ND280 upgrade, detector consisting of novel scintillator cubes.

SI	Secondary Interactions - interactions occurring in the detector after produced particles left the target nucleus.
SK	Super-Kamiokande - T2K far detector located 295 km away from the near detector.
SPP	Single Pion Production - a process when a single pion is produced, most often from resonant interaction.
SRC	Short Range Correlations - part of SF where on top of mean potential there are nucleon correlations resulting in two nucleons being ejected from the target nucleus after neutrino interaction.
T2K	Tokai to Kamioka - long baseline neutrino experiment located in Japan.
TPC	Time Projection Chamber, ND280 sub-detector, part of the tracker.
xsec	Cross-Section.